THE RISE OF TAYLOR BUBBLES IN VERTICAL AND INCLINED PIPES

Enass Z. Massoud

A thesis submitted in fulfilment of the requirements for the degree of

Doctor of Philosophy

Department of Naval Architecture, Ocean and Marine Engineering

University of Strathclyde

Glasgow

2019

I would like to dedicate this thesis to my loving parents, husband & son…

Declaration

This thesis is the result of the author's original research except where otherwise indicated. It has been composed by the author and has not been previously submitted for examination, which has led to the award of a degree.

The copyright of this thesis belongs to the author under the terms of the United Kingdom Copyright Acts as qualified by University of Strathclyde Regulation 3.50. Due acknowledgement must always be made of the use of any material contained in, or derived from, this thesis.

Enass Z. Massoud

Signature: Date:

Acknowledgements

In the beginning, I would like to thank "Allah Taala" for his infinite blessings and guidance that assisted me to complete this work successfully.

I wish to extend my deepest gratefulness and sincere appreciation to all those who offered me advice and suggestions. First of all, I would like to express my gratitude to my first supervisor, Dr. Xiao, who has supported me throughout my PhD stages. I want to thank my second supervisor, Professor Atilla Incecik, for offering his continuous help and support during my PhD study.

Secondly, I am indebted to my senior colleague, Professor Hassan A. El-Gamal, for his continuous guidance, patience and support during the progress of this research and his comments on the draft of the thesis. From the inception of this study until its completion, Prof. El-Gamal has generously provided me with both the guidance and encouragement which have measurably contributed to the completion of this work. He taught me how to be a researcher. He always inspires me with his enthusiasm for life and work.

I am thankful to Prof. Elsayed Saber, Head of Mechanical Engineering Department, Arab Academy for Science, Technology and Maritime Transport (AASTMT), for his continuous support and valuable suggestions during my research work.

I am also thankful to my colleagues in both the Mechanical Engineering Department, AASTMT, Egypt and the Department of Naval Architecture, Ocean and Marine Engineering, Faculty of Engineering, University of Strathclyde, Glasgow UK, for their support and continuous guidance during my PhD study.

I am indebted to my parents for their support in all respects. I wish to express my gratitude to my husband, Dr Aly El-Haridi, and my son, Adham, who have gracefully shared and endured my ups and downs during this endeavour, in addition to all efforts, patience and support for without them, none of this would have ever been possible.

I would like to thank the Department of Naval Architecture, Ocean and Marine Engineering, Faculty of Engineering, the University of Strathclyde for giving me access to HPC facility for my numerical simulations.

Finally, I would like to thank the financial assistance from the Arab Academy for Science and Technology and Maritime Transport (AASTMT). This work would not have been possible without their help and support.

Abstract

Slug flow is one of the key flow regimes encountered in multiphase flow systems. Through reviewing the literature, the researcher identified a research gap in performing a theoretical treatment to the problem, specifically using the dimensionless treatment and the order of magnitude analysis of equations of motions. To the best of the researcher's knowledge, an analysis of the literature identifies that there is a lack in the numerical studies on the drift of Taylor bubbles in inclined pipes with stagnant liquid.

This thesis focuses on studying the flow of the Taylor bubble in the stagnant liquid, which is considered an essential characteristic part of the slug flow regime in pipes by performing theoretical treatment of the problem. To achieve this, the following two steps are carried out (i) Performing a complete dimensionless analysis to the rise of Taylor bubble through stagnant liquid in a vertical and inclined pipe, covering inclination range of $0 \leq \gamma \leq 90°$ with respect to the vertical position, (ii) Using the guideline of the order of magnitude analysis and the dimensionless group analysis, performing CFD study using the volume-of-fluid (VOF) methodology implemented in the commercial software ANSYS Fluent (Release 16.0) investigating the dynamics of single Taylor bubble drifting through stagnant Newtonian liquid in vertical and inclined pipe.

The dimensionless analysis shows that different governing parameters appear according to the range of pipe inclination angle.

The adopted CFD model shows good results for the dynamics of the Taylor bubble covering three main regions the bubble nose, the bubble body and the bubble wake regions.

The simulation results show good agreement with the developed dimensionless treatment of the problem for all pipe inclination. No bubble propagates in a zero axial pressure gradient horizontal pipe, hence, a simplified model is suggested to solve the challenging problem of the three-dimensional Taylor bubble in the near horizontal and horizontal pipes.

Table of Contents

List of Figures

List of Tables

Nomenclature

Symbol	Definition	Units
C	Constant given in equation (2-3)	(-)
C_∞	Coefficient given in equation (2-16) according to Bendiksen (1984)	(-)
D, D_{pipe}	Pipe diameter	(m)
F	Force	(N)
f_m	Coefficient given in equation (2-21)	(-)
g	Acceleration due to gravity	(m s^{-2})
$\grave{g}$	Coefficient given in equation (2-16)	(m s^{-2})
h_B	The distance of the Taylor bubble initial shape from the pipe bottom	(m)
K	Radius of curvature	(m)
L	Length of pipe	(m)
L_{min}	The perturbed distance below the bubble	(m)
m	Coefficient given in equation (2-5)	(-)
$\dot{m}$	Mass transfer	(kg s^{-1})
n	Unit normal of the interface	(-)
n_{step}	Time step	(s)
N	Number of phases	(-)
P, p	Pressure	(Pa)
Q	Coefficient given in equations (2-19) and equation (2-23)	(-)
r	Radial coordinate	(m)
r_1 and r_2	Local principal radii of curvature at the bubble surface by Mao and Dukler (1990)	(m)
R	Pipe radius	(m)
R_B	The curvature radius of the bubble bottom	(m)
R_N	The radius of curvature at the nose	(m)
R_V	Corresponding coordinates of the recirculation core behind the bubble	(m)
S	Mass source per unit volume	(kg m^{-3} s^{-1})
t	Time	(s)
t_{bubble}	Bubble's passage time	(s)
$\bar{t}_{bubble}$	The criterion for film breakup	(-)
u	Velocity in x direction	(m s^{-1})
u_{ch}	Characteristic velocity	(m s^{-1})
$u_{squeeze}$	maximum squeeze liquid velocity in the liquid film	(m s^{-1})
U_f	Volume flux through the control volume face	(m^3 s^{-1})
v	Velocity in y-direction	(m s^{-1})
v_d	Bubble drift velocity in an inclined pipe	(m s^{-1})
$v_{d\infty}$	Drift velocity according to Zukoski (1966)'s correlation	(m s^{-1})
v_r	Velocity in the radial direction	(m s^{-1})
v_s	Characteristic velocity chosen in such a way to treat the flow with low values of Reynolds number $\left(Re_{v_s}\right)$	(m s^{-1})
v_θ	Velocity in the tangential direction	(m s^{-1})
v_z	Velocity in the axial direction	(m s^{-1})
V	Velocity vector	(m s^{-1})

Symbol	Definition	Units
V_S	Characteristic velocity for stagnant fluid	(m s^{-1})
V_L	Relative liquid velocity to the bubble in moving reference frame (MRF)	(m s^{-1})
$\mathcal{V}$	Volume	(m^3)
$\mathcal{V}_W$	The volume of the wake	(m^3)
w	Velocity component in z direction	(m s^{-1})
x	x coordinate	(m)
y	y coordinate	(m)
y_{tip}	Bubble tip position with respect to the pipe axis	(m)
z	z coordinate	(m)
Z'	Interaction distance above the bubble	(m)
Z_V	Corresponding coordinates of the recirculation core behind the bubble	(m)
Z^*	The length needed for the fully developed annular liquid film	(m)
Δt	Time step	(s)
Δx	Cell size	(m)

Greek symbols

Symbol	Definition	Units
α	Volume fraction	(-)
δ_{LF},δ	Liquid film thickness	(m)
$\hat{\delta}_{eq}$	The dimensionless equilibrium film thickness	(-)
γ	Inclination angle	(°)
μ	Dynamic viscosity	(Pa s)
ν	Kinematic viscosity	(m^2 s^{-1})
ρ	Density	(kg m^{-3})
σ	Surface tension	(N m^{-1})
τ	Shear stress	(Pa s)
τ_{ch}	Characteristic film drainage time	(-)
τ_W	Wall shear stress	(Pa s)
φ	Scalar quantity	(-)
Γ_ρ	Density ratio, $\Gamma_\rho = \frac{\rho_L}{\rho_G}$	(-)
Γ_μ	Viscosity ratio, $\Gamma_\mu = \frac{\mu_L}{\mu_G}$	(-)

Dimensionless groups

Symbol	Name	Definition
Ar	Archimedes number	$Ar = \frac{{\rho_L}^2 g D^3}{{\mu_L}^2}$
Cr	Courant number	$Cr = \frac{u_{ch}\Delta t}{\Delta x} \leq 1$
Eo	Eötvös number	$Eo = \frac{g \rho_L D^2}{\sigma}$
$Fr_{U_{TB}}$	Froude number based on the bubble rise velocity in vertical pipes	$Fr_{U_{TB}} = \frac{U_{TB}}{\sqrt{gD}}$
Fr_{v_d}	Froude number based on the bubble drift velocity in inclined pipes	$Fr_{v_d} = \frac{{v_d}^2}{gD}$
Ga_R	Reduced Galilei number	$Ga_R = \left(\frac{g {L_{TB}}^3}{{\nu_L}^2}\right)\left(\frac{D}{2L_{TB}}\right)^2$
M	Morton number	$M = \frac{\Delta\rho g \mu_L^4}{\rho_L^2 \sigma^3}$
N_f	Inverse viscosity number	$N_f = \frac{\rho_L (gD^3)^{0.5}}{\mu_L}$
$Re_{modified}$	Modified Reynolds number	$Re_{modified} = \frac{V_s D}{\nu}$
$Re_{U_{TB}}$	Reynolds number based on the bubble rise velocity in vertical pipes	$Re_{U_{TB}} = \frac{\rho_L U_{TB} D}{\mu_L}$
$Re_{U_{LF}}$	Reynolds number based on the velocity of the annular liquid film	$Re_{U_{LF}} = \frac{\rho_L U_{LF}\, \delta_{LF}}{\mu_L}$
Re_{v_d}	Reynolds number based on the bubble drift velocity in inclined pipes	$Re_{v_d} = \frac{\rho_L v_d D}{\mu_L}$
Re_{V_L}	Reynolds number based on the mean velocity of the liquid	$Re_{V_L} = \frac{\rho_L V_L D}{\mu_L}$

Acronyms	
CFD	Computational fluid dynamics
CFL	Courant-Freidrich-Lewy
CMC	Carboxymethylcellulose
CSF	Continuum surface force
FOU	First-Order Upwind
FRF	Fixed frame of reference
FVM	Finite volume method
HEC	Hydroxyethylcellulose
LHS	Left-hand side
MRF	Moving frame of reference
PAA	Polyacrylamide polymer
PISO	Pressure implicit with splitting operators
PIV	Particle image velocimetry
PLIC	Piecewise linear interface calculation
PST	Pulsed Shadow Technique
PVP	Polyvinylpyrrolidone
RHS	Right-hand side
SFS	Slug flow simulator
SOU	Second-order upwind
VOF	Volume-of-fluid
2D	Two-dimensional
3D	Three-dimensional

Superscripts	
h	Horizontal
v	Vertical
$*$	Dimensionless
$\wedge$	Dimensionless
$-$	Dimensionless

Subscripts	
exp	Experimental
f	Face
G	Gas phase
i	initial
in	Inlet
L	Liquid phase
LF	Liquid film
min	Minimum
out	Outlet
p	Phase p
Pr	Predicted
q	Phase q
r	Radial direction
S	Surface
TB	Taylor bubble
W	Wake
wall	Pipe wall
x	x coordinate
y	y coordinate
z	z coordinate-axial direction
θ	Tangential direction

Chapter 1 Introduction

Multiphase flows occur in a wide range of applications including natural processes, chemical processes, nuclear systems and petroleum industries. The petroleum industry is considered one of the most important applications of multiphase flow, as it could be encountered in different processes/stages, such as oil processing, oil and gas transport in pipelines and sloshing in offshore separator devices.

This chapter gives a brief introduction on multiphase flow in pipes with the different flow pattern encountered according to the pipe's orientation, covering the vertical, inclined and the horizontal gas-liquid flows. The importance of slug flow in pipes and its difficulties are discussed in detail. The end of this chapter highlights the main objectives of the present work, the applied research methodology and the thesis structure.

1.1 Multiphase Flow in Pipes

The multiphase flow is defined as the simultaneous flow of more than one phase (gas, solid and liquid) (Bratland, 2010). The study of multiphase flow is increasing in extent, mostly because of the increasing importance of such flows in many natural and technological processes. The multiphase flow is involved in some industrial applications, including methods of transporting multiphase fluids through pipelines and wells, evaporators, boilers, condensers, air-conditioning and refrigeration plants, submerged combustion systems, sewerage treatment plants and cryogenic plants. Multiphase flow also plays a distinguished role in the geothermal and nuclear energy's procedures to generate electrical power, coal's transportation, grain, in addition to other solids such as slurries and petrochemicals' development.

In the oil and gas industry, multiphase flow occurs in almost all oil production stages as well as gas wells and pipes that transport produced fluids. Multiphase flow is much more complicated than the single-phase flow due to the significantly different densities and viscosities of the contained fluids. The process of predicting the behaviour of multiphase flow in oil and gas production system is complex. This complexity is due to two main aspects, first, as fluids flow through the piping system, complex heat transfer takes place; second, pressure and temperature variations result in mass transfer within hydrocarbon fluids.

This chapter discusses the difficulties of multiphase flow. This is followed by the different flow patterns encountered in pipes. Additionally, the importance of slug flow is discussed in detail in section 1.4. The thesis focuses on investigating the Taylor bubble flow, which is given in section 1.5. Subsequently, the research's aim, objectives and methods are given in detail in sections 1.6 and 1.7, respectively. Finally, the chapter ends with the thesis outline given in section 1.8.

1.2 Difficulties of Multiphase Flow in Pipes

The discoveries of offshore, initially in shallow water depths and now in ultra-deepwater and harsh arctic climates, made the production of oil and gas much more complicated. In these regions, the capital costs are very high, and thus, the production system must be designed with greater accuracy. Nowadays, production systems are not only more complicated but also they involve different fluids from numerous wells, zones and fields. The main difficulties encountered in multiphase flow in pipelines and wells are due to higher pressures and lower temperatures. This could lead to the formation of deposits, such as paraffin deposition (wax) on pipe walls and the formation of hydrate plugs. The formation of deposits could be eliminated by injecting chemicals into the flow stream, and this shows good practical solutions for avoiding pipeline blockage. Multiphase flow in pipes at its preliminary facet include empirical correlations for predicting flow patterns, liquid holdup and pressure drop.

The main difficulties of multiphase flow in pipes can be summarised in the following points:

- *Chemical, physical and thermodynamic properties* of each phase need to be properly known.
- *Fluid may flow in multiple locations*, and the fluid composition may change over time.
- *Pressures and temperatures variations* in gathering networks and flowlines can lead to *deposits* as hydrates, waxes and scales.
- *Slugging problems:* pressure transients, flooding at the receiving end and increasing deposits and corrosion.
- *Corrosion* which is strongly affected by temperature, pressure and velocity.
- Sand particles in the produced hydrocarbon can lead to *erosion* as it is transported from the well to the platform or onshore facilities through various subsea structures.
- *Erosion, in combination with corrosion,* can enhance each other to produce more damage than what they would separately (Bratland, 2010).

Deposits occur in the form hydrates, wax, asphaltenes and scales. Hydrates are ice-like structures which tend to form if the temperature falls below a specific value when gas molecules are in contact with water. Avoiding steady-state hydrate formation (hydrates forming under normal circumstances) can be done by injecting inhibitors, using thermo-insulation or even heating. Depending on the fluid’s composition, paraffin in the oil can create challenges similar to hydrates. Asphaltenes are carried out as the same as hydrates or wax, however, it is less frequently encountered due to chemical properties. Scale deposits are inorganic, come from produced water and tend to be harder. They can be prevented or removed by inhibitors, pigging and chemicals (Bratland, 2010).

1.3 Two-Phase Flow Patterns in Pipes

The most common class of multiphase flows is the two-phase flows, which includes gas-liquid flows, gas-solid flows, liquid-liquid flows and liquid-solid flows. The gas-liquid flows are probably the most critical form of multiphase flow and are found widely in a whole range of industrial applications. These include pipeline systems for the transport of oil-gas mixtures, evaporators, boilers, condensers, submerged combustion systems, sewerage treatment plants, air-conditioning and refrigeration plants and cryogenic plants.

As for the two-phase gas-liquid flow in pipes, different flow patterns can occur known as “flow pattern/flow regime”. These patterns depend on the flow rates, the geometry of the system and inclination of the pipe. Multiphase flow is classified according to the distribution of different phases building up the flow field, known as “flow regime/pattern”. Multiphase flow can be encountered in various flow patterns, such as bubbly, slug, plug, annular and dispersed flow. Fluid flow investigation includes an important aspect, which is the identification of the encountered flow pattern. In this section of the research, the different flow patterns encountered in the pipes are discussed in detail. These patterns are classified into the vertical, horizontal and inclined gas-liquid flow in pipes.

1.3.1 Flow Patterns in Vertical Pipes

In the vertical pipe, the gas and liquid phases can interrelate into different flow regimes, as indicated in Figure 1-1. These flow regimes can be described as follows (Weisman, 1983):

1. *Bubbly flow:* the gas is dispersed in the form of numerous discrete bubbles in the continuous liquid phase. Generally, these bubbles might vary in size and shape, but typically they have a smaller diameter than the pipe itself.

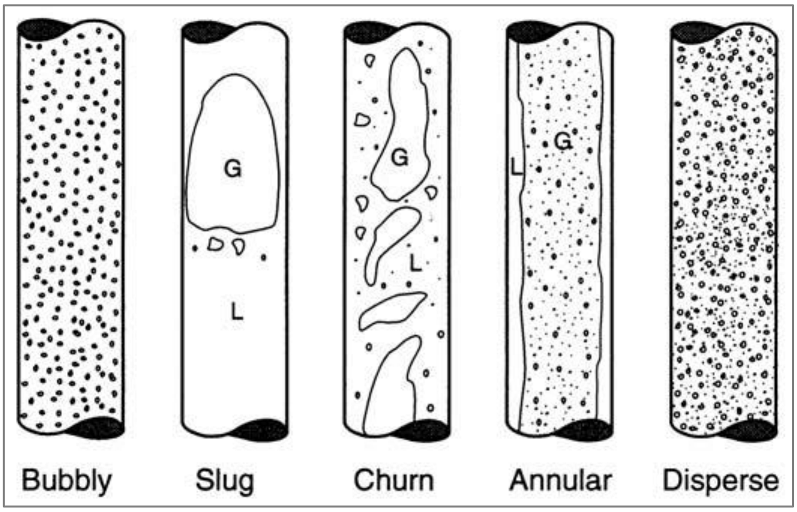

Figure 1-1. Sketches of flow regimes for two-phase flow in a vertical pipe (Weisman, 1983).

2. *Intermitted flow (Slug flow):* the increase in the gas void fraction leads to bubble collision, and larger bubbles start to develop. These bubbles are known as Taylor bubbles. Bullet shape bubbles characterise this flow with a hemispherical nose and a blunt tail. The Taylor bubbles are separated by liquid slugs, which sometimes might include some small bubbles.
3. *Churn Flow:* increasing the gas velocity leads to unstable flow structure to develop. This instability is due to gravity and shear forces acting in the opposite direction on the thin liquid film of the Taylor bubble. Churn flow is an intermediate regime between the slug flow and the annular flow.
4. *Annular Flow:* further increase in the gas velocity causes the shear force on the liquid film to become dominant over gravity. The liquid starts to develop as a thin film on the wall, while the gas flows as a continuous phase filling up the centre of the pipe.
5. *Dispersed Flow:* increasing the gas flow rates causes the liquid droplets to be entrained in the gas core as small droplets. This ends up with the gas phase being the continuous phase, and liquid droplets are the dispersed phase

1.3.2 Flow Patterns in Horizontal Pipes

An example of the flow regimes encountered in horizontal pipes is given in Figure 1-2. With the gravity acting perpendicular to flow direction, the flow patterns in the horizontal pipe can be described as follows (Weisman, 1983):

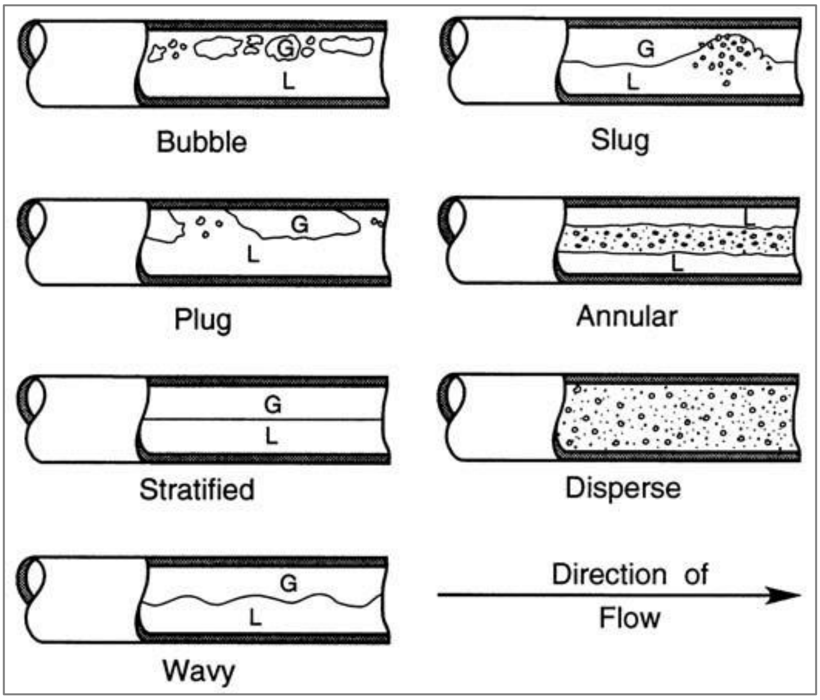

Figure 1-2. Sketches of flow regimes for the flow of air/water mixtures in a horizontal 5.1cm diameter pipe (Weisman, 1983).

1. *Bubbly flow:* due to buoyancy, the gas bubbles are dispersed in the liquid phase with a high concentration at the upper half of the pipe.
2. *Stratified flow:* the stratified flow can be either stratified smooth flow or stratified wavy flow. In the stratified smooth flow, complete dispersion of the two phases occurs where the gas moves towards the top of the pipe and the liquid moves at the bottom, separated by an un-distributed horizontal interface. While, for the stratified wavy flow, increasing the gas velocity in a stratified smooth flow causes waves to start to initiate at the interface and travel in the direction of flow. Although the amplitude of the waves is noticeable, which depend on the velocity of the two phases, but yet it doesn't reach the top of the pipe.
3. *Intermitted Flow:* further increase in the gas velocity causes the interfacial waves to grow and reach the top of the pipe. It is composed of plug and slug flows. The plug flow (Elongated bubble flow) consists of liquid plugs separated by elongated gas bubbles. In slug flow, increasing the gas velocity causes the diameter of the elongated bubbles to be almost the same as the diameter of the pipe. The body of the slug is liquid, but sometimes at high gas velocities, some gas diffuses into the liquid slug- Aerated slug.

4. *Annular flow:* at even larger gas flow rates, the liquid forms a continuous annular film around the perimeter of the pipe. The interface between the liquid annulus and the vapour gas is disturbed by small amplitude waves droplets may be dispersed in the gas core.
5. *Dispersed flow:* the liquid is dispersed in the continuous gas phase. Gas is the continuous phase and droplets are the dispersed phase.

1.3.3 Flow Patterns in Inclined Pipes

The inclination of the pipe greatly influences the gas-liquid flow pattern in pipes. In the case of upward inclined flow, the developed flow pattern is entirely similar to those observed in the vertical upward flow. Figure 1-3 illustrates an example of the flow pattern encountered in upwards inclined pipe (Hernandez Perez, 2008). Other regimes are encountered in the near horizontal cases, such as the stratified flow.

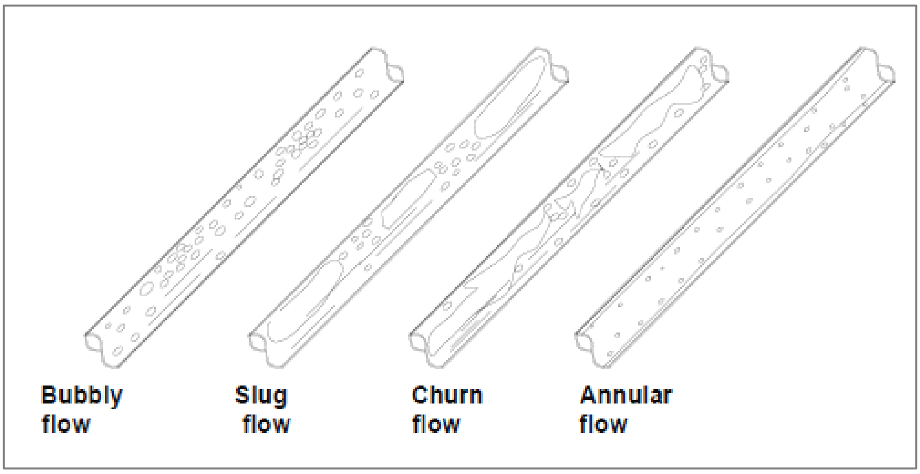

Figure 1-3. Sketches of flow regimes of co-current gas-liquid flow in inclined pipes (Hernandez Perez, 2008).

The case of downward simultaneous gas-liquid flow, though rarely encountered, is important both chemical and petroleum industries, for instance, in the process of steam injection in thermal recovery (Hernandez Perez, 2008). Similarly, the flow pattern is greatly influenced by the angle of inclination. According to Barnea et al. (1982), the flow pattern can be stratified wavy in horizontal cases and changes to annular flow in near vertical cases.

To simulate the multiphase flow in pipelines with any elevation, flow regime maps are used to determine the type of flow regime in addition to performing calculations for that exact regime.

The flow regime map is a diagram that shows the transition boundaries between the flow patterns, and it is typically displayed on log-log axes using dimensionless parameters to represent liquid and gas velocities. Examples of flow regimes maps are those given by Baker (1954); Hewitt and Roberts (1969); Mandhane et al. (1974); Taitel and Dukler (1976); Weisman (1983); Bratland (2010).

In brief, flow regime maps are valuable tools for obtaining a general idea over which flow regimes is expected for a specific set of input data. However, generally, each map is not enough to be valid for other data sets.

1.4 Slug Flow

For gas-liquid flow in pipes, one of the common and complex patterns encountered is known as “slug flow”. Slug flow is an intermitted flow between the stratified and annular flow. Flow intermittence is the main remarkable hydrodynamic characteristic causing the complex structure of slug flow. Figure 1-4 shows a schematic representation of the slug flow pattern encountered in vertical and horizontal pipes.

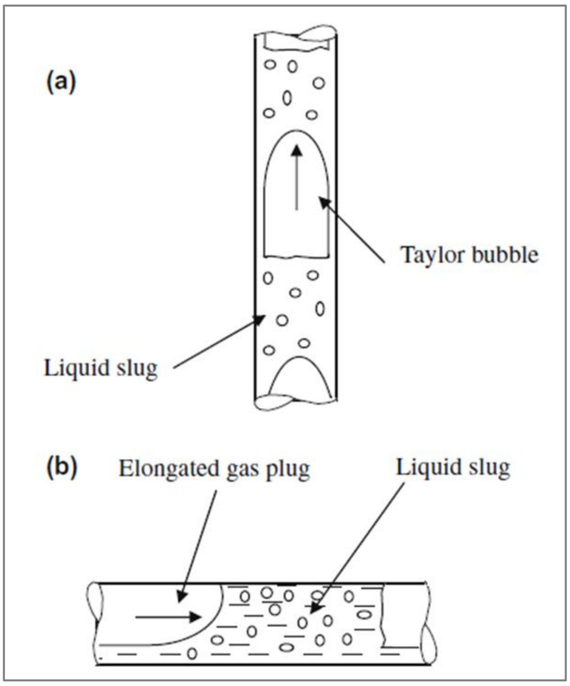

Figure 1-4. Schematic representation of slug flow in (a) vertical pipe and (b) horizontal pipe (Mandal et al., 2010).

The flow is characterised by an elongated bubble, known as Taylor bubble, that occupies almost the whole cross-section of the pipe, and annular falling liquid film that might entrain many small bubbles, known as a “liquid slug”.

In offshore petroleum production systems, the fluids that leave the well are often transported to platforms using flexible pipes. The pipes are composed of a pipeline (or flowline), which conducts the fluids over the seabed topography and a riser, which elevates the fluids to the separator vessel located at the platform. Usually, the transported fluids are composed of gas, oil and water, but due to the severe conditions of pressure and temperature, the formation of emulsions, hydrates and wax is possible. These features make the modelling of the multiphase flow dynamics a complex task.

Slugging is a terrain dominated phenomenon, characterised by the formation and cyclical production of long liquid slugs and fast gas blowdown. Severe slugging may appear for low gas and liquid flow rates when a section with a downward inclination angle (pipeline) is followed by another section with an upward inclination (riser). This configuration is common in offshore petroleum production systems.

According to Xing et al. (2014), the liquid slugs generated in the oil and gas multiphase flowlines can be classified based on their initiation mechanism into four slugs:

- *Terrain-induced slugs* caused by a periodic accumulation of the liquid in elevation changes along flowline, particularly at low flow rates,
- *Hydrodynamic slugs* that is formed due to wave instabilities at the gas-liquid interface, these instabilities are due to Kelvin-Helmholtz instability (horizontal and near horizontal pipelines),
- *Operation-induced slugs* that are formed in the system during the operation transfer between steady-state and transient states such as start-up or pigging operation,
- *Riser-based slugs* which are known as severe slugging and is associated with the pipeline risers often found in offshore oil production facilities.

Slugging problems in offshore oil and gas systems can be summarised as follow:

- Flooding of downstream processing facilities.
- Production loss caused by the high average back pressure at the wellhead.
- Separator shutdown due to instabilities in liquid control system resulting from the high instantaneous flow rates (Nemoto and Baliño, 2012).
- Further induction of the reservoir flow oscillations and poor reservoir management.
- Severe pipe corrosion and structural instability of pipeline.
- Unsteady loading on a pipeline that carries fluids and on the receiving devices, such as separators caused due to the intermittency of slug flow. This results in design problems that can eventually lead to detriments in the efficiency and /or size of the processing plant (Ansari and Shokri, 2011).

The prediction of the appropriate flow pattern regimes, the governing correlations, and the hydrodynamic characteristics of slug flow are essential for successful operation, simulation and optimisation of any industrial applications encountering slug flow.

1.5 The Rise of Taylor Bubbles in Stagnant Liquids

This thesis focuses on studying the flow of the Taylor bubble in the stagnant liquid, which is considered an essential characteristic part of the slug flow regime in pipes. Taylor bubble flow is essential in a various number of applications, including the boiling and condensing process in thermal power plants, the production and transportation of hydrocarbons in the oil and gas industry, capillary flows, microfluidic, the boiling and condensing process in thermal power plants and emergency cooling of nuclear reactors.

Following the fundamental unit concept of vertical slug flow of Fernandes et al. (1983), Figure 1-5 illustrates a schematic representation of the slug unit concept. The flow consists of an elongated bullet-shaped bubble that fills almost the entire pipeline cross section, Taylor bubble, a liquid film flowing downwards between the bubble interface and pipe wall in a liquid film region, known as a liquid slug. Referring to Figure 1-5, the flow can be divided into three regions, the Taylor bubble nose region, the falling liquid film region and the Taylor bubble wake region (liquid slug zone). In the Taylor bubble nose region, the Taylor bubble moves up with a velocity (U_{TB}) due to buoyancy, pushing the liquid sideways where the liquid film zone starts to develop. In the falling liquid film region, the liquid moves downwards with velocity (U_{LF}) and decreases the liquid film thickness (δ_{LF}). Once a balance between the gravitational and the friction forces is reached, a constant terminal liquid film velocity and thickness is developed. In the Taylor bubble wake region, the falling liquid film starts to plug into the liquid slug ending with highly mixing zone in the wake structure of the bubble.

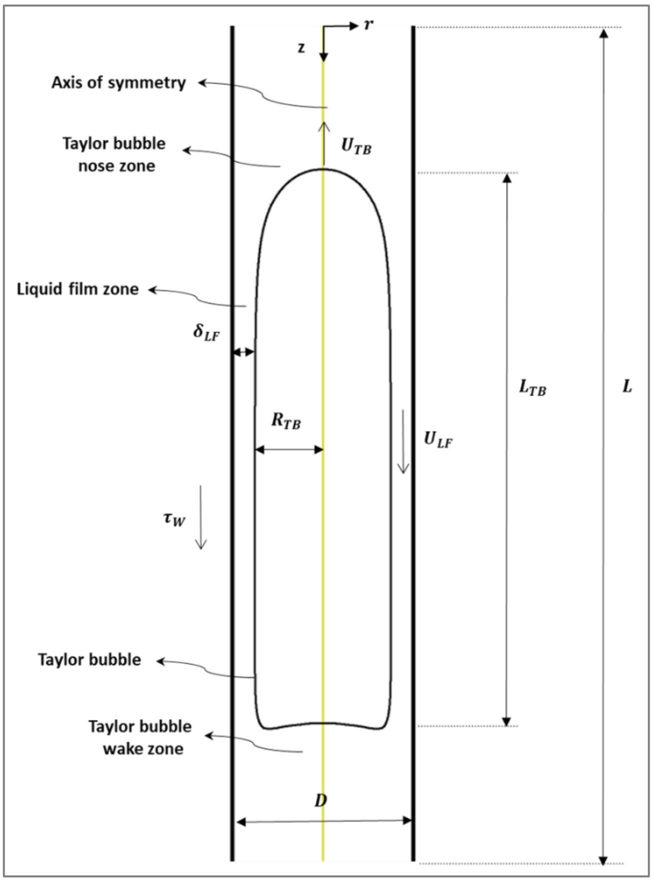

Figure 1-5. Schematic representation of the main hydrodynamic features of a single Taylor bubble rising through a stagnant liquid.

Regardless of a large number of researches done on Taylor bubble flow, based on the critical review given in chapter 2, there are still gaps in the published data. In the literature, to the best of the researcher's knowledge, most of the work is done on Taylor bubble flow in vertical and horizontal pipes, which is the primary motivation for the research presented in this thesis. In this thesis, the Taylor bubble flow in various inclined pipes, including vertical and horizontal pipes, is examined.

1.6 Research Aims and Objectives

The main aim of this work is performing a better understanding of the rise of an individual Taylor bubble through a stagnant liquid in pipes (including vertical, inclined and horizontal pipes). In the literature, there are conflicts in the theoretical treatment of the problem in terms of the forces that control the dynamics of Taylor bubble flow in pipes, defined as dimensionless governing groups. Understanding the governing parameters and the hydrodynamic characteristics of Taylor bubble flow are considered an essential characteristics part for the successful operation, simulation and optimisation of any system encountering slug flow.

The present study can be implemented to the oil/gas/offshore industrial applications to a certain extent as far as the moving fluid flow Reynolds number in these applications is practically small as is the case for dense liquids available in these systems. Accordingly, the stagnant liquid under investigation in the present work can to some extent predict the actual practical conditions. It is to be noted that Reynolds number can be calculated for dense liquids and their velocities available in industry to show the low values of Reynolds number.

To achieve the thesis aims, the following objectives have been considered:

I. Performing a complete dimensionless analysis of the problem to show the main dimensionless parameters that govern the problem and their relative merits or order of magnitudes.
II. Based on the dimensionless analysis, Computational Fluid Dynamics (CFD) study is employed that supports this developed logical approach to the problem. The main hydrodynamic characteristics of Taylor bubbles are investigated through the employed CFD study in a wider range that is expensive and difficult to perform in the practical application.
III. To support other important theoretical and experimental work available in the literature, correlations for Taylor bubble drift velocity and the wall shear stress are suggested based on the developed numerical results and the guidelines of the order of magnitude analysis.
IV. In the literature, various contradicting discussions are describing the bubble behaviour in horizontal pipes. One of the main objectives of this work is understanding the flow

of Taylor bubbles in the neighborhood of horizontal pipes, where the drift velocity becomes significantly slow and almost approaching zero at the horizontal pipe case.

1.7 Research Methodology

To achieve the main aim of this work, which is performing a better understanding of the problem of Taylor bubble flow in pipes, the following methodology is followed:

1. Performing theoretical treatment for the rise of an individual Taylor bubble through a stagnant liquid in pipes (including vertical, inclined and horizontal pipes) using both the Buckingham-Pi theorem and a dimensionless treatment followed by order of magnitude analysis to the governing equations of motion to show the sole dimensionless parameters and their relative merits or order of magnitudes. This is given in the first parts of chapters 4 to 6.
2. To support this logical developed approach of the problem, CFD study is employed where the commercial CFD code ANSYS Fluent (Release 16.0) is used for CFD modelling. The CFD model is verified and validated. The verification process is mainly done to ensure that the results have an acceptable error level or preferably without any sensible errors. This is done by checking the spatial and temporal discretisation error and iterative convergence error. Further details are given in chapter 3. In addition, the CFD model is validated against published benchmark studies and widely acknowledged empirical correlations as those by Campos and De Carvalho (1988); Shosho and Ryan (2001); Bugg and Saad (2002) and Nogueira et al. (2006a; 2006b), which are reported in chapter 2.
3. Once the CFD model is verified and validated, three parametric studies are conducted in chapters 4 to 6. The first parametric study is for the rise of an individual Taylor bubble through a stagnant vertical liquid, reported in chapter 4. A dimensionless treatment is first performed, which is followed by the numerical investigation of the main hydrodynamic characteristics of Taylor bubble flow in a vertical pipe. The second study is for the drift of an individual Taylor bubble in the stagnant liquid in an inclined pipe. Various inclination angles are considered, including the horizontal pipe, which is reported in chapter 5 and 6.

1.8 Thesis Outline

This thesis is divided into seven chapters, as follows:

- *Chapter 1- Introduction.* This chapter provides an introduction to the thesis, outlining the aims and objectives of the study, the methodology and the structure of the thesis.

- *Chapter 2 - Literature Review.* This chapter provides an extensive survey of two-phase slug flow in pipes, in particular, the rise of Taylor bubbles in vertical and inclined pipes. Important hydrodynamic characteristics of Taylor bubble flow are discussed. Also, a review of the main conclusions and subsequent shortcomings is presented.

- *Chapter 3 – CFD Model Description and Validation.* In the first section of this chapter, the CFD model used in this thesis is described, with full details about the governing equations, the multiphase model used and the solution method. A number of validation studies are given at the end of the chapter, where the adopted CFD model is validated against published data.

- *Chapter 4 – Theoretical and CFD Treatments of an Individual Taylor Bubble Rising in a Vertical Pipe* $(\gamma = 0)$. This chapter starts with the dimensionless treatment of the problem using both the Buckingham-Pi theorem and a dimensionless treatment followed by order of magnitude analysis to the governing equations of motion. Based on this analysis, the numerical model discussed in chapter 3 is used to model the rise of an individual Taylor bubble through a stagnant vertical liquid. The main hydrodynamic features of Taylor bubble flow are investigated, including the Taylor bubble shape, the Taylor bubble rise velocity, the flow in the nose region, the flow in the liquid film region and finally the flow in the wake region.

- *Chapter 5 –Theoretical and CFD Treatments of an Individual Taylor Bubble Drifting in an Inclined Pipe* $(\gamma \leq 70°)$. As performed in chapter 4, this chapter starts with the dimensionless treatment of the drift of a Taylor bubble in an inclined pipe for inclination range of $0 \leq \gamma \leq 70°$, with respect to the vertical position. Based on this developed approach, a CFD study is carried out to investigate the hydrodynamic characteristics of Taylor bubbles in inclined pipes covering inclination range of $0 \leq \gamma \leq 70°$.

- *Chapter 6 – Theoretical and CFD Treatments of Taylor Bubble Drifting in Near Horizontal and Horizontal Pipes* ($\gamma \cong 90°$). A particular treatment, in both the dimensionless treatment and the numerical investigation, is performed in this chapter to the near horizontal and horizontal Taylor bubble flow. Simplification in the numerical model based on the dimensionless analysis of the problem is suggested.

- *Chapter 7 – Conclusions and Recommendations.* This chapter provides a summary of the key conclusions from this work. A list of the main contributions of the study is also provided. Recommendations for future work are also given at the end of the chapter.

Chapter 2 Literature Review

Two-phase slug flow has a wide range of applications, including natural processes, chemical processes, nuclear systems and petroleum industries. Despite the significant development of the experimental techniques, the need for a combination of experimental and numerical approaches is essential in understanding the complex nature of slug flow problem that eliminates the experimental limitation and the difficulties while providing robust analysis and accurate results. This chapter aims to summarise the tremendous amount of data published on the subject of Taylor bubble flow in pipes in order to understand the limitations of the techniques used and highlighting the main finding gaps. This review covers the rise of Taylor bubble trough Newtonian fluids, from 1943 to 2019, covering theoretical, experimental and numerical approaches. In addition, the key outcomes and concluding deficiencies are discussed throughout this chapter. Finally, the main contributions of the present work are highlighted at the end of this chapter.

2.1 Introduction

This chapter aims at introducing the important research done on two-phase slug flow in both vertical and inclined pipes with Newtonian liquid, emphasising the most appropriate characteristics associated with two-phase slug flow. These are included into two main sections, a review on gas-liquid slug flow in vertical pipes and a review on gas-liquid slug flow in inclined pipes. In each section, a brief discussion on the dimensionless analysis of the problem, followed by the hydrodynamic characteristics of the flow are given.

In gas-liquid slug flow in vertical pipes section, the review is categorised into four groups. Group 1 (Theoretical and experimental studies) mainly covers the theoretical approaches and some experimental approaches that studied the motion of a Taylor bubble in stagnant vertical liquid. Later, advances in the experimental approaches enabled research to be done with details on the hydrodynamic characteristics of the Taylor bubbles, including details about the surrounding liquid and wake structure (Advanced experimental studies). Despite the significance of these experimental work, the limitation of this kind of studies, due to the complexity of slug flow nature, is an important factor that should be considered. Numerical approaches started to develop as Computational fluid dynamics (CFD) has been proven to be a powerful and practical tool for both the analysis and the simulation of the hydrodynamic characteristics of slug flow in pipes (Numerical studies). The last group covers the research with a cooperative association between experimental and simulation studies (Cooperative associated experimental and numerical studies).

For the gas-liquid slug flow in inclined pipes section, the review discusses the research done on gas-liquid slug flow in inclined pipes according to their appearance in the literature, including the rise of the Taylor bubble through both stagnant and flowing liquid. This is divided into two main research groups, where research group 1 (Theoretical and experimental studies) covers the main experimental and/or theoretical studies and research group 2 (Experimental and numerical studies) focuses on the experimental and/or numerical studies of investigating the gas-liquid slug flow in inclined pipes.

2.2 Gas-Liquid Slug Flow in Vertical Pipes

The review on the research of slug flow in vertical pipes is categorised according to the sequence of research done. Prior to discussing the research groups, a brief discussion on the dimensionless analysis of the forces that govern the drift of a Taylor bubble through the stagnant liquid is introduced, followed by a description of the main hydrodynamic characteristics of the gas-liquid vertical slug flow.

2.2.1 Dimensionless Analysis of Gas-Liquid Vertical Slug Flow

The hydrodynamic characteristics of gas-liquid slug flow are governed by viscous, inertial, gravitational and interfacial forces (Araújo et al., 2012). Generally, the dimensionless analysis of the problem results in the following form:

$$Fr_{U_{TB}} = \frac{U_{TB}}{\sqrt{gD}} = f\left[Eo = \frac{g\rho_L D^2}{\sigma}\,,\ M = \frac{\Delta\rho g \mu_L^4}{\rho_L^2 \sigma^3}\,,\ \Gamma_\mu = \frac{\mu_L}{\mu_G},\ \Gamma_\rho = \frac{\rho_L}{\rho_G},\ \frac{L_{TB}}{D}\right] \qquad (2\text{-}1)$$

where the LHS of relation (2-1) represents the ratio between the inertia and gravitational forces and known by Froude number ($Fr_{U_{TB}}$). Relation (2-1) can be modified by introducing the Reynolds number based on bubble velocity ($Re_{U_{TB}}$) which is the ratio between the inertial forces and viscous forces. Eötvös number (Eo) is the ratio between gravitational forces and surface tension forces and Morton number (M) is known by property group as it only contains the properties of the fluid (Araújo et al., 2012). A complete dimensionless analysis of the equations of motion of gas-liquid vertical slug flow is given in chapter 4.

2.2.2 Main Hydrodynamic Characteristics of Gas-Liquid Vertical Slug Flow

The main hydrodynamic characteristics of the flow can be described using the most straightforward approach that considers the drift of a single Taylor bubble through the stagnant vertical liquid, as illustrated in Figure 2-1. The main hydrodynamic features are summarised as follow:

- Taylor bubble rise velocity (U_{TB})
- Taylor bubble nose region: two main features are commonly investigated; the radius of curvature at the nose (R_N) and the interaction distance above the bubble (Z')
- Liquid film region: four main features are commonly investigated, developed liquid film thickness (δ_{LF}), the velocity of the liquid film (U_{LF}), the wall shear stress (τ_W), the length needed for the fully developed annular liquid film (Z^*).
- Wake region: two main features are commonly investigated, wake length (L_W) and wake volume (v_W). Besides, the corresponding coordinates of the recirculation core (Z_V, R_V) and the curvature radius of the bubble bottom (R_B)
- The perturbed distance below the bubble (L_{min}).

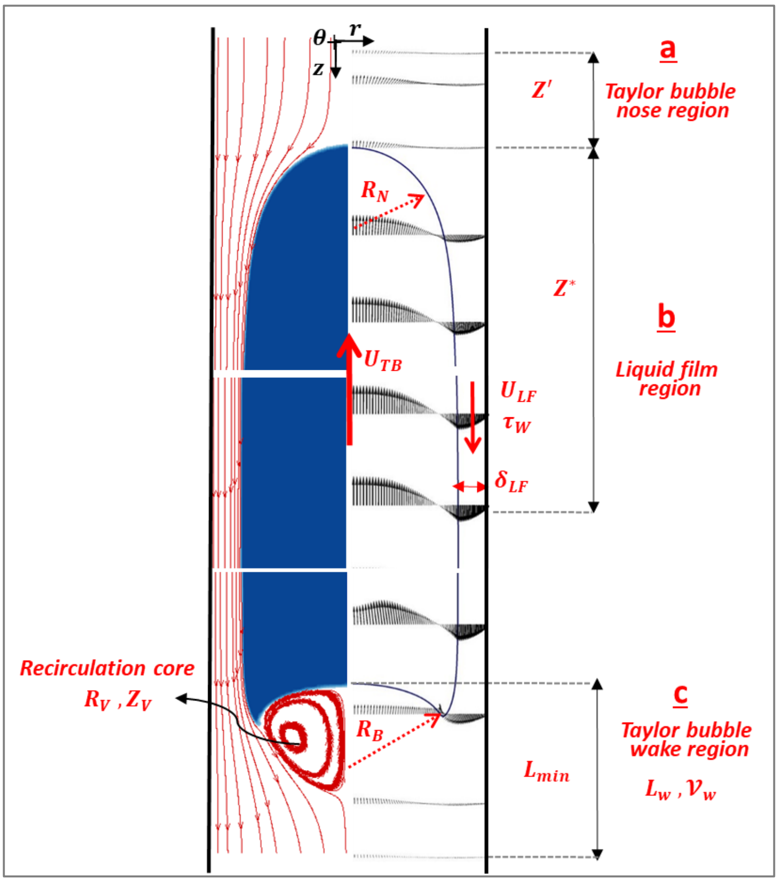

Figure 2-1. A schematic representation of the main hydrodynamic features of a single Taylor bubble rising through a stagnant vertical liquid.

2.2.3 Theoretical and Experimental Studies

In literature, since the 1940s, a significant amount of research has been done to understand the complex principles of the motion of large gas bubbles through liquids. Most of the studies in this group mainly contribute to the topic of the Taylor bubble motion. This section covers the research done on the drift of the Taylor bubble through the stagnant liquid.

2.2.3.1 Taylor Bubble Rise Velocity Through Stagnant Liquid

Early attempts to investigate the topic of Taylor bubble motion start with Dumitrescu (1943) who examines the rise of single Taylor bubble in the stagnant liquid in the vertical tube by applying potential flow theory neglecting viscous, surface tension effects and bubble expansion during its rise. He applies conservation of vorticity to find a solution for the bubble drift velocity by attaching reference coordinate fixed to the bubble. He assumes the following:

- Constant vorticity upstream the bubble.
- Bubble nose is spherical and applies an approximate solution for potential flow around it.
- The inviscid falling film with an asymptotic solution with a common tangent at the surface junction is matched to find the integration constant (Morgado et al., 2016).

Doing so, he concludes that the Taylor bubble rise velocity could be given by:

$$U_{TB} = 0.351\sqrt{gD} \tag{2-2}$$

Equation (2-2) can be expressed as:

$$U_{TB} = C\sqrt{gD} \tag{2-3}$$

Davies and Taylor (1950) perform a similar scenario with experimental measurements of bubble nose and its rise velocity using nitrobenzene and water as the working fluids. With the assumption that the pressure over bubble nose is an ideal hydrodynamic flow around a sphere and applying potential flow around the bubble, they conclude a lower value of 0.328 for constant C compared with Dumitrescu (1943) value given in equation (2-3).

Other experimental and analytical investigations agree with solution of Dumitrescu (1943) with some modification to the value of C in equation (2-3) (Davies and Taylor, 1950; Laird and Chisholm, 1956; Nicklin et al., 1962; White and Beardmore, 1962; Brown, 1965; Zukoski, 1966; Bendiksen, 1985; Campos and De Carvalho, 1988; Polonsky et al., 1999). Table 2-1 summarises the values of constant C in equation (2-3) based on analytical and/or experimental approaches done in the literature.

Table 2-1. Values of constant C *in equation (2-3) based on analytical and/or experimental approaches in the literature (Kang et al., 2010; Morgado et al., 2016).*

Reference	Values of constant $\boldsymbol{C}$
Davies and Taylor (1950)	0.328
Laird and Chisholm (1956)	0.328
White and Beardmore (1962)	0.345
Brown (1965)	0.303
Bendiksen (1985)	0.351
Campos and De Carvalho (1988)	0.350
Hasan and Kabir (1988)	0.350
Polonsky et al. (1999)	0.351

White and Beardmore (1962) perform an extensive number of experiments covering a wide range of dimensionless groups $Fr_{U_{TB}}, Eo$ and M. They develop general graphical representation of the Taylor bubble rise velocity correlation in terms of these three dimensionless groups. Through this representation, they clearly discuss different regions where the effects of some of the governing forces can be neglected. For instance, for $Eo < 4$, the bubble occupies the total pipe cross section and principally does not move. On the other hand, Bretherton (1961) suggests this value to be 3.37 (Morgado et al., 2016).

Brown (1965) investigates the effect of liquid viscosity on the Taylor bubble rise velocity through experimental and theoretical investigation. One of the remarkable conclusions drawn from his work is that the potential flow theory can only represent low viscous fluids, however, it is not valid for high viscous ones. Based on his investigation, a correlation for the Taylor bubble rise velocity is proposed and given by:

$$
\begin{aligned}
U_{TB} &= 0.35\sqrt{gD}\sqrt{1-2\left(\frac{\sqrt{1-ND}-1}{ND}\right)} \\
N &= \sqrt[3]{14.5\rho_L^2 g/\mu_L^2}
\end{aligned}
\qquad (2\text{-}4)
$$

With the following criterion: $\frac{\rho_L g D^2}{4\sigma}\left(1-2\left(\frac{\sqrt{1-ND}-1}{ND}\right)\right)^2 > 5$ and $ND > 60$.

In addition, other important factors are affecting the Taylor bubble rise velocity, such as surface tension, tube diameter, liquid density and viscosity. Zukoski (1966) performs experimental study covering the effect of most of these parameters, which are considered the most comprehensive work available in the literature. He concludes that for Reynolds number greater than 200, the viscous effects are considered negligible. For $Re_{U_{TB}} > 100$, the bubble velocity is inversely proportional to the liquid viscosity. Additionally, the bubble velocity is independent of surface tension effects if $Eo > 40$. Pipe inclination effect is as well explored, and a number of important conclusions are drawn.

Wallis (1969) develops a correlation for bubble velocity considering all affecting parameters, given by:

$$Fr_{U_{TB}} = \frac{U_{TB}}{\sqrt{gD}} = 0.345\left(1-e^{\frac{-0.01N_f}{0.345}}\right)\left(1-e^{\frac{3.37-Eo}{m}}\right)$$
$$\text{where:} \quad m = \begin{cases} 25, & N_f < 18 \\ 69N_f^{-0.35}, & 18 < N_f < 250 \\ 10 & N_f > 250 \end{cases} \tag{2-5}$$

Moreover, Tung and Parlange (1976) explore the effect of surface tension on bubble velocity with negligible viscosity effects. They conclude that the bubble velocity diminishes as surface tension increases and they develop a correlation to estimate the bubble velocity, which is given by:

$$Fr_{U_{TB}} = \frac{U_{TB}}{\sqrt{gD}} = \sqrt{0.136 - 0.944\frac{\sigma}{\rho_L g D^2}} \tag{2-6}$$

Later, Fabre and Liné (1992) perform an extensive review on two-phase slug flow modelling through which deductions regarding the controlled regimes are discussed (White and Beardmore, 1962). For instance, the inviscid fluid assumption is probably an accurate approximation for some practical cases of slug flow (Morgado et al., 2016). There is a different limiting criterion for each regime, which can be summarised as follows:

- Surface tension dominate regime: $N_f > 300$ according to Wallis (1969) and Fabre and Liné (1992) and $N_f > 550$ according to White and Beardmore (1962).
- Viscosity dominate regime: $Eo > 100$, according to Wallis (1969) and Fabre and Liné (1992) and $Eo > 70$ according to White and Beardmore (1962).
- Inertia dominate regime: $Eo > 100$ and $N_f > 300$ according to Wallis (1969) and Fabre and Liné (1992) and $Eo > 70$ and $N_f > 550$ according to White and Beardmore (1962). Where the flow is not affected by either surface tension nor viscous effects (Zheng et al., 2007a).

2.2.3.2 Detailed Hydrodynamics

The research in this group is mainly focused on investigating the Taylor bubble motion through either analytical or/and experimental approach. However, they also contribute to the main hydrodynamic features of gas-liquid vertical slug flow, including Taylor bubble nose, liquid film and wake regions. For instance, Dumitrescu (1943) is one of the early attempts to experimentally and theoretically investigate Taylor bubble shape by applying potential flow theory. As pointed out by Morgado et al. (2016), Dumitrescu (1943)'s equation for describing the Taylor bubble shape in the nose and liquid film is given by:

$$\frac{z}{R} = \begin{cases} 0.75\left(1 - \sqrt{1 - 1.778\left(\frac{r}{R}\right)^2}\right), z/R \leq 0.5 \\ \dfrac{0.123}{\left(1 - \left(\frac{r}{R}\right)^2\right)^2}, z/R \geq 0.5 \end{cases} \tag{2-7}$$

The axial distance pointing downwards is given by z/R and the distance from centreline is given by $\frac{r}{R}$. Equation (2-7) showed a strong correspondence with other experimental studies of Mao and Dukler (1990) and Nogueira et al. (2006a) even though it is only valid for inertia dominate regime.

Other significant contributions regarding the Taylor bubble nose are given by Nicklin et al. (1962) and Brown (1965). Nicklin et al. (1962), though their experimental study, suggest that the liquid velocity field and viscosity ahead of the oblate spheroidal Taylor bubble nose are the main controlling parameters. While Brown (1965) suggests a universal correlation representing the radius of curvature at the nose (R_N) that characterise the bubble shape in this region, given by:

$$R_N = 0.75R_{TB} = 0.75(R-\delta) \tag{2-8}$$

Some of the main significant contributions concerned with the liquid film region are those done by Goldsmith and Mason (1962) and Brown (1965). Both investigations derive an equation for the velocity profile in the liquid film for the case of the motion of bubbles in inviscid fluids. The model assumes that the fully developed laminar liquid distribution is established near the bubble end and with the aid of performing force balances (mainly gravity and shear stress forces), the model suggests that velocity profile liquid film can be expressed as:

$$U_{LF}(r) \; = \frac{g}{\nu}\left[\frac{R^2-r^2}{4} - \frac{(R-r)^2}{2} ln\frac{R}{r}\right] \tag{2-9}$$

And the liquid film thickness is given by:

$$\delta_{LF} = \left[\frac{3\nu}{2g(R-\delta_{LF})} U_{TB}(R-\delta_{LF})^{\,2}\right]^{1/3} \tag{2-10}$$

Lastly, for the wake region, Goldsmith and Mason (1962) through their experimental work, describes the Taylor bubble wake shape as follows:

- Flow is viscosity dominate regime: the Taylor bubble bottom has oblate spheroid shape.
- Flow is not viscosity dominate regime: flattening or concaving shape of the Taylor bubble bottom.

The critical criteria for the transformation boundary from oblate spheroid to a concave surface is $N_f > 300$ according to Wallis (1969) and Fabre and Liné (1992) and $N_f > 550$ according to (1962). Zheng et al. (2007a) conclude though simulation study that this transition occurs when $350 \leq N_f \leq 680$.

An interesting phenomenon regarding the wake region is observed by Goldsmith and Mason (1962), where small disturbance waves act at the beginning of the curvature of the bubble bottom in both viscous flow and inertia-controlled regimes. Additionally, one of their main vital observations is that the overall bubble deformation including bubble nose, liquid film and wake regions is independent of the liquid viscosity (μ_L) for a constant value of Eo (Viana et al., 2003).

2.2.4 Advanced Experimental Studies

Advance in the experimental techniques enabled research to qualitatively and quantitively investigate the hydrodynamic features of gas-liquid vertical slug flow, including details about the Taylor bubble nose, surrounding liquid and wake structure (Campos and De Carvalho, 1988; Mao and Dukler, 1990; DeJesus et al., 1995; Polonsky et al., 1999; Bugg and Saad, 2002; Viana et al., 2003; Sousa et al., 2006; Nogueira et al., 2006a; 2006b; Mayor et al., 2008a; Hayashi et al., 2011; Kurimoto et al., 2013; De Azevedo et al., 2017). These experimental facilities also helped in validating previous theoretical models available in the literature.

Campos and De Carvalho (1988) perform the first photographic study that investigates the wake structure of an individual Taylor bubbles rising through stagnant liquid using different pipe diameters and liquid viscosities. This work is considered the primary source of information about regime transition in the bubble wake region. Though this experimental work, they suggest that the wake region is mainly a function of the inverse viscosity number $\left(N_f\right)$ and categorise the wake flow pattern into three main groups, as follows:

- Type 1: Closed axisymmetric laminar wake for $N_f < 500$.
- Type 2: Closed asymmetric transitional wake for $500 < N_f < 1500$.
- Type 3: Opened turbulent wake with the recirculatory flow for $N_f > 1500$.

Additionally, they propose the following correlations for the dimensionless wake length (L_W/D) and wake volume (υ_W/D^3):

$$\frac{L_w}{D} = 0.30 + 1.22 \times 10^{-3} N_f \ for \ 100 < N_f < 500 \qquad (2\text{-}11)$$

$$\frac{\upsilon_W}{D^3} = 7.5 \times 10^{-4} N_f \; for \; 100 < N_f < 500$$

Despite the fact the Campos and De Carvalho (1988) can be considered a primary information source about regime transition in the bubble wake region, it is worth noting that replacing N_f by $Re_{U_{TB}}$ is questionable in the case of judjing turbulance or the onset of hydrodynamic instability. Further details are given in chapter 4.

Recent developments in visualisation methods lead to quantitative measurements of the flow fields in the wake region (Morgado et al., 2016). Wake flow oscillation is an exciting phenomenon examined experimentally by some authors (Polonsky et al., 1999; Van Hout et al., 2002; Liberzon et al., 2006; Shemer et al., 2007). For instance, Polonsky et al. (1999) use Particle Image Velocimetry (PIV) to investigate the wake flow oscillation phenomena for Taylor bubble rising through a stagnant liquid. They conclude that the wake oscillation depends on the liquid flow rate and bubble length. However, PIV technology fails to determine the exact shape of the bubble. To overcome this problem, Nogueira et al. (2003) use combined PIV and Pulsed Shadow Technique (PST) techniques to investigate the flow around Taylor bubble rising through liquids and co-current Newtonian flows. These technologies enable the determination of average flow fields, streamlines, the shape of the bubble end and wake dimensions in terms of length and volume (Morgado et al., 2016). A similar study is done by Nogueira et al. (2006b) where the different wake flow patterns observed earlier by Campos and De Carvalho (1988) are reported, and wake dimensions are established via averaging flow fields. However, it should be pointed out that the wake flow oscillations phenomena has many governing factors and needs further qualitative investigation.

The Particle Image Velocimetry technique (PIV) not only enables the investigation of the bubble wake region, however, it also allows many studies to obtain a deeper understanding of the hydrodynamic features regarding the bubble nose region and the liquid film region. For example, in the bubble nose region, it allows experimental identification of the interaction distance above the bubble (Z') at which the impact of the drifting bubble is observed (Polonsky et al., 1999; Bugg and Saad, 2002; Van Hout et al., 2002; Nogueira et al., 2003; 2006a; Shemer et al., 2007). Additionally, PIV allows experimental measurements of the radius of curvature at the bubble nose (R_N) where the increment in its values corresponds to an increase in both

Taylor bubble rise velocity (U_{TB}) and the inverse viscosity number $\left(N_f\right)$ (Bugg et al., 1998; Nogueira et al., 2006a).

Advances in experimental techniques enable researchers to investigate the Taylor bubble rise velocity effectually. For example, Viana et al. (2003) perform experiments as well as gather all correlations for the Taylor bubble rise velocity in the literature and propose a universal correlation for the Taylor bubble rise velocity given by:

$$Fr_{U_{TB}} = \frac{\dfrac{0.34}{\left(1+\dfrac{3805}{Eo^{30.6}}\right)^{0.58}}}{\left(1+\left(\left(\dfrac{R_G}{31.08}\right)\left(1+\dfrac{778.76}{Eo^{1.96}}\right)^{-0.49}\right)^{-1.45\left(1+\frac{7.22\times10^{13}}{Eo^{9.93}}\right)^{0.094}}\right)^{0.74\left(1+\frac{7.22\times10^{13}}{Eo^{9.93}}\right)^{-0.094}}} \tag{2-12}$$

where $R_G = \sqrt{D^3 g(\rho_L - \rho_G)\rho_L}/\mu$

They collect bi-power laws for two separate flow regions, large N_f, $N_f > 200$ and small N_f, $N_f < 10$, and fit the transition region between those ranges by a logistic dose curve. Their correlation strongly corresponds with most of the experimental and/or theoretical correlations in the literature.

Morgado et al. (2016) and Mayor et al. (2007a; 2007b; 2008a; 2008b; 2008c) publish a group of methodical research on the hydrodynamics of gas-liquid vertical slug flow in pipes. Their research combines both experimental and numerical work. In this section, purely experimental work is discussed. Mayor et al. (2008a) examine the hydrodynamics of free bubbling gas–liquid (air-water) vertical slug flow using a non-intrusive image analysis technique. The study covers fully turbulent regime in the main liquid and the near wake bubble region. They propose a correlation for the bubble to bubble interaction that relates the bubble velocity to the length of the liquid slug in advance of the bubble. The correlation is independent of pipe diameter, vertical pipe coordinate, superficial liquid and gas velocities and the velocity and length of the leading bubble.

Using simultaneous particle image velocimetry (PIV) and shadowgraphy technologies, Sousa et al. (2006) examine the flow around single Taylor bubbles rising in stagnant non-Newtonian solutions of polyacrylamide (PAA) polymer. The study includes the effect of gas expansion, which is rarely included in the previous research. One of the main findings is that the solution in the Taylor bubble nose region has Newtonian behaviour with almost uniform viscosity due to very low-velocity gradients with low shear rate noticed in such region. The gas expansion increases the Taylor bubble rise velocity, which is affected by bubble length. The bubble length affects both the bubble velocity and the velocity in the Taylor bubble nose region. Hence, they conclude that an increase in bubble velocity due to expansion can be found by subtracting the maximum liquid velocity at the pipe's axis, to the experimental values of U_{TB} to obtain a constant bubble velocity, which corresponds to that of a bubble drifting in a closed pipe (Morgado et al., 2016).

De Azevedo et al. (2017) make use of the advances in the experimental methods. They implement a pulse-echo ultrasonic technique to examine the falling liquid around single Taylor bubbles rising in a vertical pipe with stagnant liquids using a pulse-echo ultrasonic technique. Ultrasonic signals processing is used to obtain a velocity profile of the Taylor bubble and the development length and thickness of the falling liquid film. Based on the experimental result, the study proposes new correlations to estimate the dimensionless equilibrium film thickness $\left(\grave{\delta}_{eq}\right)$ and the dimensionless film development length $\left(\frac{Z'}{D}\right)$, given by:

$$\grave{\delta}_{eq} = -4.19 \times 10^{-2}\, ln\, N_f + 4.25 \times 10^{-1} \qquad (2\text{-}13)$$

$$\frac{Z'}{D} = -1.51 + 1.70 \times 10^{-3}\, ln\, N_f - 2.45 \times 10^{-8} {N_f}^2 \qquad (2\text{-}14)$$

2.2.5 Numerical Studies

The experimental studies investigating the main complex hydrodynamic nature of slug flow postulate a number of remarkable conclusions that helped in further understanding of the problem (Polonsky et al., 1999; Van Hout et al., 2002; Clanet et al., 2004; Liberzon et al., 2006; Sousa et al., 2006; Direito et al., 2017). Despite the significant effort done in most of the experimental approaches, the need for computation analysis is essential in understanding the complex nature of slug flow problem that eliminates the experimental limitation and the difficulties while providing robust analysis and accurate results. According to the viewed literature, Computational fluid dynamics (CFD) has been proven to be a powerful, practical tool for the analysis and simulation of the hydrodynamic characteristics of slug flow in pipes (Clarke and Issa, 1997; Bugg et al., 1998; Ndinisa et al., 2005; Taha and Cui, 2006; Lu and Prosperetti, 2008; Kang et al., 2010; Araújo et al., 2012; Ambrose, 2015; Lizarraga-García, 2016; Gutiérrez et al., 2017).

Ansari and Shokri (2011) classify the primary methods used to model slug flow in the literature as follows:

- Steady-state models: the complex structure of slug flow is simplified to an ''equivalent cell unit". The balance equations can be written in a frame of reference with the unit cell so that the flow appears steady with mass and momentum conserved across the boundary between the liquid slug and the long gas bubble region.
- Slug tracking models (Lagrangian slug capturing scheme): the movement, growth and disappearance of slugs are monitored by tracking individual slugs.
- Slug capturing using Two-Fluid models: the slug regime is modelled with the same set of governing equations (the one-dimensional, transient, two-fluid model) and closure laws. Available in several commercial codes, including PLAC (Black et al., 1990) (One-dimensional, steady-state or transient, model-based two-phase simulator for hydrocarbon pipeline flow), OLGA (Bendiksen et al., 1991), Ledaflow (slug capturing in Leda is a predictive tool designed for resolving hydrodynamic slugs, terrain slugging and interactions between travelling waves) and TACITE (One dimensional steady-state or transient simulation tool for two and three-phase flow in pipeline and pipeline networks).
- Slug-Interface Capturing Models: VOF method and Level set method. The degree of freedom in the modelling for the interface capturing method is lower than that for the two-fluid model because the latter has two velocity fields in the computational domain.

In the literature, different numerical techniques have been addressing the challenging problem of the Taylor bubble, by using the volume-of-fluid (VOF) method (Araújo et al. (2012; 2013a; 2013b)), Front tracking method (Kang et al., 2010), Lattice Boltzmann method (Kuzmin et al., 2013), level set method (Gutiérrez et al., 2017) and other methods (Clarke and Issa, 1997; Ndinisa et al., 2005).

The main complex feature of gas-liquid slug flow is the deformable interface (Zheng and Che, 2007b). The volume-of-fluid (VOF) method developed initially by Hirt and Nichols (1981) is frequently used to simulate complex multiphase flows, including slug flow and is dominant in tracking the interface between fluids.

Early attempts to the numerical study of slug flow problem are made by Kawaji et al. (1997) that use the volume-of-fluid (VOF) method to numerically investigate the hydrodynamic characteristics of a Taylor bubble rising through the stagnant liquid in a vertical pipe and conclude that the bubble length does not affect the bubble terminal velocity. Based on an iterative scheme that solved the velocity and shape of the Taylor bubble in a vertical tube, a different methodology is developed by Clarke and Issa (1997). They introduce a model that assumes homogenous flow in the liquid slug region and thus account for the dispersed bubble in that region (Araújo et al., 2012). Against their hypothesis, the model shows poor results that they suggest that future models should use the two-fluid model for proper simulation of the dispersed gas bubbles in the liquid slug region (Ndinisa et al., 2005). Later, Bugg et al. (1998) perform a detailed study on the motion of Taylor bubbles in vertical pipes and prove that the VOF method is capable of determining the main hydrodynamic features of slug flow including the bubble shape, bubble rising velocity, liquid film thickness and average velocity in the liquid film. The results are then compared with experimental data in the literature and show good agreement. Another different approach, based on developing a new algorithm for solving the gas-liquid interface equation, is developed by Issa and Ubbink (1999).

Other significant numerical studies using the VOF method are worth to mention as those done by Ndinisa et al. (2005); Taha and Cui (2006) and Zheng et al. (2007a). Lately, Lu and Prosperetti (2008) numerically study Taylor bubble rising in the stagnant liquid by neglecting the flow in the gas using front tracking method that deals with two-phase liquids and evades the uncertain gas-liquid interface reconstruction in VOF method. They apply a procedure based on B-splines to build smooth functions best-fitting the field variables (velocities in the gas phase) over a strip straddling the gas-liquid interface along with its whole perimeter. This method shows powerful tracking of the exact position and curvature of the interface that helps in calculating the surface tension.

On the subject of the study and modelling of continuous slug flow applied to oil and geothermal wells, Mayor et al. (2007a; 2008b) use simulators to produce numerical data for velocity and slug length distributions along the well to predict the hydrodynamics of the developing state of continuous slug flow. This type of research needs a detailed study of the systems which are composed of "fundamental units" of slug flow. However, the main input for these slug flow tracking simulators is some information that describes the interaction between consecutive bubbles as a function of these parathion distance. To obtain this crucial information, it is necessary to study in detail the systems composed of "fundamental units" of slug flow. The study includes different scenarios, fully laminar regime (Mayor et al., 2007a) and a mixed case of laminar flow in the main liquid and turbulent regime in the near-wake region (Mayor et al., 2008c). The following conclusions are drawn:

- Taking the mixed case as a reference, for fully developed flow the bubble velocity is higher when the regime is fully laminar and lower when the flow pattern in both regions is turbulent – Mayor et al. (2007b; 2008a)
- Regarding the lengths of the bubble and the liquid slug, upper values occur for the fully turbulent regime and minor ones for fully laminar.
- The values obtained for bubble length when the flow pattern is fully laminar by Mayor et al. (2007a; 2008c) are very close to those of the mixed scenario.

Kang et al. (2010) use a front tracking methodology to simulate the dynamics of gas slugs rising through stagnant liquids, where the finite difference method is used to discretise the governing equations. The study concludes that the density and viscosity ratios have minimal effect on the dynamics of Taylor bubbles rising in stagnant liquids, while both the Eötvös number and Archimedes number have a significant impact. They develop correlations for the dimensionless liquid film thickness and the dimensionless wall shear stress as a function of only Archimedes number. They also conclude that wake length and volume depend mainly on the Archimedes number. Later, Araújo et al. (2012) perform a detailed study of the dynamics of the Taylor bubble rising in stagnant liquid and include a wide range of Eötvös and Morton number. They show that Kang et al. (2010) correlations are inadequate by proving that both dimensionless liquid film thickness and the dimensionless wall shear stress are a function of Eötvös and Morton numbers. They investigate the wake structure with full details about the bubble bottom and the corresponding curvature radius (R_B) that enable them to define the transition in wake shape and its concavity limit expressed in terms of both Eötvös and Morton numbers. They conclude that the wake structure is greatly influenced by both Eötvös, and Morton numbers, and not only Archimedes number as concluded by Kang et al. (2010). They have also been able to develop correlations for the wake length and volume that show good agreement with well-known experiment correlations of Campos and De Carvalho (1988). According to the literature, the work of Araújo et al. (2012) is considered one of the significant numerical studies of an individual Taylor bubble rising through the stagnant liquid. The study also accounts for the perturbed distances above and below the bubble, Z' and L_{min}, respectively, which are considered important parameters especially for the coalescence phenomena in slug flow. It should be pointed out here, that sole governing parameters for the hydrodynamic characteristics of slug flow (wake and liquid film) are still questionable and there are many contradicting conclusions in their research.

Additionally, Yan and Che (2011) investigate the hydrodynamic characteristics of a single Taylor bubble rising in stagnant liquid with further consideration of the small dispersed bubbles in the liquid slug region. Their study account for the effect of small dispersed gas bubbles in the liquid slug region on the flow hydrodynamics features and CO2 corrosion rate. It is concluded that the small dispersed gas bubbles result in higher fluctuations in the liquid slug region, which subsequently increase the mass transfer and wall shear stress. Moreover, Araújo et al. (2013a; 2013b) investigate the rising of two consecutive Taylor bubbles through vertical stagnant Newtonian liquids under laminar regime using the volume-of-fluid (VOF) method. The results account for bubble-bubble interaction and show the dependency of the wake on the separation distance between the bubbles. A good review on slug flow is presented by Morgado et al. (2016) that summarises all of the essential correlations used in defining the problem and show the missing data that need to be further investigated.

Furthermore, the three-dimensional Taylor bubble problem is a challenging problem in terms of computational time, yet Gutiérrez et al. (2017) succeed in using a domain optimisation method (the moving mesh method), where smaller computational domains can be used to simulate the problem and hence save computational resources. The authors verify the method using broad numerical tests. The results are tested against experimental work of Bugg and Saad

(2002) for the vertical case, and Shosho and Ryan (2001) for the inclined case and good agreement is noticed. The full three-dimensional analysis of the problem enables the work to comprehensively address the problem with complete details about its dynamic features. The work investigates the effect of different parameters, such as the impact of the initial shape of the bubble, the initial volume of the bubble and the inclination of the pipe.

Recently, two main topics in the field of Taylor bubble flow become of main concern, the flow of Taylor bubbles in shear-thinning liquids in a vertical pipe and the flow of Taylor bubbles through a sudden or gradual expansion in the pipe. For instance, Araújo et al. (2017) numerically investigate the impact of liquid shear-thinning and shear-thickening rheology on the hydrodynamics of the Taylor bubble. The dependence of the flow field, covering the nose, liquid film, and wake regions, on the liquid rheological nature is examined. A typical slug flow condition, which is characterised by large variations of the shear rate, is explored by applying typical Shear-Thickening Fluid (STF) characterised by a mixed rheological behaviour. The numerical results show good correspondence when tested against in-house experimental data. Another example is Ambrose et al. (2017) who numerically investigate the rise of Taylor bubbles through a change in pipe diameter using the VOF method implemented in the commercial software ANSYS Fluent. Their simulations are conducted using an air-water system and show good matching when tested against existing experimental work. The behaviour of Taylor bubbles when passing through expansion is examined using different angles of expansion. Their main conclusion is that the bubble might remain intact or split into daughter bubbles depending on the angle of expansion. This is analysed in term of bubble critical length which is defined as the maximum length that will pass through intact. The study reveals that this length is proportional to the cosecant of the angle of the expansion. Lastly, Amani et al. (2019) numerically investigate the rise of the Taylor bubble in Newtonian and shear-thinning liquids (CarboxyMethyl Cellulose or CMC) through a change in pipe diameter. They validate the numerical results against experimental data exploring the effect of shear-thinning behaviour on the Taylor bubble splitting process across the sudden or gradual expansion. The effect of both CMC content of the aquatic solution and the strength of non-Newtonian fluid rheology is mainly reflected in the flow field structure and the corresponding length scales of the bubble. They also account for the shear-thinning behaviour and its response to the pressure variations across the necking region.

2.2.6 Cooperative Associated Experimental and Numerical Studies

Lastly, in the literature, some essential studies combine interdependent association between experimental and simulation attempts that are worth mentioning. Starting with Tomiyama et al. (1996) who use the first experimental data on the effects of the dimensionless number, Eötvös and Morton numbers, on the shape of Taylor bubbles to evaluate the practicability of numerical solution using the volume-of-fluid (VOF) methodology of gas-liquid vertical slug flow. Good correspondence between both approaches regarding bubble shape and terminal bubble velocity is achieved. The simulation results show similar behaviour associated with wake oscillation phenomena where the bubble bottom revealed disturbances as those observed by of Goldsmith and Mason (1962); Polonsky et al. (1999); Van Hout et al. (2002); Liberzon et al. (2006) and Shemer et al. (2007).

Later, Bugg and Saad (2002) investigate the flow field around the air bubble rising through stagnant olive oil using (PIV) measurements. Flow field measurements include three main regions, the bubble nose, the falling film and the wake regions. The PIV measurements enable measurement of the interaction distance above the bubble (Z') and the radius of curvature at the nose (R_N) supporting the conclusions of Polonsky et al. (1999); Van Hout et al. (2002); Shemer (2003) and Nogueira et al. (2003; 2006a) that an increase in R_N is associated with an increase in the bubble velocity, and accordingly Froude number, along with the inverse viscosity number. A volume-of-fluid based finite difference technique is used as well to predict the flow fields and compared with the experimental data.

Additionally, the work of Mayor et al. (2007a; 2008c) use Slug Flow Simulator (SFS) to examine the effect of the inlet slug length distribution on the development of continuous slug flow. They include different situations, fully turbulent regime (in the near wake of the leading bubble and the main liquid), fully laminar regime and a mixed situation of laminar flow in the main liquid and turbulent one in the wake. The input of SFS is an empirical bubble-to-bubble interaction correlation relating the bubble velocity and the length separating consecutive Taylor bubbles, taken from the experimental analysis.

More recently, other works contribute to modify bubble rise velocity correlation as the work of Hayashi et al. (2011) and Kurimoto et al. (2013). Hayashi et al. (2011)'s correlation is based on their experimental data and dimensionless analysis based on the instantaneous local fields equations and the jump conditions (Ishii, 1975), to obtain the correlation functional form, and using the limiting cases of ($Eo \to \infty$, $Re_{U_{TB}} \to \infty$) and ($Eo \to \infty$, $Re_{U_{TB}} \to 0$) to define the correlations' coefficients (Morgado et al., 2016). However, Kurimoto et al. (2013) modify Hayashi et al. (2011) correlations' coefficients to show better matching with other important correlation in literature, Wallis (1969) and Viana et al. (2003), especially for low Morton number cases. Both studies use an Interface tracking method for the numerical approach.

2.3 Gas-Liquid Slug Flow in Inclined Pipes

In the literature, most of the research is done on gas-liquid slug flow in vertical and horizontal pipes. The research on the inclined pipes is mainly experimental and/or analytical approaches. There is a moderate amount of numerical work done on gas-liquid slug flow in inclined pipes because this type of simulation is considerably computationally expensive. This section discusses the research done on gas-liquid slug flow in inclined pipes according to their appearance in the literature, including the rise of the Taylor bubble through both stagnant and flowing liquid. The main experimental and/or theoretical studies are given in research group 1 (theoretical and experimental studies), and the experimental and/or numerical studies investigating the gas-liquid slug flow in inclined pipes are given in research group 2 (experimental and numerical studies). Similar to vertical slug flow, a brief discussion on the dimensionless analysis of the forces that govern the drift of the Taylor bubble through a stagnant liquid in inclined pipes is first introduced. Afterwards, a description of the main hydrodynamic characteristics of the gas-liquid slug flow in inclined pipes is discussed.

2.3.1 Dimensionless Analysis of Gas-Liquid Slug Flow in Inclined Pipes

Similar to the vertical slug flow, the hydrodynamic characteristics of gas-liquid slug flow inclined by an angle (γ) are governed by viscous, inertial, gravitational and interfacial forces. In general, the Taylor bubble drift velocity (v_d) can be expressed as follows:

$$Fr_{v_d} = \frac{{v_d}^2}{gD} = f\left[Eo = \frac{g\rho_L D^2}{\sigma}, Re_{v_d} = \frac{\rho_L v_d D}{\mu_L}, \frac{L_{TB}}{D}\right] \qquad (2\text{-}15)$$

A complete dimensionless analysis of the equations of motion of the problem of gas-liquid slug flow in an inclined pipe, covering inclination range of $0 \leq \gamma \leq 90°$ with respect to the vertical pipe case, is given in detail in chapters 5 and 6.

2.3.2 Main Hydrodynamic Characteristics of Gas-Liquid Slug Flow in Inclined Pipes

The main hydrodynamic characteristics of the flow can be described using the same approach of the vertical case, which is considering the drift of a single Taylor bubble through a stagnant liquid in an inclined pipe. Figure 2-2 illustrates the main hydrodynamic features of the inclined case, which are similar to the vertical case, where the flow field can be divided into three regions the front, the body and the tail.

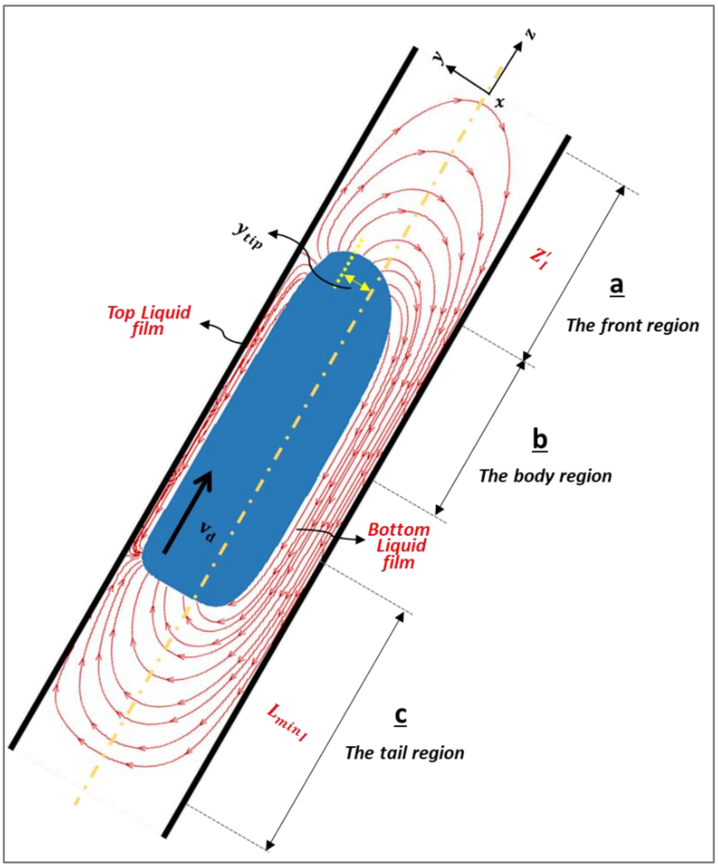

Figure 2-2. A schematic representation of the main hydrodynamic features of a single Taylor bubble rising through a stagnant liquid in an inclined pipe (Lizarraga-García, 2016).

The main hydrodynamic features are summarised as follow:

- Taylor bubble drift velocity (v_d)
- Front region: the interaction distance above the bubble (Z').
- Bubble tip position with respect to the pipe axis $\left(y_{tip}\right)$.
- Body region: the liquid film has two regions top liquid and bottom liquid films. The liquid film region has an interface separating the Taylor bubble at the upper portion of the pipe and bottom liquid film at the lower portion.
- Tail region: the perturbed distance below the bubble (L_{min}).

2.3.3 Theoretical and Experimental Studies

Generally, the drift velocity of long bubbles rising in pipes with stagnant liquid principally depends on the pipe diameter, liquid viscosity, liquid and gas densities, surface tension and inclination angle. Zukoski (1966) expresses the bubble drift velocity by the following relationship:

$$v_d = C_\infty\left[Eo, N_f, \gamma\right]\sqrt{\grave{g}D} \qquad \textit{(2-16)}$$

where $\grave{g} = \frac{g\Delta\rho}{\rho_L}$.

Zukoski (1966) investigates the effect of pipe inclination on the dynamics of Taylor bubbles in inclined pipes including the effects of viscosity and surface tension with an inclination angle of 0-90° with respect to the horizontal position. He concludes that the viscous effects are considered negligible when $Re_{U_{TB}} > 200$. The experimental results for the bubble motion follow the "peculiar trend" with the inclination angle, where the bubble velocity increases with inclination angle until it reaches a maximum value, then it starts to decrease once again.

Bonnecaze et al. (1971) clarify the maximum in the drift velocity detected at 30-50° qualitatively in terms of the gravitational potential. They claim that the gravitational potential drives the liquid velocity along the curved surface at the bubble nose initially increases and then declines with the inclination angle variation from the vertical to the horizontal position.

Vermeulen and Ryan (1971) propose a semi-empirical theory based on a simple model to calculate the pressure gradient along the slug, which showed good predictions against other correlations. Besides, they perform experiments using the air-water system to examine the flow pattern, pressure gradient, pressure fluctuation and slug frequency in horizontal and inclined pipes. Their main contributions can be summarised as follows:

- *Flow pattern:* A comparison between the developed flow pattern based on Baker (1954)'s chart is discussed.
- *Pressure gradient:* An offset due to the static head is found between the curve for pressure gradient in the inclined and the horizontal cases. The pressure gradient is significantly affected by the gas flow rate and slug breakup starts at high frequencies.
- *Pressure fluctuations:* The gas flow rate has a higher effect on the pressure fluctuations than the liquid rates. Both liquid and gas flow rates affect the flow transition in terms of pressure fluctuations. The pressure gradients differ in inclined cases only because of the static head, which is a function of the liquid holdup.
- *Slug frequency:* Gas flow rates have a minor effect on the slug frequency. Nevertheless, the high increment in slug frequency is noticed at very low gas flow rates and an increase in liquid rates. The effect of pipe inclination is observed only on the location of the sudden rise in slug frequency.

Maneri and Zuber (1974) perform an experimental study using finite air bubbles in water and methanol in inclined pipes with an inclination angle of 0-85° with respect to the vertical position. They express the bubble drift velocity in terms of tank width, tank spacing, fluid properties, bubble volume and inclination angle. Their main contributions can be summarised as follows:

- *Tank width:* As the angle of inclination rises the edge wall effect declines. Vertical tanks exhibiting a substantial wall effect for all bubble sizes have almost no wall effect for a small range of bubble sizes when being inclined.
- *Tank spacing:* The velocity of finite volume bubbles increases or remains the same with increasing the tank spacing, regardless of the bubble volume and the inclination.

- *Fluid properties*: For vertical tanks and inclined tanks of infinite extent, the bubble rise velocity in fluids of low viscosity is moderately independent of fluid properties. Though, in inclined tanks of finite width, the rise velocity increases with reducing surface tension.
- *Bubble volume*: As the bubble volume increases, the rise velocity increases for all inclination angles.
- *Inclination angle:* As the angle of inclination falls, increase the bubble velocity is noticed, although the composition of the buoyancy force along the tube axis drops that acts to subordinate the bubble velocity.
- Defining three different bubble shape regimes depending on the duct inclination which is inertial dominant (extends from 0-10°), properties dependent (extends from 30-90°) and transition (the region between 10-30°).

Spedding and Nguyen (1978) extend the work of Zukoski (1966) to include a broader range of dimensionless groups using finite/tube-draining air bubbles in the water with an inclination angle of 0-90° with respect to the horizontal position. The main purpose is to develop data plots as those done by White and Beardmore (1962) for other inclination angles and bubble volumes showing the effect of viscosity, surface tension and inertial forces on the bubble drift velocity. They observe the same “peculiar trend” of Taylor bubble velocity with the inclination angle, as observed by Zukoski (1966). They analyse the governing forces that act in inclined pipes. Firstly, the buoyancy force enhances the bubble velocity to increase along with the inclination angle of the pipe and the resistive force initiating from the draining of the liquid down past the rising bubble, that act in the opposite direction. Secondly, the bubble velocity increases with tube diameter, reaching a maximum value at Eo equals to 10,000. At this range of Eo, a secondary effect commences where the surface tension begins altering the shape of the bubble nose in such a way that the bubble speed reduces more rapidly but in a similar way to that observed in the vertical bubble rise case. Lastly, bubble volume is considerably important in the prediction of the actual magnitude of the bubble rise velocity, but it does not affect the determination of the tube angle at which the maximum bubble rise occurs.

Bendiksen (1984) performs an essential experimental study using finite air bubbles in the water in pipes with an inclination angle of 30-90° with respect to the horizontal position. The experimental data support the hypothesis of Nicklin et al. (1962) for all inclination angle the bubble propagation rate is that of the liquid in front of the tip of its nose, in addition to a possible drift velocity due to buoyancy or level effects. Based on the experimental data, a correlation to estimate the bubble drift velocity is proposed, given by:

$$\begin{aligned} v_d &= {v_d}^h \cos\gamma + {v_d}^v \sin\gamma \\ {v_d}^h &= 0.351\sqrt{gD} \\ {v_d}^v &= 0.542\sqrt{gD} \end{aligned} \tag{2-17}$$

From the main contributions of this work is that for pipes with one end opened and partly filled with liquid and gas, the value of ${v_d}^h$ is not zero, as concluded by Nicklin et al. (1962) and Dukler and Hubbard (1975). In addition, he expresses the coefficient C_∞ in equation (2-16) for high N_f values to be:

$$C_\infty = 0.344\frac{1-0.96e^{(-0.0165Eo)}}{[1-0.52e^{(-0.0165Eo)}]^{1.5}}\sqrt{\left(1+\frac{20}{Eo}\left(1-\frac{6.8}{Eo}\right)\right)} \tag{2-18}$$

Later, Weber et al. (1986) experimentally investigate the effect the liquid viscosity on the velocity of the extended bubble using air bubbles in water, methanol, sucrose and corn syrup solutions in pipes with an inclination angle of 0-90° with respect to the horizontal position. They propose a correlation for bubble drift velocity, based on modifying Bendiksen (1984)'s correlation (equation (2-17)), to account for the case of $\Delta Fr_{v_d} < 0$, given by:

$$\begin{aligned} Fr_{v_d} &= {Fr_{v_d}}^h \cos\gamma + {Fr_{v_d}}^v \sin\gamma + Q \\ Q &= \begin{cases} 1.37\left(\Delta Fr_{v_d}\right)^{\frac{2}{3}} \sin\gamma\,(1-\sin\gamma) & if\,\Delta Fr_{v_d} > 0 \\ 0 & if\,\Delta Fr_{v_d} \le 0 \end{cases} \end{aligned} \tag{2-19}$$

They suggest that for the case of a closed horizontal tube initially filled with liquid with one end opened, the liquid will drain out due to the hydrostatic pressure difference between the top and the bottom of the tube. Thus, an extended bubble will propagate along the tube in the opposite direction replacing the liquid (Hernandez-Perez et al., 2010; Lizarraga-Garcia et al., 2016). For horizontal pipes, they suggest that the critical value of Eo is at 8.5, which agree with the conclusion of Zukoski (1966) who concludes that draining occurs in a range of Eo =8.3 and Eo =12.1.

Hasan and Kabir (1988) propose a correlation for bubble drift velocity in an inclined pipe through an experimental study $30° < \gamma < 90°$, assuming ${v_d}^h = 0$, given by:

$$
\begin{aligned}
v_d &= {v_d}^v \sqrt{sin\,\gamma}\,(1 + cos\,\gamma)^{1.2} \\
{v_d}^v &= 0.35\sqrt{gD}
\end{aligned}
\qquad (2\text{-}20)
$$

with ${Fr_{v_d}}^v$ being constant with large values of N_f and Eo values.

Alves et al. (1993) perform an experimental and analytical study on the effect of surface tension on the velocity of Taylor bubbles in inclined pipes using finite air bubbles in stagnant kerosene with inclination angle 0-90° with respect to the horizontal position. They extend Benjamin (1968)'s straightforward approach, based on inviscid flow theory, to apply to the inclined and the vertical cases and taking into consideration surface tension effects. Their experimental results reveal the expected "peculiar trend" of the Taylor bubble velocity with respect to the inclination angle with a maximum velocity at inclination angle about 40°.

Abdul-Majeed (2000) develops a simple mechanistic model capable of predicting the flow behaviour for upward vertical and inclined two-phase slug flow with flowing liquid. Based on the relationships between the two-phase velocities, expressions for bubble rise velocity, liquid film velocity, liquid holdup around the Taylor bubble and liquid slug void fraction are derived. He develops a new expression for estimating the liquid slug void fraction as a function of superficial gas and liquid velocities, inclination angle and fluid properties, which shows the best performance when tested against commonly used slug models in the literature.

Petalas and Aziz (2000) develop a unified mechanistic model for two-phase flow applicable to all-around pipe geometries and fluid properties. They propose correlation for drift bubble velocity in inclined pipes, based on modifying Wallis (1969)'s correlation for vertical slug flow, given by:

$$v_d{}^h = \left(0.54 - \frac{1.76}{Eo^{0.56}}\right)\sqrt{\frac{gD(\rho_L - \rho_G)}{\rho_L}}$$

$$v_d{}^v = 0.345\left(1 - e^{-Eo-exp\,(3.278-1.424\,ln\,Eo)}\right)\sqrt{\frac{gD(\rho_L - \rho_G)}{\rho_L}} \qquad (2\text{-}21)$$

$$v_d = f_m\left(v_d{}^h\,cos\,\gamma + v_d{}^v\,sin\,\gamma\right)$$

$$where\;\; f_m = min\left(0.316\sqrt{\frac{v_{d\infty}D\rho_L}{2\mu_L}}, 1\right)\; (Zukoski,\, 1966)$$

Shosho and Ryan (2001) perform experiments on the motion of long bubbles in inclined pipes with an inclination of 5-90° with respect to the horizontal position, for both Newtonian and non-Newtonian fluids. They observe the same "peculiar trend" of Taylor bubble velocity with the inclination angle, however, the maximum velocity occurs at larger angles of inclination when the fluid is non-Newtonian (30° and 45° for Newtonian fluids and non-Newtonian fluids with low M while it occurred between 60° and 75° for non-Newtonian fluids with high M). They conclude that the tube diameter, viscosity, and surface tension have a dramatic effect on bubble drift velocity, their effects can be highlighted as follow:

- *Diameter effect:* At a given angle of inclination, Fr_{v_d} increases with increase pipe diameter.
- *Viscosity effect:* As the viscosity increases (larger values of M), the bubble nose becomes blunter, which results in a lower rise velocity.
- *Surface tension effect:* At a given angle of inclination, the increase in surface tension (higher values of Eo) results in a reduction in bubble velocity and correspondingly lower Froude number values.

More recently, advances in the experimental techniques enabled detailed investigation of the hydrodynamic characteristics of two-phase slug flow in inclined pipes, for instance, the studies by Roitberg et al. (2008); Shuhua et al. (2009); Hua et al. (2009) and Zhang et al. (2009). Roitberg et al. (2008) use a wire-mesh sensor that facilitates quantitative measurements of the cross-sectional void fraction distribution, statistical analysis of characteristic parameters of downward slug flow with flowing liquid, such as bubble and liquid slug length distributions, and the ensemble-averaged shapes of the bubble nose, liquid film and bubble tail. Whereas, the other studies use high-speed motion analyser technique to investigate the effect of inclination on liquid slug and Taylor bubble velocity for the Taylor bubble rising through a stagnant liquid.

Gokcal et al. (2009) perform experiments using water and viscous oil in inclined pipes with inclination angles of 5-90° with respect to the horizontal position, to investigate the effect of high oil viscosity on bubble drift velocity for horizontal and inclined pipes. They combine the work of Benjamin (1968) and Joseph (2003). Through which, they extend the work of Benjamin (1968) for the horizontal drift velocity to include viscosity, and used the expression of Joseph (2003) for the vertical drift velocity. They conclude that the maximum drift velocity develops at 40° and the lowest is achieved in the vertical case.

Jeyachandra et al. (2012) modify Gokcal et al. (2009)'s work by performing experiments using water and high viscous oil, to account for the effect of pipe diameter and proposing a new horizontal drift velocity closure relation that is based on both the viscosity and piped diameter is proposed, given by:

$$\begin{aligned} &Fr_{v_d} = {Fr_{v_d}}^{h} \cos\gamma + {Fr_{v_d}}^{v} \sin\gamma, \\ &{Fr_{v_d}}^{h} = 0.35 exp\left(13.7 N_f^{-0.46} Eo^{-0.1}\right), \\ &{Fr_{v_d}}^{v} = \frac{-8}{3} N_f^{-1} \sqrt{\frac{2}{9}\frac{\rho_L}{(\rho_L-\rho_G)} + \frac{64}{9} N_f^{-2}} \end{aligned} \qquad (2\text{-}22)$$

Generally, the drift velocity increases with the increase in pipe diameter and decreases with the increase in viscosity. The maximum drift velocity occurs at 30-50°. Their main contributions is that correlation (2-19), and Joseph (2003)'s correlation for the vertical flow could be used in correspondence with the modified Bendiksen (1985)'s equation to afford accurate values for drift velocity in horizontal and upward inclined case.

Similar experiments are conducted by Moreiras et al. (2014) using medium viscosity oil exploring the effect of viscosity, pipe diameter and pipe inclination angle on the bubble drift velocity. They unify dimensionless closure relationship for drift velocity using the similar correlation of Weber et al. (1986) (equation (2-19)), given by:

$$Fr_{v_d} = {Fr_{v_d}}^{h} \cos^{a}\gamma + {Fr_{v_d}}^{v} \sin^{b}\gamma + Q \qquad (2\text{-}23)$$

$$Fr_{v_d}{}^{v} = \frac{-8}{3} N_f^{-1} \sqrt{\frac{2}{9} \frac{\rho_L}{(\rho_L - \rho_G)} + \frac{64}{9} N_f^{-2}} - \left(\frac{\sqrt{2}}{3} - 0.35\right) \sqrt{\frac{\rho_L}{(\rho_L - \rho_G)}}$$

$$Fr_{v_d}{}^{h} = 0.54 - \frac{N_f^{-1}}{1.886 + 0.01443 N_f^{-1}}$$

$$Q = \begin{cases} c\left(\Delta Fr_{v_d}\right)^{d} sin\,\gamma\,(1 - sin\,\gamma), & if\,\Delta Fr_{v_d} > 0 \\ 0, & if\,\Delta Fr_{v_d} \leq 0 \end{cases}$$

where the parameters a, b, c and d are given by 1.2391, 1.2315, 2.1589 and 0.70412, respectively.

Other recent experimental studies of slug flow in inclined pipes have been carried out by Losi and Poesio (2016) and Bhagwat and Ghajar (2016). The first study investigates the effect of viscosity on the drift velocity of an air bubble in a horizontal and inclined pipe with the main focus on the force analysis in the inclined case via applying the momentum equations and showing the significance of hydrostatic pressure gradients, buoyancy body force, wall viscous force and surface tension force. Their conclusion contradicts Benjamin (1968), the bubble drift velocity is not constant, whereas the front displaces along the pipe and, on the whole, the viscosity slows down the propagation rate of the bubble. The second study experimentally investigates the two-phase flow phenomenon in upward inclined pipes with particular focus on flow visualisation, void fraction, pressure drop and heat transfer measurements in non-boiling gas-liquid two-phase flow. Based on their heat transfer measurements, the circumferential variation of two-phase heat transfer coefficient and its relation to the flow symmetry is discussed.

Lastly, Roitberg et al. (2016) experimentally investigate the effect of pipe inclination and gas and liquid flow rates on elongated bubble shape in continuous slug flow in pipes with inclination angle 2-90° with respect to the horizontal position. Also, they develop a theoretical film drainage model to predict the extent of the upper liquid film domain. The results show that the length of the liquid film above the elongated bubble increases with the inclination angle along with the mixture velocity. They develop ensemble-averaged representative bubble shapes for several flow conditions and link them with those predicted theoretically by combining the model of Taitel and Barnea (1990) for the lower liquid film, added to it the extension of the developed model to the upper liquid film and generally both agree reasonably well.

In conclusion, it should be pointed out that most of the discussed studies (mainly experiment ones) observe the "peculiar trend" of Taylor bubble velocity with the inclination angle, which is defined the inclination angle increases from the vertical position ($\gamma = 0$), Fr_{v_d} increases reaching a maximum value and then decreases. However, there are different contributions regarding the inclination angle at which maximum Taylor bubble velocity is noticed. Table 2-2 summarises the experimental and/or analytical studies with their corresponding working fluids and their conclusion regarding the angle at which maximum Fr_{v_d} is noticed.

Table 2-2. Summary of the experimental studies of Taylor bubbles in inclined pipes with their corresponding inclination angles, working fluids and angle at which maximum Fr_{v_d} is noticed.

Reference	Inclination angle ($\boldsymbol{\gamma}$) in degrees	Working fluids	$\boldsymbol{\gamma}$ at which maximum $\boldsymbol{Fr_{v_d}}$ occurs
Zukoski (1966)	0 to 90° from the horizontal position	Air in water, carbon tetrachloride, mercury, glycerin and ethylene glycol solutions	$40° < \gamma < 60°$
Spedding and Nguyen (1978)	0 to 90° from the horizontal position	Finite/tube-draining air bubbles in the water	35°
Bendiksen (1985)	-90 to 90° from the horizontal position	Finite air bubbles in the water	$40° < \gamma < 60°$
Hasan and Kabir (1988)	30 to 90° from the horizontal position	Air bubbles in the water	$40° < \gamma < 60°$
Weber et al. (1986)	0 to 90° from the horizontal position	Tube-draining/finite air bubbles in water, methanol, sucrose and corn syrup solutions	$40° < \gamma < 60°$
Alves et al. (1993)	0 to 90° from the horizontal position	Finite air bubbles in kerosene	40°
Shosho and Ryan (2001)	5 to 90° from the horizontal position	Newtonian fluids: Water and corn syrup mixture. Non-Newtonian fluids: carboxymethylcellulose (CMC), hydroxyethylcellulose (HEC), polyacrylamide (PAA) and polyvinylpyrrolidone (PVP).	$30 < \gamma < 45°$
Gokcal et al. (2009)	5 to 90° from the horizontal position	Water and high viscous oil	40°
Hua et al. (2009)	0 to 50° with respect to normal	Liquid nitrogen-cryogenic fluid	$20° < \gamma < 30°$

2.3.4 Experimental and Numerical Studies

This section covers the experimental and/or numerical studies of investigating the gas-liquid slug flow in inclined pipes. Earlier attempts by Couët and Strumolo (1987) to develop a numerical solution, with 2D analysis (based on Newton's method), determining the bubble shape and the influence of surface tension and viscosity and inclination angle on Fr_{v_d}. The numerical results for bubble shape and rise velocity show good correspondence when tested against theoretical and experimental work in the literature. Their main contribution is that the dependence on the angle of inclination decreases as viscous effects increase.

Generally, in the literature, there are no extensive CFD studies on Taylor bubbles in inclined pipes. The assumption of axisymmetry as in the vertical pipes can no longer be applied, and hence full 3D simulations are necessary for such simulations. Yet, there are no extensive studies on this problem in the literature. It is worth to mention that few numbers of CFD studies are available in the literature that investigates the motion of Taylor bubble with flowing liquid in inclined pipes (Hernandez Perez, 2008; Hernandez-Perez et al., 2010; Mazza et al., 2010; Pokusaev et al., 2016). For instance, the work of Hernandez Perez (2008) is experimentally and numerically investigation of the behaviour of two-phase flow in inclined pipes, using water and air, with a wide range of gas and liquid velocities. The simulation is done using the volume-of-fluid (VOF) method implemented in the commercial software ANSYS Fluent. Mazza et al. (2010) develop a complete analysis of liquid film model for horizontal and near horizontal gas-liquid (up to 30°off horizontal position) slug flows with flowing liquid, that employs one-dimensional separated phase momentum equations. They develope a liquid film model that is tested against experiment performed for an air-water system for the horizontal pipe.

Finally, Pokusaev et al. (2016) perform an experimental and numerical study of the gas projectile mass transfer when moving in an inclined pipe. They mainly focus on the dependence of the velocity of the gas projectile motion and effective dimensionless mass transfer coefficient on the pipe inclination angle. Their main contribution is that the rate of the bubble, expressed as a function of the inclination angle of the pipe, is non-monotonous and extreme.

However, the CFD studies on the rise of Taylor bubbles through a stagnant liquid in inclined pipes are very limited. For instance, Taha and Cui (2006) perform 2D axisymmetric simulations of vertical pipes with stagnant fluid and reported only one case of 3D simulations of inclined cases. Through applying this, they present the capability of the volume-of-fluid (VOF) method in tackling the 3D complex slug flows in inclined pipes as well as providing a complete analysis of the problem.

Most of the studies mainly focus on investigating Taylor bubble drift velocity in inclined pipes, however, some of the studies deal with the liquid film region and its effect on the bubble motion. For instance, Behafarid et al. (2015) perform numerical simulations using PHASTA (Parallel Hierarchic Adaptive Stabilized Transient Analysis) computer code, combined with the level set method for interface tracking to investigate the dynamics of large deformable bubbles in pipes with stagnant liquid of different geometries and orientations (30°,45° and 60° from vertical position). They conclude that Taylor bubble velocity in inclined pipes mainly depends on the pipe wall wettability. According to their conclusion, if the wall is thoroughly wetted, the liquid film is likely to be very thin, and this thickness has a negligible effect on bubble motion. This occurs when the pipe's size is largely related to the bubble's size, which that the effective drag force is controlled by bubble shape and size instead of the wall shear. Moreover, the thickness of the thin liquid film attained in inclined pipes has almost no impact on both bubble shape and motion.

Recently, Lizarraga-García (2016) perform an experimental and numerical investigation of Taylor bubble rise velocity in the stagnant and flowing liquid in vertical and inclined pipes, with a wide range of dimensionless groups M, Eo and γ. Experiments, using air, ethanol and methanol in pipes with an inclination of 0-90°from the horizontal position, are done as a part of the validation of the numerical method. Different hydrodynamics of the Taylor bubble problem are examined including most of the parameters given in Figure 2-2. Additionally, he examines most of the correlations in literature for estimating Taylor rise velocity in inclined pipes and concludes that they all need some improvement. Thus, based on the results, the author suggests a correlation to predict Taylor bubble rise velocity in inclined pipes. Moreover, another important part of this study is the analytical film drainage model that predicts the gravity-driven drainage of the lubricating film between the bubble and the pipe wall in inclined pipes. Generally, in inclined pipes, as the inclination increases the bubble approaches the pipe wall, and the liquid film becomes considerably thinner and non-axisymmetric. Due to axial gravity-driven drainage, the thickness of the film diminishes along the Taylor bubble. If the film breaks up, the surface tension force at the triple contact line reduces the velocity of the bubble meaningfully (Behafarid et al., 2015). Subsequently, Lizarraga-García (2016) proposes a criterion for film breakup, given by:

$$\bar{t}_{bubble} = t_{bubble}/\tau_{ch} < 0.01 \qquad (2\text{-}24)$$

The characteristic film drainage time (τ_{ch}) is based on fluid properties, pipe geometry and critical film thickness. If the criterion given in equation (2-24) is satisfied, then the thin film would not break up.

Lastly, the computational domain in buoyant bubble problems needs to be large enough to capture the phenomena effectively. This to enable the bubble to reach a steady-state condition. Different approaches are used in literature, aiming to minimise computational resources. For instance, Gutiérrez et al. (2017) employ a domain optimisation method and used an Arbitrary Lagrangian-Eulerian formulation to numerically solve the three dimensional Taylor bubbles drifting in stagnant liquid. The method is based on a moving mesh that follows the rise of the Taylor bubble. Numerical stability and worthy performance are achieved when applying the method and testing the three-dimensional standard rising bubble against experimental data from the literature. They handle the main withdraw of the technique, which is the need of using open boundaries (namely, inflow and outflow), by applying a new outflow boundary condition. A full analysis of the problem is done, including examining the effect of initial Taylor bubble shape, the initial volume of the bubble, and the tube inclination on the dynamics of Taylor bubbles. Regarding the tube inclination, a quantitative analysis is carried out where the authors show the effect of inclination through:

- *TB terminal shape:* Average diameter of the bubble is reduced as the inclination increases, leading to a growth in the bubble length.
- *Pressure fields:* The range of variation of the pressure is similar to the different angles and the pressure isosurfaces have a trend of being perpendicular to the gravity vector.
- *Plotting the streamlines in xy and yz planes:* Two regions of opposite vorticity can be found in both sides of the bubble which becomes increasingly apparent when the inclination rises.

In brief, it should be pointed out that most of the research on Taylor bubbles problems focus on the bubble motion and the effect of different parameters, such as surface tension, viscosity and pipe diameter on it. Table 2-3 summarises the main correlations proposed in the literature

Table 2-3. Summary of the main correlations proposed in the literature for the rising velocity of a Taylor bubble in inclined pipes with stagnant liquid.

Reference/Type of study	Correlation, assumptions and comments
Bendiksen (1985) Experimental and theoretical	$v_d = {v_d}^h \cos\gamma + {v_d}^v \sin\gamma$, ${v_d}^h = 0.351\sqrt{gD}$, ${v_d}^v = 0.542\sqrt{gD}$ • γ ranges from $-90°$ to $90°$, $Fr_{v_{d_{max}}}$ at $40° < \gamma < 60°$ • Eo ranges from 50—340, $M \approx 2.63{\cdot}10^{-11}$
Weber et al. (1986) Experimental	$Fr_{v_d} = {Fr_{v_d}}^h \cos\gamma + {Fr_{v_d}}^v \sin\gamma + Q$, $Q = \begin{cases} 1.37(\Delta Fr_{v_d})^{\frac{2}{3}} \sin\gamma\,(1-\sin\gamma), & if\,\Delta Fr_{v_d} > 0 \\ 0, & if\,\Delta Fr_{v_d} \leq 0 \end{cases}$ • γ ranges from 0 to 90° from the horizontal position, $Fr_{v_{d_{max}}}$ at $30° < \gamma < 60°$ • Eo ranges from 4.9—490, M= $2.2{\cdot}10^{-11} - 1.5{\cdot}10^{4}$ • Applicable for High-viscosity Newtonian liquids
Hasan and Kabir (1988) Experimental and theoretical	$v_d = {v_d}^v \sqrt{\sin\gamma}\,(1+\cos\gamma)^{1.2}$, ${v_d}^v = 0.35\sqrt{gD}$, ${v_d}^h = 0$ • γ ranges from 30 to 90° from the horizontal position. • Assume ${v_d}^h = 0$, • Eo=2200, $M = 2.63{\cdot}10^{-11}$ • Applicable for systems with large N_f and Eo values
Petalas and Aziz (2000) Theoretical	${v_d}^h = \left(0.54 - \frac{1.76}{Eo^{0.56}}\right)\sqrt{\frac{gD(\rho_L-\rho_G)}{\rho_L}}$, ${v_d}^v = 0.345\left(1 - e^{-Eo-exp\,(3.278-1.424\ln Eo)}\right)\sqrt{\frac{gD(\rho_L-\rho_G)}{\rho_L}}$, $v_d = f_m({v_d}^h \cos\gamma + {v_d}^v \sin\gamma)$, $f_m = min\left(0.316\sqrt{\frac{v_{d_\infty} D\rho_L}{2\mu_L}}, 1\right)$ (Zukoski, 1966) • γ ranges from $-90°$ to $90°$, $Fr_{v_{d_{max}}}$ at $40°$ • Applicable for high Reynolds numbers
Gokcal et al. (2009) Experimental	$h/D = 0.1038\ln\mu_L + 0.9684$, $S/D = \sqrt{1-(2h/D-1)^2}$, $\gamma_1 =, \begin{cases} \pi - \sin^{-1}(S/D) & if\ h/D < 0.5 \\ \sin^{-1}(S/D) & if\ h/D \geq 0.5 \end{cases}$ $\gamma = min(\gamma_1, 1.444784)$, $\zeta = (\gamma - 0.5\sin 2\gamma)/\pi$, $\Delta = 2.2\frac{1+\zeta}{\zeta}\left(\left(\frac{D}{2}(1-\cos\gamma)\right) - \left(\frac{\left(\frac{D}{2}(1-(1-\zeta)\cos\gamma)\right)+\frac{2}{3\pi}\sin\gamma}{1-\zeta^2}\right)\right)$, $v_2 = \sqrt{gD\left((1-(1-\zeta)\cos\gamma) - \frac{2}{3\pi}\sin^3\gamma\right) - 2\Delta g(1-\zeta)}$, ${v_d}^h = v_1 = (1+\zeta)v_2, {v_d}^v = \frac{-8}{3}\frac{\mu_L}{\rho_L D} + \sqrt{\frac{2}{9}gD + \frac{64}{9}\left(\frac{\mu_L}{\rho_L D}\right)^2}$, $v_d = {v_d}^h\,(\cos\gamma)^{1.5} + {v_d}^v\,(\sin\gamma)^{0.7}$ • γ ranges from 5 to 90° measured from the horizontal position, $Fr_{v_{d_{max}}}$ at 40°. • Eo=776, $M = 4.52{\cdot}10^{-10} - 1.63{\cdot}10^{3}$ • Applicable for high viscosity oil.
Jeyachandra et al. (2012) Experimental	$Fr_{v_d} = {Fr_{v_d}}^h \cos\gamma + {Fr_{v_d}}^v \sin\gamma$, ${Fr_{v_d}}^h = 0.53exp\left(-13.7N_f^{-0.46}Eo^{-0.1}\right)$,${Fr_{v_d}}^v = \frac{-8}{3}N_f^{-1} +$ $\sqrt{\frac{2}{9}\frac{\rho_L}{(\rho_L-\rho_G)} + \frac{64}{9}N_f^{-2}}$ • γ ranges from 0 to 90° measured from the horizontal position • Eo=776—6985, $M = 0.254$—49.1 • $Fr_{v_{d_{max}}}$ at $30° < \gamma < 50°$
Moreiras et al. (2014) Experimental	$Fr_{v_d} = {Fr_{v_d}}^h \cos^a\gamma + {Fr_{v_d}}^v \sin^b\gamma + Q$, ${Fr_{v_d}}^v = \frac{-8}{3}N_f^{-1} + \sqrt{\frac{2}{9}\frac{\rho_L}{(\rho_L-\rho_G)} + \frac{64}{9}N_f^{-2}} - \left(\frac{\sqrt{2}}{3} - 0.35\right)\sqrt{\frac{\rho_L}{(\rho_L-\rho_G)}}$, ${Fr_{v_d}}^h = 0.54 - \frac{N_f^{-1}}{1.886+0.01443N_f^{-1}}$, $Q = \begin{cases} c(\Delta Fr_{v_d})^d \sin\gamma\,(1-\sin\gamma), & if\,\Delta Fr_{v_d} \geq 0 \\ 0, & if\,\Delta Fr_{v_d} < 0 \end{cases}$ a = 1.2391, b = 1.2315, c = 2.1589, d = 0.70412 • γ ranges from 0 to 90° measured from the horizontal position, $Fr_{v_{d_{max}}}$ at $30° < \gamma < 50°$ • Eo=804, $M = 1.25{\cdot}10^{-3} - 10.412$
Lizarraga-García (2016) Experimental and Numerical work	${Fr_{v_d}}^v = \frac{0.34/\left(1+(14.793/Eo)^{3.06}\right)^{0.58}}{\left(1+\left(\left(\frac{N_f}{31.08\left(1+(29.868/Eo)^{1.96}\right)^{0.49}}\right)\right)^a\right)^b}$, $a = -1.45(1+(24.867/Eo)^{9.93})^{0.094}$, $b = -1.0295/a$ $Fr_{v_d} = {Fr_{v_d}}^v\left(1 - exp\left(-B((Eo,M))\gamma\right)\right)\left(1 + \left(C(Eo,M)\right)\sin(2\gamma)\right)$, $B(Eo,M) = 47.06{Fr_{v_d}}^v + 4$ $C(Eo,M) = -0.9118{Fr_{v_d}}^v + 0.67 + \frac{\left(-0.0148(\log_{10}M)^2 + 0.125\log_{10}M + 0.9118{Fr_{v_d}}^v + 1.118\right)}{(1+(Eo/20)^8)^8}$ • γ ranges from 5 to 90° measured from the horizontal position, $Fr_{v_{d_{max}}}$ at 45°. • The horizontal pipe case is not included. • Eo=10:700, $M = 1{\cdot}10^{-6} - 5{\cdot}10^{3}$

for the rising velocity of a Taylor bubble in inclined pipes with stagnant liquid with their limitations.

2.4 Concluding Remarks

The primary purpose of this chapter is to introduce an extensive survey of two-phase slug flow in pipes, in particular, the rise of Taylor bubbles in vertical and inclined pipes. It can be concluded that there are conflicts in defining the problem in terms of the dimensionless governing groups. For instance, most studies reveal that the rise of Taylor bubbles could be defined in terms of a number of dimensionless parameters, namely the Froude, Eötvös and Morton numbers. There is no need to use a dimensionless number like Morton number (M) which is defined as a property group that doesn't represent any important governing forces. Other studies use the inverse viscosity number (N_f) rather than Morton number (M). However, N_f can be interpreted physically as the ratio between gravity force and the viscous force, which can hardly be indicative of the onset of turbulence, which is inertial in the first place and probabilistic in essence.

Based on the review discussed, despite the significant numerical and theoretical data published on the rise of Taylor bubble through a stagnant vertical liquid, to the author's knowledge, there is not yet a study investigating the problem using the order of magnitude analysis of equations of motion. Thus, the main scope of the thesis is performing a complete dimensionless analysis of the rise of Taylor bubbles in pipes using both the Buckingham-Pi theorem and the dimensionless treatment followed by order of magnitude analysis to the governing equations of motion. This theoretical treatment is important for the visualisation of the real parameters or groups that influence the equations of motion. Besides, it is important for developing a phenomena-logical approach to the physical problem that can bring up useful relations between the system parameters. In addition, the order of magnitude analysis along with the dimensional analysis provides a way to show the relative merits of the different terms available in the governing equations, which makes the understanding of the problem more pronounced and any simplifications to the governing equations, if available, more reliable.

Additionally, based on the review discussed, despite the recent development of the experimental techniques, there are still limitations and difficulties in performing experiments in such field. As shown in the literature, there are main difficulties in showing the developed Taylor bubble shape, while exploring the effect of the main forces on it. This includes the wake structure as well, where it can be concluded that there are difficulties in obtaining the wake parameters, mainly wake length and volume, especially in the concave of the bubble rear. Furthermore, the main limitation of the experimental studies of the present problem is the question of the reliability of the experiments available in the literature as far as the provision of zero pressure gradient along the pipe and the absence of positive direct non-intrusive measurements of two-phase flow characteristics other than the present questionable methods. An accurate and reliable CFD analysis is a must, particularly when the code is tailored specifically for the problem rather than a commercial one. Hence, the second scope of this work is employing a CFD study using the volume-of-fluid (VOF) methodology to support the developed logical approach of the problem obtained from the dimensionless treatment.

Based on the previous numerical work given in the literature, the choice of the numerical model (VOF model) for the numerical studies presented in this thesis is influenced. The VOF model has proven to be an accurate and robust method for tracking the interface and modelling the hydrodynamic characteristics of slug flow in pipes. Details about the adopted numerical method are given in chapter 3.

Based on the dimensionless analysis, the main hydrodynamic features of rising of an individual Taylor bubbles through stagnant Newtonian liquids are investigated by applying computational fluid dynamics (CFD) simulation using the volume-of-fluid (VOF) methodology implemented in the commercial software ANSYS Fluent. To support other important theoretical and experimental work available in the literature, different correlations for the Taylor bubble drift velocity and wall shear stress in vertical pipes, based on the developed numerical results and the guidelines of the order of magnitude analysis, are suggested.

Based on the analysis of the background literature, it can be concluded that there is a lack of numerical work in simulating the drift of the Taylor bubble in an inclined pipe. Even though this type of simulations is considered computationally expensive in terms of the computational time and resources, the lack of simulation studies is the motivation for the work given in chapter

5, which is a summary of the computational results of the hydrodynamic features of Taylor bubbles in inclined pipes.

Finally, in the literature, various contradicting discussions are describing the bubble behaviour in horizontal pipes. This conclusion motivates the computational analysis given in chapter 6. Through which a particular treatment, in both the dimensionless treatment and the numerical investigation, is performed to the near horizontal and horizontal pipe Taylor bubble flow.

Chapter 3 CFD Model Description and Validation

In this chapter, the employed CFD model in this thesis is described with full details about the governing equations, the multiphase model used and the solution method. The model is then validated against experimental data, theoretical correlations and empirical models for some of the main hydrodynamics features of slug flow, including Taylor bubble terminal velocity, Taylor bubble shape, liquid film thickness, wall shear stress and wake region length and volume. The validation study reveals that the numerical results are accurate enough to investigate the drift of Taylor bubbles in vertical and inclined pipes.

3.1 Introduction

This chapter starts with addressing the numerical model used throughout the thesis. This includes a description of the governing equations, discretisation and method of solution, solver controls and mesh employed. This is followed by the verification part that discusses the different types of errors, including the error and uncertainty, spatial and temporal discretisation error, convergence, computer round off error and computer programming errors.

In addition, discussion on the base model where the 2D axisymmetric model is discussed. The model geometry, initial and boundary conditions, initial Taylor bubble shapes, grid dependency study and verification of the base model are all addressed.

Lastly, section 3.4 gives a brief discussion on the computational resources used in the thesis, including the number of cores, CPU hours and estimated run time of the simulations. Section 3.5 deals with validation studies, where a number of experimental cases are simulated for the sake of model validation. This covers the base model, which is a 2D axisymmetric model and the inclined model, which is a 3D model. The validation study for vertical pipes is based on the experimental work of Bugg and Saad (2002) and Nogueira et al. (2006a; 2006b) on a single Taylor bubble rising through a stagnant viscous liquid in a vertical pipe under laminar flow regime. This includes comparison on the developed Taylor bubble shape, flow field around the Taylor bubble and other critical hydrodynamic characteristics. Lastly, the current CFD model is used to validate the experiment cases of Shosho and Ryan (2001) for the drift of Taylor bubbles in inclined pipes.

To sum up, the chapter ends with a conclusion section that reports the findings from the CFD model and cases tested.

3.2 Numerical Model

3.2.1 Governing Equations

Two-phase slug flow is complex in nature due to its intermitted flow pattern behaviour. Figure 1-4 shows a schematic of two-phase gas-liquid vertical slug flow composed of an alternate succession of two main bodies, a bullet shape elongated gas bubble known by Taylor bubble flowing over a thin liquid film and a liquid slug region. This known by the concept of the unit cell (Medina et al., 2015).

The slug flow intermittence nature makes the accurate prediction of flow characteristics a complex and challenging task. As discussed in chapter 2, various numerical methods are available for numerical modelling of two-phase slug flow. Throughout the thesis, the developed CFD method used is a slug tracking method using the Volume-of-fluid method (VOF method) implemented in the commercial code ANSYS Fluent. The CFD method is based on the fundamental concept of slug unit cell where the flow is assumed to consist of a single unit cell to avoid time-consuming simulations.

In the present model, the fluids share a well-defined interface, and hence, the volume-of-fluid (VOF) method for two-phase flow is selected. The VOF model is a surface-tracking technique applied to a fixed Eulerian mesh. This model is designed for two or more immiscible fluids to track the interface between them. This model solves a single set of momentum equation that is shared by the two fluids, and the volume fraction of each of the fluids in each computational cell is followed throughout the domain. Details of the governing equations and the treatment of the interface can be obtained from Fluent (2015).

One set of continuity and momentum equations are solved for the two-phase system. Firstly, the continuity equation in a VOF model for N number of phases can be expressed as follows;

$$\frac{\partial \rho}{\partial t} + \nabla.(\rho V) = \sum_{q=1}^{N} S_q \tag{3-1}$$

For the present two-phase flow, N=2 and the mass source, S_q, is set to zero. For incompressible flow, (3-1) would result in the following form:

$$\nabla.V = 0 \tag{3-2}$$

In addition, the momentum equation is solved throughout the computational domain, and all phases share the same resulting velocity field. The momentum equation for unsteady incompressible flow can be written as follows:

$$\rho\left[\frac{\partial V}{\partial t}+(V.\nabla)V\right]=-\nabla P+\mu(\nabla.\nabla)V+F \tag{3-3}$$

The additional forces could be a gravitational term or surface tension. Thus, the LHS of equation (3-3) represents the unsteady term and convection terms. While, the RHS represents the pressure term, the diffusion term, the body force and other external forces that might act on the system. The surface tension at the gas-liquid interface is calculated using the continuum surface force (CSF) of Brackbill et al. (1992), which is given by:

$$F_S=\sigma K n \tag{3-4}$$

The unit normal of the interface (n) is defined in terms of the volume fraction (α_G) as follows:

$$n=\nabla\alpha_G \tag{3-5}$$

and K is given by:

$$K=\nabla.\frac{\nabla\alpha_G}{|\nabla\alpha_G|} \tag{3-6}$$

The VOF formulation depends on the impossible interpenetration among two or more fluids (or phases). For each additional phase that is added to the model, a variable is introduced, which is the volume fraction of the phase in the computational cell. In each control volume, the volume fractions of all phases sum to unity. If the volume fraction of the q^{th} fluid in a cell is given by α_q, thus the following relationship is valid for each computational cell:

$$\sum_{q=1}^{N}\alpha_q=1 \tag{3-7}$$

The fields for all variables and properties are shared by the phases and represent volume-averaged values, as long as the volume fraction of each of the phases is known at each location. Thus the variables and properties in any given cell are either purely representative of one of the phases, or representative of a mixture of the phases, depending upon the volume fraction values (Fluent, 2015). Hence, there are three possible conditions:

1. If $\alpha_q = 0$, the cell is empty of the q^{th} fluid.
2. If $\alpha_q = 1$, the cell is occupied mainly by the q^{th} fluid.
3. If $0 < \alpha_q < 1$, the cell contains the interface between the q^{th} fluid and the other fluid.

The continuity and the momentum equations are thus dependent on the volume fractions of all phases through the volume-fraction-averaged properties ρ and μ. Hence, depending on the local value of α_q as discussed above, the volume-fraction-averaged density and viscosity are calculated as follows:

$$\rho = \sum_{q=1}^{N} \rho_q \, \alpha_q \tag{3-8}$$

$$\mu = \sum_{q=1}^{N} \mu_q \alpha_q \tag{3-9}$$

Tracking the interface between the two phases is achieved by the treatment of the volume fraction of the q^{th} fluid (α_q) through solving a separate continuity equation, given by Fluent (2015), as follows:

$$\frac{1}{\rho_q}\left[\frac{\partial}{\partial t}\left(\alpha_q \rho_q\right) + \nabla.\left(\alpha_q \rho_q V_q\right)\right] = S_q + \sum_{p=1}^{n_{step}} \left(\dot{m}_{pq} - \dot{m}_{qp}\right) \tag{3-10}$$

According to Fluent (2015), the source term on the RHS of equation (3-10) is by default set to zero. The volume fraction, equation (3-10), will only be used to solve the volume fraction of the q^{th} fluid (α_q) and not the primary phase (liquid phase). The gas phase is computed according to the constraint given in equation (3-7).

Finally, for unsteady incompressible flow, equation (3-10) can be written as follows:

$$\frac{\partial \alpha_q}{\partial t} + \nabla.\alpha_q V_q = 0 \tag{3-11}$$

3.2.2 Mesh

An essential part of the numerical solution is the mesh or grid generation process to ensure a valid and therefore accurate numerical solution. Mesh or grid generation is the process of sub-dividing the computational domain into a number of discrete control volumes (cells) for the finite volume process to solve the governing equations. In this thesis, the meshing is done using the mesh incorporated in ANSYS Fluent (Release 16.0) and then imported to solver section (Fluent) where calculations are performed.

The gird density and distribution can significantly affect the numerical stability and accuracy of the solution. There are different cell types for mesh generation. For instance, quadrilateral or triangular elements can be used for the 2D domain. While, tetrahedral, hexahedral, pyramidal and prismatic cells can be used for the 3D domain.

The mesh generation could be either encountered in structured or unstructured topology. The advantage of the structured mesh is the flexibility of data access and storage. However, the mesh needs to be preserved at the time, and hence, additional cells might be required. Thus, to have structure mesh, there is a restriction to use quadrilateral cells for a 2D domain and hexahedral cells for the 3D domain. The mesh generation, according to the different domains used, either 2D or 3D, is given in detail in sections 3.4.1 and 3.4.2, respectively. However, throughout the thesis, structure quadrilateral mesh is used for the 2D domain, and block-structured grid with an O-Grid topology is used for the 3D domain.

The quality of the mesh can be examined by a variety of criteria, such as element quality, cell skewness, cell aspect ratio, orthogonal quality, parallel deviation and maximum corner angle. For each mesh generated, two main criteria are examined, the cell skewness and the orthogonal quality to ensure good mesh quality.

3.2.3 Discretisation and Method of Solution

After dividing the computational domain into a number of discrete cells, the governing equations are now to be numerically solved. To numerically solve the governing equations, discretisation of the equations is required to convert the continuous partial differential equations to discrete finite difference equations. Throughout the thesis, the Finite Volume

Method (FVM) with an algebraic segregated solver and co-located grid arrangement, as implemented in ANSYS Fluent, is used.

3.2.3.1 Spatial Discretisation

The process of discretisation ends with discrete values of a scalar quantity (φ) which are stored at the cell-centroids, but face values (φ_f) are required and must be interpolated from the values at the cell centroid. There are various types of discretisation schemes that could be used to calculate these face values. For instance, the First-Order Upwind (FOU) scheme assumes that the values of a variable at the cell centroid are representative of an average value throughout the cell. The Second-Order Upwind (SOU) scheme uses a Taylor series expansion of the cell centred solution about the cell centroid to obtain the face values.

Lastly, the Quadrilateral Upwind Interpolation for Convective Kinematics (QUICK) scheme is based on a weighted average of second order upwind and central interpolations of variables (Ambrose, 2015). The QUICK scheme is used for computing high-order value of the convected variables at the face (φ_f). Referring to Figure 3-1 for one-dimensional control volume, assuming flow direction from left to right, for face e, the face value (φ_e) can be given as follows:

$$\varphi_e = \grave{\theta}\left[\frac{S_d}{S_c+S_d}\varphi_P + \frac{S_c}{S_c+S_d}\varphi_E\right] + \left(1-\grave{\theta}\right)\left[\frac{S_u+2S_c}{S_u+S_c}\varphi_P + \frac{S_c}{S_u+S_c}\varphi_W\right] \qquad (3\text{-}12)$$

where S is the control volume average (Leonard and Mokhtari, 1990). Setting $\theta^{`} = 1/8$ in (3-12), gives the traditional QUICK scheme. For more accurate results, it is advised to be used with structured meshes associated with the flow (Fluent, 2015).

Details about the Finite Volume Method (FVM) discretisation methods are given by Versteeg and Malalasekera (2007). In this study, different schemes are tested, and the following spatial discretisation schemes are employed throughout the work, Green-Gauss Node Based for the gradient, PRESTO for pressure, Geo-reconstruct for volume fraction and QUICK scheme for momentum.

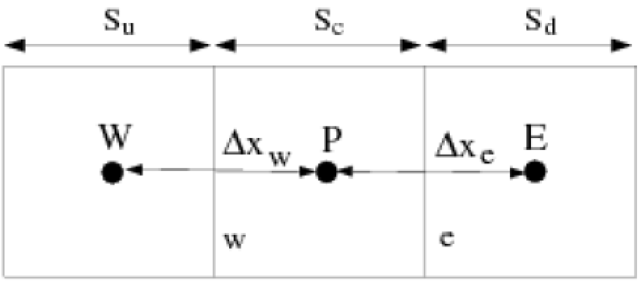

Figure 3-1. Schematic representation of one-dimensional control volume used for QUICK scheme discrtisation method.

3.2.3.2 Temporal Discretisation

For transient simulations, discretisation of the time domain into a number of discrete cells, known as a time step, is required. For transient formulations, there are a different number of discretisation methods, as discussed in ANSYS Fluent (Fluent, 2015). For instance, the backward differencing scheme with either first order or second order accuracy can be used. Implicit or explicit time integration schemes can be used to calculate the discretised time derivative. The implicit scheme is solved with each time step and is considered stable. However, the explicit scheme is partially stable. The temporal discretisation employed in this thesis is the implicit time integration method due to its stability. There is a restriction on the time step size, according to Courant-Freidrich-Lewy (CFL) condition, given by:

$$Cr = \frac{u_{ch}\Delta t}{\Delta x} \leq 1 \qquad (3\text{-}13)$$

For explicit CFD methods, the time step must be adjusted such that the Courant number is sufficiently small (Fluent, 2015). In the thesis, the implicit first-order temporal discretisation is used with an explicit VOF scheme (described in section 3.2.3.4). Thus, the value of the Courant number is fixed to 0.25 in all simulation cases.

3.2.3.3 Pressure-Velocity Coupling

Based on the segregated solver in ANSYS Fluent shown in Figure 3-2, a coupling between the pressure and velocity terms is required to link both the continuity and momentum equations. In the literature, different algorithms, such as SIMPLE, SIMPLEC, PISO and NITA are reported in ANSYS Fluent that can perform this coupling. For instance, it is recommended to use SIMPLE or SIMPLEC algorithms when performing steady-state calculations. On the other hand, it is recommended to use PISO for transient calculations.

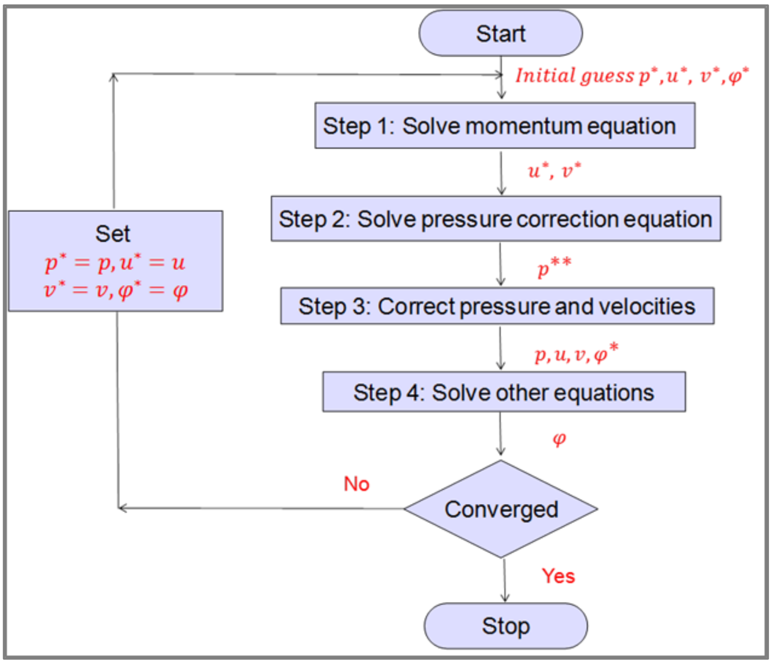

Figure 3-2. Segregated solution flowchart.

The Pressure Implicit with Splitting Operators (PISO) scheme (Issa, 1986) uses the neighbour correction iteration where more accuracy is done when correcting the velocities to satisfy Navier Stokes equations. It might take longer computational time, however, fewer iterations are needed for solution convergence. With the proper choice of under-relaxation factors, PISO scheme can provide both accuracy and fast convergence, and hence it is selected for pressure-velocity coupling throughout the thesis (Hernandez-Perez et al., 2010; Fluent, 2015).

3.2.3.4 VOF-Interface Reconstruction

The VOF method solves a separate continuity equation for the volume fraction to track the interface between the two phases. This equation could be solved either using explicit or implicit time discretisation. The implicit scheme requires an iterative solution of VOF at each time step (n_{step}), can be used for complex flows and can be run with large time steps. However, the explicit scheme does not require an iterative solution of the VOF equation during each time step, can be used for solving time-dependent calculations and provide a sharper interface and more accurate solution. Additionally, it applies finite-difference interpolation schemes to the volume fraction values from the previous time step, and it has the following general form:

$$\frac{{\alpha_q}^{n_{step}+1}{\rho_q}^{n_{step}+1} - {\alpha_q}^{n_{step}}{\rho_q}^{n_{step}}}{\Delta t}\mathcal{V} + \sum_f \left(\rho_q U_f^{n_{step}} \alpha_{q,f}^{n_{step}}\right) = 0 \qquad (3\text{-}14)$$

However, for unsteady incompressible flow, equation (3-14) can be written as follows:

$$\frac{{\alpha_q}^{n_{step}+1} - {\alpha_q}^{n_{step}}}{\Delta t}\mathcal{V} + \sum_f \left(U_f^{n_{step}} \alpha_{q,f}^{n_{step}}\right) = 0 \qquad (3\text{-}15)$$

According to ANSYS Fluent theory guide (Fluent, 2015), there is a variety of volume fraction spatial discretization schemes when using the explicit VOF scheme, such as First order upwind (Eulerian Multiphase model only), CICSAM (VOF model and Eulerian Multiphase with Multi-Fluid VOF enabled), Geo-Reconstruct (VOF model and Eulerian Multiphase with Multi-Fluid VOF enabled), Compressive, Modified HRIC and QUICK. The accuracy of the interface tracking and hence, the accuracy of the solution depends on the method used. According to the scheme comparison in terms of accuracy, the Geo-Reconstruct offers the sharpest interface tracking, and in terms of speed comparison, the implicit compressive scheme is the fastest. Figure 3-3 shows a comparison between the interface shapes when using the Geo-Reconstruct and the donor-acceptor schemes, and it can be concluded that the Geo-Reconstruct scheme predicts sharper and more accurate interface than the donor-acceptor scheme.

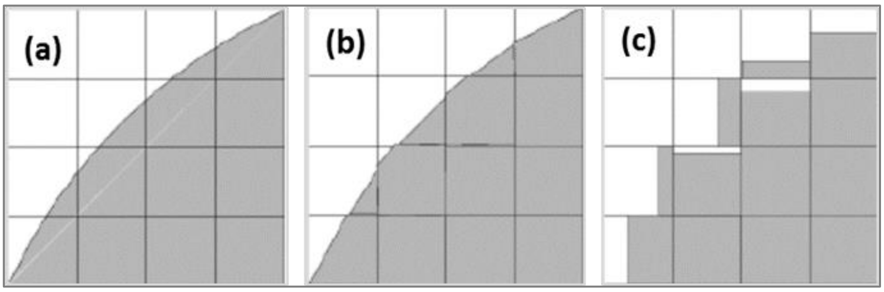

Figure 3-3. Comparison between different interface calculation schemes (a) actual interface shape, (b) interface predicted using the Geometric reconstruction (piecewise-linear) scheme and (c) interface predicted using the donor-acceptor scheme.

The Geo-Reconstruct scheme is one of the most commonly used scheme that is based on the "piecewise linear interface calculation" (PLIC) method (Youngs, 1982). It assumes a linear slope within each cell that is used for the calculation of the advection of fluid through the cell faces. The steps for interface capturing can be summarised as follow:

1. Using the volume fraction and its derivatives in the cell for calculating the position of the linear interface relative to the centre of each partially-filled cell,
2. using the computed linear interface illustration and information about the normal and tangential velocity distribution on the face for calculating the advecting amount of fluid through each face,
3. calculating the volume fraction in the individual cell using the balance of fluxes calculated in step 2.

The geometric reconstruction scheme is recommended by ANSYS Fluent (Fluent, 2015) as the scheme which produces the sharpest interface. Thus, in this thesis, the multiphase model selected is the explicit VOF model, and the geometric reconstruction scheme is used for the calculation of fluxes at control volume faces.

3.2.4 Solver Controls

All simulations performed in this study are transient, where the sole governing factor is the time step size. Different time step sizes are tested, and the time step size selected is 0.0001s. However, in some cases, according to the mesh size used, a smaller time step size is needed. So, to avoid this problem with the proper choice of the time step size, a variable time step is applied to the governing equations that are based on initial time step size of 0.0001s and a global Courant number fixed to 0.25. The maximum number of iterations is varied according to the case studied. In some cases, to ensure convergence, it is essential to control the change of the variables from one iteration to the other by controlling the under-relaxation factors (Hernandez Perez, 2008; Hernandez-Perez et al., 2010). In addition, plotting the residual error for the governing equations is done at the end of each time step to ensure convergence, which is discussed in detail in section 3.3. To sum up, Table 3-1 gives the solver control and the discretisation schemes used for all simulations done in this thesis.

Table 3-1. Solver controls

Unsteady calculation parameters	
Time Step (s)	0.0001
Max. Iterations Per Time Step	1000
Discretization Scheme	
Pressure	PRESTO
Pressure-Velocity Coupling	PISO
Gradient	Green-Gauss Node Based
Volume fraction	Geo-reconstruct
Momentum	QUICK scheme
Unsteady formulation	First-order implicit

3.3 Verification

Verification is an essential part of any numerical study to ensure that the results have an acceptable error level or preferably with negligible errors. This section discusses the verification part of evaluating and eliminating the error. This is then followed by a validation section that ensures that the numerical results agree with real experimental and theoretical data.

In general, the error is defined as a detectable deficiency in any stage of modelling and simulation that is not as a result of a lack of knowledge (AIAA, 1998; Ambrose, 2015). The error can be spatial and temporal discretisation error, convergence criterion for governing equations residuals' error, computer round off error and computer programming error.

The computer round off error occurs when the computer rounds values. The precision is 10 digits for floating point number. Regarding the computer programming error, this study uses a full version of a commercial CFD code ANSYS Fluent and hence, code verification is accompanied by ANSYS afore the full release of any software (ANSYS Fluent).

The next section focuses on two main errors the spatial and temporal discretisation error and iterative convergence error.

3.3.1 Spatial and Temporal Discretisation Error

During the process of grid generation, where the computational domain is subdivided into control volumes, the spatial discretisation errors may be formed. Generally, to account for this type of error, three different mesh sizes coarse, intermediate and fine are selected, and simulations using these mesh sizes are performed to determine the value of some of the key variables of the problem. For instance, in the base model discussed in section 3.4, different mesh sizes are used to determine some of the main hydrodynamic characteristics of drift of Taylor bubbles through stagnant liquid in vertical pipes, including Taylor bubble velocity, liquid film thickness, wall shear stress, wake length and wake volume, with particular concentration on the Taylor bubble velocity (U_{TB}). Details on the spatial discretisation errors according to the case investigated (2D or 3D simulations) are given in section 3.4.

As discussed in section 3.2.3, transient solution necessitates the definition of discrete time steps that describes the transition from one solution to the other. Thus, similar to the mesh distribution, the solution should be independent of the time step used. Different time steps are tested in 2D, and 3D simulations and the most appropriate settings are using a variable time step to the governing equations that are based on initial time step size of 0.0001s and a global Courant number fixed to 0.25.

3.3.2 Iterative Convergence Error

The equations given in section 3.2 are computed iteratively. The conservation equation for a general variable (φ_P) at a cell P can be written as follow:

$$\begin{aligned} a_P\varphi_P &= \sum_{nb} a_{nb}\varphi_{nb} + b \\ a_P &= \sum_{nb} a_{nb} - S_P \end{aligned} \tag{3-16}$$

Where a_P is the centre coefficient, a_{nb} are the influence coefficients for the neighboring cells, b is the contribution of the constant part of the source term S_c in $S = S_c + S_P\varphi$ and of the boundary condition.

The residual error is a measure of the solution convergence. The residual is defined as the difference between the computed numerical value of any variable and the values required to satisfy the conservation of that variable. The "unscaled residual" (R^{φ}) is the sum of the residual over the whole computational cells in the computational domain and it is given by:

$$R^{\varphi} = \sum_{cells\ P} \left| \sum_{nb} a_{nb}\varphi_{nb} + b - a_P\varphi_P \right| \tag{3-17}$$

Averaging the "unscaled residual" throughout the computational domain gives the "globally scaled residual". These residuals are useful indicators of solution convergence. The scaled residual is given by:

$$R^{\varphi} = \frac{\sum_{cells\ P} -|\sum_{nb} a_{nb}\varphi_{nb} + b - a_P\varphi_P|}{\sum_{cells\ P} |a_P\varphi_P|} \tag{3-18}$$

For the momentum equations the denominator term is replaced by $a_P v_P$, where v_P is the magnitude of the velocity at cell P.

For the continuity equation, the unscaled residual is given by:

$$R^{c} = \sum_{cells\ P} |rate\ of\ mass\ creation\ in\ cell\ P| \tag{3-19}$$

The scaled residual for the continuity equation is defined as:

$$\frac{R^{c}{}_{iteration\ \ N}}{R^{c}{}_{iteration\ \ 5}} \tag{3-20}$$

where $R^{c}{}_{iteration\ \ 5}$ is the largest absolute value of the continuity residual in the first five iterations (Fluent, 2015).

A further measure of convergence is to determine how much a residual has decreased during calculations. In ANSYS Fluent, it is possible to compute and store the residual sum for each of the conserved variables at the end of each solver iteration. A pre-determined value for each of the equations being solved are specified, and the scheme iterate up until these residual reaches those defined values.

For all of the numerical solutions developed in this thesis, a reduction of three orders of magnitude within each timestep is used as a convergence criterion for the residuals. In some cases, an increase in residuals is noticed at the beginning of the run, which is likely to happen, however, this is fixed by reducing the under-relaxation factors that subsequently causes the residuals to drop.

Figure 3-4 gives an example of the residuals from the base model of a single Taylor bubble drifting through a stagnant liquid in a 0.032m vertical pipe at 1s from the start of the simulation. As indicated in Figure 3-4, the residuals of the continuity equation are 1×10^{-4}, and the x and y momentum equations are 1×10^{-8}.

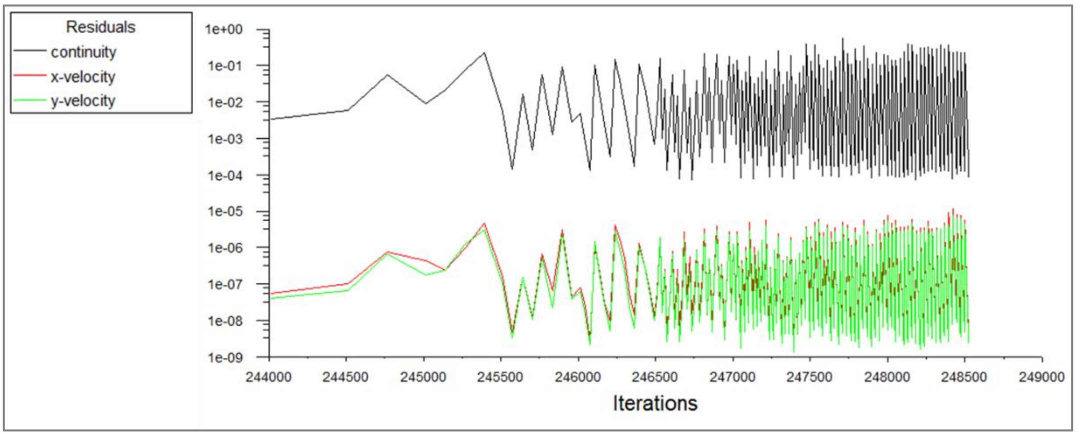

Figure 3-4. Example of plotting residuals for the base model at 1s from the start of the simulation.

3.4 Computational Resources

As discussed earlier, the Taylor bubble flow problems are considerably computationally expensive. To conduct such a large number of simulations a need for a high-performance computing is essential. Computer resources for this work include the EPSRC funded ARCHIE-WeSt High-Performance Computer (www.archie-west.ac.uk). EPSRC grant no. EP/K000586/1. For this study, around one million core hours have been used.

As the machine is used by multiple users, the run times depend on the availability of the assigned cores and the priority of the users on the machine server at the time of running the simulations. The number of cores ranges from 4 cores up to 48 cores depending on the simulation requirements.

3.5 Validation Studies

In this section, validation of the current numerical code against published benchmark studies and widely acknowledged empirical correlations is discussed through two validation studies. The first validation study is for the drift of an individual Taylor bubble through a stagnant liquid in a vertical pipe. The second validation section covers the drift of an individual Taylor bubble in an inclined pipe with stagnant liquid.

3.5.1 Validation Study 1

The numerical results are tested against the experimental work of Campos and De Carvalho (1988); Bugg and Saad (2002) and Nogueira et al. (2006a; 2006b). The capability of the two-dimensional axisymmetric model to efficiently predict the dynamics of the Taylor bubble drifting through a stagnant liquid in vertical pipes is deliberated.

Before introducing validation study 1, a discussion on the base model is given in the next section.

3.5.1.1 The Base Model

According to the literature, for the drift of Taylor bubble through a stagnant liquid in vertical pipes, the Taylor bubble is axisymmetric with a round cup and moves up along the centre of the pipe in a long ogival-shaped finger (Figure 1-5 in chapter 1). The bubble pushes the surrounding liquid that moves downstream as a thin falling film with a constant thickness (Zukoski, 1966; Mao and Dukler, 1990; Bugg and Saad, 2002; Bhagwat and Ghajar, 2016; Lizarraga-García, 2016).

Thus, the base model used for simulating the hydrodynamic characteristics of the Taylor bubble in a vertical pipe with stagnant liquid assumes 2D axisymmetric flow. The next section discusses the base model details, including the model geometry and boundary conditions, the spatial domain and finally the validation studies.

3.5.1.2 Model Geometry and Boundary Conditions

The solution domain of the base model, given in Figure 3-5, is a vertical pipe with diameter, D and length L with symmetry along the centreline. The length of the domain is 10 times the pipe diameter to avoid disturbance of the continuous phase (liquid phase) at the entrance and the exit regions and to ensure that a uniform velocity profile is restored. The initial bubble shape is a cylinder connected to a hemisphere with the same radius giving an overall bullet shape of the Taylor bubble. The length and radius of the Taylor bubble are given by L_{TB} and R_{TB}, respectively. This initial shape is simulated until a steady bubble shape is reached. Different bubble shapes are tested and the final steady shape of the bubble is similar, but this only affects the solution convergence. Further details about the initial Taylor bubble shape are given in chapter 4.

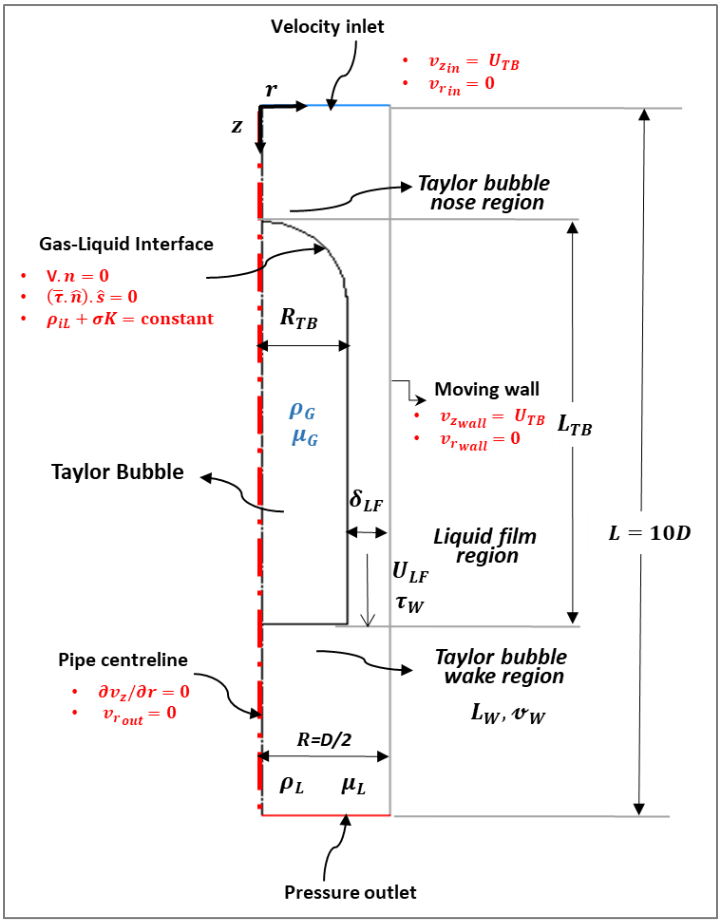

Figure 3-5. Schematic representation of the computational domain of the base model showing the initial and boundary conditions.

The simulation is performed by attaching a reference frame to the rising Taylor bubble. Enabling moving reference frame (MRF) in the simulation causes the rising Taylor bubble to be stationary, and the pipe wall moves downwards with a velocity equal to that of the bubble (Mao and Dukler, 1990). Discussion on the computational time problems and different reference frames techniques used for simulating Taylor bubbles is given in chapter 4.

Referring to Figure 3-5, using MRF the inlet flow boundary condition is applied with liquid entering at an average uniform velocity equal to the velocity of the Taylor bubble. The symmetry boundary condition is applied at the pipe centreline. At the wall, the no-slip condition is applied with wall moving downwards with the following velocities. The gas phase usually has lower density and viscosity than the liquid phase; thus, full slip can be assumed at the gas-liquid interface. Further details on the boundary conditions are given in chapter 4.

3.5.1.3 Spatial Domain

A uniform grid of quadrilateral control elements is used for the base model. The flow is within the laminar regime in all regions of the flow domain, and hence, no turbulence model is needed. Near-wall refinement is done for the proper capture of the liquid film region. Figure 3-6 shows an example of the uniform grid used in the base model.

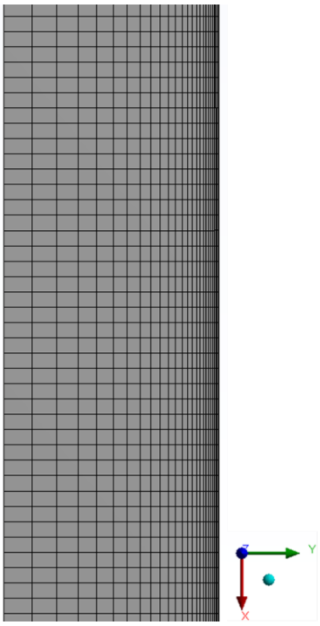

Figure 3-6. Example of the uniform quadrilateral grid (26×280) used in the base model.

3.5.1.4 Verification of the Base Model

Some verification studies are done on the base model, including spatial and temporal discretisation errors and convergence iterative errors. As discussed earlier in section 3.3, for the temporal discretisation, different time step sizes are tested, and the best setup is a variable time step to the governing equations, which is based on an initial time step size of 0.0001s and a global Courant number fixed to 0.25.

As for the convergence iterative errors check, for most of the base model simulation cases, the results converge well. Figure 3-7 illustrates an example of the residuals from the base model of a single Taylor bubble drifting through a stagnant liquid in 19 mm inner diameter vertical pipe with air and aqueous glycerol solution as working fluids (Campos and De Carvalho, 1988). It can be well noticed that the solution converges well with a decrease of three orders of magnitude in the normalised residuals of the continuity equation, and seven orders of magnitude for the x and y components of the momentum equations. For the spatial discretisation errors check, a mesh dependence test is done to ensure grid independence results. Three different grid densities are used to simulate a selective experimental case of Campos and De Carvalho (1988) with air and aqueous glycerol solution as working fluids in 19 mm inner diameter vertical pipe. The relevant dimensionless numbers of the selected case are Eo=64, $Re_{U_{TB}}$=60, $Fr_{U_{TB}}$=0.3409.

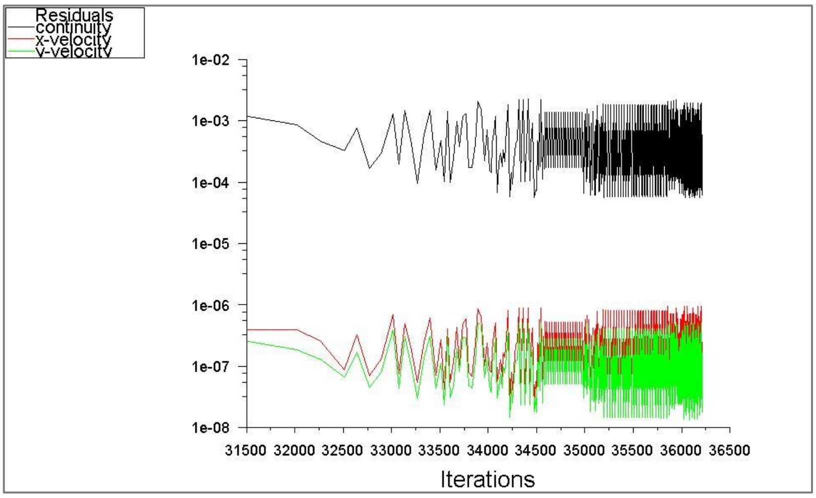

Figure 3-7. Example of plotting residuals for base model simulation of the experimental case of Campos and De Carvalho (1988) with air and aqueous glycerol solution as working fluids in 19mm inner diameter vertical pipe.

Table 3-2 shows the mesh characteristics, the relevant selected hydrodynamic characteristics to be examined and the corresponding deviations (Eo=64, $Re_{U_{TB}}$=60 and $Fr_{U_{TB}}$=0.3409). The reference mesh for the deviation calculation is the denser mesh (104×1120 elements). It can be assumed that the results are completely independent, particularly when using mesh 2 and mesh 3. Subsequently, based on the results shown in Table 3-2, the simulations done using the base model are conducted using either mesh 2 or mesh 3 depending on pipe geometry.

Table 3-2. Mesh dependence test results (Eo=64, $Re_{U_{TB}}$=60, $Fr_{U_{TB}}$=0.3409).

Mesh	U_{TB} **(m/s)**	**|Error |** U_{TB} **(%)**	δ_{LF} **(m)**	**|Error |** δ_{LF} (%)	τ_W **(Pa)**	**|Error |** τ_W **(%)**	$\frac{L_w}{D}$	**|Error |** $\frac{L_w}{D}$ (%)	$\frac{\upsilon_w}{D^3}$	**|Error |** $\frac{\upsilon_w}{D^3}$ (%)
26×280	0.1431	5	0.001972	1.7	20.74	1.1	0.5080	8.4	0.781	5.4
52×560	0.1373	1	0.001947	0.5	20.58	0.3	0.480	3	0.805	2.2
104×1120	0.1359	--	0.001938	--	20.52	--	0.4654	--	0.823	--

3.5.1.5 Validation Cases

Table 3-3 shows the test matrix for simulations of the drift of a Taylor bubble through a stagnant liquid in vertical pipes ($\gamma = 90°$). Cases 1a, 4a-6a are based on the experimental work of Campos and De Carvalho (1988) with air and aqueous glycerol solution as working fluids in 19 mm inner diameter vertical pipe. Case 2b is based on the experimental work of Bugg and Saad (2002) with air and stagnant olive oil as working fluids in 19 mm in diameter. Finally, 3c is based on the experimental work of Nogueira et al. (2006a; 2006b) with water and aqueous glycerol solutions as working fluids in 32 mm diameter pipe.

Table 3-3. Test matrix for simulations of the drift of a Taylor bubble through a stagnant liquid in vertical pipes ($\gamma = 90°$).

Case Number	**D (m)**	$Re_{U_{TB}}$	Eo	$Fr_{U_{TB}exp}$
1a	1.9×10^{-2}	25	66	0.2976
2b	1.9×10^{-2}	27	98.6	0.3034
3c	3.2×10^{-2}	37	185.95	0.3355
4a	1.9×10^{-2}	60	64	0.3409
5a	1.9×10^{-2}	72	63.36	0.3512
6a	1.9×10^{-2}	114	62.4	0.3508

a Campos and De Carvalho (1988).
b Bugg and Saad (2002).
c Nogueira et al. (2006a; 2006b).

This validation study is subdivided into four parts, including Taylor bubble velocity, Taylor bubble nose region, velocity fields, flow in the liquid film and flow in the bubble wake.

3.5.1.5.1 Taylor Bubble Rise Velocity

Table 3-4 shows the numerical, experimental and theoretical values of Taylor bubble velocity for all test cases given in Table 3-3. The theoretical values are based on the correlation of Viana et al. (2003), which is given by:

$$Fr_{U_{TB}} = \frac{0.34/\left(1+\frac{3805}{Eo^{30.6}}\right)^{0.58}}{\left(1+\left(\left(\frac{R_G}{31.08}\right)\left(1+\frac{778.76}{Eo^{1.96}}\right)^{-0.49}\right)^{-1.45\left(1+\frac{7.22\times10^{13}}{Eo^{9.93}}\right)^{0.094}}\right)^{0.74\left(1+\frac{7.22\times10^{13}}{Eo^{9.93}}\right)^{-0.094}}} \tag{3-21}$$

$$where\ R_G = \sqrt{D^3 g(\rho_L-\rho_G)\rho_L}/\mu_L$$

Table 3-4. Numerical, experimental and predicted values of U_{TB} for all test cases in Table 3-3 with their corresponding deviations with respect to numerical data.

Case Number	Simulation	Experimental	Theoretical
1a			
UTB (m/s)	0.1247	0.1285a	0.1231d
|Error | (%)	--	3	1.3
2b			
UTB (m/s)	0.1238	0.131b	0.1263d
|Error | (%)	--	5.8	2
3c			
UTB (m/s)	0.1729	0.188c	0.1712d
|Error | (%)	--	8.7	1
4a			
UTB (m/s)	0.1365	0.1472a	0.1369d
$\|Error\|$ (%)	--	7.8	0.3
5a			
UTB (m/s)	0.1380	0.1516a	0.1385d
|Error | (%)	--	9.9	0.4
6a			
UTB (m/s)	0.1432	0.1514a	0.1419d
|Error | (%)	--	5.7	0.9

a Campos and De Carvalho (1988).
b Bugg and Saad (2002).
c Nogueira et al. (2006a; 2006b)
d Viana et al. (2003)

It can be noticed from Table 3-4 that the simulation results of Taylor bubble velocity are closer to the theoretical predictions of Viana et al. (2003) rather than the experimental ones. However, generally, all deviations are within the accepted range (below 10%).

3.5.1.5.2 Taylor Bubble Nose

The bubble shape profile in the nose region is considered an important characteristic to validate. The bubble shape profile in the nose region for case 3c in Table 3-3 is given in Figure 3-8 with the corresponding experimental data of Nogueira et al. (2006a; 2006b). As indicated in Figure 3-8, good matching is found between both data. It can also be concluded that the liquid film thickness is predicted well by the simulation, which is discussed in further detail in section 3.4.1.5.4.

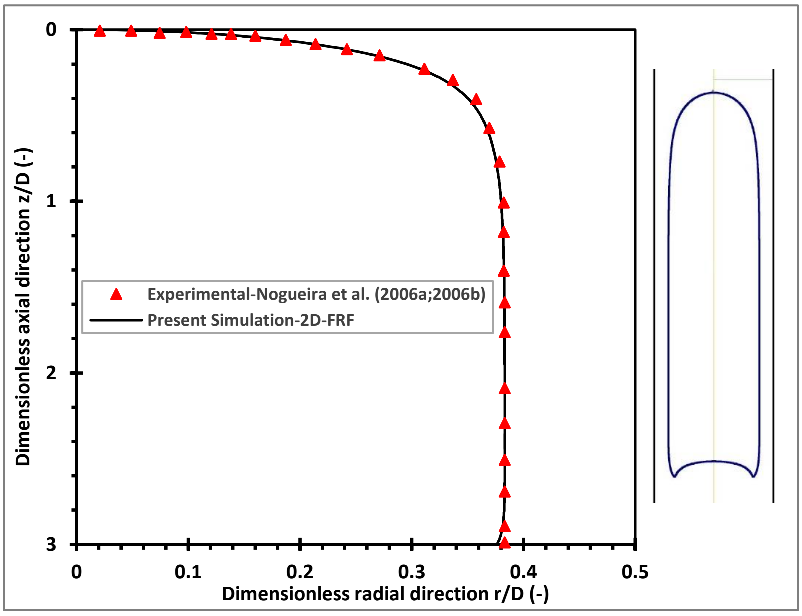

Figure 3-8. The experimental and numerical shape of the Taylor bubble in the nose region- z is the axial distance from bubble nose for case 3c of Nogueira et al. (2006a; 2006b) (Eo=185.9, $Re_{U_{TB}}$=37, $Fr_{U_{TB}}$=0.3355).

Inspired by the work of Araújo et al. (2013a), a comparison between the experimental and simulations results for the shape of the Taylor bubble front ends is illustrated in Figure 3-9 for cases 1a and cases 4a to 6a given in Table 3-3. The simulation results are overlaid on the background taken from the photos of cited reference (Campos and De Carvalho, 1988). It can be concluded from this comparison that the simulation predicts the front-end bubble shapes well except case 5a where the simulation predicts bubble nose end with a larger radius than the experimental one. However, it can be generally concluded that there is good matching between the simulation and experimental data regarding the Taylor bubble shape profile and bubble front ends.

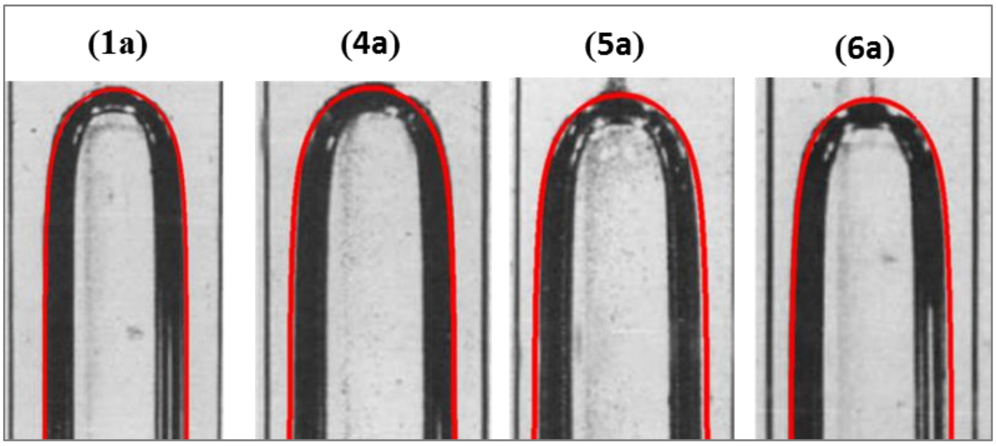

Figure 3-9. Comparison between the experimental (Campos and De Carvalho, 1988) and numerical shape of the Taylor bubble front ends for cases 1a and cases 4a to 6a given in Table 3-3.

3.5.1.5.3 Velocity Field

The simulation and experimental dimensionless velocity profiles in three different regions, flow in Taylor bubble nose, flow in the liquid film and flow in the wake for Cases 3c and 2b are given in Figure 3-10 and Figure 3-11, respectively. The simulation and experimental data of the axial velocity profile $\left(\frac{v_z}{U_{TB}}\right)$ are potted for different axial iso-surfaces, where the z/D coordinate refers to a point placed in the bubble nose region.

For the flow in the bubble nose region, as seen in Figure 3-10(a) and Figure 3-11(b), the bubble is moving upwards with a velocity (U_{TB}) due to buoyancy, pushing the liquid sideways where the liquid film zone starts to develop. Thus, the drifting bubble has a strong influence on the surrounding liquid. Nonetheless, as indicated in Figure 3-11(a), the bubble does not have a forceful power on the fluid above it, since at a distance almost D/3, the axial velocity inclines toward zero. The fluid is strongly radial near the bubble nose, as the bubble is moving upwards and the surrounding fluid is pushed sideways. In the falling liquid film zone, the liquid moves downwards with velocity (U_{LF}) and decreasing liquid film thickness (δ_{LF}).

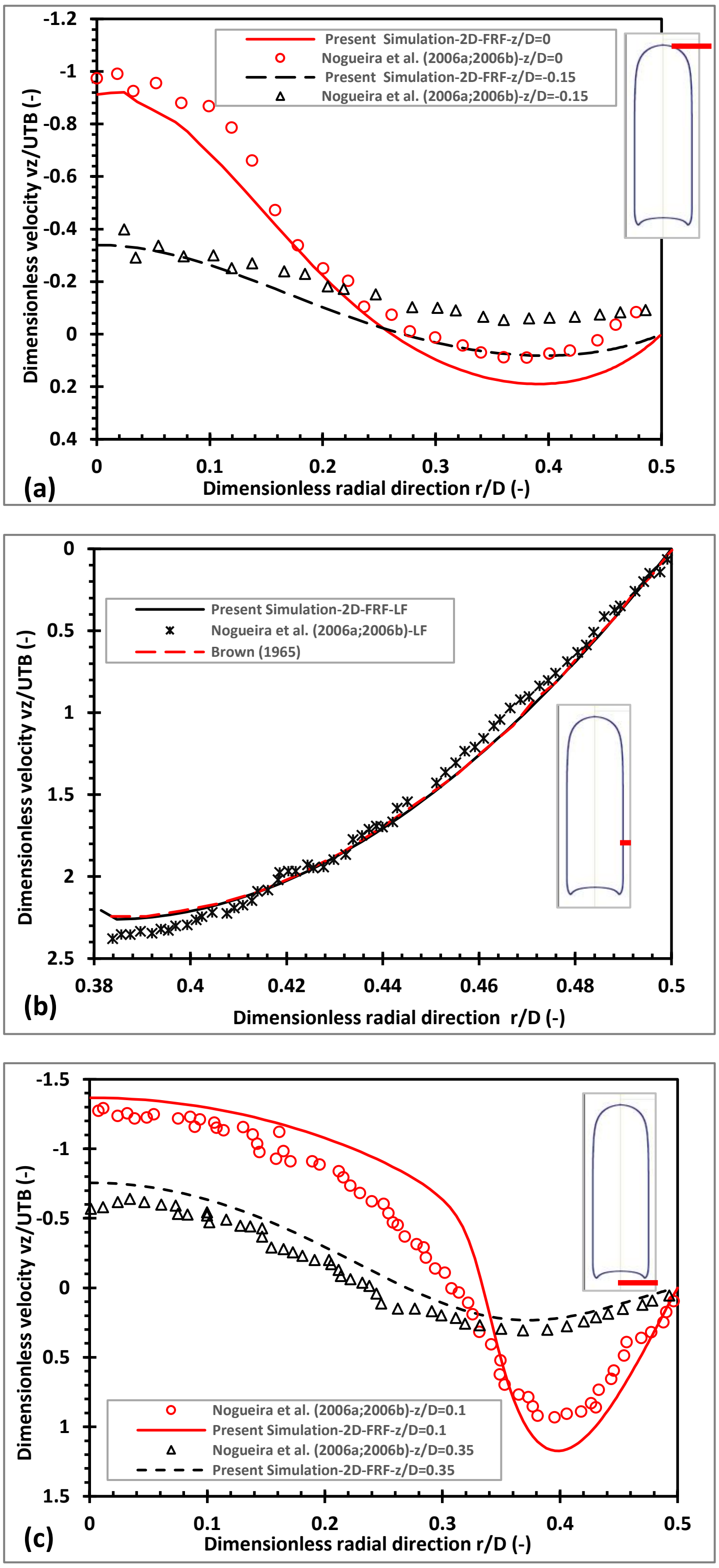

Figure 3-10. Numerical, experimental and theoretical dimensionless axial velocity profile for case 3c of Nogueira et al. (2006a; 2006b) for Taylor bubble nose region, liquid film region and wake region using FRF (Eo=185.9, $Re_{U_{TB}}$=37, $Fr_{U_{TB}}$=0.3355).

Referring to Figure 3-10(b) and Figure 3-11(c), a strong radial velocity component is observed, especially close to the fluids' interface in the liquid film region. The developing film speeds up and thins as it falls down until the wall shear stress is adept of tolerating the weight of the film. At this stage, the fully developed film is then formed, giving growth to basically axial and constant flow. The dimensionless velocity profile of the simulation results showed good matching when plotted against both the experimental results and the theoretical predictions of Brown (1965) as shown in Figure 3-10(b) and Figure 3-11(c).

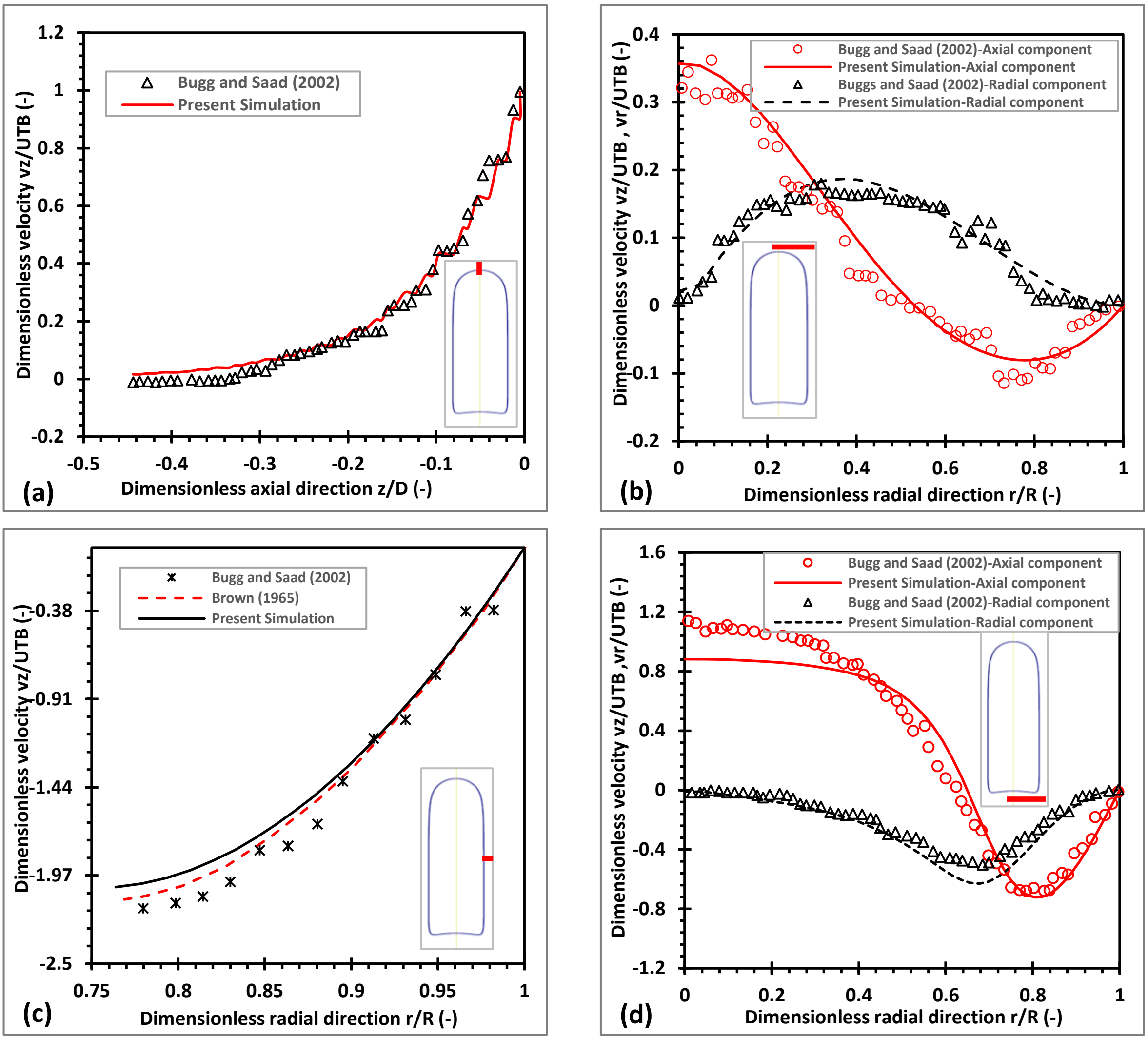

Figure 3-11. Numerical and experimental dimensionless axial velocity profile along the tube axis above the bubble for case 2b (Bugg and Saad, 2002) in a FRF (Eo=100, $Re_{U_{TB}}$=27, $Fr_{U_{TB}}$=0.303).

The theoretical velocity profile given by Brown (1965) is given by:

$$U_{LF} = \frac{g}{\nu}\left[\frac{R^2 - r^2}{4} - \frac{(R-r)^2}{2} ln\frac{R}{r}\right] \tag{3-22}$$

In the Taylor bubble wake zone, the falling liquid film starts to plugs into the liquid slug ending with highly mixing zone in the wake structure of the bubble. As shown in Figure 3-10(c) and Figure 3-11(d), the axial velocity is intensely reduced. At this stage, the flow is transferred from the wall towards the pipe centre, and hence the flow turns to be strongly radial. Near the pipe axis, the surrounding fluid is moving upward with an equal velocity as the bubble's one and hence the radial velocity component speedily declines to zero near the pipe axis. This agrees well with Gutiérrez et al. (2017).

3.5.1.5.4 Flow in The Liquid Film

For the flow in the fully developed liquid film, the dimensionless velocity profiles are already discussed in section 3.4.1.5.3 with the theoretical predictions of Brown (1965). In this section, the numerical results regarding the related shear stress along the liquid annulus and the liquid film thickness are discussed.

Table 3-5 shows the numerical, experimental and predicted values of δ_{LF} and τ_W for cases 1a, 2b and 3c in Table 3-3 with their corresponding deviations. The theoretical liquid film thickness is tested against the theoretical prediction of Brown (1965), which is given by:

$$\delta_{LF} = \left[\frac{3\nu}{2g(R-\delta_{LF})} U_{TB}(R-\delta_{LF})^{\ 2}\right]^{1/3} \tag{3-23}$$

Using the velocity profile in the fully developed liquid film (equation (3-23)) the shear stresses along the fully developed liquid film can be determined from the following relation:

$$\tau = -\mu_L \frac{dv_z}{dr} \tag{3-24}$$

$$\tau_W = \rho_L g\left[\frac{R}{2} - \frac{(R-\delta_{LF})^2}{2R}\right] \tag{3-25}$$

It can be concluded from Table 3-5 that the numerical wall shear stress and liquid film thickness are very close to both the experimental values and the theoretical predictions. The deviations between the simulation, experimental and theoretical data are lower than 5%.

Table 3-5. Numerical, experimental and predicted values of δ_{LF} *and* τ_W *for cases 1a, 2b and 3c in Table 3-3 with their corresponding deviations with respect to the numerical data.*

Case Number	Simulation	Experimental	Theoretical
1a			
δLF (mm)	0.002362	--	0.0024 d
|Error | (%)	--	--	1.6
τW (Pa)	24.75	--	25.33e
|Error | (%)	--	--	2.3
2b			
δLF (mm)	0.002356	0.002337 b	0.002396 d
|Error | (%)	--	0.8	1.7
τW (Pa)	18.48	--	18.72e
|Error | (%)	--	--	1.3
3c			
δLF (mm)	0.003732	0.00384 c	0.0038 d
|Error | (%)	--	2.9	1.8
τW (Pa)	39.79	39.6 c	40.74 e
|Error | (%)	--	0.5	2.4

a Campos and De Carvalho (1988).
b Bugg and Saad (2002).
c Nogueira et al. (2006a; 2006b)
d Brown (1965)
e Equation (3-25)

3.5.1.5.5 Flow in the Bubble Wake

Referring to Figure 3-12, when the liquid leaves the annular film region (region b), it smoothly expands after the bubble trailing edge and commonly prompting the development of recirculation in the wake (region c) attached to the bubble. Due to this mixing process, the velocity of the falling liquid film rapidly decays, which stops the continuous downward movement of the liquid film. The size and intensity of the wake depend on Eötvös and Reynolds number, which will be discussed in detail in chapter 4. The wake characteristics are generally essential in cases of the interaction between consecutive Taylor bubbles.

In this section, the validity of the numerical result in terms of the wake hydrodynamics, mainly the dimensionless wake length (L_W/D) and dimensionless wake volume (υ_W/D^3) are examined against experimental data of Campos and De Carvalho (1988). The validation is also done against both the experimental correlations developed by Campos and De Carvalho (1988), which is given by:

$$\frac{L_W}{D} = 0.30 + 1.22 \times 10^{-3} N_f \;\; for\; 100 < N_f < 500$$
$$\frac{\mathcal{V}_W}{D^3} = 7.5 \times 10^{-4} N_f \; for\; 100 < N_f < 500 \qquad (3\text{-}26)$$

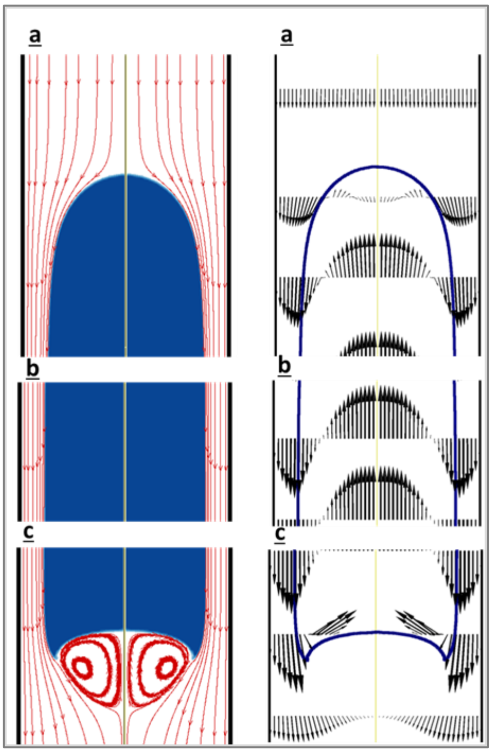

Figure 3-12. Numerical results of the Streamlines (left) and velocity fields (right) of a rising Taylor bubble through a stagnant liquid for case 3c of Nogueira et al. (2006a; 2006b) using MRF (Eo=185.9, $Re_{U_{TB}}$=37, $Fr_{U_{TB}}$=0.3355).

Referring to Table 3-6, it can be seen that the simulation results agree with both the experimental data and theoretical correlations. It should be pointed out that the method used in the experimental work for the wake structure depends on dye transportation inside the wake, whose accuracy can be restricted by diffusion. In the current numerical code, the whole wake structure is accounted for, including as well the streamlines in the concave structure of the bubble wake. However, the validation is generally quite acceptable.

In addition, Figure 3-13 shows a comparison between the experimental (Campos and De Carvalho, 1988) and numerical shape of the Taylor bubble for cases 1a and cases 4a to 6a given in Table 3-6. The flow field (not up to scale) is represented as streamlines that clearly shows the wake region. The numerical bubble wakes quantitatively match the experimental ones.

Table 3-6. Numerical and experimental values of L_W/D and υ_W/D^3 for cases 4a to 6a in Table 3-3 and their respective deviations with respect to the numerical data.

Case Number	Simulation	Experimental	Campos and De Carvalho (1988) correlation
4a			
L_W/D(-)	0.47824	0.5145a	0.5145b
|Error | (%)	--	7.6	7.6
υ_W/D^3(-)	0.12157	0.1268a	0.1319b
|Error | (%)	--	4.3	8.5
5a			
L_W/D(-)	0.5462	0.549 a	0.5498 b
|Error | (%)	--	0.5	0.7
υ_W/D^3(-)	0.1528	0.1662 a	0.1536b
|Error | (%)	--	8.8	0.5
6a			
L_W/D(-)	0.7688	0.764a	0.6961b
|Error | (%)	--	0.5	9.4
υ_W/D^3(-)	0.2454	0.235a	0.2435b
|Error | (%)	--	4.4	0.8

a Campos and De Carvalho (1988).
b Equation (3-26)

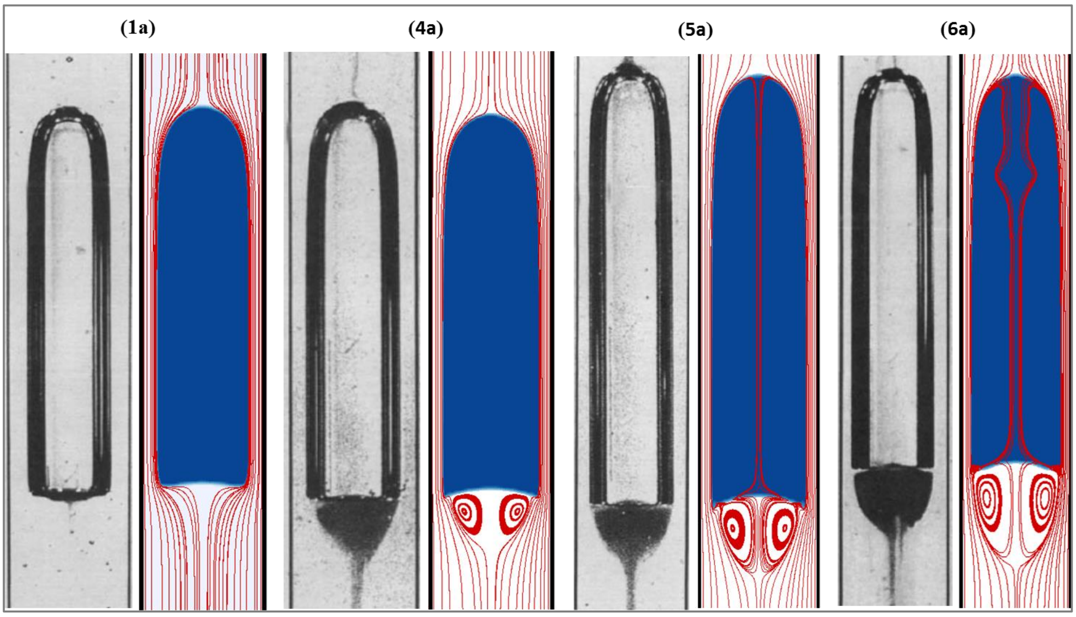

Figure 3-13. Comparison between the experimental (Campos and De Carvalho, 1988) and numerical shape of the Taylor bubble wake for cases 1a and cases 4a to 6a given in Table 3-3.

In conclusion, the validation study covering the flow in a different region of Taylor bubble drifting through a stagnant liquid flow field, including experimental and theoretical predictions reveal the capability of the developed CFD model to simulate the problem of single Taylor bubble drifting through a stagnant liquid in a vertical pipe. The hydrodynamic characteristics of a Taylor bubble in vertical pipes are then thoroughly investigated in chapter 4.

3.5.2 Validation Study 2

The experimental work of Shosho and Ryan (2001) are used to compare some of the vital hydrodynamics of Taylor bubbles in inclined pipes against the simulation data obtained from the developed CFD model. The capability of the 3D symmetry planes model to efficiently predict the dynamics of the Taylor bubble drifting in inclined pipes with stagnant liquid is considered.

Prior to introducing this validation study, the modifications done to the base model to adequately capture the dynamics of Taylor bubbles in inclined pipes are discussed.

3.5.2.1 The 3D Inclined Model

Based on validation study 1, it can be concluded that the CFD model is capable of simulating the rise of Taylor bubbles in pipes. However, this section gives a brief validation of the model against experimental data for the drift of Taylor bubbles in inclined pipes. For inclined pipes, the assumption of flow being axisymmetric can no longer be applied. The symmetry of the vertical pipe configuration is lost as the pipe is inclined. However, the flow can be simplified as a plane of symmetry that crosses the pipe's diameter line with a normal orthogonal to the gravity acceleration (Mazza et al., 2010).

Figure 3-14 shows a schematic for drifting of Taylor bubbles in inclined pipes with stagnant liquid. Due to buoyancy, the elongated gas bubble occupies the upper section of the pipe. The liquid film has two regions, top liquid and bottom liquid films. The liquid film region has an interface separating the Taylor bubble at the upper portion of the pipe and bottom liquid film at the lower portion. The flow field can be divided into three regions, the front, the body and the tail. The body region, which is much greater in size than the other two regions, can be simply represented as gas-liquid stratified flow with a plane interface at the pipe's cross section. The other two regions are more complex as they contain the stresses in control of developing the shape of the Taylor bubble nose and the complex wake structure at the bubble's tail. Complex three-dimensional flows characterise regions 1 and 3, and they are smaller in length with a range of 1-3D_{pipe} (Mazza et al., 2010).

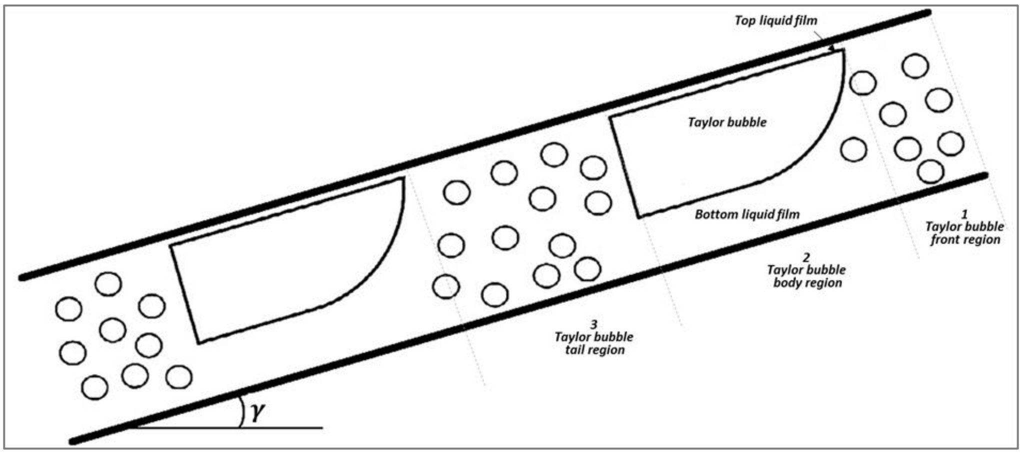

Figure 3-14. A schematic of gas-liquid slug flow in an inclined pipe (Taitel et al., 2000).

Different models are compared and tested against experimental data. These include the 2D model, 3D full domain model and 3D with a symmetry plane model. The models are compared in terms of computational time and accuracy by testing against experimental data. The 2D model fail to predict the actual developed Taylor bubble shape since Taylor bubbles have curvature in the spacing direction. However, it is used just used to give predictions on the estimated developed Taylor bubble shape due to its acceptable computational time. In this section, the 3D model is covered with its boundary conditions, grid dependency study, verification and validation.

3.5.2.2 Model Geometry and Boundary Conditions

Figure 3-15 shows the geometry for the inclined pipe geometry to be simulated. The 3D model is a vertical cylindrical domain, and the inclination of the pipe is configured by setting the angle (γ) between the pipe's axis and the gravity vector with respect to the vertical case. The length of the computational domain is kept 10D similar to the base model to ensure the solution is affected by neither the bottom nor the top of the pipe.

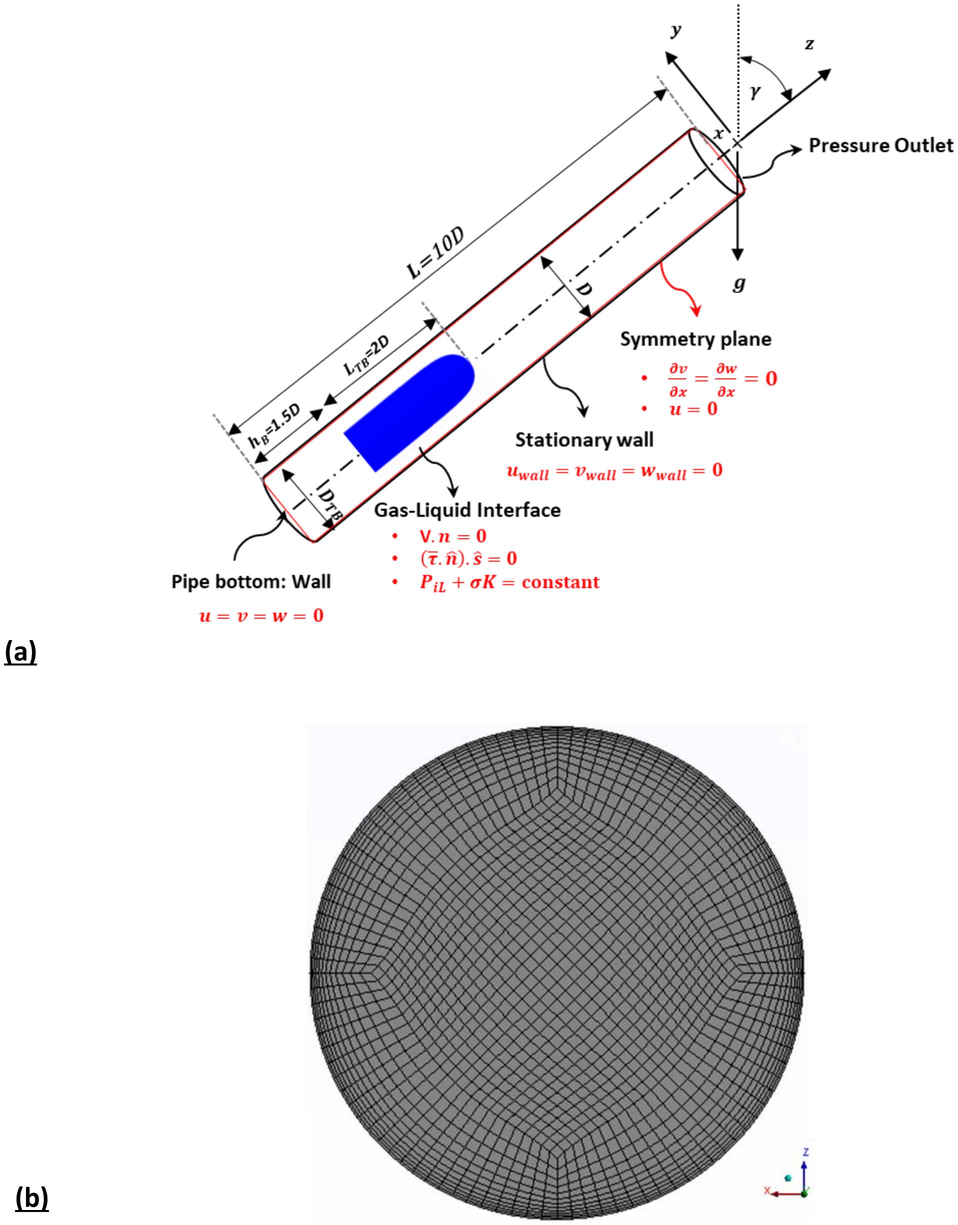

Figure 3-15. (a) Schematic representation of the computational domain for a single Taylor bubble drifting through a stagnant liquid in an inclined pipe showing the initial and boundary conditions and (b) 3D block-structured O-Grid hexahedral mesh used.

The boundary conditions are similar to the base model. However, all simulations for the inclined cases are done using fixed reference frames (FRF), and further details are given in chapter 5. Referring to Figure 3-15, the boundary conditions are no-slip condition at the wall boundaries, a pressure outlet condition is applied at the pipe outlet and zero normal velocity and zero normal gradients for all variables at the symmetry plane. Additionally, all the velocity components are set at zero.

The initial conditions are as well similar to the base model. The initial bubble shape is chosen to be a cylinder connected to a hemisphere with the same radius giving an overall bullet shape of the Taylor bubble. The volume of the gas phase is specified using the patch option in Fluent.

3.5.2.3 Spatial Domain

The 3D full domain model and 3D with a symmetry plane model are tested. The 3D full domain mesh is selected based on the work Hernandez-Perez et al. (2011) and Ambrose (2015) who use block-structured O-Grid hexahedral, as shown in Figure 3-15. This mesh has proven to predict the flow behaviour in liquid film regions accurately and is also suitable for the modelling of slug flow applications, and accordingly the drift of Taylor bubbles in pipes.

Depending on the case study, the size of the mesh is selected and refined until the terminal velocity stabilises and converges. The number of cells generally ranges from 1 million up to 10 million elements. Following the same mesh chosen, the 3D model with the symmetry plane is created and using the same procedure; the mesh is refined based on the nature of the terminal bubble drift velocity.

The two models are tested against experimental data of Shosho and Ryan (2001) for a selected case using 80% corn syrup-air mixture in an inclined pipe of the inside diameter of the pipe (D) 0.0127m. The bubble's initial shape is selected based on the work of Gutiérrez et al. (2017), which is composed of a cylinder with a diameter (D_{TB}) of 0.84D. The total length of the cylinder is $2D_{TB}$ and it is ended by two hemispheres. The density, viscosity and surface tension of the surrounding liquid are 1320.02 kg/m^3, 0.191Pa s and 0.051 N/m, respectively. These properties correspond to Eötvös number (Eo) of 40.95 and a Morton number (M) of 0.0746. Figure 3-16 shows that both models predict almost the same developed Taylor bubble shape. Table 3-7 gives a comparison between the predicted terminal drift velocities (v_d) using both models together with the computational time consumed. The two simulations have been assigned the same number of nodes, which are 4 nodes equivalent to 48 cores.

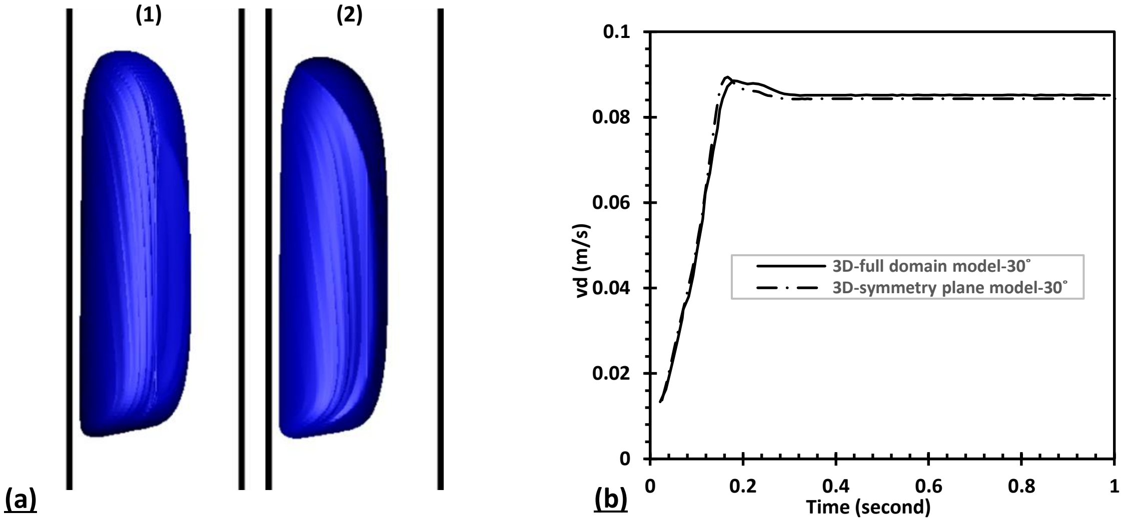

Figure 3-16. (a) The terminal developed Taylor bubble shape for drifting through stagnant liquid in 30° inclined pipe (Shosho and Ryan, 2001) in yz plane view using (1) 3D full domain model and (2) 3D with symmetry plane model and (b) Terminal bubble drift velocity time evolution using both models.

Table 3-7. Numerical and experimental values of v_d using 3D full domain and symmetry plane models for the experimental case of Shosho and Ryan (2001) with their corresponding deviations with respect to the experimental data.

Angle	Model	Number of nodes	Run time in hours per 1s real time	v_d (m/s)	|Error | (%)
15°	3D full domain	3.28E+06	68	0.2111	6.6
	3D symmetry plane	2.86E+06	62	0.2129	7.5
	Shosho and Ryan (2001)	---	---	0.1981	---
30°	3D full domain	3.28E+06	59	0.2250	6.8
	3D symmetry plane	2.86E+06	54	0.2210	5.9
	Shosho and Ryan (2001)	---	---	0.2105	---

It is concluded from that both models almost predict the same terminal drift velocity. However, the computational time is reduced when using symmetry planes models. Accordingly, throughout the thesis, all simulations done for inclined pipes are done using 3D symmetry planes model. In addition, Figure 3-16 shows the predicted terminal drift velocity using both models. It should be pointed out that the convergence noticed in v_d curves is an indication for the proper choice of the mesh size.

3.5.2.4 Verification of the 3D Model

Similar to the base model, a number of verification studies are done on the 3D model, including spatial and temporal discretisation errors and convergence iterative errors. In the 3D model, the same temporal discretization for the base model is used, where a variable time step to the governing equations that is based on initial time step size of 0.0001s and a global Courant number fixed to 0.25.

For the convergence iterative errors check, for most of the 3D model simulation cases, the results converge well. Figure 3-17 illustrates an example of the residuals from the 3D model with a symmetry plane of case 15° given in Table 3-7 (Shosho and Ryan, 2001). The solution converges well with a decrease of four orders of magnitude in the normalised residuals of the continuity equation and seven orders of magnitude for the x, y and z component of the momentum equations.

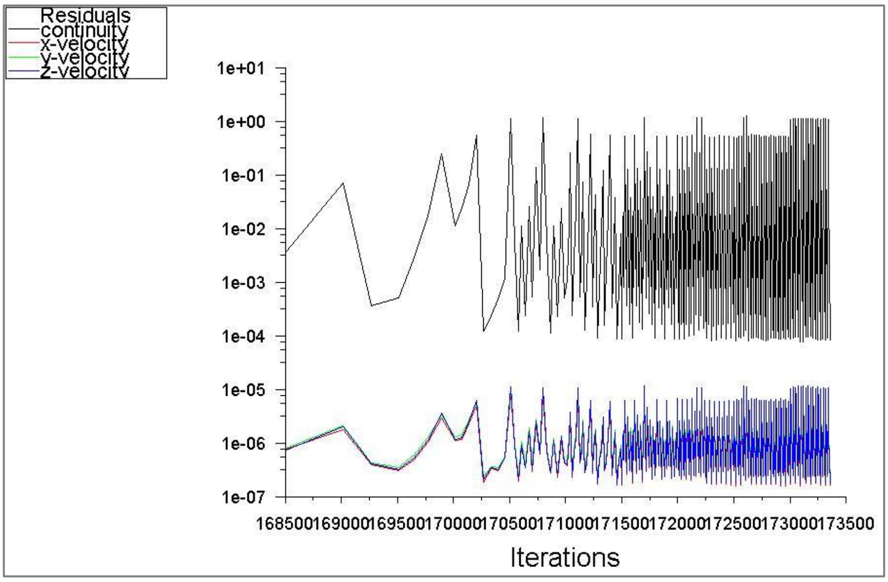

Figure 3-17. Example of plotting residuals for the 3D model with symmetry planes for the experimental case of Shosho and Ryan (2001) with corn syrup-air mixture in a pipe inclined by 15° from the vertical position.

As for the spatial discretisation errors check, the inclined case is different as the mesh size depends on the simulated case. The mesh size selection process is as follows; an initial mesh size is selected based on pipe geometry, and the terminal bubble drift velocity convergence is monitored. Once convergence and stability in the velocity are achieved, then the mesh size chosen is appropriate. Based on the simulated cases, the extreme case is likely to be the case when the pipe is inclined with an angle of 75° from the vertical. Subsequently, in each simulation, a mesh check is done on a 75° angle to test the mesh size on the Taylor bubble velocity convergence and as well as developed Taylor bubble shape. Examples of spatial discretisation errors check are given in the following section.

3.5.2.5 Validation Cases

In literature, most of the research focuses on exploring the bubble drift velocity, expressed in terms of Froude number, with the inclination angle. In chapter 2, a summary of the main correlations proposed in the literature for bubble drift velocity with their limitations is discussed. One of the reliable experimental work is proposed by Shosho and Ryan (2001) who studied the motion of long bubbles in inclined tubes for Newtonian and non-Newtonian fluids covering a wide range of dimensionless groups. In Table 3-8, two cases based on the work of Shosho and Ryan (2001) are also selected for the sake of comparison of the present simulation against the experimental data. The working fluids for these cases are air and sucrose solutions with different concentrations.

Table 3-8. Test matrix for simulations of the drift of a Taylor bubble through a stagnant liquid in inclined pipes (Shosho and Ryan, 2001).

Case Number	Working fluid	D (m)	Density (Kg/m^3)	Viscosity $(Pa\ s)$	Surface tension (N/m)	Eo
1	60% Corn syrup	1.27×10^{-2}	1195.75	3.60E-02	0.049	38.6
2	80% Corn syrup	1.27×10^{-2}	1320.02	1.91E-01	0.051	163.8

Figure 3-18 shows the developed Taylor bubble shape and the terminal Froude number (Fr_{v_d}) compared against the experimental results of Shosho and Ryan (2001) for case 1 given in Table 3-8. For the Taylor bubble shape, the bubble loses it symmetry once the pipe is inclined with respect to the vertical position. In fact, the bubble hydraulic diameter ($4 \times cross\ sectional\ area/perimeter$) is reduced with the inclination angle which leads to an elongation of the bubble length. While, the upper liquid film thickness (the upper distance between the bubble and the wall) is reduced with the increase in the inclination angle as the bubble nose is shifted from the centre of the pipe, at the vertical position, towards the wall.

Additionally, referring to Table 3-9 and Figure 3-19, it should be pointed out that for inclination angle $\gamma = 75°$, a mesh check is done to ensure the convergence of the terminal drift velocity and stability in a terminal bubble shape. However, increasing the cells' number requires large computational resources, and subsequently, the mesh selected for such case ($\cong$7 million cells) is considered suitable to obtain a converged Taylor bubble velocity. Nevertheless, the instability in the developed Taylor bubble shape is caused by large values of reduced Galilei number ($Ga_R = 9311$) which is inconvenient to have for these inclination ranges. Further details regarding the applicable values of the dimensionless groups that govern the problem are given provided in chapter 5.

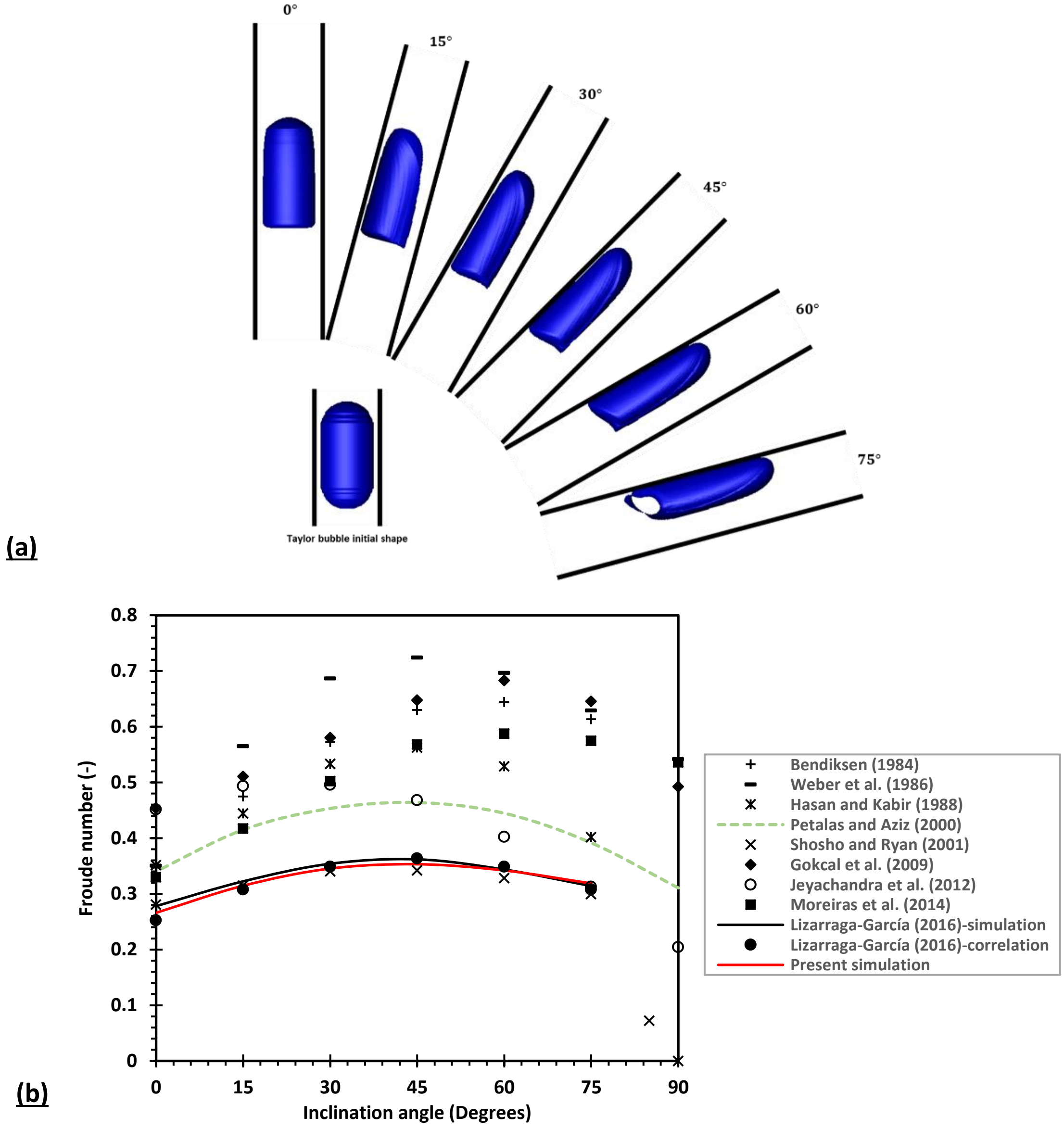

Figure 3-18. (a) Three dimensional Taylor bubble shape in the yz plane for all inclination angles and (b) terminal Froude number against the experimental result of Shosho and Ryan (2001) and other correlations given in Table 2-3 for case 1 in Table 3-8.

Table 3-9. Mesh dependence test results on the extreme case ($\gamma = 75°$) for case 1 in Table 3-8 for 80% corn syrup-air mixture in 75° inclined pipe (Shosho and Ryan, 2001).

Case	Number of Elements	UTB terminal-Simulation (m/s)	UTB terminal -Shosho and Ryan (2001) (m/s)	|**Error** | (%)
75°	2.8E+06	0.32351	0.30	7.5
	4.7E+06	0.32656	0.30	8.9
	6.9E+06	0.31640	0.30	6.2

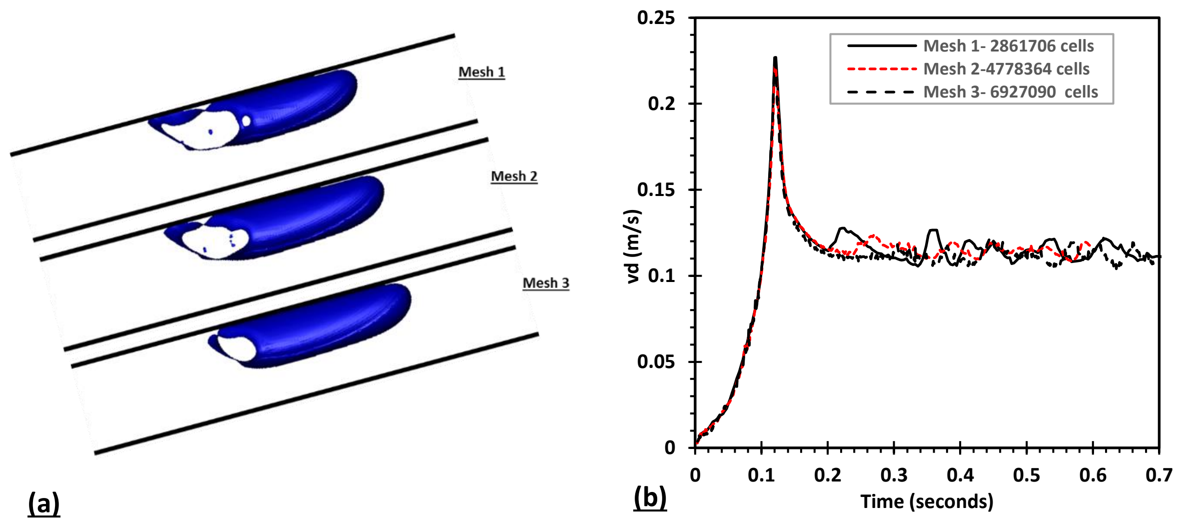

Figure 3-19. Mesh check on the extreme case ($\gamma = 75°$) for case 1 in Table 3-8 showing (a) Taylor bubble shape in yz plane and (b) convergence of terminal bubble drift velocity.

For the Taylor bubble drift velocity, the bubble drift velocity follows the expected "peculiar trend" concerning the inclination angle. This "peculiar trend" is noticed by most of the researchers with different conclusions on the angle at which maximum Froude number (Fr_{v_d}) occurs. However, the general conclusion is that the Froude number (Fr_{v_d}) reaches its maximum value at an inclination angle $30° < \gamma < 60°$ as a result of the opposing effects of buoyancy and the drag coefficient. For inclination angles approaching the horizontal position, the bubble terminal velocity drops expressively to approach a zero value.

Some of the main correlations in the literature are presented in Figure 3-18 to compare the present simulation results. Most of the correlations follow the expected "peculiar" trend with respect to the inclination angle. It should be pointed out that the differences noticed between these correlations are due to the limitations given by each correlation, as given in detail in Table 2-3 in chapter 2. For instance, the correlations by Hasan and Kabir (1988); Gokcal et al. (2009); Jeyachandra et al. (2012); Moreiras et al. (2014) are applicable for high Eo values. Petalas and

Aziz (2000)'s correlation is applicable for high Re_{v_d} values. One of the reliable correlations is suggested by Lizarraga-García (2016) as it can predict the Froude number for a wide range of Eo with almost no limitations. It shows good matching with all simulation cases.

Additionally, Figure 3-20 shows the terminal Froude number (Fr_{v_d}) compared against the experimental results of Shosho and Ryan (2001) for case 2 given in Table 3-8. It can be concluded that the simulation results show a qualitative agreement with the experimental results of Shosho and Ryan (2001) and the correlation proposed by Lizarraga-García (2016) for the two cases provided in Table 3-8.

The evidence presented in this section suggests that, based on the main correlations proposed in the literature, improvements in predicting Taylor bubble drift velocity are essential. Moreover, the numerical results show a reasonable agreement with the experimental data and the correlations of bubble drift velocity.

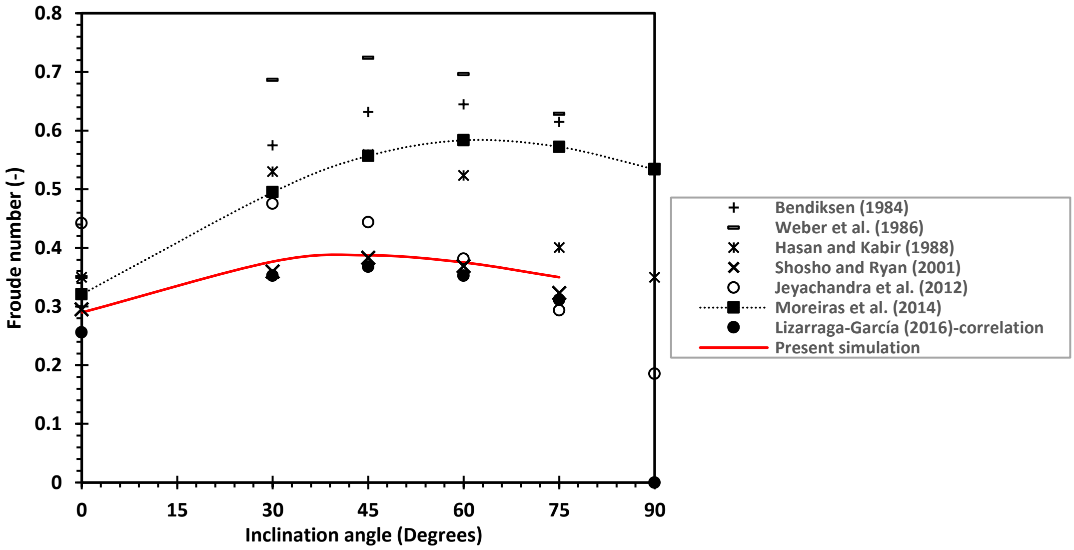

Figure 3-20. Terminal Froude number against the experimental result of Shosho and Ryan (2001) and other main correlations in the literature for case 2 in Table 3-8.

3.6 Concluding Remarks

In this chapter, the adopted numerical method (VOF method) is discussed in detail, covering the governing equations, the mesh incorporated, the discretisation and solution method and solver control. In addition, discussion on the verification process, to ensure that the results have an acceptable error level or preferably without any errors, is given in section 3.3.

Moreover, two validation studies are given in section 3.4, where the current numerical code is validated against published benchmark studies and widely acknowledged empirical correlations. A discussion on the base model used to simulate the drift of Taylor bubbles through a stagnant vertical liquid is given within the validation study 1. Additionally, the modification done in the base model to accurately capture the dynamics of Taylor bubbles in inclined pipes is discussed in detail.

In section 3.4.1, the hydrodynamic modelling feature of a Taylor bubble in vertical pipes is validated using five test cases with different working conditions. The Taylor bubble rise velocity (U_{TB}) is validated against experimental data and some of the main correlations given in the literature. Added to this, other main hydrodynamic feature, including the Taylor bubble shape, the velocity fields, flow in the liquid film region and flow in the wake region, are validated against experimental data and other important correlations. Generally, for the rise of a Taylor bubble in a vertical stagnant liquid, good agreement is achieved between present simulation results and published data, which validates the basic model.

Furthermore, in section 3.4.2, the modifications done in the base model to properly capture the dynamics of Taylor bubbles in inclined pipes are discussed. Details about the model geometry, initial and boundary conditions, spatial domain and verification of the 3D inclined model are pointed out. In validation study 2, given in section 3.4.2.5, two test cases are used to validate the present simulation data against published data further. Based on the literature review, given in chapter 2, the main hydrodynamic feature of Taylor bubble flow in inclined pipes is the drift velocity (v_d). Based on this conclusion, validation study 2 mainly focuses on validating the Taylor bubble drift velocity (v_d), and the present numerical results agree generally well with the experimental results.

In conclusion, based on validation studies given in this chapter, the good agreement between both experimental and the present numerical data, illustrate that the adopted numerical method is capable of simulation of Taylor bubble rising through a stagnant liquid, in both vertical and inclined pipes, with good satisfaction degree of results.

Chapter 4 Theoretical and CFD Treatments of an Individual Taylor Bubble Rising in a Vertical Pipe ($\boldsymbol{\gamma = 0}$)

In this chapter, the drift of a single Taylor bubble through a vertical stagnant Newtonian liquid is investigated by performing a complete dimensionless treatment followed by order of magnitude analysis of the terms of equations of motion. Based on this analysis, it is concluded that Froude, Eötvös and Reynolds numbers are the main physical parameters influencing the dimensionless slug flow equations. Using the guidelines of the order of magnitude analysis, computational fluid dynamics simulation is carried out to investigate the dynamics of Taylor bubbles in a vertical pipe using the volume-of-fluid (VOF) method. Good agreement with previous experimental data and models available in the literature is established confirming that the density ratio, viscosity ratio and the initial ratio of bubble size to pipe diameter $(L_{TB}/D)_i$ *have minimal effect on the main hydrodynamic features of slug flow. Based on the developed results, correlations for the terminal velocity of the Taylor bubble and the dimensionless wall shear stress are proposed showing the significance of these main dimensionless parameters and support other important theoretical and experimental work available in the literature.*

4.1 Introduction

Based on the review done in chapter 2, the scope of this chapter can be divided into two main folds:

1. Performing complete dimensionless analysis of the problem using both the Buckingham-Pi theorem and a dimensionless treatment followed by order of magnitude analysis to the governing equations of motion to show the sole dimensionless parameters, $Re_{U_{TB}}$, $Fr_{U_{TB}}$ and Eo numbers, and their relative merits or order of magnitudes. Based on this analysis, the main hydrodynamic features of rising of an individual Taylor bubble through stagnant Newtonian liquids are investigated by applying computational fluid dynamics (CFD) simulation using the volume-of-fluid (VOF) methodology implemented in the commercial software ANSYS Fluent. These simulations are based on the base model discussed in chapter 3.
2. Developing a correlation between $Re_{U_{TB}}$, $Fr_{U_{TB}}$ and Eo numbers based on the developed numerical results and on the guidelines of the order of magnitude analysis to predict Taylor bubble rise velocity (U_{TB}). This correlation enables the present study to support other important theoretical and experimental work available in the literature.

This chapter is divided as follows; the dimensionless equations of motion and order of magnitude analysis are given in section 4.2. The CFD model is discussed in section 4.3. This is followed by the results and discussion, given in section 4.4, which is divided into four main parts, including the Taylor bubble rise velocity, the Taylor bubble shape, the liquid film region and the wake region. The chapter ends with a conclusion and discussions section that summarises all the important outcomes of this chapter.

4.2 Dimensionless Analysis

The hydrodynamic characteristics of gas-liquid slug flow are governed by viscous, inertial, gravitational and interfacial forces. The problem can be analysed using either Buckingham-Pi theorem or the dimensionless treatment of the governing equations. This section covers both methods.

4.2.1 Buckingham-Pi Theorem

In literature, the problem is mostly analysed into the dimensionless form using Buckingham-Pi theorem. Details on the theorem analysis are given in Appendix A.

Morgado et al. (2016) neglect the effect of the expansion of gas during its rise and show that the dimensionless analysis of the problem results in the following form:

$$\frac{{U_{TB}}^2 \rho_L}{gD\Delta\rho} = f\left[Eo = \frac{g\rho_L D^2}{\sigma}\ , M = \frac{\Delta\rho g \mu_L^4}{\rho_L^2 \sigma^3}\ ,\ \Gamma_\mu = \frac{\mu_L}{\mu_G}, \Gamma_\rho = \frac{\rho_L}{\rho_G}, \frac{L_{TB}}{D}\right] \tag{4-1}$$

Relation (4-1) can be modified by introducing the Reynolds number based on bubble velocity ($Re_{U_{TB}}$) which is the ratio between the inertial forces and viscous forces.

It can be shown in this respect that Morton number (M) does not represent any particular physical quantity as it can be written as:

$$M = \left(\frac{Fr_{U_{TB}}}{Re_{U_{TB}}}\right)^4 Eo^3 = \frac{Eo^3}{{N_f}^4} \tag{4-2}$$

where the inverse viscosity number (N_f) is defined as:

$$N_f = \frac{Re_{U_{TB}}}{Fr_{U_{TB}}} = \frac{\rho_L (gD^3)^{0.5}}{\mu_L} \tag{4-3}$$

In fact, the inverse viscosity number (N_f) can be interpreted physically as the ratio between gravity force and the viscous force. This can hardly be indicative of the onset of turbulence, which is inertial in the first place and probabilistic in essence. It should also be pointed out that large values of N_f cannot only be ascribed to large values of $Re_{U_{TB}}$ but to small values of $Fr_{U_{TB}}$ as well. The similarity requirements posed by Froude and Reynolds numbers can typically not be satisfied simultaneously.

It can be easily shown here that using the Buckingham-Pi theorem can lead to the same form of the dimensionless groups with Morton number replaced by Reynolds number that is given by:

$$Fr_{U_{TB}} = \frac{U_{TB}}{\sqrt{gD}} = f\left[Eo = \frac{g\rho_L D^2}{\sigma}, Re_{U_{TB}} = \frac{\rho_L U_{TB} D}{\mu_L}, \Gamma_\mu = \frac{\mu_L}{\mu_G}, \Gamma_\rho = \frac{\rho_L}{\rho_G}, \frac{L_{TB}}{D}\right] \tag{4-4}$$

4.2.2 Dimensionless Governing Equations

Figure 4-1 shows the vertical pipe configuration and the coordinate system used. The main governing equations of the problem are the continuity and momentum equations. The Navier-stokes equations in polar coordinates assuming axisymmetric flow are:

$$\rho_L\left(\frac{\partial v_r}{\partial t} + v_r\frac{\partial v_r}{\partial r} + v_z\frac{\partial v_r}{\partial z}\right) = \rho_L g_r - \frac{\partial p}{\partial r} + \mu\left[\frac{\partial^2 v_r}{\partial r^2} + \frac{1}{r}\frac{\partial v_r}{\partial r} + \frac{\partial^2 v_r}{\partial z^2} - \frac{v_r}{r^2}\right] \tag{4-5}$$

$$\rho_L\left(\frac{\partial v_z}{\partial t} + v_r\frac{\partial v_z}{\partial r} + v_z\frac{\partial v_z}{\partial z}\right) = \rho_L g_z - \frac{\partial p}{\partial z} + \mu\left[4\frac{\partial^2 v_z}{\partial r^2} + \frac{1}{r}\frac{\partial v_z}{\partial r} + \frac{\partial^2 v_z}{\partial z^2}\right] \tag{4-6}$$

$$0 = -\frac{1}{r}\frac{\partial p}{\partial \theta} \qquad (v_\theta = 0) \tag{4-7}$$

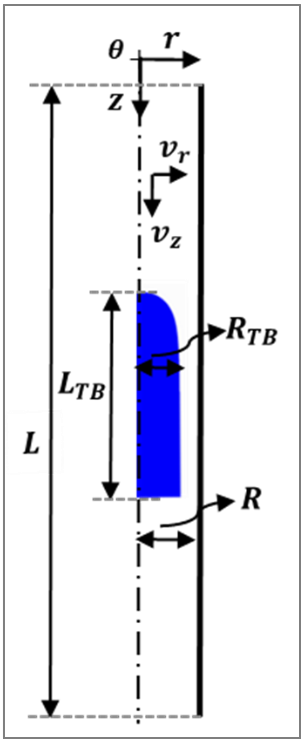

Figure 4-1. The vertical pipe configuration and the coordinate system used.

And the continuity equation is:

$$\frac{\partial v_r}{\partial r} + \frac{v_r}{r} + \frac{\partial v_z}{\partial z} = 0 \tag{4-8}$$

Introducing the following dimensionless variables:

$$\begin{gathered} {v_r}^* = \frac{v_r}{U_{TB}}, {v_z}^* = \frac{v_z}{U_{TB}}, t^* = t\left(\frac{U_{TB}}{L_{TB}}\right), r^* = \frac{r}{(D/2)}, z^* = \frac{z}{L_{TB}}, p^* = \frac{p}{\frac{1}{2}\rho_L {U_{TB}}^2}, \\ {g_r}^* = \frac{g_r}{g}, {g_z}^* = \frac{g_z}{g}, {\sigma_r}^* = \frac{\sigma_r}{\sigma}, \sigma_z^* = \frac{\sigma_z}{\sigma}, \sigma_\theta^* = \frac{\sigma_\theta}{\sigma}, K^* = \frac{K}{(1/D^2)} \end{gathered} \tag{4-9}$$

Substituting the dimensionless variables given in (4-9) into the momentum and continuity equation, dividing by $\left(\frac{\rho_L U^2}{D}\right)$ and rearragning the terms would give the following dimensionless form:

$$\begin{aligned} &\left(\frac{D}{L_{TB}}\right)\frac{\partial {v_r}^*}{\partial t^*} + 2\,{v_r}^*\frac{\partial {v_r}^*}{\partial r^*} + \left(\frac{D}{L_{TB}}\right){v_z}^*\frac{\partial {v_r}^*}{\partial z^*} \\ &\quad = \frac{1}{Fr_{U_{TB}}^2}{g_r}^* - \frac{\partial p^*}{\partial r^*} + \frac{1}{Re_{U_{TB}}}\left[4\frac{\partial^2 {v_r}^*}{\partial r^{*2}} + \frac{4}{r^*}\frac{\partial {v_r}^*}{\partial r^*} + \left(\frac{D}{L_{TB}}\right)^2\frac{\partial^2 {v_r}^*}{\partial z^{*2}} - \frac{4{v_r}^*}{r^{*2}}\right] \end{aligned} \tag{4-10}$$

$$\begin{aligned} &\left(\frac{D}{L_{TB}}\right)\frac{\partial {v_z}^*}{\partial t^*} + 2\,{v_r}^*\frac{\partial {v_z}^*}{\partial r^*} + \left(\frac{D}{L_{TB}}\right){v_z}^*\frac{\partial {v_z}^*}{\partial z^*} \\ &\quad = \frac{1}{Fr_{U_{TB}}^2}{g_z}^* - \left(\frac{D}{L_{TB}}\right)\frac{\partial p^*}{\partial z^*} + \frac{1}{Re_{U_{TB}}}\left[4\frac{\partial^2 {v_z}^*}{\partial r^{*2}} + \frac{4}{r^*}\frac{\partial {v_z}^*}{\partial r^*} + \left(\frac{D}{L_{TB}}\right)^2\frac{\partial^2 {v_z}^*}{\partial z^{*2}}\right] \end{aligned} \tag{4-11}$$

$$0 = \frac{\partial p^*}{\partial \theta^*} \tag{4-12}$$

$$2\left(\frac{\partial {v_r}^*}{\partial r^*} + \frac{{v_r}^*}{r^*}\right) + \left(\frac{D}{L_{TB}}\right)\frac{\partial {v_z}^*}{\partial z^*} = 0 \tag{4-13}$$

The following conditions are applied on the gas-liquid interface:

$$0 = \left[-\frac{\partial p}{\partial r}\right]_S + \left[\mu\left[\frac{\partial^2 v_r}{\partial r^2} + \frac{1}{r}\frac{\partial v_r}{\partial r}\right]\right]_S + [K\sigma_r]_S \tag{4-14}$$

$$\left[\rho_L\left(\frac{\partial v_z}{\partial t} + v_z\frac{\partial v_z}{\partial z}\right)\right]_S = \rho_L g_z + \left[-\frac{\partial p}{\partial z}\right]_S + \left[\mu\left[\frac{\partial^2 v_z}{\partial r^2} + \frac{1}{r}\frac{\partial v_z}{\partial r} + \frac{\partial^2 v_z}{\partial z^2}\right]\right]_S + [K\sigma_z]_S \tag{4-15}$$

$$0=\left[-\frac{1}{r}\frac{\partial p}{\partial \theta}\right]_S+\left[K\sigma_\theta\right]_S \tag{4-16}$$

Using the dimensionless variables given (4-9), and rearranging the terms, equations (4-14) to (4-16) in a dimensionless form may be written as:

$$\left[-\frac{\partial p^*}{\partial r^*}+\frac{1}{Fr_{U_{TB}}^2 Eo}K^*\sigma_r^*\right]_S+\frac{4}{Re_{U_{TB}}}\left[\frac{\partial^2 {v_r}^*}{\partial {r^*}^2}+\frac{1}{r^*}\frac{\partial {v_r}^*}{\partial r^*}\right]_S=0 \tag{4-17}$$

$$\begin{aligned}\left[\left(\frac{D}{L_{TB}}\right)\frac{\partial {v_z}^*}{\partial t^*}+\left(\frac{D}{L_{TB}}\right){v_z}^*\frac{\partial {v_z}^*}{\partial z^*}\right]_S&=\left[-\left(\frac{D}{L_{TB}}\right)\frac{\partial p^*}{\partial z^*}\right]_S\\&+\frac{1}{Re_{U_{TB}}}\left[4\frac{\partial^2 {v_z}^*}{\partial {r^*}^2}+\frac{4}{r^*}\frac{\partial {v_z}^*}{\partial r^*}+\left(\frac{D}{L_{TB}}\right)^2\frac{\partial^2 {v_z}^*}{\partial {z^*}^2}\right]_S+\frac{1}{Fr_{U_{TB}}^2}\left[{g_z}^*+\frac{1}{Eo}K^*\sigma_z^*\right]_S\end{aligned} \tag{4-18}$$

$$0=\left[-\frac{1}{r^*}\frac{\partial p^*}{\partial \theta^*}\right]_S+\frac{1}{Fr_{U_{TB}}^2 Eo}\left[K^*\sigma_\theta^*\right]_S \tag{4-19}$$

Performing a similar analysis with respect to gas and liquid sides would show the additional dimensionless groups, which are the density ratio (Γ_ρ) and the viscosity ratio (Γ_μ).

To perform an order of magnitude analysis to the dimensionless governing equations, the following orders are introduced:

$$\begin{aligned}&r^*=o(1), z^*=o(1), {v_z}^*=o(1), K^*=o(1), \sigma_z^*=o(1), {g_z}^*=o\left(\frac{D}{L_{TB}}\right)\\&{g_r}^*=o\left(\frac{D}{L_{TB}}\right)^2\ and\ t^*=o(1)\end{aligned} \tag{4-20}$$

Introducing the orders given in (4-20) to the continuity equation (4-13) would lead to the following:

$$\frac{\overbrace{\partial {v_r}^*}^{o\left(\frac{D}{L_{TB}}\right)}}{\underbrace{\partial r^*}_{o(1)}}+\frac{\overbrace{{v_r}^*}^{o\left(\frac{D}{L_{TB}}\right)}}{\underbrace{r^*}_{o(1)}}+\left(\frac{D}{L_{TB}}\right)\frac{\overbrace{\partial {v_z}^*}^{o(1)}}{\underbrace{\partial z^*}_{o(1)}}=0 \tag{4-21}$$

It can be concluded from equation (4-21) in order to keep the continuity equation intact ${v_r}^*$ should be of the order $\frac{D}{L_{TB}}$, that is ${v_r}^*=o\left(\frac{D}{L_{TB}}\right)$.

Similarly, performing order of magnitude analysis to the momentum equation in the z^* direction (equation (4-11)), will give the following:

$$\left(\frac{D}{L_{TB}}\right)\frac{\overbrace{\partial v_z{}^*}^{o(1)}}{\underbrace{\partial t^*}_{o(1)}} + 2\,\overbrace{v_r{}^*}^{o\left(\frac{D}{L_{TB}}\right)}\frac{\overbrace{\partial v_z{}^*}^{o(1)}}{\underbrace{\partial r^*}_{o(1)}} + \left(\frac{D}{L_{TB}}\right)\overbrace{v_z{}^*}^{o(1)}\frac{\overbrace{\partial v_z{}^*}^{o(1)}}{\underbrace{\partial z^*}_{o(1)}} = \frac{\overbrace{g_z{}^*}^{o\left(\frac{D}{L_{TB}}\right)}}{\underbrace{Fr_{U_{TB}}^2}_{o(1)}}$$

$$-\left(\frac{D}{L_{TB}}\right)\frac{\partial p^*}{\partial z^*} + \frac{1}{\underbrace{Re_{U_{TB}}}_{o\left(\frac{L_{TB}}{D}\right)}}\left[4\frac{\overbrace{\partial^2 v_z{}^*}^{o(1)}}{\underbrace{\partial r^{*2}}_{o(1)}} + \frac{4}{\underbrace{r^*}_{o(1)}}\frac{\overbrace{\partial v_z{}^*}^{o(1)}}{\underbrace{\partial r^*}_{o(1)}} + \cancel{\left(\frac{D}{L_{TB}}\right)^2\frac{\overbrace{\partial^2 v_z{}^*}^{o(1)}}{\underbrace{\partial z^{*2}}_{o(1)}}}\right] \quad \text{Very small order} \tag{4-22}$$

Hence, it can be concluded from equation (4-22) that Fr_{v_d} should be of the order $o(1)$ and Re_{v_d} should be of the order $o\left(\frac{L_{TB}}{D}\right)$.

Applying the same analysis to the momentum equation in the r^* direction (equation (4-10)) will give the following:

$$\left(\frac{D}{L_{TB}}\right)\frac{\overbrace{\partial v_r{}^*}^{o\left(\frac{D}{L_{TB}}\right)}}{\underbrace{\partial t^*}_{o(1)}} + 2\,\overbrace{v_r{}^*}^{o\left(\frac{D}{L_{TB}}\right)}\frac{\overbrace{\partial v_r{}^*}^{o\left(\frac{D}{L_{TB}}\right)}}{\underbrace{\partial r^*}_{o(1)}} + \left(\frac{D}{L_{TB}}\right)\overbrace{v_z{}^*}^{o(1)}\frac{\overbrace{\partial v_r{}^*}^{o\left(\frac{D}{L_{TB}}\right)}}{\underbrace{\partial z^*}_{o(1)}} = \frac{\overbrace{g_r{}^*}^{o\left(\frac{D}{L_{TB}}\right)^2}}{\underbrace{Fr_{U_{TB}}^2}_{o(1)}} - \frac{\partial p^*}{\underbrace{\partial r^*}_{o(1)}}$$

$$+\frac{1}{\underbrace{Re_{U_{TB}}}_{o\left(\frac{L_{TB}}{D}\right)}}\left[4\frac{\overbrace{\partial^2 v_r{}^*}^{o\left(\frac{D}{L_{TB}}\right)}}{\underbrace{\partial r^{*2}}_{o(1)}} + \frac{4}{\underbrace{r^*}_{o(1)}}\frac{\overbrace{\partial^2 v_r{}^*}^{o\left(\frac{D}{L_{TB}}\right)}}{\underbrace{\partial r^{*2}}_{o(1)}} + \underbrace{\cancel{\left(\frac{D}{L_{TB}}\right)^2\frac{\overbrace{\partial^2 v_r{}^*}^{o\left(\frac{D}{L_{TB}}\right)}}{\underbrace{\partial z^{*2}}_{o(1)}}}}_{o\left(\frac{D}{L_{TB}}\right)^3} - \frac{4\,\overbrace{v_r{}^*}^{o\left(\frac{D}{L_{TB}}\right)}}{\underbrace{r^{*2}}_{o(1)}}\right] \tag{4-23}$$

It can be concluded from equation (4-23):

$$\frac{\partial p^*}{\partial r^*} = o\left(\frac{D}{L_{TB}}\right)^2, p^* = \left(\frac{D}{L_{TB}}\right)^2, \frac{\partial p^*}{\partial z^*} = o\left(\frac{D}{L_{TB}}\right)^2 \; \textit{which is very small} \tag{4-24}$$

Finally, applying the same analysis to the gas-liquid interface (equation (4-18)) gives the following:

$$\left[\left(\frac{D}{L_{TB}}\right)\frac{\overbrace{\partial v_z{}^*}^{o(1)}}{\underbrace{\partial t^*}_{o(1)}}+\left(\frac{D}{L_{TB}}\right)\overbrace{v_z{}^*}^{o(1)}\frac{\overbrace{\partial v_z{}^*}^{o(1)}}{\underbrace{\partial z^*}_{o(1)}}\right]_S=\left[-\left(\frac{D}{L_{TB}}\right)\frac{\overbrace{\partial p^*}^{o\left(\frac{D}{L_{TB}}\right)^2}}{\underbrace{\partial z^*}_{o(1)}}\right]_S$$

$$+\underbrace{\frac{1}{Re_{U_{TB}}}}_{o\left(\frac{L_{TB}}{D}\right)}\left[4\frac{\overbrace{\partial^2 v_z{}^*}^{o(1)}}{\underbrace{\partial r^{*2}}_{o(1)}}+\frac{4}{\underbrace{r^*}_{o(1)}}\frac{\overbrace{\partial v_z{}^*}^{o(1)}}{\underbrace{\partial r^*}_{o(1)}}+\left(\frac{D}{L_{TB}}\right)^2\frac{\overbrace{\partial^2 v_z{}^*}^{o(1)}}{\underbrace{\partial z^{*2}}_{o(1)}}\right]_S+\underbrace{\frac{1}{Fr^2_{U_{TB}}}}_{o(1)}\left[\overbrace{g_z{}^*}^{o\left(\frac{D}{L_{TB}}\right)}+\frac{1}{\underbrace{Eo}_{o\left(\frac{L_{TB}}{D}\right)}}\overbrace{K^*}^{o(1)}\overbrace{\sigma_z^*}^{o(1)}\right]_S \tag{4-25}$$

It follows that Eo should be of order $o\left(\frac{L_{TB}}{D}\right)$.

Based on the literature review given in chapter 2, the main source of information about regime transition is Campos and De Carvalho (1988) where they put N_f in place of $Re_{U_{TB}}$ to judge turbulence or the onset of hydrodynamic instability which is considered questionable. N_f effectively represents the ratio of the gravity force to the viscous force, which can hardly be indicative of the onset of turbulence, which is inertial in the first place and probabilistic in essence.

However, N_f can be treated differently as being a modified Reynolds number, rather than a new number; suitable to govern the bubble motion in stagnant fluid in the following way:

$$N_f=\frac{Re_{U_{TB}}}{Fr_{U_{TB}}}=\frac{Inertia\,force}{viscous\,force}\times\frac{gravity\,force}{Inertia\,force}=\frac{gravity\,force}{viscous\,force} \tag{4-26}$$

It is worth noting that, if the characteristic velocity U_{TB} is placed by a new characteristic velocity $\left(V_s=(gD)^{1/2}\right)$, the dimensionless variables will be modified as follows:

$$\widehat{v_r}=\frac{v_r}{V_s},\widehat{v_z}=\frac{v_z}{V_s},\hat{t}=t\left(\frac{V_s}{L_{TB}}\right),\hat{p}=\frac{p}{\frac{1}{2}\rho_L V_s{}^2}, \tag{4-27}$$

Thus, for instance, the dimensionless momentum equation in the radial direction (equation (4-10)) will be as follows:

$$\left(\frac{D}{L_{TB}}\right)\frac{\partial\widehat{v_r}}{\partial\hat{t}} + 2\,\widehat{v_r}\frac{\partial\widehat{v_r}}{\partial r^*} + \left(\frac{D}{L_{TB}}\right)\widehat{v_z}\frac{\partial\widehat{v_r}}{\partial z^*} = {g_r}^* - \frac{\partial\hat{p}}{\partial r^*} + \frac{1}{Re_{modified}}\left[4\frac{\partial^2\widehat{v_r}}{\partial r^{*2}} + \frac{4}{r^*}\frac{\partial\widehat{v_r}}{\partial r^*} + \left(\frac{D}{L_{TB}}\right)^2\frac{\partial^2\widehat{v_r}}{\partial z^{*2}} - \frac{4\widehat{v_r}}{r^{*2}}\right] \tag{4-28}$$

Where $Re_{modified}$ is the modified Reynolds number, which is defined as follows:

$$Re_{modified} = \frac{V_s D}{\nu} = \frac{(gD)^{1/2}D}{\nu} = \frac{(gD^3)^{1/2}}{\nu} = N_f \tag{4-29}$$

It is concluded that $Fr_{U_{TB}}$ disappeared from the governing equations, which is equivalent of saying that it is of the order of magnitude unity or less, as follows:

$$Fr_{U_{TB}} = \frac{V_s}{(gD)^{1/2}} = \frac{o(gD)^{1/2}}{(gD)^{1/2}} = o(1) \tag{4-30}$$

Hence, in this frame with the new definition of the characteristic velocity (V_s), the inverse viscosity number (N_f) can represent the ratio of inertia force to viscous force, and Froude number is no longer a similarity parameter. Additionally, it is wise to mention that the characteristic velocity (V_s) is of order $(gD)^{1/2}$ which puts a limitation on $Re_{modified}$.

To sum up, based on the dimensionless analysis of the equations of motions followed by order of magnitude analysis in all directions and on the boundaries, the following conclusions are drawn:

1. The radial velocity component $({v_r}^*)$ should be of the order $\left(\frac{D}{L_{TB}}\right)$ in order to keep the continuity equation intact without any approximation;
2. The pressure gradient in the radial direction should be of the order $\left(\frac{D}{L_{TB}}\right)^2$;
3. For all terms in the momentum equations and on the boundaries to remain of the same order of magnitude, $Fr_{U_{TB}}$ should be of the order (1), $Re_{U_{TB}}$ and Eo both should be of the order $\left(\frac{L_{TB}}{D}\right)$.

4. The inverse viscosity number is, in fact, a modified Reynolds number provided that the characteristic velocity for stagnant fluid given by $V_s = (gD)^{1/2}$.

In conclusion, the dimensionless analysis shows that any analysis of the Taylor bubble problem should include three main dimensionless groups, $Fr_{U_{TB}}$, Eo and $Re_{U_{TB}}$or N_f. It is worth to mention that Reynolds number is an independent parameter, which governs the viscous flow in general, and it comes out of the dimensionless treatment and the order of magnitude analysis of Navier-Stokes equations of motion. In fact, there is no need to use a dimensionless number like Morton number and as far as the numerical simulation is concerned and whether the bubble velocity is an outcome of it, Reynolds number stays along with Froude number and Eötvös number (on the interface between the gas and liquid sides) the sole physical parameters influencing the dimensionless slug flow equations. It is worth stating here that the direct solution of the dimensionless governing equations requires the specifications of $Fr_{U_{TB}}$, $Re_{U_{TB}}$ and Eo numbers a prior to carrying out the numerical computations.

Thus, the problem is analysed in terms of six main dimensionless groups, namely the Eötvös number (Eo), Froude number ($Fr_{U_{TB}}$), Reynolds number based on bubble velocity ($Re_{U_{TB}}$), density ratio (Γ_ρ),viscosity ratio (Γ_μ) and the initial ratio of bubble size to pipe diameter $(L_{TB}/D)_i$. In this chapter, the effects of density ratio (Γ_ρ), viscosity ratio (Γ_μ) and the initial ratio of bubble size to pipe diameter $(L_{TB}/D)_i$ are done for the sake of supporting other previous experimental and numerical works in the literature. This is to allow dealing carefully with the main influencing parameters Eötvös number (Eo) and Reynolds number ($Re_{U_{TB}}$) rather than Eötvös number (Eo) and Morton number (M) as done by most of the other studies.

4.3 CFD Model Development

The base model is discussed in detail in chapter 3, however, some essential details about the boundary conditions and the reference frame used are given in this section. The flow domain is constructed and solved using the volume-of-fluid (VOF) methodology implemented in the computational fluid dynamics software package, ANSYS Fluent (Release 16.0). In all simulated cases, a uniform grid of quadrilateral control elements is applied. The simulation is performed for unsteady flow with constant fluid properties. The two phases are assumed as incompressible, viscous, immiscible and not penetrating each other. The flow regime could be laminar, which means the transition or the turbulent is depending on the value of Reynolds number in different flow regions of the slug flow domain.

Figure 4-2 shows that the flow regions in vertical slug flow that can be divided into three main regions according to the definition of Reynolds number, into flow in the main liquid region (liquid slug), Re_{U_∞} or $Re_{U_{TB}}$, flow in the liquid film (annular film), $Re_{U_{LF}}$ and flow near bubble wake, Re_{V_L}. The definition of Reynolds number according to each region is given by:

$$Re_{U_{TB}} = \rho_L U_{TB} D/\mu_L \tag{4-31}$$

$$Re_{U_{LF}} = \rho_L U_{LF}\, \delta_{LF}/\mu_L \tag{4-32}$$

$$Re_{V_L} = \rho_L V_L D/\mu_L \tag{4-33}$$

For the case of Taylor bubble rising in stagnant liquid only two parameters, namely Re_{U_∞}, and $Re_{U_{LF}}$, are used to characterise flow type into laminar, transient, or turbulent flow regime. Various experimental work is done to investigate the characteristic Reynolds number for the onset of transition in the flow regime in each region discussed above. For instance, to ensure laminar flow regime in the main liquid region, $Re_{U_{TB}}$ should be less than 2100 as reported by Fulford (1964); Frechou (1986) and Mayor et al. (2007b).

Also, the range of Reynolds numbers for the transitional region in the liquid film region is $[250{:}\,400] < Re_{U_{LF}} < 800$ as indicated by Fulford (1964). It should be pointed out that the transition criterion from laminar into turbulent flow is not clear enough and need to be further investigated. For instance, the wake pattern is identified into laminar or turbulent flow according to the value of inverse viscosity number (N_f). Nevertheless, according to the problem definition, it should be mainly, in terms of Reynolds number. However according to data in the literature, to ensure laminar flow regime in the main liquid region for the present study, $Re_{U_{TB}}$ ought to be less than 200. Regarding the flow in the liquid film, $Re_{U_{LF}}$ never exceeded 30 which ensures that the developed liquid films are entirely under the laminar regime.

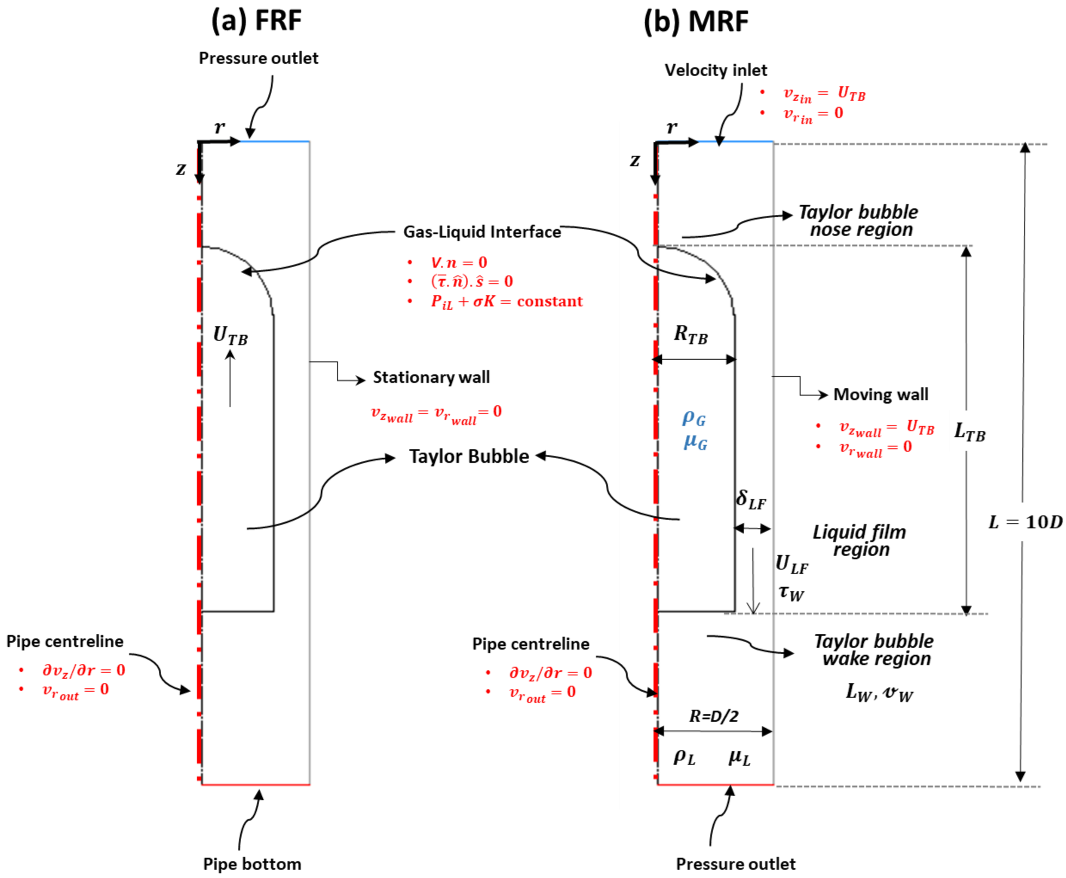

Figure 4-2. Schematic representation of the computational domain and the main hydrodynamic features of a single Taylor bubble rising through stagnant liquid, showing the initial and boundary conditions and the change from a fixed reference frame system (a) to a moving reference frame system (b).

4.3.1 Model Geometry

The solution domain is a vertical pipe with a diameter (D) and length (L) with symmetry along the centreline of the pipe. In order to minimise computational time and effort, all the simulations are performed in axisymmetric flow situation, assuming symmetry about the centreline of the pipe. This assumption is adequate and based on the laminar state of flow. In all simulation cases, the length of the domain is 10 times larger than pipe diameter to avoid disturbance of the continuous phase (liquid phase) at the entrance and the exit regions, and to ensure that a uniform velocity profile is restored. Figure 4-2 shows a schematic representation of the computational domain for the present problem. The initial bubble shape is a cylinder connected to a hemisphere with the same radius giving an overall bullet shape of the Taylor bubble. The length and radius of the Taylor bubble are given by L_{TB} and R_{TB}, respectively.

The initial ratio of the Taylor bubble length to pipe diameter $(L_{TB}/D)_i$ is an input parameter prior to simulation, and it is fixed to the value of 3 in most of the investigated cases. This initial shape is simulated until a steady bubble shape is reached. Different bubble shapes are tested, and the final steady shape of the bubble is found to be similar, but this only affects the solution convergence, and this is discussed in detail in section 4.4.2.1.1.

4.3.2 Fixed and Moving Reference Frame Techniques

The simulation is performed by attaching a reference frame to the rising Taylor bubble. Enabling moving reference frame (MRF) in the simulation, causes the rising Taylor bubble to be stationary and the pipe wall moves downwards with a velocity equal to that of the bubble (Mao and Dukler, 1990). The transformation of the boundary conditions using MRF is given in Figure 4-2.The initial guess of Taylor bubble velocity (U_{TB}) is estimated according to the general correlation of Wallis (1969), which is given by:

$$Fr_{U_{TB}} = \frac{U_{TB}}{\sqrt{gD}} = 0.345\left(1 - e^{\frac{-0.01N_f}{0.345}}\right)\left(1 - e^{\frac{3.37-Eo}{m}}\right)$$

where

$$m = \begin{cases} 25, & N_f < 18 \\ 69N_f^{-0.35}, & 18 < N_f < 250 \\ 10 & N_f > 250 \end{cases} \tag{4-34}$$

Once the Taylor bubble ceases moving up or down in the axial direction, and hence the pseudo-steady solution is reached, the velocity is then adjusted and set to be the terminal velocity. The initial guess of the liquid film thickness (δ_{LF}) is estimated using Brown (1965)'s equation, which is given by:

$$\delta_{LF} = \left[\frac{3\nu}{2g(R-\delta_{LF})}U_{TB}(R-\delta_{LF})^{2}\right]^{1/3} \tag{4-35}$$

Problems dealing with the rise of the Taylor bubble in stagnant liquid require the use of large computational domain to capture the phenomena effectively. A large domain in essential for Taylor bubble to reach their terminal velocity and hence reach its steady state. However, this leads to the problem of computational time. This domain captures areas which are not significant for this problem as the main region of interest is the Taylor bubble and its surroundings (Araújo et al., 2013b; Gutiérrez et al., 2017).

In general, computational domains used in most studies can be categorised into two main groups, fixed reference frames (FRF) and moving reference frames (MRF). According to the literature review given in chapter 2, it is clear that computational time is the main concern of modelling two-phase slug flow and accordingly, most of the studies use moving reference frame technique, which is less complicated than FRF, to avoid time-consuming simulations. This section shows a comparison between the two techniques discussing the advantages of using moving reference frame rather than a fixed frame in a vertical pipe, and how the computational time is reduced when using MRF without affecting the accuracy of the solution.

Figure 4-2 shows a schematic representation of the computational domain for the Taylor bubble in a vertical pipe and different reference frames, fixed and moving techniques. In the fixed reference frame technique, the bubble is left to drift under buoyancy and gravitational effects in a vertical pipe. The boundary conditions at the pipe outlet are pressure outlet, stationary no-slip boundary conditions at the wall and symmetry at the pipe centreline. The bubble velocity is tracked, and the simulation continues running until a constant terminal Taylor bubble velocity, U_{TB} is reached. Using this technique, the simulation time might be long and larger computational domain might be essential.

However, referring to Figure 4-2, using MRF the inlet flow boundary condition is applied with liquid entering at an average uniform velocity equal to the velocity of the Taylor bubble. The symmetry boundary condition is applied at the pipe centreline. At the wall, the no-slip condition is applied with wall moving downwards with the following velocities, $v_{z_{wall}} = U_{TB}$, $v_{r_{wall}} = 0$. The gas phase usually has lower density and viscosity than the liquid phase; thus, full slip can be assumed at the gas-liquid interface. The internal circulatory flow within Taylor bubbles has an almost negligible effect on the outer surrounding liquid leading to zero interfacial shear stress at the interface. Thus, the pressure variation within Taylor bubble is small and constant pressure is assumed at the interior of the Taylor bubble (Akagawa and Sakaguchi, 1966; Mao and Dukler, 1990; Zheng et al., 2007a; Morgado et al., 2016). Thus, the kinematic condition, $V.n = 0$, assuming full slip at the gas-liquid interface is applied. The dynamic boundary condition can be divided into two separate boundary conditions, the tangential stress balance assuming zero interfacial shear stress along the interface $\left((\bar{\tau}.\hat{n}).\hat{s} = 0\right)$ and the normal stress balance $(\rho_{iL} + \sigma K = \text{constant})$. According to Mao and Dukler (1990), the curvature of the interface (K) is expressed in terms of radii of the curvature of the bubble surface, as follows:

$$K = \left[\frac{1}{r_1} + \frac{1}{r_2}\right] \tag{4-36}$$

For 2D axisymmetric simulations in a vertical pipe, trial simulations are conducted to examine the effect of using both FRF and MRF techniques. Table 4-1 shows a comparison between the FRF and MRF applied to a selective experimental case of Nogueira et al. (2006a; 2006b) with water and aqueous glycerol solutions as working fluids in 32mm diameter vertical pipe. It should be pointed out that the computational domain in both cases has the same size ($10D_{pipe}$), which means that there is no need for a larger domain while enabling FRF technique. As indicated in Table 4-1, it can be concluded that both techniques give the same results, but FRF runs longer. Thus, for 2D simulations in a vertical pipe, MRF is selected.

Table 4-1. Numerical values of U_{TB} using the 2D axisymmetric domain with different reference frames for the experimental case of Nogueira et al. (2006a; 2006b) with their corresponding deviations with respect to the experimental data.

Domain-Reference frame	Run time in hours per 1s real time	UTB terminal (m/s)	UTB – Experimental (m/s)	$\lvert\textbf{Error}\rvert$ (%)
2D-FRF	4.5 hours	0.1702	0.188	9.5
2D-MRF	3 hours	0.1733	0.188	7.8

Figure 4-3 shows the predicted terminal Taylor bubble shape and the flow field around it (streamlines) using both techniques. Both reference frames gave the same terminal Taylor bubble shape. However, the flow field using the MRF shows better representation for the wake structure. Hence, for all simulations for vertical pipes, a 2D-axisymmetric coordinate system with MRF is selected.

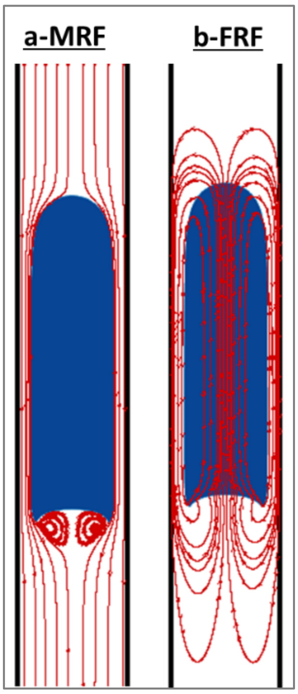

Figure 4-3. Comparison between the predicted terminal Taylor bubble shape and the flow field around it (streamlines) using (a) MRF and (b) FRF for the experimental case of Nogueira et al. (2006a; 2006b).

A comparison between the predicted terminal drift velocity (U_{TB}) for the experimental case of Nogueira et al. (2006a; 2006b) using the 3D model with different mesh sizes and the 2D axisymmetric model is given in Figure 4-4. Increasing the number of nodes controls the convergence of the terminal velocity, however, longer computation time is noticed. Increasing the number of nodes in the 3D model also helps in effectively predicting the gas-liquid interface. It should be mentioned that when comparing both the 2D axisymmetric model and the 3D model for this vertical case, better predictions for terminal velocity is noticed while using the 2D model with acceptable computational time. For that reason, all simulations done for the vertical cases are done using 2D axisymmetric model.

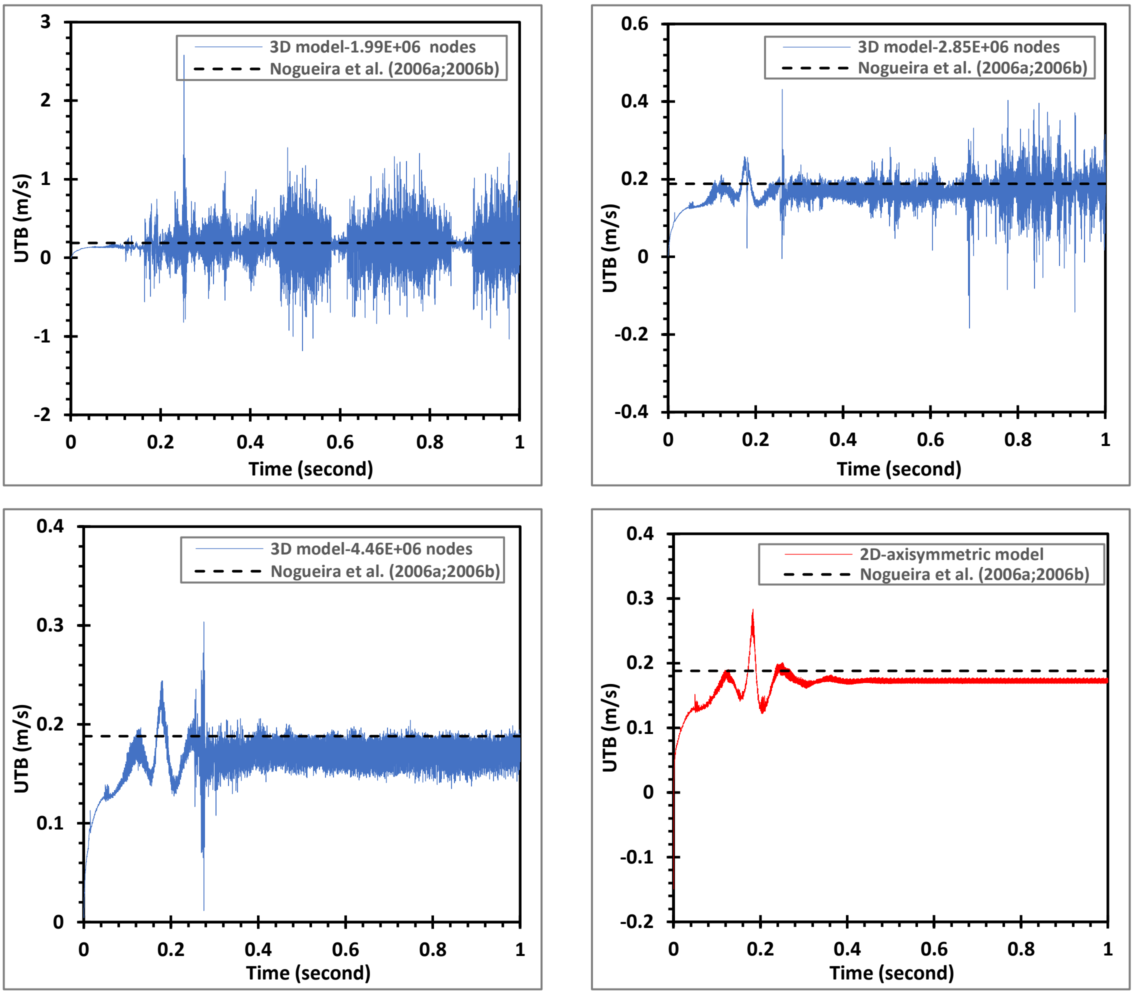

Figure 4-4. Example of mesh modification for obtaining converged terminal bubble velocity in the 3D model with a comparison between the 3D model and the 2D-axisymmetric model for the experimental case of Nogueira et al. (2006a; 2006b) for a vertical pipe.

4.4 Results and Discussions

In chapter 3, a mesh dependence study is discussed, followed by a validation study of a single Taylor bubble rising through a stagnant liquid in a vertical pipe. This section discusses the results that cover the main aims of this chapter which is investigating the main hydrodynamic features of the rise of single Taylor bubble through a stagnant Newtonian fluid in a vertical pipe, including the developed Taylor bubble shape, Taylor bubble rise velocity (U_{TB}), the liquid film thickness (δ_{LF}), maximum liquid film velocity (U_{LF}), wall shear stress (τ_W), wake length (L_w) and wake volume (ϑ_W), with a particular focus on the governing dimensionless numbers Eötvös number and Reynolds number. The results are divided into two sections, Taylor bubble rise velocity and detailed hydrodynamics covering the Taylor bubble shape, flow in the liquid film region and flow in the wake region. In addition, correlations for the terminal velocity of the Taylor bubble and for the dimensionless wall shear stress are proposed showing the significance of these main dimensionless parameters.

Table 4-2 lists the simulation cases and their corresponding results. The ranges of Eo, $Re_{U_{TB}}$, $Fr_{U_{TB}}$, Γ_ρ, Γ_μ, $(L_{TB}/D)_i$ are 6–700, 2.6-165, 0.031-0.330, 60-200, 66.7-6674, and 2–10, respectively. The input parameters prior simulation are Eo, $\Gamma_\rho, \Gamma_\mu, (L_{TB}/D)_i$, while the predicted values from the simulation are $Re_{U_{TB}}, Fr_{U_{TB}}, (L_{TB}/D)_{Pr}$ (δ_{LF}/D), $U_{LF_{max}}$, $\left(\frac{\tau_W}{\rho_L g D}\right)_{max}$, L_W/D and $\mathcal{V}_W/D^3$. The initial ratio of bubble size to pipe diameter is given by $(L_{TB}/D)_i$ and the average predicted ratio of the bubble size to the pipe diameter is given by $(L_{TB}/D)_{Pr}$. Based on the dimensionless analysis given in section 4.2, the primary aim of studying the effect of density ratio (Γ_ρ), viscosity ratio (Γ_μ) and the initial ratio of bubble size to the pipe diameter $(L_{TB}/D)_i$ on the hydrodynamic characteristics of the rise of single Taylor bubble in stagnant liquid is to support previous numerical work and experimental work in the literature. Cases 1 to 3 in Table 4-2 clearly emphasises that the density ratio has almost no effect on the dynamics of Taylor bubbles. The density ratio has minimal effect on liquid film thickness, maximum the velocity of the liquid film, maximum wall shear stress, wake length and wake volume. The simulation results as well agree with the numerical result of Kang et al. (2010). For the viscosity ratio effect, three cases denoted by cases 3, 4 and 5 are simulated with viscosity ratios of 66.7, 667 and 6674, respectively. Referring to Table 4-2, it is also concluded that the viscosity ratio (Γ_μ) has minimal effect on the dynamics of Taylor bubbles including as well the liquid film thickness, the maximum velocity of the liquid film, maximum wall shear stress and wake length and volume.

In conclusion, the simulated cases 1 to 6 have almost the same values of $Re_{U_{TB}}$ and Eo, which is 24.34 and 66, respectively. Thus, the simulation results further assist the conclusion made by Lu and Prosperetti (2008) and Kang et al. (2010) that both density ratio (Γ_ρ) and viscosity ratio (Γ_μ) have a negligible effect on the dynamics of Taylor bubbles.

Table 4-2. Simulation cases and their corresponding results

Input Parameters					**Predicted Values**							
								Flow in liquid film region			***Flow in wake region***	
Case No.	Eo	$\Gamma_\rho = \frac{\rho_L}{\rho_G}$	$\Gamma_\mu = \frac{\mu_L}{\mu_G}$	$\left(\frac{L_{TB}}{D}\right)_i$	$Fr_{U_{TB}}$	$Re_{U_{TB}}$	$\left(\frac{L_{TB}}{D}\right)_{Pr}$	$\frac{\delta_{LF}}{D}$	$U_{LF_{max}}$	$\left(\frac{\tau_W}{\rho_L g D}\right)_{max}$	L_w/D	υ_W/D^3
Effect of density ratio (Γρ)												
1	66	6E+01	6.67E+03	3	0.290	24.3	3.1	0.1250	0.1870	0.1074	0	0
2	66	9.98E+02	6.67E+03	3	0.290	24.3	3.1	0.1243	0.1086	0.109	0	0
3	66	2E+02	6.67E+03	3	0.287	24.1	3.1	0.1246	0.1873	0.1084	0	0
Effect of density ratio (Γ_μ)												
4	66	9.98E+02	6.67E+01	3	0.288	24.2	3.12	0.1251	0.1848	0.1071	0	0
5	66	9.98E+02	6.67E+02	3	0.289	24.3	3.1	0.1244	0.1863	0.1085	0	0
6	66	9.98E+02	6.67E+03	3	0.290	24.3	3.1	0.1243	0.1086	0.109	0	0
Effect of L_{TB}/D												
7	66	9.98E+02	6.67E+03	2	0.2898	24.3	2.14	0.1246	0.1083	0.1083	0	0
8	66	9.98E+02	6.67E+03	3	0.2898	24.3	3.1	0.1243	0.1086	0.109	0	0
9	66	9.98E+02	6.67E+03	4	0.2898	24.3	4.1	0.1244	0.1087	0.1087	0	0
10	66	9.98E+02	6.67E+03	10	0.2847	23.9	9.9	0.1232	0.1084	0.1084	0	0
Effect of Reynolds number (Re_{UTB})												
11	66	9.98E+02	6.67E+03	3	0.246	12	3.04	0.138	0.1437	0.1188	0	0
12	66	9.98E+02	6.67E+03	3	0.292	29	3.09	0.1183	0.1993	0.2350	0	0
13	66	9.98E+02	6.67E+03	3	0.307	46	3.08	0.1063	0.1041	0.0948	0.3775	0.06779
14	66	9.98E+02	6.67E+03	3	0.315	63	3.11	0.0982	0.2596	0.0882	0.5717	0.1305
15	66	9.98E+02	6.67E+03	3	0.320	80	3.1	0.0922	0.2815	0.0831	0.6542	0.1786
16	66	9.98E+02	6.67E+03	3	0.324	97	3.12	0.0875	0.2995	0.0791	0.7341	0.2212
17	66	9.98E+02	6.67E+03	3	0.325	114	3.14	0.0822	0.3185	0.0788	0.8087	0.2571
18	66	9.98E+02	6.67E+03	3	0.328	131	3.23	0.0799	0.3281	0.0728	0.8824	0.2870
19	66	9.98E+02	6.67E+03	3	0.329	148	3.21	0.0779	0.3413	0.0708	0.9023	0.3048
20	66	9.98E+02	6.67E+03	3	0.330	165	3.27	0.0746	0.3914	0.0689	0.9331	0.32780
Effect of Eötvös number (Eo)												
21	6	9.98E+02	6.67E+03	3	0.031	2.6	3.06	0.0440	0.0540	0.1290	0	0
22	10	9.98E+02	6.67E+03	3	0.118	9.9	3.14	0.0765	0.1179	0.1510	0	0
23	20	9.98E+02	6.67E+03	3	0.216	18.2	3.1	0.1033	0.1631	0.1360	0	0
24	40	9.98E+02	6.67E+03	3	0.272	22.9	3.06	0.1221	0.1797	0.1069	0	0
25	66	9.98E+02	6.67E+03	3	0.290	24.3	3.1	0.1243	0.1864	0.1086	0	0
26	70	9.98E+02	6.67E+03	3	0.290	24.4	3.1	0.1245	0.1873	0.1087	0	0
27	80	9.98E+02	6.67E+03	3	0.292	24.5	3.1	0.1247	0.1884	0.1089	0	0
28	100	9.98E+02	6.67E+03	3	0.295	24.8	3.12	0.1251	0.1907	0.1092	0.5511	0.00561
29	120	9.98E+02	6.67E+03	3	0.296	24.9	3.12	0.1253	0.1916	0.1093	0.1796	0.01633
30	140	9.98E+02	6.67E+03	3	0.297	25.0	3.14	0.1253	0.1921	0.1094	0.2323	0.01947
31	150	9.98E+02	6.67E+03	3	0.298	25.0	3.14	0.1254	0.1924	0.1095	0.2227	0.02507
32	160	9.98E+02	6.67E+03	3	0.298	25.1	3.14	0.1254	0.1931	0.1097	0.2290	0.02702
33	170	9.98E+02	6.67E+03	3	0.298	25.1	3.14	0.1255	0.1930	0.1096	0.2552	0.0246
34	180	9.98E+02	6.67E+03	3	0.298	25.1	3.14	0.1251	0.1940	0.1102	0.2556	0.0318
35	200	9.98E+02	6.67E+03	3	0.299	25.1	3.16	0.1251	0.1941	0.1101	0.2730	0.03241
36	250	9.98E+02	6.67E+03	3	0.301	25.3	2.98	0.1249	0.1951	0.1109	0.3734	0.10823
37	300	9.98E+02	6.67E+03	3	0.301	25.3	3	0.1250	0.1955	0.1110	0.4246	0.08719
38	350	9.98E+02	6.67E+03	3	0.299	25.1	2.9	0.1247	0.1944	0.1107	0.4875	0.17962
39	400	9.98E+02	6.67E+03	3	0.299	25.2	2.89	0.1248	0.1926	0.1096	0.5867	0.13278
40	500	9.98E+02	6.67E+03	3	0.301	25.3	3.04	0.1253	0.1918	0.1094	0.5921	0.11758
41	600	9.98E+02	6.67E+03	3	0.297	24.9	2.86	0.1248	0.1953	0.1109	0.3346	0.07387
42	700	9.98E+02	6.67E+03	3	0.297	24.9	2.88	0.1247	0.1945	0.1107	0.4989	0.09641

Lastly, to explore the effect of $(L_{TB}/D)_i$, four cases are simulated denoted by cases 7 to 10 in Table 4-2 corresponding to $(L_{TB}/D)_i$ of 2, 3, 4 and 10, respectively. It can also be concluded that $(L_{TB}/D)_i$ as well has minimal effect on the dynamics of Taylor bubbles. Table 4-2 shows that these four cases have almost the same value of $Fr_{U_{TB}}$ which agrees with the conclusion of previous studies that the bubble length has no effect on the bubble terminal speed as long as the bubble length is more than 1.5D_{pipe} (Davies and Taylor, 1950; Goldsmith and Mason, 1962; White and Beardmore, 1962; Zukoski, 1966; Maneri and Zuber, 1974; Campos and De Carvalho, 1988; Kawaji et al., 1997; Shosho and Ryan, 2001; Ndinisa et al., 2005; Lu and Prosperetti, 2008; Hua et al., 2009; Morgado et al., 2016). Based on that, the results focus on investigating the dynamics of Taylor bubbles in terms of the sole dimensionless parameters, which are Reynolds number and Eötvös number. The problem can now be treated in terms of three main dimensionless groups, given by:

$$Fr_{U_{TB}} = \frac{U_{TB}}{\sqrt{gD}} = f\left[Eo = \frac{g\rho_L D^2}{\sigma}\ , Re_{U_{TB}} = \frac{\rho_L U_{TB} D}{\mu_L}\ \right] \qquad (4\text{-}37)$$

In additions, based on the simulation results and using guidelines from the order of magnitude analysis, correlations for the terminal velocity of the Taylor bubble, and the dimensionless wall shear stress are proposed showing the significance of these main governing parameters. These are discussed in detail in the following section.

4.4.1 Taylor Bubble Rise Velocity

The Taylor bubble rise velocity (U_{TB}) is one of the main hydrodynamic features used for the hydrodynamic description of vertical slug flow systems. In this section, a detailed discussion on the Taylor bubble terminal velocity is introduced. Based on the discussion given in section 4.2, it can be concluded that the terminal bubble velocity (U_{TB}) is mainly governed by viscosity, surface tension, buoyancy and inertia forces. In literature, various studies, either theoretical and/or experimental, are done to account for the terminal bubble velocity. A good review of the main correlations for $Fr_{U_{TB}}$, to account for bubble terminal velocity, starting from the theoretical investigation of Dumitrescu (1943) and ending with the study of Kurimoto et al. (2013), is given by Morgado et al. (2016).

Referring to Table 4-2, the effect of Reynolds number $\left(Re_{U_{TB}}\right)$ on the Taylor bubble rise velocity is noticed throughout cases 11 to 20. The surrounding stagnant liquid has a high viscous effect that can sufficiently outbreaks the drift of the Taylor bubble which is noticed at lower values of $Re_{U_{TB}}$. The increment in $Re_{U_{TB}}$ values is followed by an increase in the Taylor bubble velocity until the value of $Re_{U_{TB}} = 80$. Further increase in $Re_{U_{TB}}$ above the value of 80, $Fr_{U_{TB}}$ is almost constant which is in agreement with the experimental conclusions of Wallis (1969). In addition, for cases 21 to 42 in Table 4-2, it can be concluded that the increase in Eo causes an increase in the inertial forces which is seen subsequently followed by a rise in $Fr_{U_{TB}}$ values.

Based on relation (4-37), a proposed correlation to estimate $Fr_{U_{TB}}$ that depends mainly on Eo and $Re_{U_{TB}}$ is developed. Using the surface fitting tool (SF tool) in MATLAB@ (2015a), the proposed correlation is given by:

$$
\begin{aligned}
Fr_{U_{TB}} &= \frac{U_{TB}}{\sqrt{gD}} \\
&= 0.0359 - 0.3596Eo - 0.7067Re_{U_{TB}} + 0.5801Eo^2 - 1.014EoRe_{U_{TB}} + 0.3447Eo^3 \\
&\qquad + 1.594Eo^2Re_{U_{TB}} - 0.1931Eo^4 + 0.9647Eo^3Re_{U_{TB}} - 0.001814Eo^5 \\
&\qquad - 0.5481Eo^4Re_{U_{TB}}
\end{aligned}
\tag{4-38}
$$

Additionally, Figure 4-5 shows that the values obtained from the proposed correlation fit quite well with the behaviour of other well-known correlations from literature for different domains. Values predicted from Viana et al. (2003) correlations, and values from the recent correlation of Kurimoto et al. (2013) are added to Figure 4-5 for comparison purposes. It can be seen that the proposed correlation agrees well with a wide range of correlations with a maximum deviation of ±10%. In general, there is a proper matching between the data, especially in surface tension dominant domain. However, in inertia dominant domains with high values of Eo, the proposed correlation predicts the correlation of Viana et al. (2003). The only explanation is most probable to be a numerical problem for situations of high inertial forces as pointed out by Araújo et al. (2012). In brief, the proposed correlation shows an accepted behaviour with other correlations with a maximum deviation of ±10%.

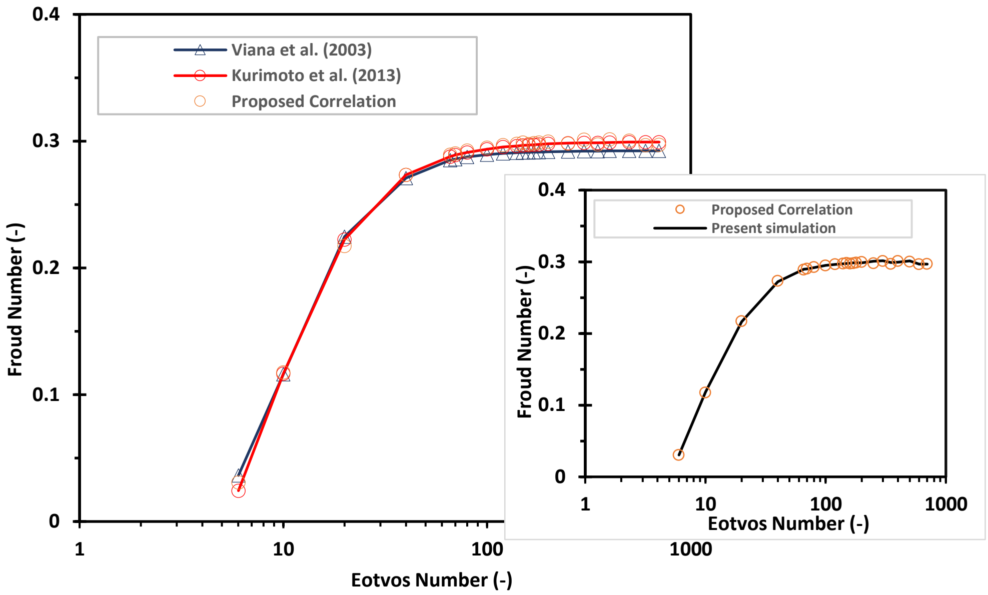

Figure 4-5. Numerical results of U_{TB} expressed in terms of $Fr_{U_{TB}}$ for a several Eo with corresponding values obtained from the proposed correlation given in equation (4-38) and different correlations from literature for comparison $-Re_{U_{TB}}$ varies from 2.6 to 25.3.

4.4.2 Detailed Hydrodynamics

In this section, detailed hydrodynamics of Taylor bubble problem is investigated by dividing the flow field into three main sections, flow in the Taylor bubble nose region, flow in the liquid film region and flow in the wake region.

4.4.2.1 Taylor Bubble Shape

In this section, the effect of the main dimensionless groups that govern the problem is discussed. This includes representing the final shape of the developed Taylor bubble, the flow field around it (streamlines) and the Taylor bubble shape profile for each of the dimensionless groups examined.

4.4.2.1.1 Effect of Taylor Bubble Initial Shape

To check the impact of the initial Taylor bubble shape on the final predicted results, three different initial Taylor bubble shapes, given in Figure 4-6, are tested. These different initial bubble shapes are a standard cylinder, a cylinder with a hemisphere at the front end (bullet shape) and a cylinder with two hemispheres. The simulations are done using FRF to examine the effect of the different shape of the Taylor bubble on the transient period and the total time required to reach the terminal results. It can be concluded that the initial Taylor bubble shape controls the time needed to reach the terminal state. Both of bullet shape and a cylinder with two hemispheres initial shapes show similar time evolution, however, the standard cylinder shows a different time evolution. This conclusion is in good agreement with Gutiérrez et al. (2017).

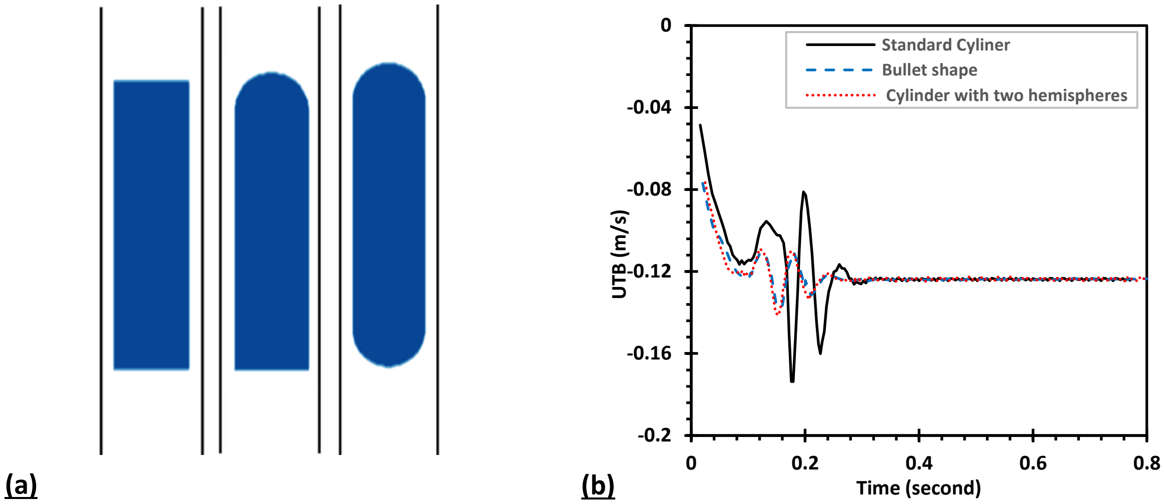

Figure 4-6. Sketch of (a) the different Taylor bubble initial shapes tested to solve drift of Taylor bubble through a stagnant liquid in 19mm vertical pipe (Eo=63.3, $Re_{U_{TB}}$=65.7, $Fr_{U_{TB}}$=0.32) and (b) their corresponding velocity evolution.

4.4.2.1.2 Effect of Reynolds Number

In literature, most of the studies done on the dynamics of the Taylor bubble rising through stagnant liquid highlight the significant effect of inverse viscosity number or Archimedes number without considering the significant impact of Reynolds number. In this section ten cases namely case 11 to 20 in Table 4-2. Simulation cases and their corresponding results are simulated to investigate the significant effect of $Re_{U_{TB}}$ on the dynamics of the Taylor bubble. Figure 4-7 demonstrates the effect of $Re_{U_{TB}}$ number on the final shape of the developed Taylor bubble and the flow field for cases 11, 13, 15 and 18 with $Re_{U_{TB}}$ values corresponding to 12, 46, 80 and 131, respectively. It can be shown that $Re_{U_{TB}}$ has a prodigious effect on the final shape of the bubble, as indicated in Figure 4-7. Particularly, for low values of $Re_{U_{TB}}$, the viscous forces of liquid phase surrounding the bubbles are high enough to encumber the rise of the Taylor bubble, and hence the terminal bubble velocity will be at its lowest values (lowest $Fr_{U_{TB}}$), as indicated in Table 4-2. It can be concluded from Table 4-2 that for $Re_{U_{TB}}$ values approximately above 80, $Fr_{U_{TB}}$ is almost the same which is in agreement with the experimental conclusions of Wallis (1969). It can also be concluded from Figure 4-7, that the high viscous forces enhance the elongation of the terminal developed Taylor bubble. The gradual increase in $Re_{U_{TB}}$ increases the concavity of the rear of Taylor bubble which is in good agreement with the experimental observation of Goldsmith and Mason (1962) that the rear of Taylor bubbles is characterised by being flat or concave when the flow is not viscosity dominated and oblate spheroid when it is viscosity dominated. The shape of the rear of the Taylor bubble and its critical transition criteria is discussed in detail in section 4.4.2.3.

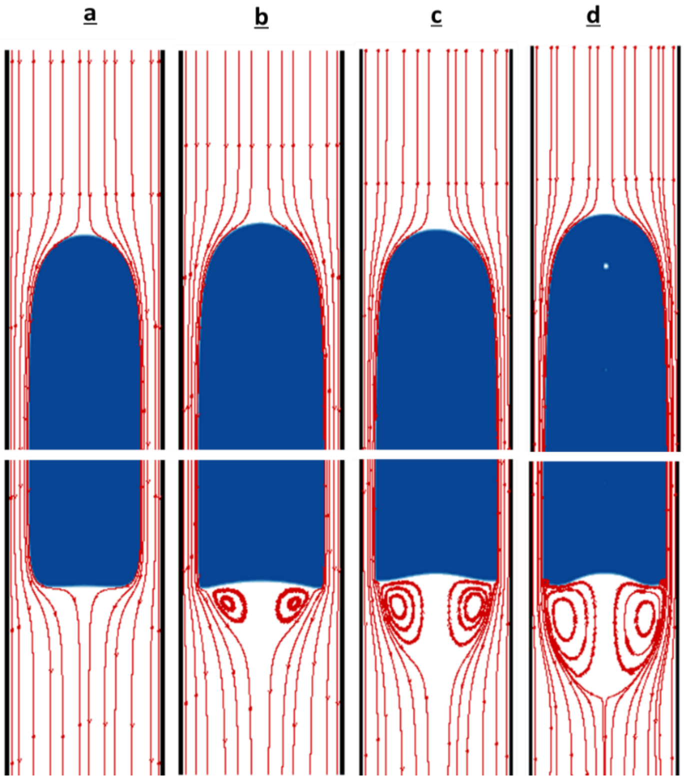

Figure 4-7. Effect of $Re_{U_{TB}}$ on the terminal shape of the Taylor bubble and streamlines representing the flow field (a) Case (11) $Re_{U_{TB}}$ =12, (b) Case (13) $Re_{U_{TB}}$ =46, (c) Case (15) $Re_{U_{TB}}$ =80 and (d) Case (18) $Re_{U_{TB}}$ =131.

In addition, it is also concluded from Figure 4-7 that $Re_{U_{TB}}$ has a significant effect on wake development. For low values of $Re_{U_{TB}}$, the liquid from the liquid film region expands directly and smoothly over the Taylor bubble bottom, which is noticed by parallel streamlines in the wake region. Increasing the values of $Re_{U_{TB}}$, the Taylor bubble becomes wider in size squeezing the liquid film region that subsequently increases the velocity of the trailing liquid plugging into the Taylor bubble bottom. This leads to the development of circulatory rear of vortices as liquid plugs into the Taylor bubble bottom. The scale and intensity of the vortex increases with higher values of $Re_{U_{TB}}$. Furthermore, Figure 4-8 shows the effect of $Re_{U_{TB}}$ on the bubble shape profile where it is clearly seen that the increase in $Re_{U_{TB}}$ causes the bubble nose to becomes less slender, and reduces the thickness of the developed liquid film.

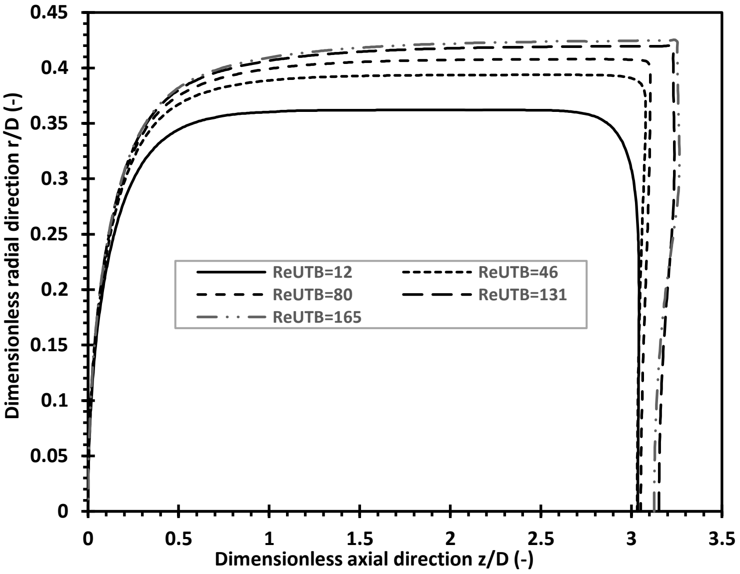

Figure 4-8. Effect of $Re_{U_{TB}}$ on the bubble shape profile- z is the axial distance from the bubble nose.

4.4.2.1.3 Effect of Eötvös Number

Eötvös number (Eo) represents the effect of buoyancy and surface tension forces, which are two of the significant forces acting on Taylor bubbles. In order to investigate the effect of Eo number on the dynamics of Taylors bubble rising through stagnant liquids, 21 cases, namely case 21 to case 42 in Table 4-2 are simulated. This covers a wide range of Eo varying from 6-700.

Figure 4-9 shows the effect of Eo on the final shape of the developed Taylor bubble and the flow field for cases 22, 25, 28 and 32 with Eo values corresponding to 10, 66, 100 and 160, respectively. At low values of Eo, the surface tension forces are high enough to maintain any distortion at the gas-liquid interface. The bubble is noticed to have a prolate spheroidal nose and oblate spheroid bottom. The increment in the surface tension increases the curvature of the bubble nose and subsequently increases the liquid film thickness. Hence, the velocity of fully developed falling liquid film decreases.

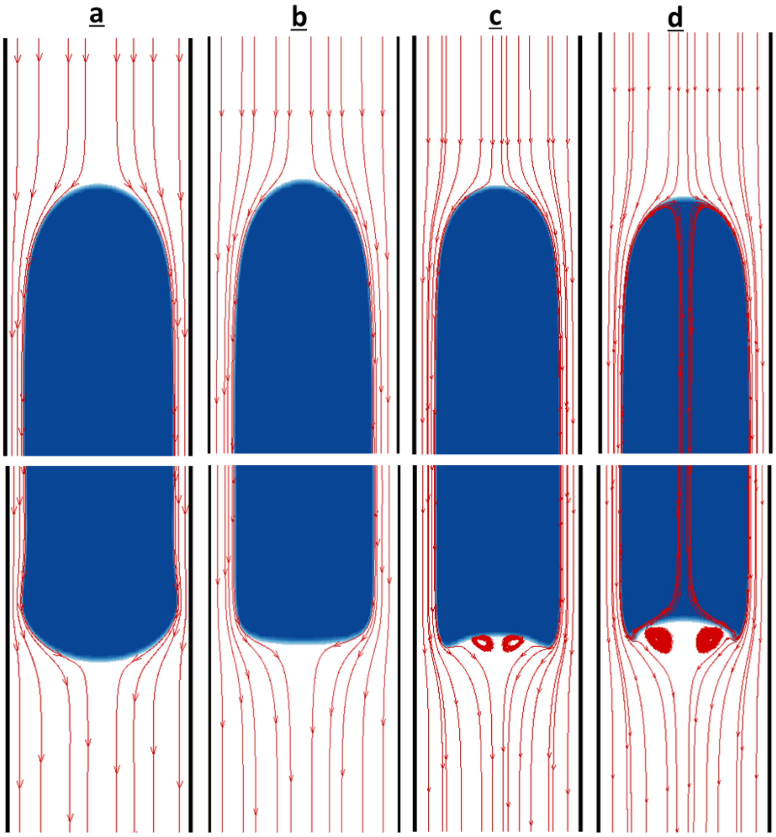

Figure 4-9. Effect of Eo *on the terminal shape of the Taylor bubble and streamlines representing the flow field (a) Case (22)* $Eo = 10$*, (b) Case (25)* $Eo = 66$*, (c) Case (28)* $Eo = 100$ *and (d) Case (32)* $Eo = 160$*.*

Regarding the rear of the bubble, the increase in Eo leads to an increase in inertial forces which is seen as values of $Fr_{U_{TB}}$ increases. The increase in Eo also significantly affects the rear of the bubble by gradually turning the bottom shape from convex or flat into a concave structure, as indicated in Figure 4-9. This causes wakes to be developed at the rear of the bubble, and hence wake length and volume increases with the increase in Eo values, as indicated in Table 4-2. This has a similar trend as that shown in Figure 4-7 exploring the effect of $Re_{U_{TB}}$. At a certain critical value of Eo, the further increase in Eo with its corresponding deficiency of surface tension results in deformation at the gas-liquid interface. The shape of the bubble's rear turns from concave into wave and subsequently into breaking up. The breaking up concept is characterised by very unstable phenomena that occurs at the rear of the bubble and is noticed by the small bubbles shedding off from Taylor bubble into the wake region. Higher values of Eo, cause the gas-liquid interface to lose its structure and strong breaking up concept is noticed (Morgado et al., 2016). A phase diagram map is discussed later in section 4.4.2.3 that describes the interesting phenomena that occur at the rear of Taylor bubbles, which is strongly affected by surface tension and inertia forces.

Furthermore, Figure 4-10 shows the effect of Eo on the bubble shape profile for different selected cases from Table 4-2. The increase in Eo increases the bluntness of the nose of the bubble, decreases the flatness of the bubble tail and increment the liquid film thickness. This conclusion refutes that of Kang et al. (2010) that Eo has no effect on the dynamics at bubble nose, and liquid film thickness, but agrees with the conclusion of Taha and Cui (2006) and which entails that Eo increases the degree of prolateness of the Taylor bubble nose.

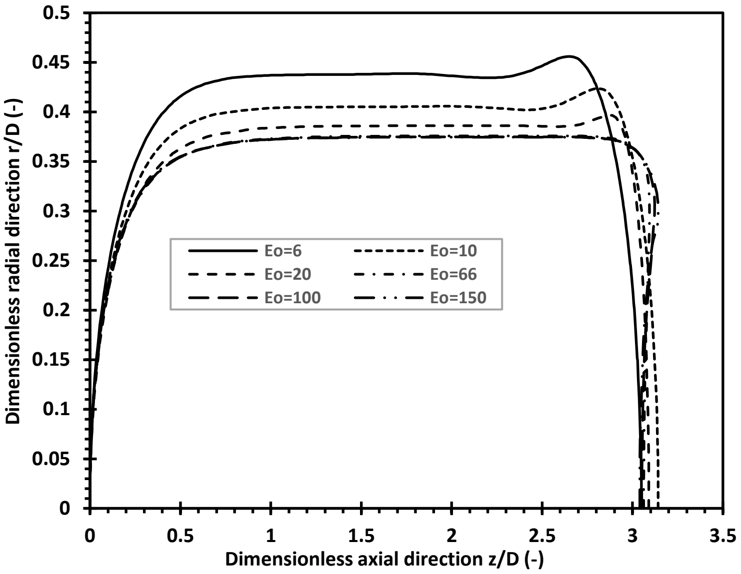

Figure 4-10. Effect of Eo on the bubble shape profile – z is the axial distance from the bubble nose.

In conclusion, Eo and $Re_{U_{TB}}$ significantly control the developed shape of Taylor the bubble. The results show that the surface tension forces are significant with low values of Eo, while the large contribution of $Re_{U_{TB}}$ on the dynamics of the Taylor bubble, is noticed with higher values of $Re_{U_{TB}}$. These conclusions agree well with the results of the order of magnitude analysis discussed earlier in this chapter.

4.4.2.2 Liquid Film Region

The flow in the liquid film is investigated by three key features, the dimensionless developed liquid film thickness (δ_{LF}/D), the dimensionless velocity of the liquid film (U_{LF}/U_{TB}) and the dimensionless wall shear stress $\left(\frac{\tau_W}{\rho_L g D}\right)_{max}$. This section discusses the effect of the main dimensionless parameters, given in section 4.2, on these three key features characterising the flow in the liquid film region.

4.4.2.2.1 Liquid Film Velocity and Thickness

Figure 4-11 represents the effect of $Re_{U_{TB}}$on the dimensionless normalised thicknesses and velocity of falling liquid film along the Taylor bubble length. At low values of $Re_{U_{TB}}$, the liquid film thickness (δ_{LF}/D) decreases with the increase in the dimensionless distance measure from the bubble nose (z/D) until it reaches a constant thickness at around z/D=1. At that point, a balance between the gravitational and friction forces is reached, and hence a constant liquid film thickness and velocity is established. However, the dimensionless velocity of the liquid film (U_{LF}/U_{TB}) changes contrarily. The increase in $Re_{U_{TB}}$ diminishes the long slender shape

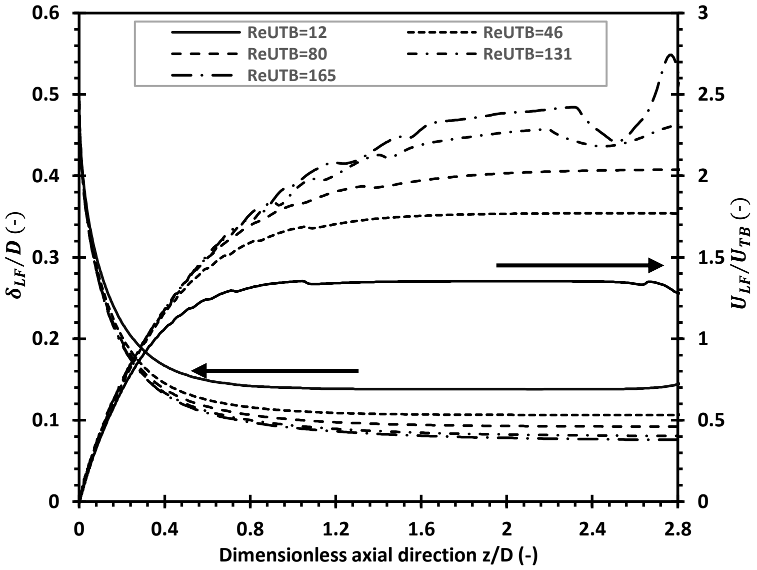

Figure 4-11. The effect of $Re_{U_{TB}}$ on the dimensionless normalized thicknesses (δ_{LF}/D) and dimensionless velocity of falling liquid film (U_{LF}/U_{TB}) along the Taylor bubble length- z is the axial distance from bubble nose.

of the Taylor bubble and turns it into shorter and flatter bubbles which in turns reduces (δ_{LF}/D). In addition, the higher viscosity of the surrounding liquid at low values of $Re_{U_{TB}}$ increment the shear stress in the liquid, thus, the momentum diffusion opposes the liquid flowing from the liquid film into the bubble wake region. Therefore, the increase in $Re_{U_{TB}}$ increases the dimensionless velocity of the liquid film (U_{LF}/U_{TB}). This conclusion agrees well with Zheng et al. (2007a) and Kang et al. (2010).

Finally, the effect of Eo on the dimensionless normalized thicknesses and velocity of falling liquid film along the Taylor bubble length is given in Figure 4-12. As discussed earlier, the increase in Eo affects the curvature of the bubble nose, thus increases (δ_{LF}/D), increases stabilization length (distance needed for the formation of fully developed falling liquid film) and finally increases U_{LF}. However, the dimensionless velocity of the liquid film (U_{LF}/U_{TB}) decreases with the increment in Eo due to the fact that the inertia forces are increased leading to increment in U_{TB} values. It is concluded from Figure 4-12 that (δ_{LF}/D) and (U_{LF}/U_{TB}) are affected with the increase in Eo till $Eo \leq 66$, where a further increase in Eo shows almost no effect on the flow in the liquid film.

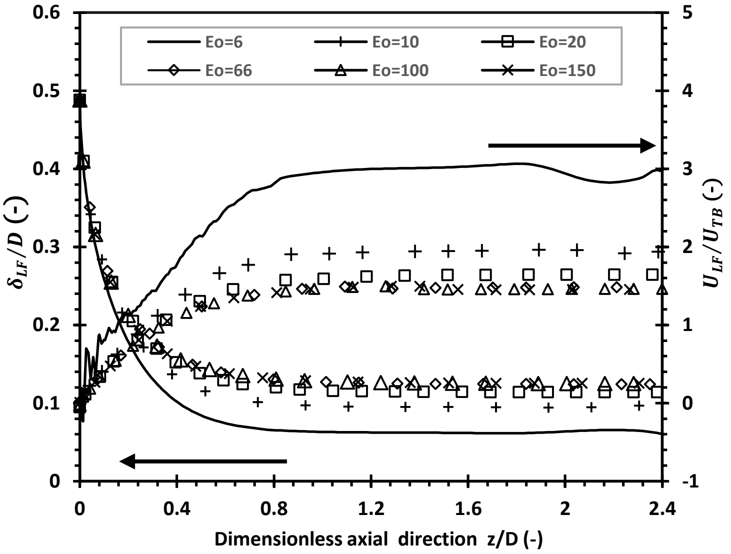

Figure 4-12. The effect of Eo on the dimensionless normalized thicknesses (δ_{LF}/D) and dimensionless velocity of falling liquid film (U_{LF}/U_{TB}) along the Taylor bubble length- z is the axial distance from bubble nose.

In conclusion, it should be pointed out that both of (δ_{LF}/D) and (U_{LF}/U_{TB}) are strongly dependent on Eo and $Re_{U_{TB}}$. This conclusion contradicts those made by; Kang et al. (2010) -

the liquid film thickness is only dependent on Archimedes number ($Ar = {N_f}^2$) and that of Araújo et al. (2012) - the liquid film thickness is a function of N_f and M.

4.4.2.2.2 Wall Shear Stress Distribution

If the two-phase slug flow problem is involved in heat or mass transfer, then the wall shear stress becomes a primary significant hydrodynamic parameter. This process is often referred to as slug flow-induced corrosion as discussed by Zheng and Che (2006); Zheng et al. (2007a; 2007b); and Araújo et al. (2012). The main problems that result from slug flow corrosion are pipeline damage, decrease pipe lifetime and may lead to the shutdown of the pipeline.

Figure 4-13 shows the wall shear stress distribution along the Taylor bubble length for different $Re_{U_{TB}}$. For low values of $Re_{U_{TB}}$, the wall shear stress distribution starts with an increase in the wall shear stress near the bubble nose then it reaches a maximum positive value with the formation of a constant liquid film characteristics (thickness and velocity). The wall shear stress then starts to decrease until it reaches zero value in the bubble tail or wake region.

The increase in $Re_{U_{TB}}$, results in less the viscous liquid surrounding the Taylor bubble, that subscribes to decrement in wall shear stress. This conclusion agrees well with that made by Taha and Cui (2006). On the other hand, the dimensionless wall shear stress in the nose region is not affected by the increase in $Re_{U_{TB}}$, however, the plateau behaviour at the developed liquid film is shortened with the increase in $Re_{U_{TB}}$. This occurs as a result of the shape in Taylor bubble shape which is characterised by being a long slender that turns into shorter and flatter bubbles with the increase in $Re_{U_{TB}}$. Additionally, it should be pointed out that the effect of an increase in $Re_{U_{TB}}$ on the bubble wake region is seen as a jump in dimensionless wall shear values that increases with higher values of $Re_{U_{TB}}$; this further assists the conclusion made by Kang et al. (2010).

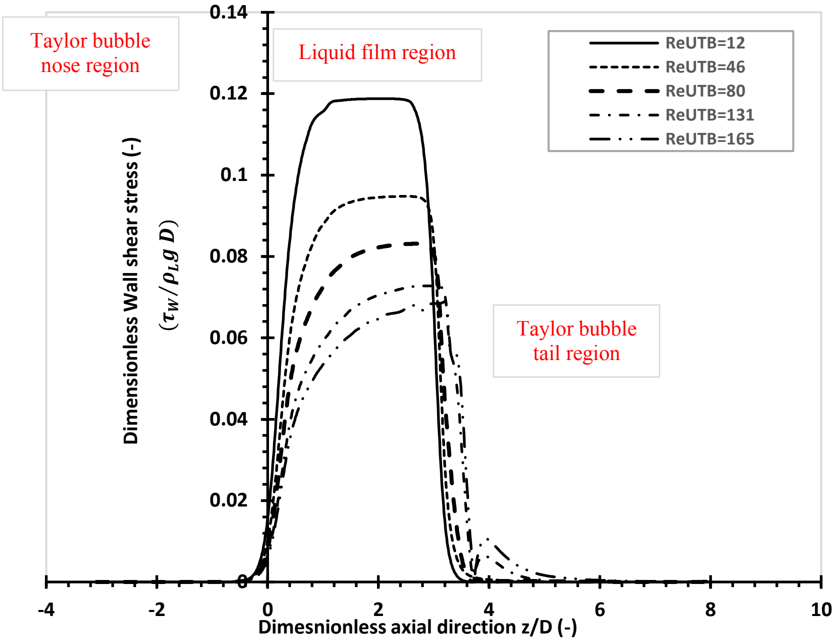

Figure 4-13. Effect of $Re_{U_{TB}}$ *on the wall shear stress distribution* $(\tau_W/\rho_L g\ D)$ *along Taylor bubble length - z is the axial distance from bubble nose.*

Further validation for the flow in liquid film region is given in Figure 4-14 where a comparison takes place between the numerical results for dimensionless wall shear stress and δ_{LF}/D and the theoretical values by Brown (1965). It is clear that the numerical results strongly correspond with the theoretical data. Brown (1965)'s equation for δ_{LF} prediction is given by equation (4-35), while the prediction for τ_W is given by:

$$\tau_W = \rho_L g \left[\frac{R}{2} - \frac{(R-\delta_{LF})^2}{2R}\right] \tag{4-39}$$

Finally, the effect of Eo on the distribution of the dimensionless wall shear stress along the Taylor bubble is given in Figure 4-15. Generally, for most values of Eo, the distribution is almost the same, which starts with an increase in wall shear stress near the bubble nose, then a constant value is reached at the developed liquid film, followed by a reduction in dimensionless wall shear stress near the bubble tail. As indicated in Figure 4-15, lower values of Eo possess different distribution with a noticeable peak value in dimensionless shear stress right before the Taylor bubble rear. This is due to the sharp flat and convex shape of the bubble attained at lower values of Eo, which coincides with Araújo et al. (2012).

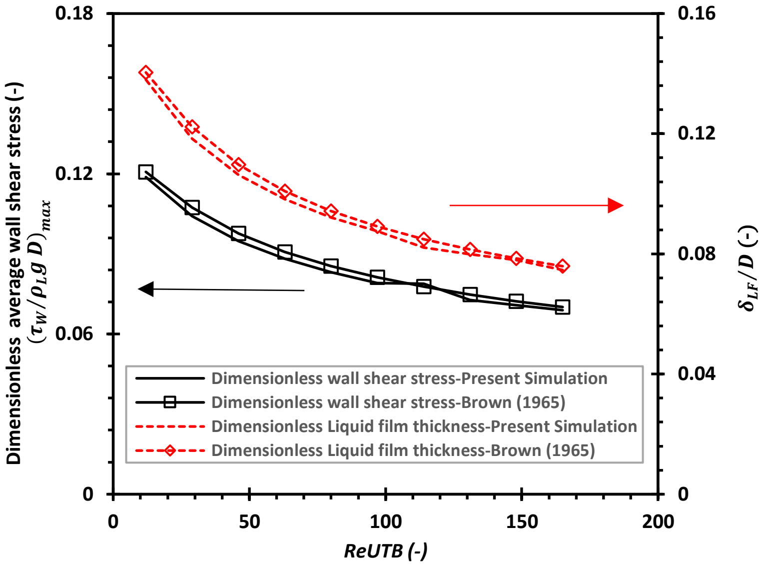

Figure 4-14. Variation of the dimensionless normalised thickness (δ_{LF}/D) and dimensionless maximum wall shear stress $(\tau_W/\rho_L g\ D)_{max}$ distribution along Taylor bubble length with $Re_{U_{TB}}$ plotted with the theoretical prediction of Brown (1965).

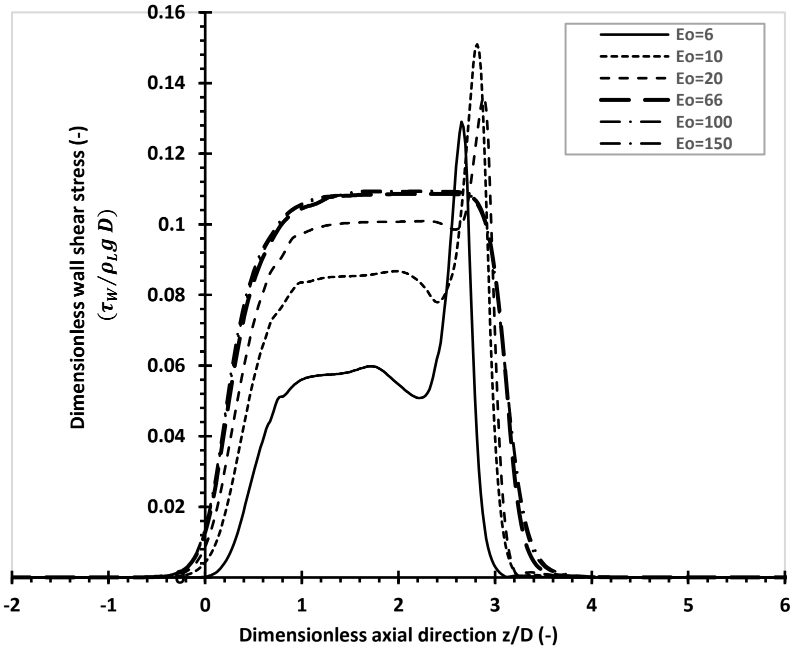

Figure 4-15. Effect of Eo on the wall shear stress distribution along Taylor bubble length - z is the axial distance from bubble nose, $Re_{U_{TB}}$ varies from 2.6 to 25.

In conclusion, the numerical results show that the dimensionless wall shear stress is dependent on both Eo and $Re_{U_{TB}}$ which again contradicts the conclusion made by Kang et al. (2010) that the wall shear stress is only function of Ar, and supports Araújo et al. (2012) conclusion in a different scenario. Subsequently, a correlation based on the numerical results for all simulated cases in Table 4-2 for dimensionless maximum wall shear stress is suggested, given by:

$$\left(\frac{\tau_W}{\rho_L g D}\right)_{max} = 0.242 + 0.238Eo + 0.5544Re_{U_{TB}} - 0.1196Eo^2 + 1.037EoRe_{U_{TB}} + 0.5294Re_{U_{TB}}^2 - 2.818e^{-05}Eo^3 - 0.3202Eo^2Re_{U_{TB}} + 1.083EoRe_{U_{TB}}^2 - 0.0008579Re_{U_{TB}}^3 \qquad (4\text{-}40)$$

Figure 4-16 illustrates the present numerical results, and values obtained from proposed correlation given in equation (4-40) for the maximum dimensionless wall shear stress along the Taylor bubble length for different values of Eo (cases 21 to 42 in Table 4-2). It is obvious that the correlation matches the simulation data to a considerable extent. For comparison issues, the theoretical prediction given by Brown (1965) (equation (4-39)).

$$\left(\frac{\tau_W}{\rho_L g D}\right)_{max} = -0.02log_{10}Ar + 0.2 \qquad (4\text{-}41)$$

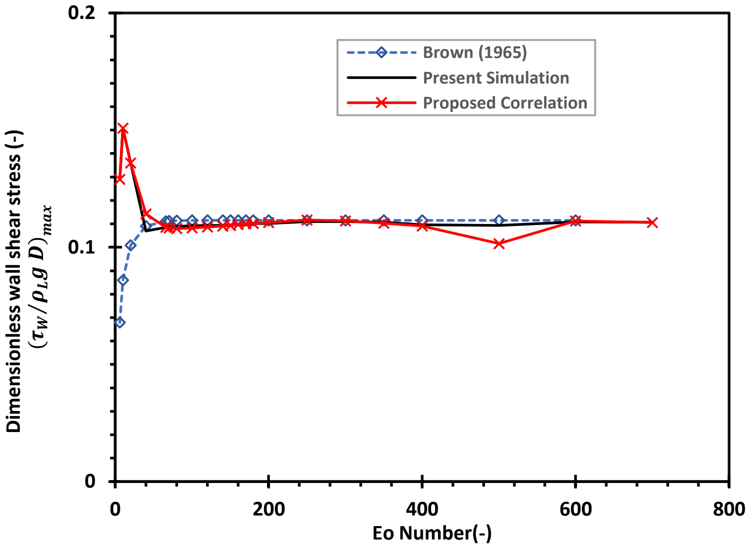

Figure 4-16. Numerical results of $\left(\frac{\tau_W}{\rho_L g D}\right)_{max}$ *for a several* Eo *with corresponding values obtained from proposed correlation given in equation (4-40), theoretical prediction given by Brown (1965) for cases 21 to 42 in Table 4-2.*

It can be seen from Figure 4-16 that the suggested correlation matches well with the theoretical predictions calculated by Brown (1965) with very small deviations. However, there is an exception for that proper matching for small values of Eo. Generally, these cases with low values of Eo (especially around 6) possess low values of U_{TB} with almost non-moving bubbles. These cases are more sensitive to numerical errors as clarified by Zheng et al. (2007a) and Araújo et al. (2012).

It should be pointed out that $Re_{U_{TB}}$ is not constant for these selected cases, and its values are indicated in Table 4-2. Similarly, as discussed before for the liquid film thickness, the dimensionless wall shear stress is a function of both Eo and $Re_{U_{TB}}$, and not only a function of Ar as concluded by Kang et al. (2010). This conclusion completely agrees with Araújo et al. (2012) that dimensionless wall shear stress depends on Eo and M, but with a different scenario, as discussed in section 4.2.

In conclusion, the flow in the liquid film is considerably affected by Eo and $Re_{U_{TB}}$. It should be pointed out that both Eo and $Re_{U_{TB}}$ significantly control the wall shear stress distribution, which in turns control the corrosion process related to two-phase flow, which is known as slug flow-induced corrosion. In the next section, the contribution of these dimensionless groups on the flow in the wake region is discussed.

4.4.2.3 Wake Region

The wake structure is one of the vital hydrodynamic characteristics of slug flow systems, especially in describing the interaction and coalescences between successive Taylor bubbles and in the modelling process (Araújo et al., 2012). Understanding the mechanism by which the wake region is developed is essential prior to introducing the simulation results for flow in the wake region. The annular falling film from the liquid film region plugs into the rear of the Taylor bubble and creates mixing and recirculation zone, which is known by bubble wake. The intensity and size of the recirculation vortices in the wake region depend on the properties of the surrounding liquid, especially its viscosity as indicated by the experimental work of Campos and De Carvalho (1988). As discussed earlier in this chapter, Campos and De Carvalho (1988) conclude three flow patterns for the wake depending on the inverse viscosity number, N_f. In the present study, most of the cases bump into a closed axisymmetric laminar wake.

Stimulated by the work of Morgado et al. (2016), and based on the simulated cases given in Table 4-2, phase diagram of the presence and nature of wake and of the shape of the rear Taylor bubble, are presented in Figure 4-17 and Figure 4-18, respectively. The diagrams are given in terms of Eo and $Re_{U_{TB}}$. Throughout the present study, only two kinds of wake are observed, either closed axisymmetric wake or no wake. For the shape of the rear of the Taylor bubble, when the surface tension is significantly reduced, the gas-liquid interface is easily deformed, and the shape of the Taylor bubble rear becomes unstable. Stable bubble shape is classified into concave, convex, or flat bubbles. However, the unstable bubble wakes are either wavy or breaking up bubbles. Figure 4-18 shows the type of bubble rear shape for all data simulated which strongly corresponds with Kang et al. (2010) and Morgado et al. (2016) which to conclude that the sudden elongation in the bubble tail, based on investigating the effect of Eo on the dynamics of Taylor bubbles, is around unity which corresponds to $Eo > 250$. Referring to cases 21 to 42 in Table 4-2, it is observed that the gas-liquid interface starts to become unstable approximately at $Eo > 200$. Numerical solutions with either wavy or breaking up bubble wakes and cases with small bubble detachment require refined meshes be accurate.

Figure 4-19 illustrates an example of this unstable nature of gas-liquid interface for case 36 in Table 4-2.

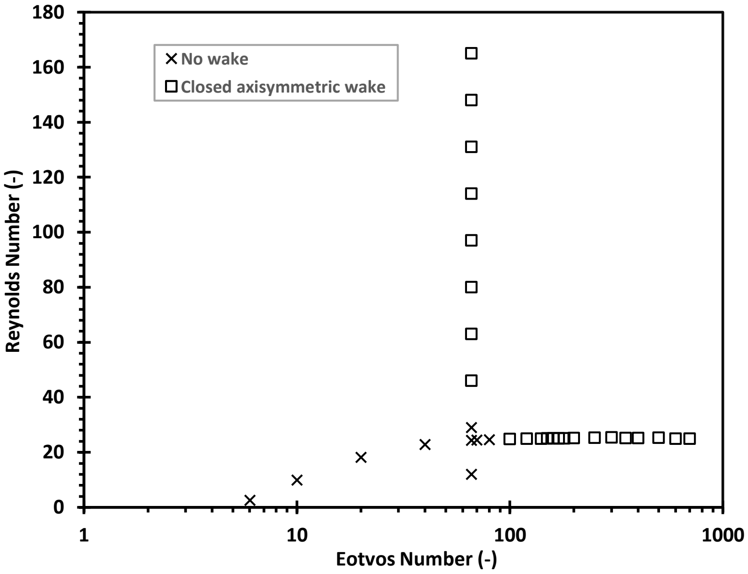

Figure 4-17. Phase diagram of the presence and kind of wake of Taylor bubbles rising through vertical columns of stagnant liquid.

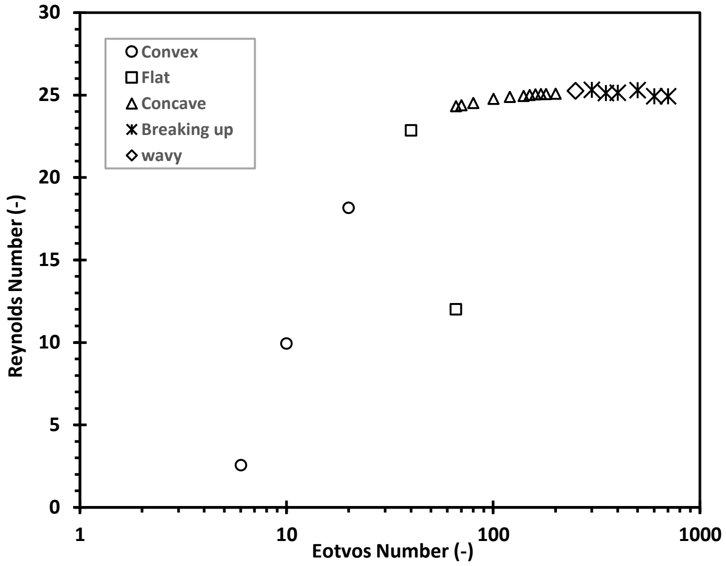

Figure 4-18. Phase diagram of the rear of Taylor bubble shape expressed in terms of Eo *and* $Re_{U_{TB}}$ *of a Taylor bubble rising through vertical columns of stagnant liquid.*

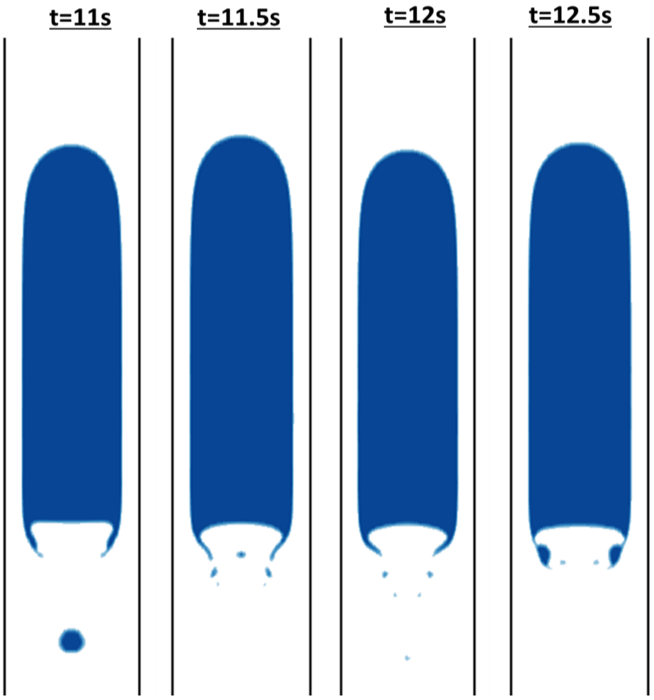

Figure 4-19. Development of wake flow pattern of Taylor bubble rising vertical columns of stagnant liquid for case (36) with a time interval of 0.5s ($Eo = 250$*,* $Re_{U_{TB}} = 25.26$ *and* $Fr_{U_{TB}} = 0.3$*).*

The wake region is investigated by two main parameters, namely dimensionless wake length (L_W/D) and dimensionless wake volume $(\mathcal{v}_W/D^3)$. One of the main correlations used to predict these parameters is that of Campos and De Carvalho (1988), which is given by:

$$\begin{aligned} \frac{L_W}{D} &= 0.30 + 1.22 \times 10^{-3} N_f \;\; for\; 100 < N_f < 500 \\ \frac{\mathcal{v}_W}{D^3} &= 7.5 \times 10^{-4} N_f \; for\; 100 < N_f < 500 \end{aligned} \qquad (4\text{-}42)$$

Recently, Araújo et al. (2012) suggested an equation for the dimensionless wake length (L_W/D) and dimensionless wake volume $(\mathcal{v}_W/D^3)$ function in Eo and M, given by:

$$\begin{aligned} \frac{L_W}{D} &= \frac{1}{4} \times [0.555 - 7.793 \times 10^3 ln\,(M)] \times ln\left(\frac{Eo^3}{M}\right) - 2.133 + 8.046 \times 10^{-2} ln\,(M) \\ \frac{\mathcal{v}_W}{D^3} &= 1.365 \times 10^{-1} \left(\frac{L_W}{D}\right)^2 + 2.176 \times 10^{-1} \left(\frac{L_W}{D}\right) - 2.91910^{-2} \end{aligned} \qquad (4\text{-}43)$$

Following the same procedure of Araújo et al. (2012) for measuring L_W/D, and $\mathcal{v}_W/D^3$, Table 4-2 gives the simulation results for these two parameters for all cases under investigation.

As discussed earlier, the effect of $Re_{U_{TB}}$ on the flow in the wake region is noticed by the change in the shape of the rear the Taylor bubble from flat into convex. In addition, the increase in $Re_{U_{TB}}$ decreases the liquid film thickness, thus squeezing liquid in a narrower region. As a result, the intensity and size of the wake increases, which is noticed by the increment of L_W/D and $\mathcal{v}_W/D^3$, as indicated in Figure 4-20.

Furthermore, a similar scenario is noticed for the increase in $Eo,$ for cases 21 to 42 in Table 4-2, that results in an increase in L_W/D and $\mathcal{v}_W/D^3$ values. It should be pointed out that for cases 36 to 42 in Table 4-2, L_W/D and $\mathcal{v}_W/D^3$ are calculated as average values once the solution is converged, and most of the hydrodynamics characteristics investigated are developed. This is because the developed bubble shape is unstable, which is either wavy or breaking up. A good matching between simulation results for L_W/D and $\mathcal{v}_W/D^3$ and the experimental correlation given by Campos and De Carvalho (1988) is shown in Figure 4-20.

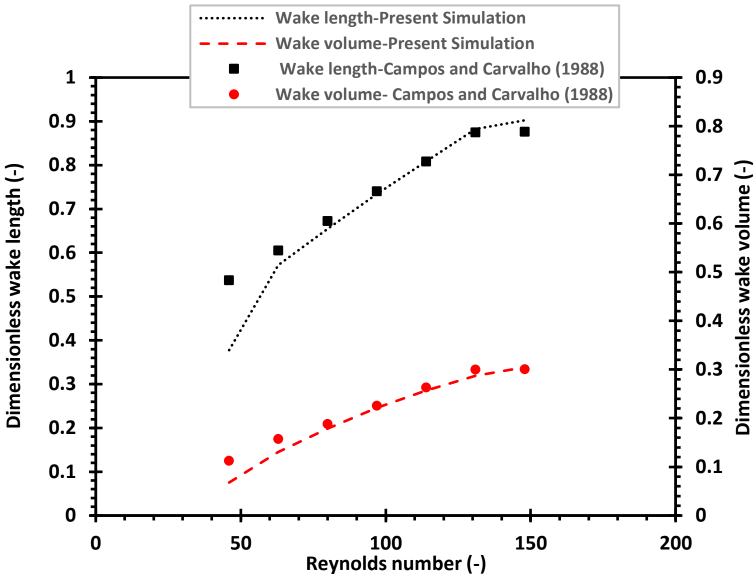

Figure 4-20. Numerical results of dimensionless wake length (L_W/D) *and dimensionless wake volume* $(\mathcal{V}_W/D^3)$ *for cases 13 to 19 in Table 4-2.*

In conclusion, the flow in the wake region is significantly affected by both Eo, and $Re_{U_{TB}}$, which can be clarified by the change in corresponding dimensionless wake length and volume. Additionally, the results reveal that both L_W/D and $\mathcal{V}_W/D^3$ are mainly dependent on Eo and $Re_{U_{TB}}$, which again agrees with the predictions of Kang et al. (2010), and contradicts Araújo et al. (2012) conclusion with a different point of view based on the significance of Reynolds number $(Re_{U_{TB}})$ rather than Morton number (M).

4.5 Concluding Remarks

In this chapter, a complete dimensionless analysis of single Taylor bubble rising through a vertical stagnant Newtonian liquid problem is performed followed by order of magnitude analysis of the equations of motion. The main conclusion is that Froude number $(Fr_{U_{TB}})$, is a function of Eötvös number (Eo), Reynolds number $(Re_{U_{TB}})$, density ratio (Γ_ρ), viscosity ratio (Γ_μ) and L_{TB}/D. The effect of density ratio (Γ_ρ), viscosity ratio (Γ_μ) and the bubble size to the pipe diameter $(L_{TB}/D)_i$ are examined for the sake of supporting other previous experimental and numerical works in the literature.

Based on the dimensionless analysis, the hydrodynamic characteristics of single Taylor bubble rising through a vertical stagnant Newtonian liquid is investigated using the volume-of-fluid (VOF) methodology implemented in the computational fluid dynamics software package, ANSYS Fluent (Release 16.0), with a particular focus on the sole dimensionless parameters, Froude number $(Fr_{U_{TB}})$, Reynolds number $(Re_{U_{TB}})$ and Eötvös number (Eo). The results cover the following, Taylor bubble rise velocity and detailed hydrodynamics including Taylor bubble shape, the liquid film region and the wake region. The numerical results predict the problem effectively as they are validated by testing some of the selective numerical cases against both theoretical and experimental data in the literature.

Based on the numerical results and using guidelines from the order of magnitude analysis, correlation to estimate Taylor bubble rise velocity (U_{TB}) as a function in only Eo and $Re_{U_{TB}}$ is proposed and shows good prediction when compared with other well-known correlations in literature, especially with Viana et al. (2003) correlation.

Detailed Hydrodynamics:

Eo shows a significant effect on all hydrodynamic features of Taylor bubbles. The increment in surface tension increases the curvature of the bubble nose, increases the liquid film thickness, decreases the dimensionless velocity of fully developed falling liquid film, and finally increases wake intensity and size. For the flow in the liquid film, the numerical results are compared with the theoretical predictions given by Brown (1965) and establishing a strong correspondence.

$Re_{U_{TB}}$ shows contribution similar to Eo number. The developed Taylor bubble shape changes from the long slender shape into shorter and flatter bubbles with the increase in $Re_{U_{TB}}$, this results in a reduction in the liquid film thickness.

Additionally, the wall shear stress is examined under the effect of both Eo and $Re_{U_{TB}}$. The increase in $Re_{U_{TB}}$ results in less viscous effect in the liquid surrounding the Taylor bubble that subscribes to decrement in wall shear stress. The wall shear stress increases with Eo, however, it should be pointed out that lower values of Eo possess different distribution for the wall shear stress with noticeable peak value right before the Taylor bubble rear due to the sharp flat and convex shape of the bubble attained at lower values of Eo. Based on the numerical results for wall shear stress, a proposed correlation for maximum wall shear stress is developed and predicts results favourably matching with the theoretical predictions of Brown (1965).

Furthermore, for the wake region, a phase diagram showing the presence and nature of wake, and the shape of the rear Taylor bubble is illustrated. Unstable bubbles are developed at Eo above 200, which are characterised by the presence of small bubbles shedding off from the main Taylor bubble into the wake region.

Last but not least, the proper dimensionless treatment of the problem developed in this chapter enabled to investigate the main hydrodynamics of Taylor bubble correctly in terms of the governing forces. For instance, the numerical result show that the key features of the flow in the liquid film, which are the dimensionless liquid film thickness and velocity are significantly controlled by both dependent on Eo and $Re_{U_{TB}}$. This conclusion contradicts those made by; Kang et al. (2010) -the liquid film thickness is only dependent on Archimedes number ($Ar = N_f{}^2$) and that of Araújo et al. (2012) - the liquid film thickness is a function of N_f and M.

Finally, it can be concluded that the developed numerical results agree well with the order of magnitude analysis. For instance, the order of magnitude analysis has shown that, in order for Reynolds number for the major viscous terms to remain intact, it should be of the order $\left(\frac{L_{TB}}{D}\right)$, which means relatively large values. The numerical result agrees well with that showing the significance of the larger values of Reynolds number on the dynamics of Taylor bubble including bubble shape, terminal velocity, flow in the liquid film and flow in the wake region.

Chapter 5 Theoretical and CFD Treatments of an Individual Taylor Bubble Drifting in an Inclined Pipe ($\gamma \leq 70°$)

The objective of this chapter is to investigate the motion of a single Taylor bubble through a stagnant Newtonian liquid in an inclined pipe by performing a complete dimensionless treatment followed by order of magnitude analysis of the terms of the equations of motion. The main contribution of this analysis is that Froude, Eötvös and Reynolds numbers are the main physical parameters prompting the dimensionless governing equations for inclination angle up to $\gamma = 70°$*. The bubble drift velocity diminishes with inclination angles near the horizontal orientation, and hence a special treatment for these inclination angles is given in chapter 6. To support the developed logical approach of the problem, the present study employs a CFD study to investigate the hydrodynamics of single Taylor bubble drifting through a stagnant liquid in an inclined pipe through using the volume-of-fluid (VOF) methodology implemented in the computational fluid dynamics software package, ANSYS Fluent (Release 16.0). The simulation results show good correspondence with the developed dimensionless treatment of the problem. The main hydrodynamics characteristics, covering the bubble nose front, body and tail regions, are discussed in detail.*

5.1 Introduction

Based on the review done in chapter 2, it can be concluded that there is a lack in the numerical studies on the drift of Taylor bubbles in inclined pipes with stagnant liquid. In addition, there is not yet a study investigating the problem using the order of magnitude analysis of equations of motions. Hence, the aim of this chapter can be divided into two main sections:

1. Performing complete dimensionless analysis of the problem using both the Buckingham-Pi theorem and a dimensionless treatment followed by order of magnitude analysis to the governing equations of motion, showing the main dimensionless groups Re_{v_d}, Fr_{v_d} and Eo with their relative merits of magnitudes.
2. Based on this analysis, the main hydrodynamic features of drifting of Taylor bubbles in inclined pipes with stagnant liquid are investigated by applying computational fluid dynamics (CFD) simulation using the volume-of-fluid (VOF) methodology implemented in the commercial software ANSYS Fluent. These simulations are based on the base model discussed in chapter 3.

This chapter covers inclination range up to $\gamma = 70°$ with respect to the vertical position. The criterion for using this inclination ranges is based on the literature review, where it is concluded that the Taylor bubble flow starts to experience numerical instabilities when the pipe's inclination reaches approximately $70°$. The theoretical treatment of the problem developed in the present study shows that in the neighbourhood of approximately 70°, the flow is mainly governed by the reduced Galilei number and Eötvös number rather than Reynolds and Froude numbers along with Eötvös number. This is the so called near horizontal case is a situation when the inertia and gravity forces are very much reduced. This interns gives rise to the so-called reduced Galilei number that represents the ratio between the decreasing gravity and viscous forces. Further details are given in chapter 6.

This chapter is divided as follows; the dimensionless equations of motion and order of magnitude analysis are given in section 5.2. The CFD model is discussed in section 5.3. This is followed by the results and discussion, given in section 5.4, which is divided into three main parts, including Taylor bubble shape, Taylor bubble rise velocity, detailed hydrodynamics covering the bubble front region, bubble body region and bubble tail region. The chapter ends with a conclusion and discussions section that summarises all the important outcomes of this chapter.

5.2 Dimensionless Analysis

Similar to the vertical pipe case, the problem of drifting of Taylor bubbles in inclined pipes with stagnant liquid can be analysed either using Buckingham-Pi theorem, which is the commonly used method in literature, or using the dimensionless analysis of governing equations. This section discusses both methods and ends up with a conclusion based on the order of magnitude analysis of the dimensionless governing equations.

5.2.1. Buckingham-Pi theorem

Appendix B shows all details of the Buckingham-Pi theorem applied to inclined pipe case with inclination angle up to 70° with respect to the vertical position. With the effect of inclination introduced through the gravitational acceleration (g), the dimensionless analysis of the problem results in the following form:

$$Fr_{v_d} = \frac{{v_d}^2}{gD} = f\left[Eo = \frac{g\rho_L D^2}{\sigma}, Re_{v_d} = \frac{\rho_L v_d D}{\mu_L}, \frac{L_{TB}}{D}\right] \tag{5-1}$$

where the LHS of relation (5-1) represents the ratio between the inertia and gravitational forces, given by Froude number $\left(Fr_{v_d}\right)$. Eötvös number (Eo) is the ratio between gravitational forces and surface tension forces, Reynolds number based on bubble drift velocity $\left(Re_{v_d}\right)$ which is the ratio between the inertial forces and viscous forces and the bubble size to the pipe diameter $\left(\frac{L_{TB}}{D}\right)$.

In most systems, the gas density is always negligible compared to the liquid density, for high-density ratios (above 500). Besides, the literature tests made for smaller density ratios also show a negligible effect on the hydrodynamic characteristics of the Taylor bubble flow (Hayashi et al., 2011). Besides, in Taylor bubble flow, the viscosity of the gas is negligible. Subsequently, the flows inside and outside the bubble are generally independent, due to zero shear stress in the liquid-gas interface for all representative ratios. Moreover, in the literature, it is well known that the velocity of cylindrical bubbles is independent of the Taylor bubble length as long as the bubble is long enough (more than 1.5D$_{\text{pipe}}$) (Nicklin et al., 1962; White and Beardmore, 1962; Zukoski, 1966; Mao and Dukler, 1990; Polonsky et al., 1999). All of these effects are explored in chapter 4 to support other experimental, numerical and theoretical work concluding that density ratio (Γ_ρ), viscosity ratio (Γ_μ), and bubble size to the pipe diameter $\left(\frac{L_{TB}}{D}\right)$ have a negligible effect of the dynamics of Taylor bubbles. Hence, the analysis given in Appendix B assumes that the effects of these dimensionless groups are negligible. Thus, the Buckingham-Pi theorem shows that the problem of drifting of Taylor bubbles in inclined pipes with stagnant liquid is mainly governed by three main dimensionless groups, Reynolds number $\left(Re_{v_d}\right)$, Froude number based on bubble drift velocity $\left(Fr_{v_d}\right)$, and Eötvös number (Eo) with the effect of inclination given through the gravitational acceleration term (g).

5.2.2. Dimensionless Governing Equations

As indicated in section 3.4.2 in chapter 3, for inclined pipes, the assumption of flow being axisymmetric can no longer be applied. The axial symmetry of the vertical pipe configuration is lost as the pipe is inclined. The governing equations of the problem are the continuity and momentum equations expressed in Cartesian coordinates. Figure 5-1 shows the inclined pipe configuration and the coordinate system used.

The Navier-stokes equations in cartesian coordinates are:

$$\rho_L\left(\frac{\partial u}{\partial t}+u\frac{\partial u}{\partial x}+v\frac{\partial u}{\partial y}+w\frac{\partial u}{\partial z}\right)=\rho_L g_x-\frac{\partial p}{\partial x}+\mu_L\left[\frac{\partial^2 u}{\partial x^2}+\frac{\partial^2 u}{\partial y^2}+\frac{\partial^2 u}{\partial z^2}\right] \tag{5-2}$$

$$\rho_L\left(\frac{\partial v}{\partial t}+u\frac{\partial v}{\partial x}+v\frac{\partial v}{\partial y}+w\frac{\partial v}{\partial z}\right)=\rho_L g_y-\frac{\partial p}{\partial y}+\mu_L\left[\frac{\partial^2 v}{\partial x^2}+\frac{\partial^2 v}{\partial y^2}+\frac{\partial^2 v}{\partial z^2}\right] \tag{5-3}$$

$$\rho_L\left(\frac{\partial w}{\partial t}+u\frac{\partial w}{\partial x}+v\frac{\partial w}{\partial y}+w\frac{\partial w}{\partial z}\right)=\rho_L g_z-\frac{\partial p}{\partial z}+\mu_L\left[\frac{\partial^2 w}{\partial x^2}+\frac{\partial^2 w}{\partial y^2}+\frac{\partial^2 w}{\partial z^2}\right] \tag{5-4}$$

And the continuity equation is:

$$\frac{\partial u}{\partial x}+\frac{\partial v}{\partial y}+\frac{\partial w}{\partial z}=0 \tag{5-5}$$

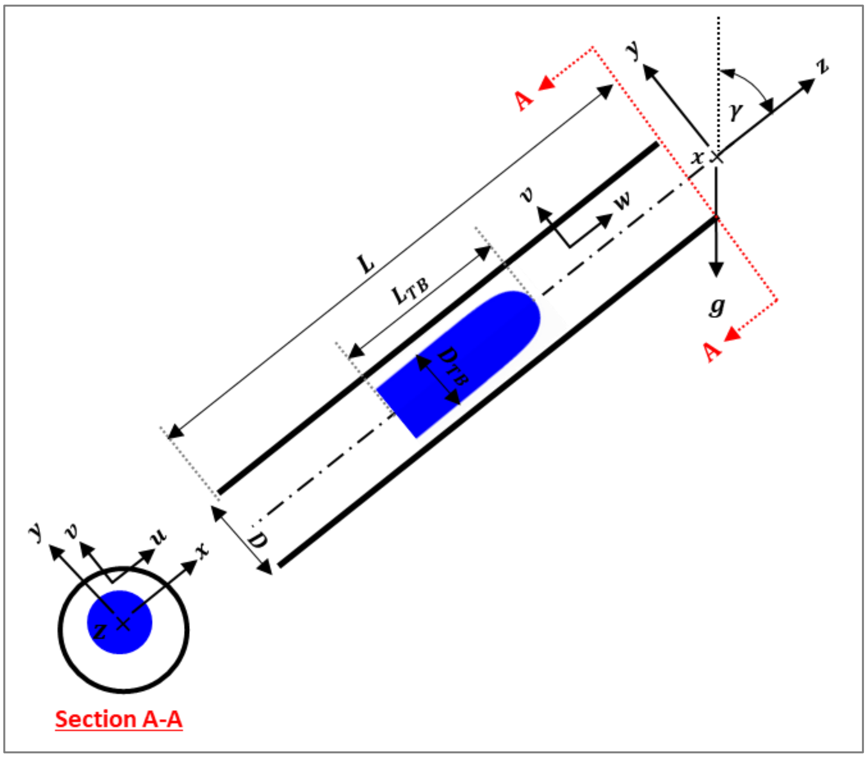

Figure 5-1. The inclined pipe configuration and the coordinate system used.

Introducing the following dimensionless variables, with characteristic drift velocity (v_d):

$$u^* = \frac{u}{v_d}, v^* = \frac{v}{v_d}, w^* = \frac{w}{v_d}, p^* = \frac{p}{\frac{1}{2}\rho_L {v_d}^2} \qquad (5\text{-}6)$$

The independent variables are:

$$x^* = \frac{x}{(D/2)}, y^* = \frac{y}{(D/2)}, z^* = \frac{z}{L_{TB}}, t^* = t\left(\frac{v_d}{L_{TB}}\right), {g_x}^* = \frac{g_x}{g}, {g_y}^* = \frac{g_y}{g}, {g_z}^* = \frac{g_z}{g},$$

$$\sigma_x{}^* = \frac{\sigma_x}{\sigma}, \sigma_y^* = \frac{\sigma_y}{\sigma}, \sigma_z^* = \frac{\sigma_z}{\sigma}, K^* = \frac{K}{(1/D^2)} \qquad (5\text{-}7)$$

Substituting the dimensionless variables given in (5-6) and (5-7) into the momentum equation given in (5-2) would lead to:

$$\begin{aligned}\rho_L\left(\left(\frac{{v_d}^2}{L_{TB}}\right)\frac{\partial u^*}{\partial t^*}+\left(\frac{2{v_d}^2}{D}\right)u^*\frac{\partial u^*}{\partial x^*}+\left(\frac{2{v_d}^2}{D}\right)v^*\frac{\partial u^*}{\partial y^*}+\left(\frac{{v_d}^2}{L_{TB}}\right)w^*\frac{\partial u^*}{\partial z^*}\right)\\ =\rho_L g {g_x}^*-\left(\frac{\rho_L {v_d}^2}{D}\right)\frac{\partial p^*}{\partial x^*}+\mu_L v_d\left(\frac{2}{D}\right)^2\left[\frac{\partial^2 u^*}{\partial x^{*2}}+\frac{\partial^2 u^*}{\partial y^{*2}}+\left(\frac{D}{2L_{TB}}\right)^2\frac{\partial^2 u^*}{\partial z^{*2}}\right]\end{aligned} \tag{5-8}$$

Dividing equation (5-8) by $\left(\frac{\rho_L L_{TB}}{{v_d}^2}\right)$ and multiplying by $\left(\frac{D}{L_{TB}}\right)$ would give the following:

$$\begin{aligned}\left(\frac{D}{L_{TB}}\right)\frac{\partial u^*}{\partial t^*}+2u^*\frac{\partial u^*}{\partial x^*}+2v^*\frac{\partial u^*}{\partial y^*}+\left(\frac{D}{L_{TB}}\right)w^*\frac{\partial u^*}{\partial z^*}\\ =\frac{{g_x}^*}{Fr_{v_d}^2}-\frac{\partial p^*}{\partial x^*}+\frac{1}{Re_{v_d}}\left[4\frac{\partial^2 u^*}{\partial x^{*2}}+4\frac{\partial^2 u^*}{\partial y^{*2}}+\left(\frac{D}{L_{TB}}\right)^2\frac{\partial^2 u^*}{\partial z^{*2}}\right]\end{aligned} \tag{5-9}$$

Applying the same steps to equation (5-3) would result in the following:

$$\begin{aligned}\left(\frac{D}{L_{TB}}\right)\frac{\partial v^*}{\partial t^*}+2u^*\frac{\partial v^*}{\partial x^*}+2v^*\frac{\partial v^*}{\partial y^*}+\left(\frac{D}{L_{TB}}\right)w^*\frac{\partial v^*}{\partial z^*}\\ =\frac{{g_y}^*}{Fr_{v_d}^2}-\frac{\partial p^*}{\partial y^*}+\frac{1}{Re_{v_d}}\left[4\frac{\partial^2 v^*}{\partial x^{*2}}+4\frac{\partial^2 v^*}{\partial y^{*2}}+\left(\frac{D}{L_{TB}}\right)^2\frac{\partial^2 v^*}{\partial z^{*2}}\right]\end{aligned} \tag{5-10}$$

Similarly, equation (5-4) would result in the following:

$$\begin{aligned}\left(\frac{D}{L_{TB}}\right)\frac{\partial w^*}{\partial t^*}+2u^*\frac{\partial w^*}{\partial x^*}+2v^*\frac{\partial w^*}{\partial y^*}+\left(\frac{D}{L_{TB}}\right)w^*\frac{\partial w^*}{\partial z^*}\\ =\frac{{g_z}^*}{Fr_{v_d}^2}-\frac{\partial p^*}{\partial z^*}+\frac{1}{Re_{v_d}}\left[4\frac{\partial^2 w^*}{\partial x^{*2}}+4\frac{\partial^2 w^*}{\partial y^{*2}}+\left(\frac{D}{L_{TB}}\right)^2\frac{\partial^2 w^*}{\partial z^{*2}}\right]\end{aligned} \tag{5-11}$$

Additionally, the dimensionless form of the continuity equation can be written as:

$$\frac{\partial u^*}{\partial x^*}+\frac{\partial v^*}{\partial y^*}+\left(\frac{D}{2L_{TB}}\right)\frac{\partial w^*}{\partial z^*}=0 \tag{5-12}$$

On the gas-liquid interface, $u = v = 0$. Hence, the following conditions are applied:

$$0=\rho_L g_x-\frac{\partial p}{\partial x}+\mu_L\left[\frac{\partial^2 u}{\partial\, x^2}+\frac{\partial^2 u}{\partial y^2}+\frac{\partial^2 u}{\partial z^2}\right]+K\sigma_x \tag{5-13}$$

$$0=\rho_L g_y-\frac{\partial p}{\partial y}+\mu_L\left[\frac{\partial^2 v}{\partial x^2}+\frac{\partial^2 v}{\partial y^2}+\frac{\partial^2 v}{\partial z^2}\right]+K\sigma_y \qquad (5\text{-}14)$$

$$\rho_L\left(\frac{\partial w}{\partial t}+w\frac{\partial w}{\partial z}\right)=\rho_L g_z-\frac{\partial p}{\partial z}+\mu_L\left[\frac{\partial^2 w}{\partial x^2}+\frac{\partial^2 w}{\partial y^2}+\frac{\partial^2 w}{\partial z^2}\right]+K\sigma_z \qquad (5\text{-}15)$$

Using the dimensionless variables given in (5-6) and (5-7), equations (5-13) to (5-15) in dimensionless form may be written as:

$$0=\frac{1}{Fr_{v_d}^2}g_x{}^*-\frac{\partial p^*}{\partial x^*}+\frac{1}{Re_{v_d}}\left[4\frac{\partial^2 u^*}{\partial x^{*2}}+4\frac{\partial^2 u^*}{\partial y^{*2}}+\left(\frac{D}{L_{TB}}\right)^2\frac{\partial^2 u^*}{\partial z^{*2}}\right]+\frac{1}{Fr_{v_d}^2 Eo}\sigma_x{}^*K^* \qquad (5\text{-}16)$$

$$0=\frac{1}{Fr_{v_d}^2}g_y{}^*-\frac{\partial p^*}{\partial y^*}+\frac{1}{Re_{v_d}}\left[4\frac{\partial^2 v^*}{\partial x^{*2}}+4\frac{\partial^2 v^*}{\partial y^{*2}}+\left(\frac{D}{L_{TB}}\right)^2\frac{\partial^2 v^*}{\partial z^{*2}}\right]+\frac{1}{Fr_{v_d}^2 Eo}\sigma_y{}^*K^* \qquad (5\text{-}17)$$

$$\begin{aligned}\left(\frac{D}{L_{TB}}\right)\left(\frac{\partial w^*}{\partial t^*}+w^*\frac{\partial w^*}{\partial z^*}\right)&\\&=\frac{1}{Fr_{v_d}^2}g_z{}^*-\left(\frac{D}{L_{TB}}\right)\frac{\partial p^*}{\partial z^*}+\frac{1}{Re_{v_d}}\left[4\frac{\partial^2 w^*}{\partial x^{*2}}+4\frac{\partial^2 w^*}{\partial y^{*2}}+\left(\frac{D}{L_{TB}}\right)^2\frac{\partial^2 w^*}{\partial z^{*2}}\right]\\&+\frac{1}{Fr_{v_d}^2 Eo}\sigma_z{}^*K^*\end{aligned} \qquad (5\text{-}18)$$

To perform an order of magnitude analysis to the dimensionless governing equations, the following orders are introduced:

$$\begin{aligned}&x^*=o(1), y^*=o(1), z^*=o(1), w^*=o(1), t^*=o(1), g_x{}^*=o\left(\frac{D}{L_{TB}}\right)\\&g_y{}^*=o\left(\frac{D}{L_{TB}}\right),\ g_z{}^*=o(1),\ K^*=o(1),\ \sigma_x^*=o(1),\ \sigma_y^*=o(1),\ \sigma_z^*=o(1)\end{aligned} \qquad (5\text{-}19)$$

Introducing the orders given in (5-19) to the continuity equation (equation (5-12)) would lead to the following:

$$\frac{\overbrace{\partial u^*}^{o\left(\frac{D}{L_{TB}}\right)}}{\underbrace{\partial x^*}_{o(1)}}+\frac{\overbrace{\partial v^*}^{o\left(\frac{D}{L_{TB}}\right)}}{\underbrace{\partial y^*}_{o(1)}}+\left(\frac{D}{2L_{TB}}\right)\frac{\overbrace{\partial w^*}^{o(1)}}{\underbrace{\partial z^*}_{o(1)}}=0 \qquad (5\text{-}20)$$

Thus, in order to keep the continuity equation intact, u^* and v^* should be of the order $o\left(\frac{D}{L_{TB}}\right)$.

Similarly, performing order of magnitude analysis to equation (5-9) would lead to the following:

$$\begin{gathered}
\left(\frac{D}{L_{TB}}\right)\frac{\overbrace{\partial u^*}^{o\left(\frac{D}{L_{TB}}\right)}}{\underbrace{\partial t^*}_{o(1)}} + 2\,\overbrace{u^*}^{o\left(\frac{D}{L_{TB}}\right)}\frac{\overbrace{\partial u^*}^{o\left(\frac{D}{L_{TB}}\right)}}{\underbrace{\partial x^*}_{o(1)}} + 2\,\overbrace{v^*}^{o\left(\frac{D}{L_{TB}}\right)}\frac{\overbrace{\partial u^*}^{o\left(\frac{D}{L_{TB}}\right)}}{\underbrace{\partial y^*}_{o(1)}} + \left(\frac{D}{L_{TB}}\right)\overbrace{w^*}^{o(1)}\frac{\overbrace{\partial u^*}^{o\left(\frac{D}{L_{TB}}\right)}}{\underbrace{\partial z^*}_{o(1)}} \\
= \frac{\overbrace{g_x{}^*}^{o\left(\frac{D}{L_{TB}}\right)}}{\underbrace{Fr_{v_d}^2}_{o(1)}} - \frac{\partial p^*}{\partial x^*} + \frac{1}{\underbrace{Re_{v_d}}_{o\left(\frac{L_{TB}}{D}\right)}}\left[4\frac{\overbrace{\partial^2 u^*}^{o\left(\frac{D}{L_{TB}}\right)}}{\underbrace{\partial x^{*2}}_{o(1)}} + 4\frac{\overbrace{\partial^2 u^*}^{o\left(\frac{D}{L_{TB}}\right)}}{\underbrace{\partial y^{*2}}_{o(1)}} + \cancel{\underbrace{\left(\frac{D}{L_{TB}}\right)^2}_{o\left(\frac{D}{L_{TB}}\right)^3}\frac{\overbrace{\partial^2 u^*}^{o\left(\frac{D}{L_{TB}}\right)}}{\underbrace{\partial z^{*2}}_{o(1)}}}\right]
\end{gathered} \tag{5-21}$$

Hence, in order to keep the inertia terms and the viscous terms in equation (5-21) of the same order of magnitude, Fr_{v_d} should be of the order $o(1)$ and Re_{v_d} should be of the order $o\left(\frac{L_{TB}}{D}\right)$.

Applying the same analysis to the momentum equation in the y^* direction (equation (5-10)) and z^* direction (equation (5-11)) will give the following:

$$\begin{gathered}
\left(\frac{D}{L_{TB}}\right)\frac{\overbrace{\partial v^*}^{o\left(\frac{D}{L_{TB}}\right)}}{\underbrace{\partial t^*}_{o(1)}} + 2\,\overbrace{u^*}^{o\left(\frac{D}{L_{TB}}\right)}\frac{\overbrace{\partial v^*}^{o\left(\frac{D}{L_{TB}}\right)}}{\underbrace{\partial x^*}_{o(1)}} + 2\,\overbrace{v^*}^{o\left(\frac{D}{L_{TB}}\right)}\frac{\overbrace{\partial v^*}^{o\left(\frac{D}{L_{TB}}\right)}}{\underbrace{\partial y^*}_{o(1)}} + \left(\frac{D}{L_{TB}}\right)\overbrace{w^*}^{o(1)}\frac{\overbrace{\partial v^*}^{o\left(\frac{D}{L_{TB}}\right)}}{\underbrace{\partial z^*}_{o(1)}} \\
= \frac{\overbrace{g_y{}^*}^{o\left(\frac{D}{L_{TB}}\right)}}{\underbrace{Fr_{v_d}^2}_{o(1)}} - \frac{\partial p^*}{\partial y^*} + \frac{1}{\underbrace{Re_{v_d}}_{o\left(\frac{L_{TB}}{D}\right)}}\left[4\frac{\overbrace{\partial^2 v^*}^{o\left(\frac{D}{L_{TB}}\right)}}{\underbrace{\partial x^{*2}}_{o(1)}} + 4\frac{\overbrace{\partial^2 v^*}^{o\left(\frac{D}{L_{TB}}\right)}}{\underbrace{\partial y^{*2}}_{o(1)}} + \cancel{\left(\frac{D}{L_{TB}}\right)^2\frac{\overbrace{\partial^2 v^*}^{o\left(\frac{D}{L_{TB}}\right)}}{\underbrace{\partial z^{*2}}_{o(1)}}}\right] \quad o\left(\frac{D}{L_{TB}}\right)^3
\end{gathered} \tag{5-22}$$

$$\begin{gathered}
\left(\frac{D}{L_{TB}}\right)\frac{\overbrace{\partial w^*}^{o(1)}}{\underbrace{\partial t^*}_{o(1)}} + 2\,\overbrace{u^*}^{o\left(\frac{D}{L_{TB}}\right)}\frac{\overbrace{\partial w^*}^{o(1)}}{\underbrace{\partial x^*}_{o(1)}} + 2\,\overbrace{v^*}^{o\left(\frac{D}{L_{TB}}\right)}\frac{\overbrace{\partial w^*}^{o(1)}}{\underbrace{\partial y^*}_{o(1)}} + \left(\frac{D}{L_{TB}}\right)\overbrace{w^*}^{o(1)}\frac{\overbrace{\partial w^*}^{o(1)}}{\underbrace{\partial z^*}_{o(1)}} \\
= \frac{\overbrace{g_z{}^*}^{o(1)}}{\underbrace{Fr_{v_d}^2}_{o(1)}} - \frac{\partial p^*}{\partial z^*} + \frac{1}{\underbrace{Re_{v_d}}_{o\left(\frac{L_{TB}}{D}\right)}}\left[4\frac{\overbrace{\partial^2 w^*}^{o(1)}}{\underbrace{\partial x^{*2}}_{o(1)}} + 4\frac{\overbrace{\partial^2 w^*}^{o(1)}}{\underbrace{\partial y^{*2}}_{o(1)}} + \cancel{\left(\frac{D}{L_{TB}}\right)^2\frac{\overbrace{\partial^2 w^*}^{o(1)}}{\underbrace{\partial z^{*2}}_{o(1)}}}\right] \quad o\left(\frac{D}{L_{TB}}\right)^2
\end{gathered} \tag{5-23}$$

Applying the same analysis to the boundaries (equations (5-16) to (5-18)) would give the following:

$$0=\frac{\overbrace{g_x^{*}}^{o\left(\frac{D}{L_{TB}}\right)}}{\underbrace{Fr_{v_d}^2}_{o(1)}}-\frac{\partial p^*}{\partial x^*}+\frac{1}{\underbrace{Re_{v_d}}_{o\left(\frac{L_{TB}}{D}\right)}}\left[4\frac{\overbrace{\partial^2 u^*}^{o\left(\frac{D}{L_{TB}}\right)}}{\underbrace{\partial x^{*2}}_{o(1)}}+4\frac{\overbrace{\partial^2 u^*}^{o\left(\frac{D}{L_{TB}}\right)}}{\underbrace{\partial y^{*2}}_{o(1)}}+\left(\frac{D}{L_{TB}}\right)^2\frac{\overbrace{\partial^2 u^*}^{o\left(\frac{D}{L_{TB}}\right)}}{\underbrace{\partial z^{*2}}_{o(1)}}\right]+\frac{1}{\underbrace{Fr_{v_d}^2}_{o(1)}\;\underbrace{Eo}_{o\left(\frac{L_{TB}}{D}\right)}}\underbrace{\sigma_x^{*}}_{o(1)}\;\underbrace{K^*}_{o(1)} \tag{5-24}$$

$$0=\frac{\overbrace{g_y^{*}}^{o\left(\frac{D}{L_{TB}}\right)}}{\underbrace{Fr_{v_d}^2}_{o(1)}}-\frac{\partial p^*}{\partial y^*}+\frac{1}{\underbrace{Re_{v_d}}_{o\left(\frac{L_{TB}}{D}\right)}}\left[4\frac{\overbrace{\partial^2 v^*}^{o\left(\frac{D}{L_{TB}}\right)}}{\underbrace{\partial x^{*2}}_{o(1)}}+\underset{o\left(\frac{D}{L_{TB}}\right)^2}{\cancel{4\frac{\overbrace{\partial^2 v^*}^{o\left(\frac{D}{L_{TB}}\right)}}{\underbrace{\partial y^{*2}}_{o(1)}}}}+\left(\frac{D}{L_{TB}}\right)^2\frac{\overbrace{\partial^2 v^*}^{o\left(\frac{D}{L_{TB}}\right)}}{\underbrace{\partial z^{*2}}_{o(1)}}\right]\overset{o\left(\frac{D}{L_{TB}}\right)^3}{\cancel{\frac{1}{\underbrace{Fr_{v_d}^2}_{o(1)}\;\underbrace{Eo}_{o\left(\frac{L_{TB}}{D}\right)}}\underbrace{\sigma_y^{*}}_{o(1)}\;\underbrace{K^*}_{o(1)}}} \tag{5-25}$$

$$\begin{aligned}\left(\frac{D}{L_{TB}}\right)\frac{\overbrace{\partial w^*}^{o(1)}}{\underbrace{\partial t^*}_{o(1)}}+\left(\frac{D}{L_{TB}}\right)\overbrace{w^*}^{o(1)}\frac{\overbrace{\partial w^*}^{o(1)}}{\underbrace{\partial z^*}_{o(1)}}&=\frac{\overbrace{g_z^{*}}^{o(1)}}{\underbrace{Fr_{v_d}^2}_{o(1)}}-\frac{\partial p^*}{\partial z^*}\\&+\frac{1}{\underbrace{Re_{v_d}}_{o\left(\frac{L_{TB}}{D}\right)}}\left[4\frac{\overbrace{\partial^2 w^*}^{o(1)}}{\underbrace{\partial x^{*2}}_{o(1)}}+4\frac{\overbrace{\partial^2 w^*}^{o(1)}}{\underbrace{\partial y^{*2}}_{o(1)}}+\left(\frac{D}{L_{TB}}\right)^2\frac{\overbrace{\partial^2 w^*}^{o(1)}}{\underbrace{\partial z^{*2}}_{o(1)}}\right]+\overset{o\left(\frac{D}{L_{TB}}\right)^3}{\cancel{\frac{1}{\underbrace{Fr_{v_d}^2}_{o(1)}\;\underbrace{Eo}_{o\left(\frac{L_{TB}}{D}\right)}}\underbrace{\sigma_y^{*}}_{o(1)}\;\underbrace{K^*}_{o(1)}}}\end{aligned} \tag{5-26}$$

Hence, it is concluded from the order of magnitude analysis applied to the gas-liquid interface that Eötvös number (Eo) should be of order $o\left(\frac{L_{TB}}{D}\right)$ and Fr_{v_d} should be of order $o(1)$ to keep the surface tension force of the same order of magnitude of the inertia force.

To sum up, based on the dimensionless analysis of the equations of motions followed by order of magnitude analysis in all directions and on the boundaries, the following conclusions are drawn:

1. The velocity components in x and y directions should be of the order $\left(\frac{D}{L_{TB}}\right)$ to keep the continuity equation intact without any approximation;
2. For all terms in the momentum equations and on the boundaries to remain of the same order of magnitude, Fr_{v_d} should be of the order $o(1)$ and Re_{v_d} and Eo both should be of the order $\left(\frac{L_{TB}}{D}\right)$.

In conclusion, the dimensionless analysis based on both methods discussed, Buckingham-Pi theorem and the dimensionless analysis of governing equations, show that the problem of drifting of Taylor bubbles in inclined pipes with stagnant liquid is mainly governed by three dimensionless groups $\left(Fr_{v_d}, Eo \text{ and } Re_{v_d}\right)$ with the effect of inclination given through the gravitational acceleration components $\left(g_x, g_y \text{ and } g_z\right)$. Additionally, the inclined pipe case analysis shows a similar analysis to the vertical case with almost the same order of magnitude analysis. In addition, it is worth to mention that there is still no need to using a dimensionless number like Morton number in the analysis of the inclined pipe case, as done on the vertical one in chapter 4, which does not seem to have a direct physical meaning.

Thus, based on this analysis, the main hydrodynamic features of drifting of Taylor bubbles in inclined pipes with stagnant liquid are investigated in terms of three main dimensionless groups, namely Eötvös number (Eo), Froude number $\left(Fr_{v_d}\right)$ and Reynolds number based on bubble drift velocity (Re_{v_d}). In this chapter, based on the simulation cases given in chapter 4, selected cases are chosen to explore the effect of these main influencing parameters. The pipe inclination covers the range of $0 < \gamma \leq 70°$, however, for the near horizontal inclination range ($70° < \gamma \leq 90°$) a separate analysis is given in chapter 6.

5.3 CFD Model Development

In section 3.4.2 in chapter 3, the 3D model are discussed in detail, however, in this section, essential detail about the boundary conditions and the reference frame are discussed. Once the pipe is inclined with respect to the vertical position, the assumption of flow being axisymmetric can no longer be applied. According to Mazza et al. (2010), the flow can be simplified as a plane of symmetry that crosses the pipe's diameter line with a normal orthogonal to the gravity acceleration.

Similar to the vertical case, the simulation are performed for unsteady flow with constant fluid properties. The two phases are assumed as incompressible, viscous, immiscible, and not penetrating each other. The simulation cases for inclined cases is based on the cases performed in chapter 4 to ensure laminar flow regime, and avoid getting into transition or turbulent flow regimes.

5.3.1 Model Geometry

Referring to Figure 3-15 in chapter 3, the solution domain is a cylindrical domain with a diameter (D) and length (L) and the inclination of the pipe is configured by setting the angle (γ) between the pipe's axis and the gravity vector with respect to the vertical case. The length of the computational domain is kept 10D similar to the base model to ensure the solution is affected by neither the bottom nor the top of the pipe. However, all simulations for the inclined pipe cases are done using fixed reference frames (FRF) system, and further detail are given in the following section. Details about the computational domain for the inclined pipe configuration and the initial bubble shape are discussed in chapter 3.

5.3.2 Fixed Reference Frame Technique

In chapter 4, different types of reference frame system the fixed reference frames (FRF) and the moving reference frames (MRF), are discussed. In the vertical pipe case, the moving reference frame (MRF) is selected based on the reasonable computational time compared against the fixed reference frame. In MRF, the Taylor bubble is stationary, and the pipe wall moves downwards with a velocity equal to that of the bubble. The simulation is considerably based on a trial and error procedure, where the wall velocity is initially assigned with an initial value, based on correlations in literature, it is regularly updated until the bubble ceases moving up or down in the axial direction, and hence the pseudo-steady solution is reached. At that stage, the wall velocity is adjusted and set to be the terminal velocity. The situation is quite different in the inclined pipe case. The model is 3D and larger computational time is essential to establish both stable developed bubble shape and a converged terminal bubble drift velocity. Enabling MRF in inclined pipe simulation would rather increase the computational time significantly. Hence, all simulation cases for the inclined pipe are performed using FRF.

5.3.3 Initial and Boundary Conditions

The boundary conditions are discussed in detail in chapter 3. However, for the initial conditions, the initial ratio of the Taylor bubble length to pipe diameter $(L_{TB}/D)_i$ is an input parameter prior to simulation. In contrast to the base model, $(L_{TB}/D)_i$ is fixed to 2 in inclined pipe simulations. In FRF, larger domains may be essential for Taylor bubble to reach their terminal velocity and hence reach its steady state. Thus, to avoid this, a smaller initial Taylor bubble length is selected. As discussed earlier in this chapter, the velocity of cylindrical bubbles is independent of the Taylor bubble length as long as the bubble is long enough (more than $1.5D_{pipe}$). Thus, using rather a shorter initial Taylor bubble length would have no effect on the terminal bubble drift velocity.

Moreover, it should be pointed out that different Taylor bubble shapes, sizes and locations are tested, and they give the same solution. The only difference is in the convergence process. However, the selected Taylor bubble initial shape and location shows a well-converged solution.

A test is done to investigate the effect of the distance from the pipe bottom, given by h_B. One of the validation cases introduced in chapter 3 is taken as a reference here with three different values of h_B, which are 1,1.5D and $2D_{pipe}$. Table 5-1 shows that the three different distance h_B almost give similar values of Froude number (Fr_{v_d}). Based on that, the distance h_B is fixed to $1.5D_{pipe}$ in all simulations performed in this chapter.

Lastly, in all simulations, the initial shape is simulated while tracking the bubble velocity until a steady terminal developed bubble shape with a converged terminal constant bubble drift velocity (v_d) is reached.

Table 5-1. Study of the influence of the distance h_B for the experimental case of Shosho and Ryan (2001), with air and 60% Corn syrup solution and inclination angle 60°, on terminal Froude number (Fr_{v_d}).

Angle	h_B	Fr_{v_d}	**|Error |** (%)
60°	1D	0.35775	--
	1.5D	0.35758	0.046
	2D	0.35753	0.015

5.4 Results and Discussions

In this section, the results that cover the main goals of this chapter are discussed, which is investigating the main hydrodynamic features of the drift of a single Taylor bubble in an inclined pipe with stagnant liquid. The results are explored with a specific focus on the effect of the governing dimensionless groups, Froude, Eötvös and Reynolds numbers. The results are divided into three sections Taylor bubble shape and flow field characteristics, Taylor bubble drift velocity, and detailed hydrodynamics covering the three main regions of the Taylor bubbles in inclined pipes (bubble front region, bubble body region and bubble tail region).

Table 5-2 lists the simulation cases and their corresponding results. The selected cases are based on those simulated in chapter 4. For instance, to explore the effect of Reynolds number (Re_{v_d}) three cases are selected covering low, intermediate and high values of Reynolds numbers based on vertical simulated cases (cases 1 to 3 in Table 5-2). For Eötvös number (Eo), three cases are selected with values of 20, 66 and 150 (cases 4 to 6 in Table 5-2). In Table 5-2, the input parameters prior simulation are Eo, $(L_{TB}/D)_i$, while the predicted values from the simulation is Re_{v_d}. Other significant predicted parameters are explored in detail in section 5.4.3. For all cases in Table 5-2, the pipe is inclined from the vertical position covering a range of $0 \leq \gamma \leq 70°$. This gives a total number of 36 cases. The vertical pipe cases are simulated using FRF for the sake of making a comprehensive comparison between the vertical and inclined pipe.

Table 5-2. Simulation cases and their corresponding results.

Input Parameters			Predicted Values
Case No.	Eo	$\left(\frac{L_{TB}}{D}\right)_i$	Re_{v_d}
Effect of Reynolds number (Revd)			
1	66	2	15
2	66	2	95
3	66	2	200
Effect of Eötvös number (Eo)			
4	20	2	25
5	40	2	25
6	66	2	25

Based on the dimensionless analysis of the problem given in section 5.2, the results focus on investigating the dynamics of Taylor bubble in inclined pipes in terms of the sole dimensionless parameters Reynolds number and Eötvös number. Hence, the problem can now be treated in terms of three main dimensionless groups, given by:

$$Fr_{v_d} = \frac{v_d{}^2}{gD} = f\left[Eo \ = \frac{g\rho_L D^2}{\sigma}, Re_{v_d} = \frac{\rho_L U_{TB} D}{\mu_L}\ \right] \tag{5-27}$$

5.4.1 Taylor Bubble Shape and Flow Field Characteristics

In this section, the effect of the main physical parameters influencing the motion of Taylor bubbles is discussed on the dynamics of Taylor bubbles, including the Taylor bubble shape and flow field characteristics. This includes representing the three-dimensional Taylor bubble shape, the pressure field, the streamlines and vorticity field for each of the dimensionless groups examined for the cases given in Table 5-2. The pipe inclination covers the following angles 0°,15°,30°, 45°, 60° and 70°, Eötvös number has values of 20, 40 and 66 and Reynolds number has average values of 15, 25, 95 and 200.

5.4.1.1 Effect of Inclination Angle

To explore the effect of inclination angle on the terminal Taylor bubble shape as well as exploring further details about the streamlines and vorticity field, a selected case of the following parameters $Eo = 66$ and $Re_{v_d} \cong 15$ (case 1 in Table 5-2), is presented. It can be noted from Figure 5-2 that the developed Taylor bubble length increases with the inclination angle. For each inclination angle, the developed bubble length is divided into three sections (section A-A to section C-C). For each section, the streamlines and vorticity field (Y-component) in the xy plane are presented in Figure 5-2. The vorticity slightly increases with the inclination angle. Through considering the highest section (section A-A), the flow shows similar configurations for all inclination angles. Nonetheless, the instability of the bubble rear is shown by the disturbed flow as demonstrates in section C-C, where secondary vortices appear at the perimeter of the pipe in almost all inclination angles.

Moreover, Figure 5-3 shows the pressure field for all inclination angle. For all cases, the pressure isosurfaces are being almost perpendicular to the gravity vector, with nearly the same variation in pressure values.

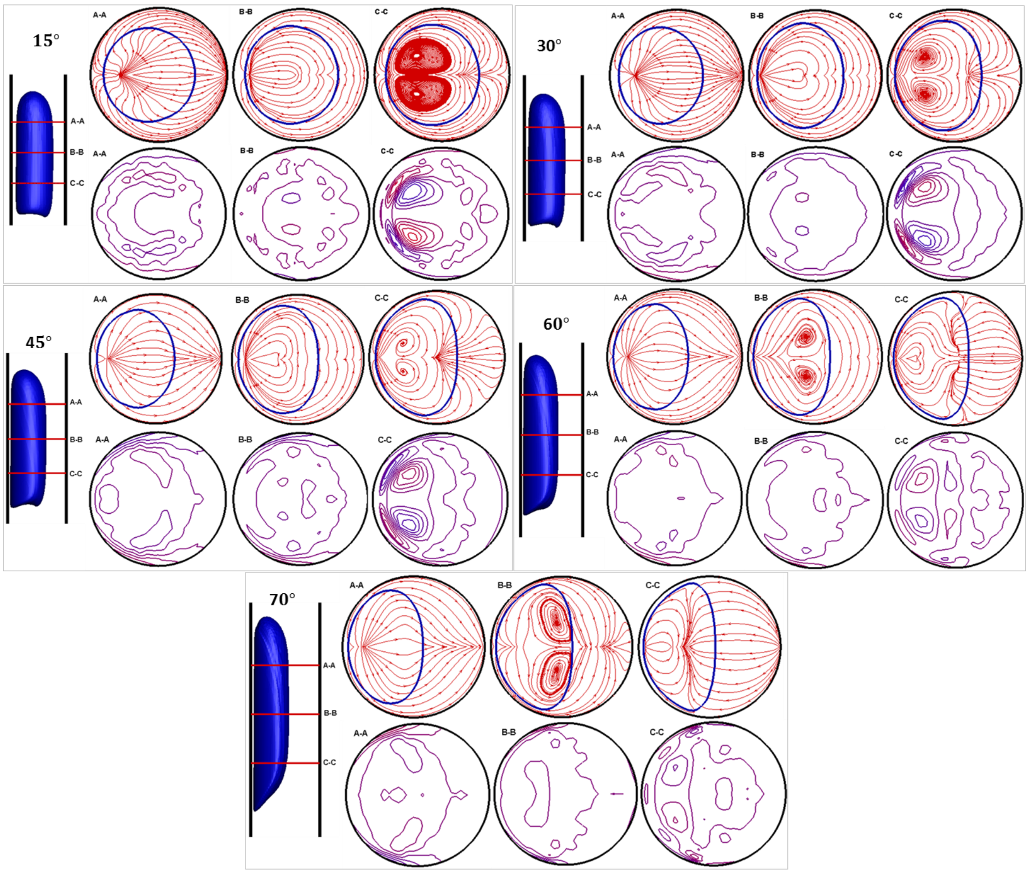

Figure 5-2. Streamlines and vorticity field (s^{-1}) in the xy plane at the three different sections, namely A-A, B-B and C-C for case 1 in Table 5-2, corresponding to inclination angles of 15° to 70° ($Eo = 66$ and $Re_{v_{d_1}} \cong 15$).

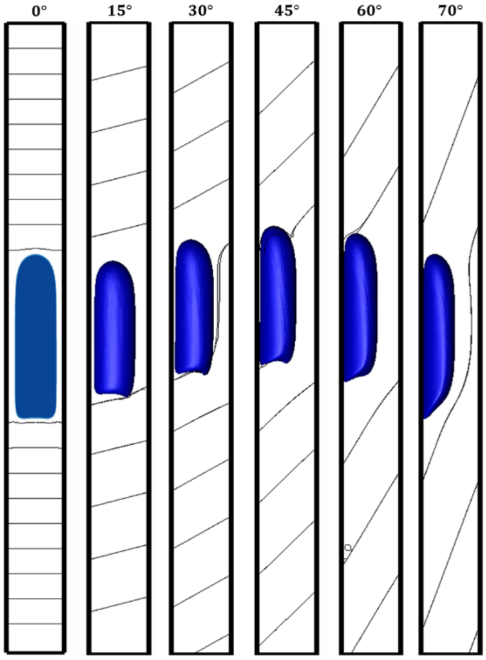

Figure 5-3. Pressure fields for case 1 in Table 5-2, for the inclination angle range of 0° to 70° ($Eo = 66$ and $Re_{v_{d_1}} \cong 15$).

5.4.1.2 Effect of Reynolds Number

In order to explore the consequences of Reynolds number on the Taylor bubble shape, three selected cases with fixed Eötvös number of 66 but with different Reynolds number corresponding to approximate values of 15, 95 and 200 are simulated (cases 1 to 3 in Table 5-2). Figure 5-4 illustrates an example of the effect of Re_{v_d} on the final shape of the developed Taylor bubble and the flow field around it for cases 1 and 2 in Table 5-2. At low values of Reynolds number, the high viscous forces increase the elongation of the terminal developed Taylor bubble with the most extended Taylor bubble being at the vertical case, as indicated in Figure 5-4. Generally, for the vertical case, a pair of elongated counter-rotating vortices are noticed in the bubble wake. As the pipe inclination increases, this configuration is lost. A vortex close to the wall starts to appear with the inclination angle, which opens up with the increase in inclination angle. Another vortex at the far side of the wall originates at a higher inclination.

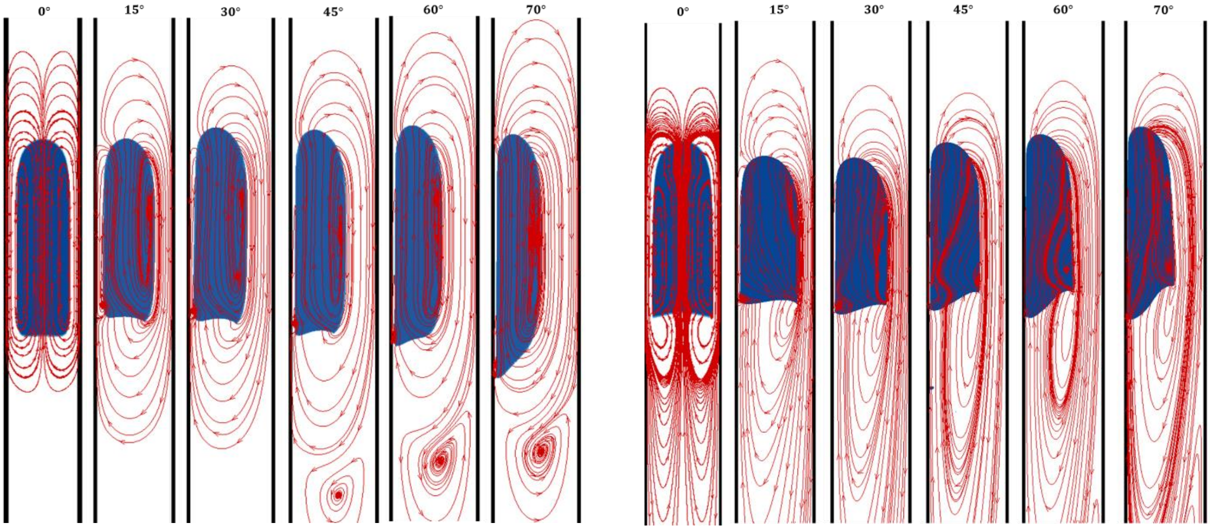

(a) **(b)**

Figure 5-4. Streamlines in the yz plane for cases 1 and 2 in Table 5-2, with inclination angle range of $0° \le \gamma \le 70°$, *(a)* $Re_{v_{d_1}} \cong 15$, *and (b)* $Re_{v_{d_2}} \cong 95$, *with* $Eo = 66$.

The increase in Reynolds number affects the average velocity of the flow for all angles, and the vortex development as well. It also changes the bubble rear shape by increasing its concavity, as shown in Figure 5-5. As for the developed bubble wake, it can be noticed that the Reynolds number has a significant effect on the intensity and scale of the wake. Additionally, it is also worth noting that at higher values of Reynolds number (Re_{v_d}= 200), little disturbances are noticed at the gas-liquid interface at higher inclination angles (70°). The main reason for that is the higher values of reduced Galilei number (Ga_R). This will be discussed in detail in chapter 6.

Additionally, it can be concluded from Figure 5-5, the increase in Re_{v_d} from 95 to 200 has almost no vital effect on all inclination angles, except for the vertical case. This can be noticed by the convex bottom noticed at the vertical pipe case in Figure 5-5.

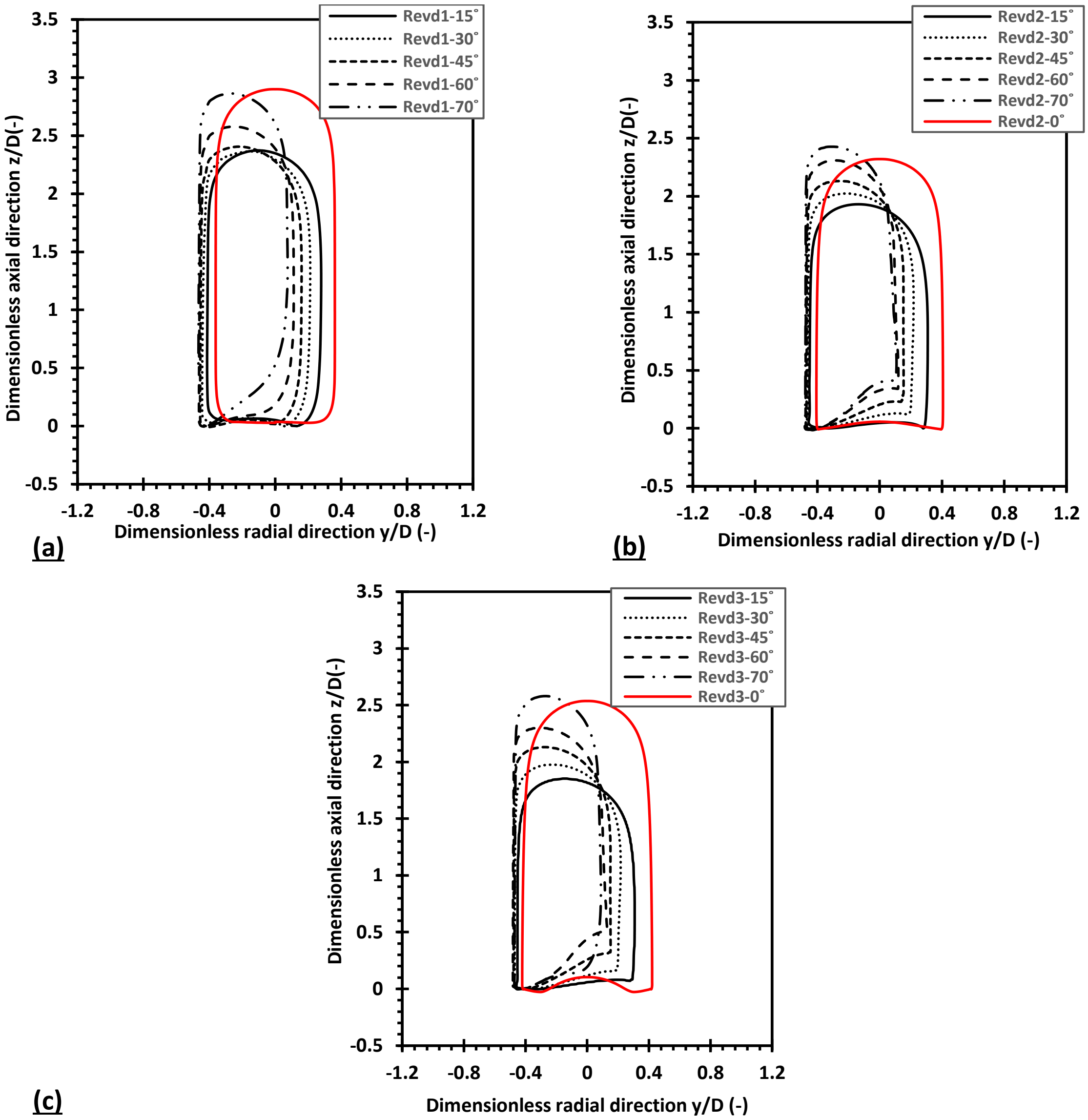

Figure 5-5. Bubble shape profile for cases 1 to 3 in Table 5-2, with inclination angle range of $0° \leq \gamma \leq 70°$, *(a)* $Re_{v_{d_1}} \cong 15$, *(b)* $Re_{v_{d_2}} \cong 95$ *and (c)* $Re_{v_{d_3}} \cong 200$, *with* $Eo = 66$.

5.4.1.3 Effect of Eötvös number

The effect of buoyancy and surface tension forces on the motion of Taylor bubbles in inclined pipes can be examined through considering the influence of Eötvös number. Three cases are simulated with Eo values of 20, 40 and 66, and Reynolds number with an average value of 25, cases 4 to 6 in Table 5-2.

Figure 5-6 shows an example for the effect of Eo number on the final shape of the developed Taylor bubble, the flow field, and the terminal Froude number, for cases 4 and 6 in Table 5-2. Similar to the vertical pipe case, the surface tension is high at low values of Eo, that avoid any possible distortion at the interface. In Figure 5-6 (a), the bubble starts with prolate spheroidal nose and oblate spheroid bottom at the vertical position. This shape is considerably maintained with most of the inclination angles with an increase in the bubble's length as a result of the pipe's inclination.

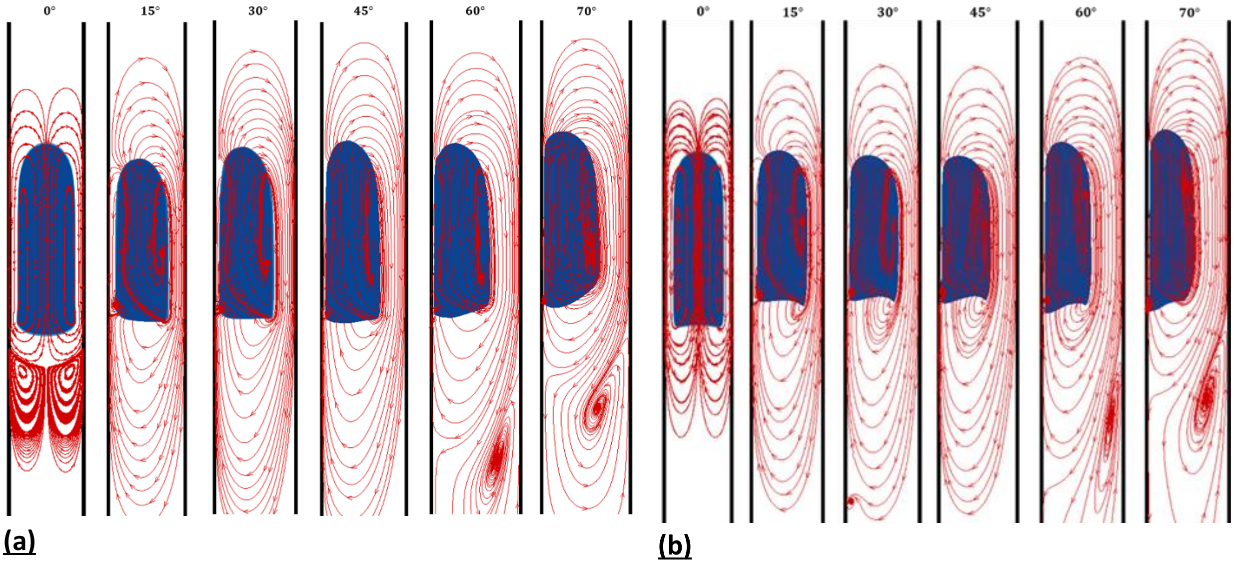

Figure 5-6. Streamlines in the yz plane for cases 4 and 6 in Table 5-2, with inclination angle range of $0° \leq \gamma \leq 70$, *(a)* $Eo_1 = 20$ *and (b)* $Eo_3 = 66$, *with* $Re_{v_d} \cong 25$.

The bubble shape profiles for cases 4 to 6 in Table 5-2 are given in Figure 5-7. It can be noticed that the increase in Eo number alters the shape of the bubble tail from convex into a concave structure, which reflects into wider wakes. It should be pointed out that for $Eo \geq 100$, highly disturbed bubble geometry is noticed for various inclination angles with an un-converged bubble velocity, especially for an inclination range of $15° \leq \gamma \leq 45°$. Thus, the results suggest that for $Eo \geq 100$, the effect of surface tension results in deformation at the gas-liquid interface, and hence, it loses its structure, and a strong breaking up concept is noticed. Also, for $Eo \leq 10$, no Taylor bubble exists especially for large inclination angles.

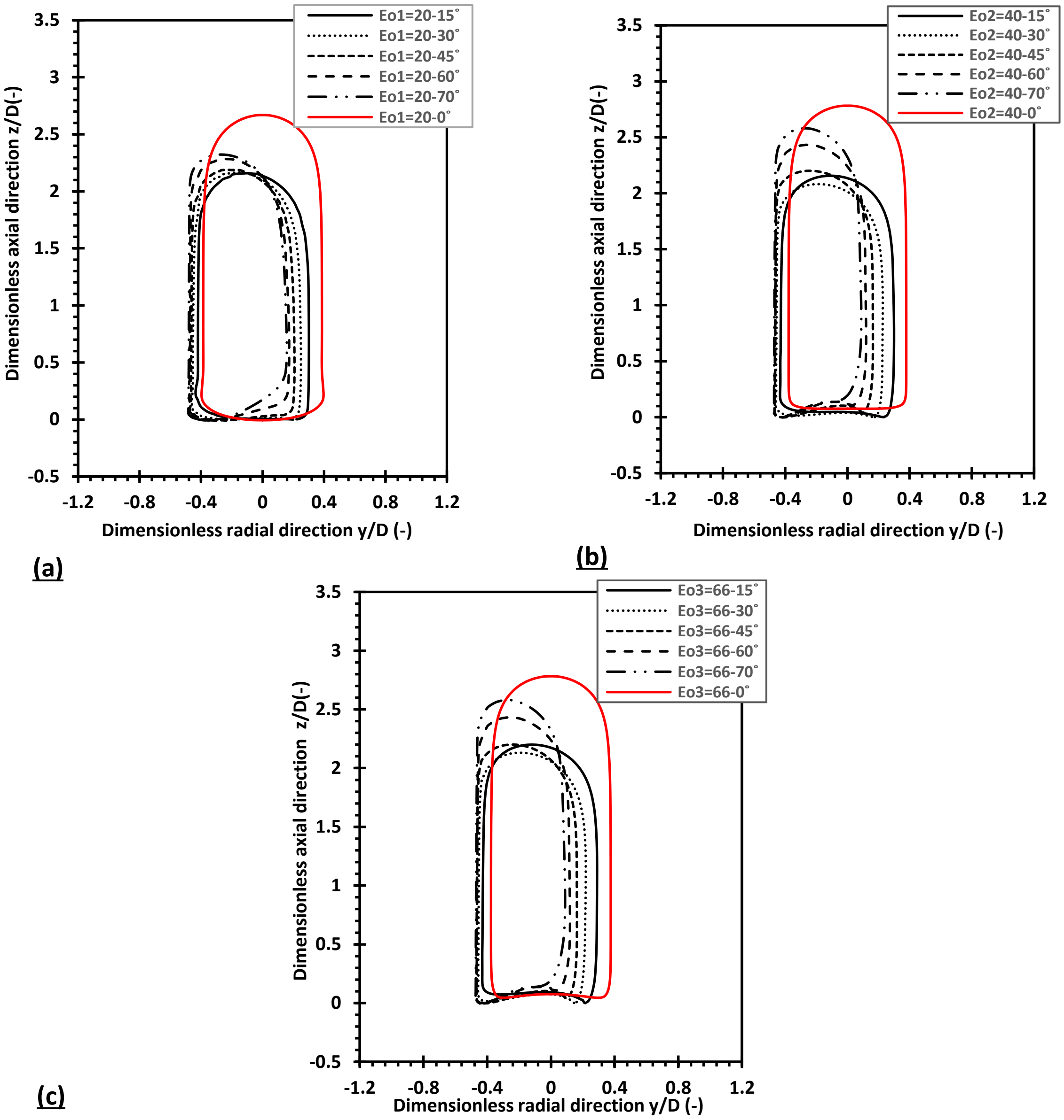

Figure 5-7. Bubble shape profile for cases 4 to 6 in Table 5-2, with inclination angle range $0° \leq \gamma \leq 70°$, *(a)* $Eo_1 = 20$, *(b)* $Eo_2 = 40$ *and (c)* $Eo_3 = 66$, *with* $Re_{v_d} \cong 25$.

In conclusion, it can be deduced that both Eo and Re_{v_d} significantly control the dynamics of the motion of bubbles in inclined pipes. Based on the simulation cases, the results suggest that a higher Eo range is essential to maintain stable Taylor bubble formation in the inclined pipe when compared with the vertical cases. Adding to that, the instability in the gas-liquid interface is also noticed for $Eo \geq 100$. The drift velocity follows the "peculiar trend" with the inclination angle for Re_{v_d} values investigated. However, the maximum Froude values occur at higher angles with the increment in Eo values.

5.4.2 Taylor Bubble Drift Velocity

The Taylor bubble drift velocity (v_d) is considered one of the main hydrodynamic features of Taylor bubbles flow in inclined pipes. In the literature, various studies, either theoretical and/or experimental, are done to estimate the terminal bubble drift velocity. In chapter 2, a summary for the main correlation estimating the bubble drift velocity is discussed (Table 2-3 in chapter 2). In this section, the effect of inclination angle, Reynolds number and Eötvös number on Taylor bubble drift velocity are discussed. In addition, a comparison between the present simulation results and other main correlations in the literature is explored.

To explore the effect of the inclination angle on the bubble drift velocity, Figure 5-8 shows the effect of pipe inclination on the time evolution of the Froude number $\left(Fr_{v_d}\right)$ showing the transient period and the time needed to achieve the final steady state as defined by Gutiérrez et al. (2017) for case 1 in Table 5-2. It can be concluded that $15°$ case is nearly first to accomplish the stationary state, at approximately 0.2s. In addition, inclination angles $15°$ to $45°$ show similar behaviour of Fr_{v_d} evolution. However, for larger inclination angles, a different evolution is noticed especially with an inclination angle of $70°$, where longer simulation time is essential for establishing a constant terminal Fr_{v_d}, and subsequently a final steady state.

In chapter 3, the present simulation is tested against experimental data and main correlations in the literature. Based on this validation study, it is concluded that one of the reliable correlations is given by Lizarraga-García (2016) as it can predict the Froude number for a wide range of Eo. Hence, for the sake of comparison, Figure 5-9 shows the terminal Froude number for cases 1 in Table 5-2 compared against the correlation of Lizarraga-García (2016). It can be concluded that there is a good matching between the present simulation results and those predicted by Lizarraga-García (2016).

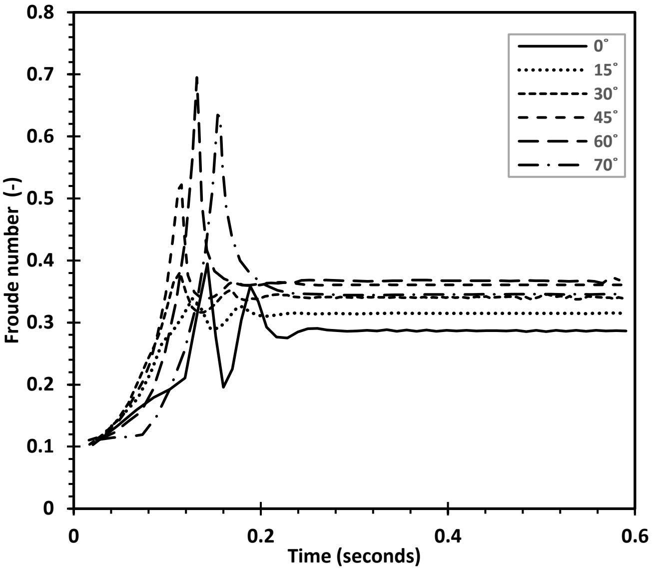

Figure 5-8. Sketch of the evolution of the Froude number over time for case 1 in Table 5-2, with inclination angles of 15° to 70° ($Eo = 66$ and $Re_{v_{d_1}} \cong 15$).

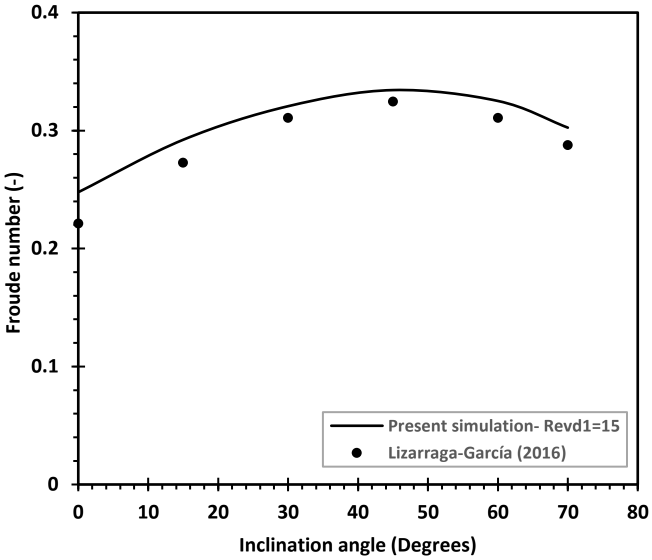

Figure 5-9. Comparision between the present simulation results for the Terminal Froude number for cases 1 in Table 5-2, with inclination angle range of $0° \leq \gamma \leq 70°$ and the correlation given by Lizarraga-García (2016).

The effect of Reynolds number on the terminal Froude number is given in Figure 5-10. For low Reynolds number values, the viscous forces of liquid phase surrounding the bubbles are high enough to weaken the drift of the Taylor bubble, and the resistance for the bubble to penetrate the stagnant liquid is high and is capable of reducing its drift velocity. Generally, for a fixed

Reynolds number, the bubble velocity increases with the inclination angle reaching its maximum value at 45°. Obviously, a further increase in the inclination angle reduces the terminal bubble velocity. This behaviour is clearly examined by Maneri and Zuber (1974) and Spedding and Nguyen (1978), as the angle of inclination increases, the buoyancy forces increase, which subsequently increases the bubble velocity. A resistive force opposes this force from the draining of the liquid past the rising bubble. The results agree with the conclusions of Maneri and Zuber (1974) where the maximum Froude value occurs at an angle (45° based on current cases) at which the transition from a blunt-nosed bubble-double falling film system to a streamlined bubble with almost one falling film system occurs. Hence, it can be concluded that at lower Reynolds number, the blunter bubble nose is observed to result in a reduction in the bubble drift velocity.

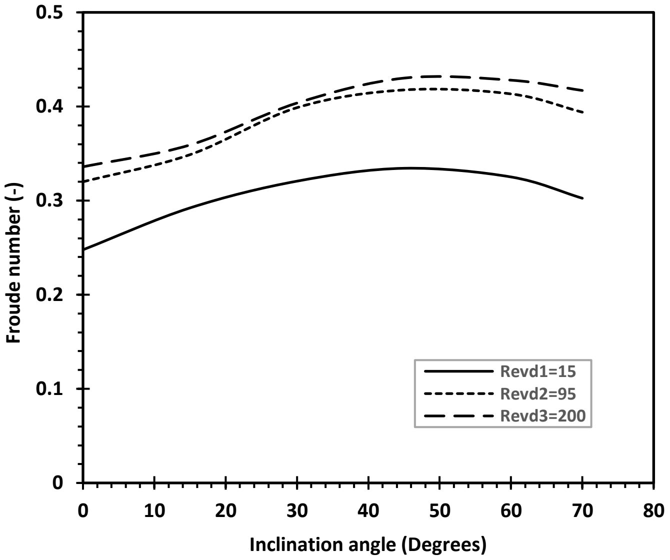

Figure 5-10. Terminal Froude number for cases 1 to 3 in Table 5-2, with inclination angle range $0° \leq \gamma \leq 70°$ *and* $Eo = 66$.

In addition, the effect of the Eötvös number on the terminal Froude number is given in Figure 5-11. For $Eo = 20$, the terminal velocity increases with the inclination angle with maximum values of 45°. Whereas, the increase in Eo values result in an increase in the gravitational potential that enables the bubble to drift through the stagnant liquid. Both the drift velocity and the gravitational potential reach a maximum value of 45° for $Eo1 = 20$ and 60° for $Eo2 = 40$ and $Eo3 = 66$. Due to the increase in Eo values, there is a tendency of change in maximum Eo number values with a larger inclination angle. This conclusion agrees with the findings of

Maneri and Zuber (1974); Weber et al. (1986); Shosho and Ryan (2001) and Jeyachandra et al. (2012).

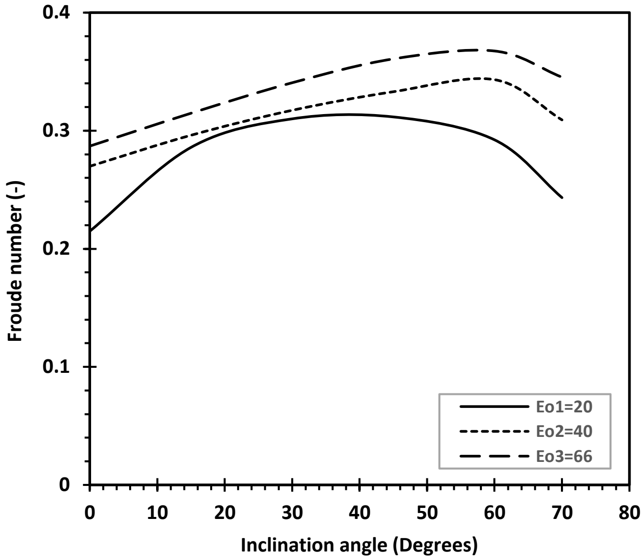

Figure 5-11. Terminal Froude number for cases 4 to 6 in Table 5-2, with inclination angle range $0° \leq \gamma \leq 70°$ *and* $Re_{v_d} \cong 25$.

5.4.3 Detailed Hydrodynamics

In this section, detailed hydrodynamics of Taylor bubble problem is investigated by dividing the flow field into three main sections flow in the Taylor bubble nose region, flow in the liquid film region and flow in the wake region. For each region, the main hydrodynamics characteristics are investigated with emphasis on the role of the main dimensionless groups (Re_{v_d} and Eo). The notation of the main characteristics discussed in this section are related to Araújo et al. (2012), who investigated the main hydrodynamics of Taylor bubbles in the vertical pipe over a wide range of dimensionless groups (Eo, M and N_f). The results are given in a dimensionless form, similar to the vertical case given in chapter 4, mostly by dividing by the pipe diameter. Figure 5-12 shows the main hydrodynamic features of Taylor bubbles in a stagnant liquid in both vertical and inclined pipe. The inclined pipe features are given the subscript I.

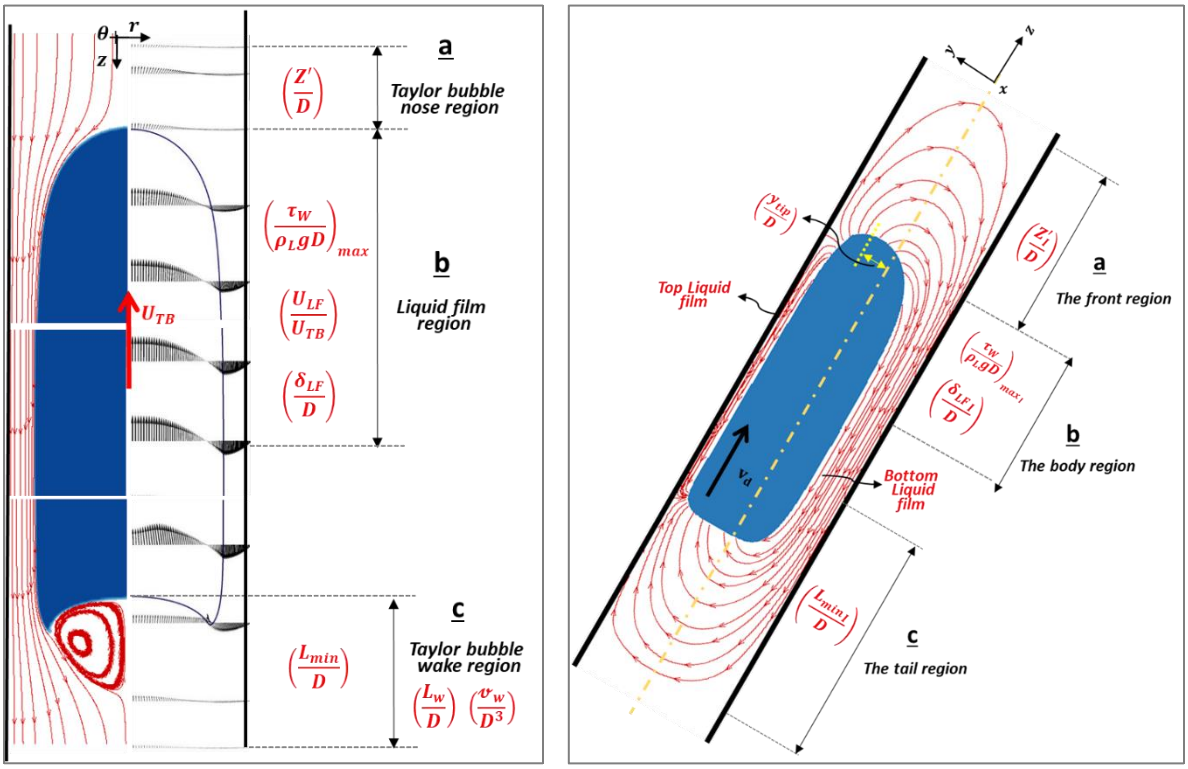

(a) (b)

Figure 5-12. A schematic representation of the main hydrodynamic features of a single Taylor bubble rising through a stagnant liquid (a) in a vertical pipe and (b) in an inclined pipe.

5.4.3.1 Bubble Front Region

The bubble front region is mainly investigated by two main features, the minimum interaction distance above the bubble (Z'_I) and the bubble tip position with respect to the pipe axis (y_{tip}). In this section, the effect of the main dimensionless parameters, given in section 5.2, on these two key features characterising the bubble front region is discussed.

Firstly, the minimum interaction distance above the bubble (Z'_I) is defined as the length needed to stabilise the flow field above the Taylor bubble, and it is sometimes known as the perturbed distance upstream. This distance is essential in the case of coalescence phenomena in transient slug flow (Lizarraga-García, 2016). According to Araújo et al. (2012), the criteria used to estimate this distance is based on determining the region ahead of the bubble where the vertical liquid velocity is equal to 1% of the value of Taylor bubble drift velocity (U_{TB}). Applying the same criterian, as done by Lizarraga-García (2016), to the inclined pipe case, this distance is defined as the distance above the bubble where the maximum liquid velocity component (w_{max}) is equal to 1% of the value of Taylor bubble drift velocity (v_d), $\left(\frac{w_{max}}{v_d} = 0.01\right)$. Figure 5-13 shows the effect of both Eo and Re_{v_d} on the dimensionless interaction distance above the bubble $\left(\frac{Z'_I}{D}\right)$. As the pipe is inclined from the vertical position, an increase in the dimensionless interaction distance above the bubble $\left(\frac{Z'_I}{D}\right)$ is noticed up to 20°, as indicated in Figure 5-13 (b). The dimensionless interaction distance is not significantly affected by a further increase in the inclination angle. This is due to the sudden change in bubble shape (especially bubble nose) as indicated in Figure 5-6 and Figure 5-7. Based on Eo values investigated, the increase in Eo shows negligible effect on $\left(\frac{Z'_I}{D}\right)$. However, referring to Figure 5-13 (a), the increase in Re_{v_d}, which means lower viscous forces, enhances larger distances to diffuse inertia at the bubble nose. Consequently, this is reflected in larger values of $\left(\frac{Z'_I}{D}\right)$. Additionally, any further increase in Re_{v_d} shows almost no effect on $\left(\frac{Z'_I}{D}\right)$. It is also expected the same to happen with the bubble wake region $\left(\frac{L_{min_I}}{D}\right)$ but with different profile with the inclination angle.

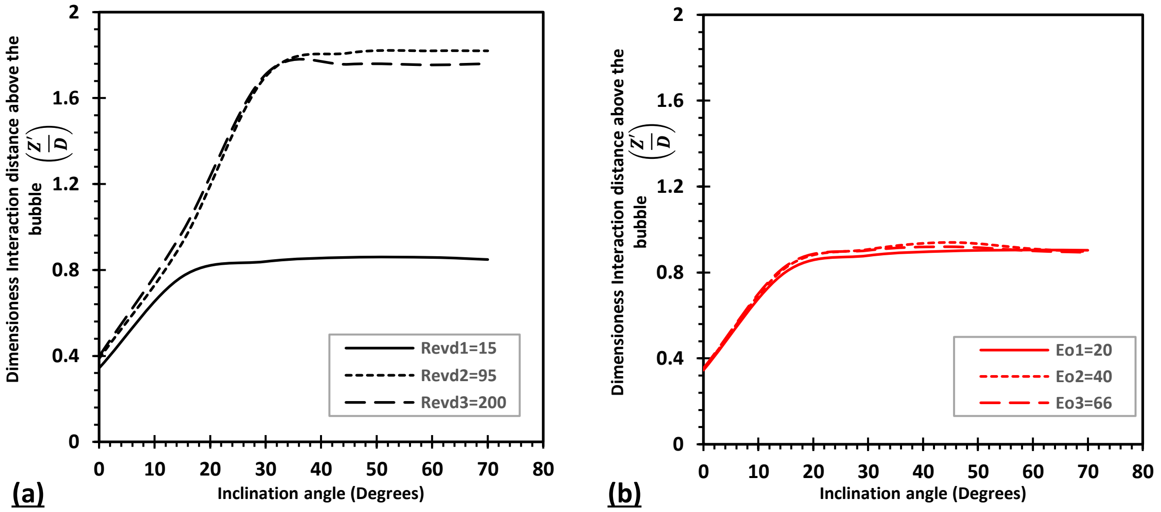

Figure 5-13. The effect of Eo and Re_{v_d} *on the dimensionless interaction distance above the bubble* (Z'_I/D) *and* (Z'/D).

Secondly, the bubble tip position with respect to the pipe axis (y_{tip}) is given in a dimensionless form as $\left(\frac{y_{tip}}{D}\right)$, as indicated in Figure 5-14. It can be generally noticed that an increase in Re_{v_d} accompanied by the increase in the bubble drift velocity, causing the bubble to move more noticeably to the pipe wall as the pipe inclines. However, referring to Figure 5-14 (b), it can be seen that the bubble tip motion with respect to the pipe wall is almost linear. This is in good agreement with the conclusions by Lizarraga-García (2016).

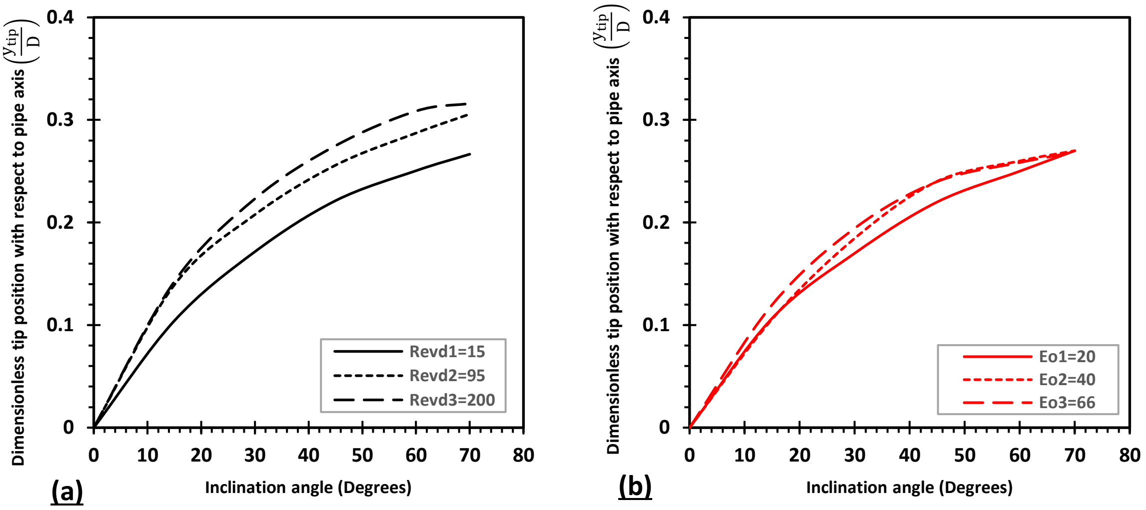

Figure 5-14. The effect of Eo *and* Re_{v_d} *on the dimensionless tip position with respect to the pipe axis* (y_{tip}/D).

5.4.3.2 Bubble Body Region

The main characteristic to be investigated in the bubble body region is the dimensionless liquid film thickness $\left(\frac{\delta_{LF_I}}{D}\right)$ and the dimensionless wall shear stress $\left(\frac{\tau_W}{\rho_L g D}\right)_{max}$. Figure 5-15 shows the effect of both Eo and Re_{v_d} on the dimensionless liquid film thickness $\left(\frac{\delta_{LF_I}}{D}\right)$.

Figure 5-15 indicates that the dimensionless liquid film thickness $\left(\frac{\delta_{LF_I}}{D}\right)$ increases with the inclination angle as the bubble moves towards the pipe wall. In Figure 5-15 (a), Re_{v_d} has a negligible effect on $\left(\frac{\delta_{LF_I}}{D}\right)$ especially for larger angles. The effect of Eo on $\left(\frac{\delta_{LF_I}}{D}\right)$ is given in Figure 5-15 (b), where Eo shows almost no effect on $\left(\frac{\delta_{LF_I}}{D}\right)$ for inclination angle up to $15-20°$. On the contarary, for larger angles, the increase in Eo values increases $\left(\frac{\delta_{LF_I}}{D}\right)$ due to the change in the bubble nose shape caused by Eo.

In addition, Figure 5-16 shows the effect of both Eo and Re_{v_d} on the dimensionless wall shear stress $\left(\frac{\tau_W}{\rho_L g D}\right)_{max}$. A similar behaviour for the dimensionless wall shear stress with the inclination angles is noticed for all values of Eo and Re_{v_d}. A slight reduction in the dimensionless wall shear stress is noticed when the pipe is inclined up to 15° from the vertical position. However, a further increase in inclination angle shows an increase in the wall shear stress. Similar to the vertical pipe case, reduction in the wall shear stress is noticed with the increase in Re_{v_d} due to the lower viscosity of the surrounding liquid.

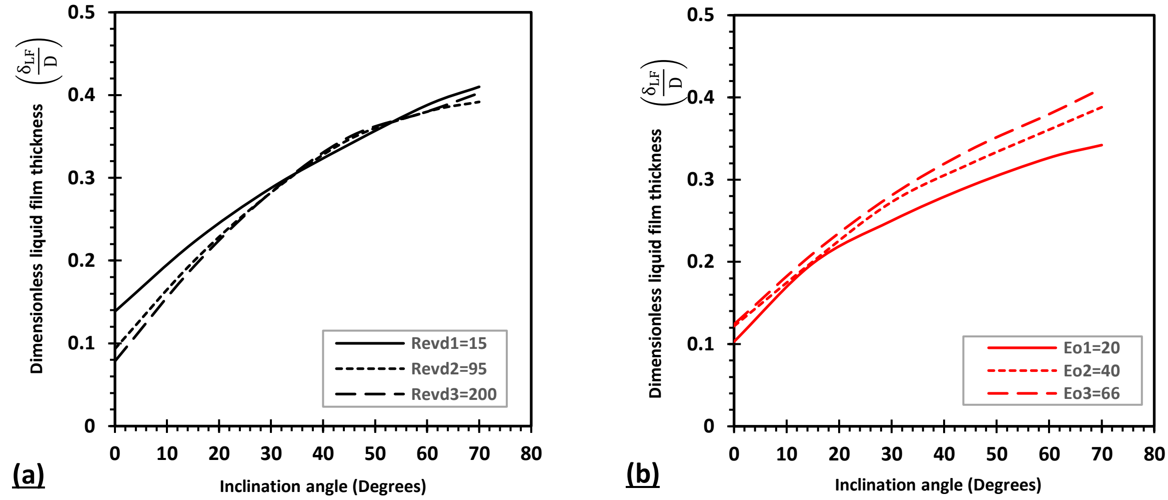

Figure 5-15. The effect of Eo and Re_{v_d} *on the dimensionless liquid film thickness* (δ_{LF_I}/D)*and* (δ_{LF}/D).

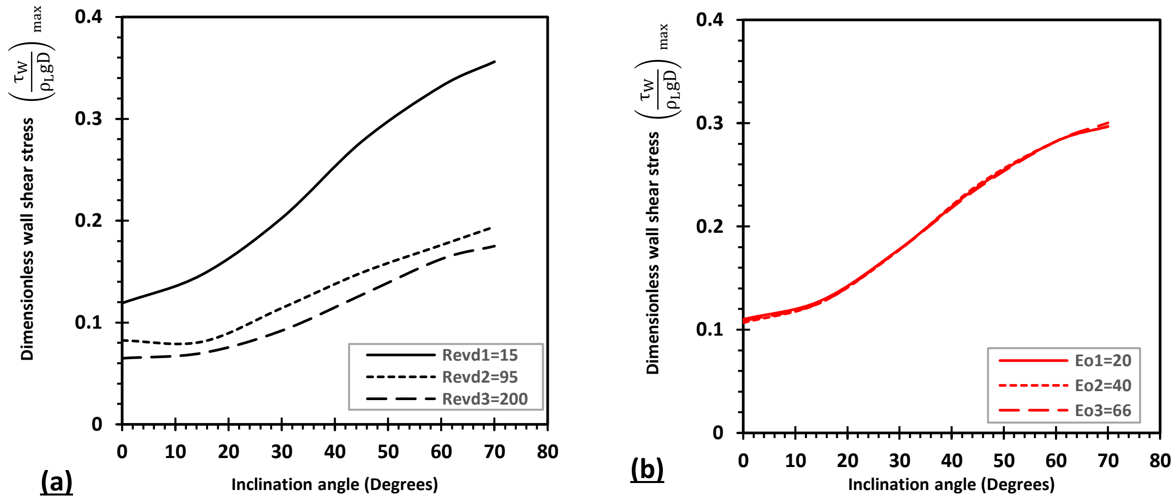

Figure 5-16. The effect of Eo and Re_{v_d} *on the dimensionless wall shear stress* $\left(\frac{\tau_W}{\rho_L g D}\right)_{max}$

5.4.3.3 Bubble Tail Region

In this region, the main characteristics to be investigated is the perturbed distance below the bubble which is given in a dimensionless form as $\left(\frac{L_{min_I}}{D}\right)$. The same criteria used to determine the minimum interaction distance above the bubble (Z'_I) is used here to determine the perturbed distance below the bubble $\left(L_{min_I}\right)$. Hence, the perturbed distance below the bubble is the distance below the bubble at which the maximum liquid velocity component (w_{max}) is equal to 1% of the value of Taylor bubble drift velocity (v_d), $\left(\frac{w_{max}}{v_d} = 0.01\right)$. Figure 5-17 shows the effect of both Eo and Re_{v_d} on the dimensionless perturbed distance below the bubble $\left(\frac{L_{min_I}}{D}\right)$. Comparing Figure 5-13 and Figure 5-17, it can be generally concluded that higher values for $\left(\frac{L_{min_I}}{D}\right)$ is noticed and it is greatly influenced by both Eo and Re_{v_d}. For the effect of Re_{v_d}, Figure 5-17 (a) shows similar behaviour for $\left(\frac{L_{min_I}}{D}\right)$ with the inclination angle for all Re_{v_d}. When the pipe is inclined up to 30° from the vertical position, there is an increase in $\left(\frac{L_{min_I}}{D}\right)$, while further increase in inclination angles reduces $\left(\frac{L_{min_I}}{D}\right)$. This reduction in $\left(\frac{L_{min_I}}{D}\right)$ is due to the development of secondary vortices as explained in section 5.4.1. In Figure 5-17 (b), Eo shows a similar effect on $\left(\frac{L_{min_I}}{D}\right)$ with the inclination angle, however, a significant reduction in $\left(\frac{L_{min_I}}{D}\right)$ is noticed for higher inclination angles.

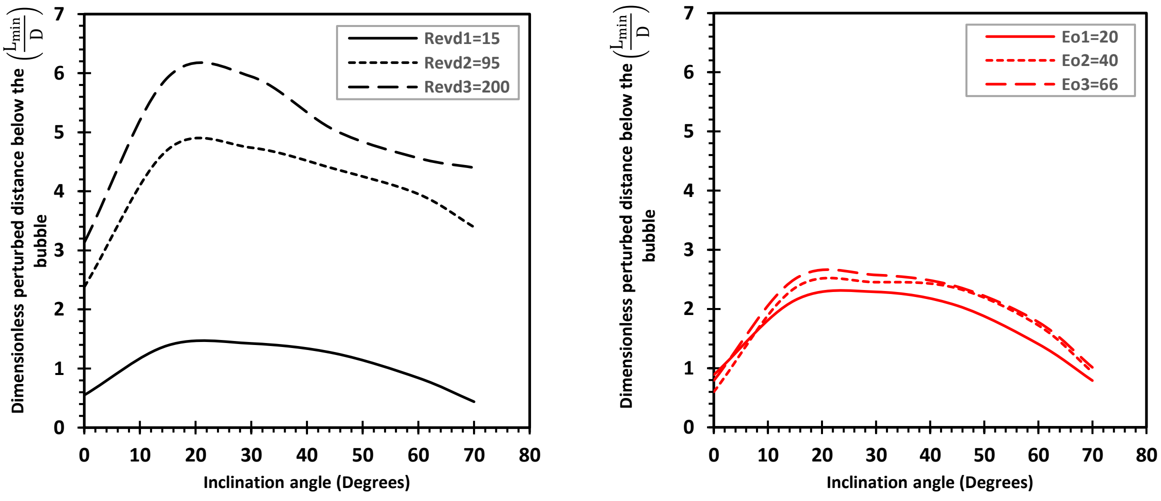

Figure 5-17. The effect of Eo and Re_{v_d} on the dimensionless perturbed distance below the bubble (L_{min_I}/D) and (L_{min}/D).

It can be concluded that Re_{v_d} has a vital effect on both the interaction distances above and below the bubble $\left(\frac{Z'_I}{D} \& \frac{L_{min_I}}{D}\right)$.

5.5 Concluding Remarks

Through this chapter, a complete dimensionless analysis of single Taylor bubble drifting through a stagnant Newtonian liquid in an inclined pipe, followed by order of magnitude analysis of the equations of motion is carried out. The main conclusion is that for inclination range of $0 \leq \gamma \leq 70°$; the problem is mainly governed by Froude, Eötvös and Reynolds numbers. However, for different inclination angles, the near horizontal cases $(70° < \gamma < 90°)$, a special treatment is essential for these cases, which will be given in detail in the following chapter.

Using the guideline of the order of magnitude analysis and the dimensionless group analysis, a CFD study investigating the hydrodynamics of a single Taylor bubble drifting through a stagnant Newtonian liquid in an inclined pipe is performed. Particularly, the current study is focused on the main similarity parameters, that is Froude number $\left(Fr_{v_d}\right)$, Reynolds number $\left(Re_{v_d}\right)$ and Eötvös number (Eo). The main hydrodynamic characteristics discussed include the developed Taylor bubble shape, the Taylor bubble drift velocity and detailed hydrodynamic characteristics covering the bubble front region, bubble body region and the bubble tail region.

The main findings of this chapter can be summarised as follows:

- The bubble motion follows the “peculiar trend” with the inclination angle, where the bubble velocity increases with inclination angle until it reaches a maximum value, then it starts to decrease once again. The bubble shape is significantly affected by the inclination of the pipe where elongation in Taylor bubble length with a reduction in size is established with the pipe inclination.
- Eo has a significant effect on the Taylor bubble shape and velocity. The rise in surface tension alters the shape of the bubble tail from a convex into a concave structure which

is reflected into wider wakes. The increase in Eo values raises the gravitational potential that enables the bubble to drift through the stagnant liquid. There is also a tendency of change in maximum Froude number values with a larger inclination angle due to the increase in Eo values.

- Re_{v_d} shows a similar role to Eo where the increase in Re_{v_d} alters the bubble shape from the long slender bubble into shorter and flatter ones. At low Re_{v_d}, blunter bubble nose is observed and thus leads to a reduction in the bubble motion.
- Furthermore, the bubble tip position is affected by Re_{v_d} where the increase in Re_{v_d} increases the bubble motion to the pipe wall, as the pipe is inclined from the vertical position. However, for all values of Eo investigated, a linear relationship is noticed for the bubble motion with respect to the pipe wall.
- Moreover, the wall shear stress is examined under the effect of both Eo and $Re_{U_{TB}}$. It is noticed that the increase in $Re_{U_{TB}}$ results in less viscous effect in the liquid surrounding the Taylor bubble that leads to a reduction in the wall shear stress. The wall shear stress is not affected by Eo for all the values investigated. Additionally, the wall shear stress increases as the pipe is inclined from the vertical position.
- Finally, the present simulation results show a reasonable agreement when tested against the previous experimental data and the main correlations available in the literature. Nevertheless, it can be noticed that further improvements are still necessary for predicting the Taylor bubble drift velocity.

Chapter 6 Theoretical and CFD Treatments of an Individual Taylor Bubble Drifting in Near Horizontal and Horizontal Pipes ($\boldsymbol{\gamma \cong 90°}$)

The bubble motion in inclined pipes follows the "peculiar trend" with the inclination angle, where the bubble velocity increases with inclination angle until it reaches a maximum value, then it starts to decrease once again. The bubble drift velocity diminishes in inclination angles near the horizontal orientation, and hence, this chapter aims at introducing a special treatment for these inclination angles. In this chapter, a complete dimensionless treatment followed by order of magnitude analysis of the terms of equations of motion for the near horizontal and the horizontal pipes is performed. Based on the fact that the bubble drift velocity diminishes in inclination angles near the horizontal orientation, the reduced Galilei number is suggested to govern the bubble dynamics. Additionally, this chapter employs a CFD study to investigate the hydrodynamics of a single Taylor bubble drifting through a stagnant liquid in a near horizontal pipe $(70° < \gamma < 90°)$*, using the volume-of-fluid (VOF) methodology implemented in the computational fluid dynamics software package, ANSYS Fluent (Release 16.0). Finally, based on the fact that bubble cannot propagate in a zero axial pressure gradient horizontal pipe, a simplified model is suggested to solve the challenging problem of the three-dimensional Taylor bubble in near horizontal and horizontal pipes, and thus saving computational resources.*

6.1 Introduction

Similar to the previous two chapters, the scope of this chapter can be divided into two main folds:

1. Performing a complete dimensionless analysis of the problem for inclination range $70° < \gamma \leq 90°$ using both the Buckingham-Pi theorem and a dimensionless treatment followed by order of magnitude analysis to the governing equations of motion, showing the main physical parameters influencing the flow, the so-called reduced Galilei number and Eötvös number. While taking into consideration that the Reynolds and Froude numbers are vanishingly small and are no longer acting as influencing parameters. For the horizontal pipe case ($\gamma = 90°$), the pressure field distribution around the stagnant deformed bubble is mainly governed by the Eötvös number, where the reduced Galilei number ceases to be effectively similar to the Reynolds and Froude numbers.
2. Based on this analysis, the main hydrodynamic features of drifting of Taylor bubbles in inclined pipes with stagnant liquid are investigated by applying computational fluid dynamics (CFD) simulation using the volume-of-fluid (VOF) methodology implemented in the commercial software ANSYS Fluent. The simulations performed in this chapter are based on the cases given in chapter 4.

This chapter is divided as follows, the dimensionless equations of motion and order of magnitude analysis are given in section 6.2. Section 6.3 discusses the CFD model. Moreover, the results and discussion are given in section 6.4, which is divided into two main parts, the near horizontal pipe ($70° < \gamma < 90°$) and the horizontal pipe ($\gamma = 90°$). In each section, the main dynamics of Taylor bubbles are discussed, including the developed Taylor bubble shape, the bubble length, the bubble drift velocity and the pressure distribution around the bubble. Finally, the chapter ends with a concluding remarks section that summarises all the important outcomes of this chapter.

6.2 Dimensionless Analysis

This section discusses the two methods used for analysing the problem of drifting of Taylor bubbles in near horizontal and horizontal pipes with stagnant liquid, which are the Buckingham-Pi theorem and the dimensionless analysis of governing equations. This section ends up with a conclusion based on the order of magnitude analysis of the dimensionless governing equations.

6.2.1 Buckingham-Pi theorem

Appendix C shows all details of the Buckingham-Pi theorem applied to near horizontal and horizontal pipe case with the inclination angle ($70° < \gamma \leq 90°$) with respect to the vertical position. The problem for the near horizontal pipe case ($70° < \gamma < 90°$) can be expressed as follows:

$$\sigma = f\ [\rho_L, \mu_L, g, L_{TB}, D] \qquad (6\text{-}1)$$

Based on the theorem given in Appendix C, it can be concluded that the sole governing parameters for the near horizontal case are the reduced Galilei number (Ga_R), Eötvös number (Eo) and $\frac{L_{TB}}{D}$.

However, the problem for the horizontal pipe case ($\gamma = 90°$) can be expressed as follows:

$$\sigma = f\ [\rho_L, g, L_{TB}, D] \qquad (6\text{-}2)$$

Based on the theorem given in Appendix C, it can be shown that the main similarity parameters that govern the pressure field distribution around the stagnant deformed bubble are Eötvös number (Eo) and $\frac{L_{TB}}{D}$.

6.2.2 Dimensionless Governing Equations

Applying a similar coordinate system as the inclined pipe case given in chapter 5, for the near horizontal pipe case ($70° < \gamma < 90°$) a characteristic velocity (v_s) is chosen according to a way that would treat the flow in such cases, where low values of Reynolds number $\left(Re_{v_s}\right)$ exists.

Referring to the inclined pipe configuration and the coordinates system given in Figure 5-1, the Navier-stokes equations in cartesian coordinates are given as follow:

$$\rho_L\left(\frac{\partial u}{\partial t}+u\frac{\partial u}{\partial x}+v\frac{\partial u}{\partial y}+w\frac{\partial u}{\partial z}\right)=\rho_L g_x-\frac{\partial p}{\partial x}+\mu_L\left[\frac{\partial^2 u}{\partial x^2}+\frac{\partial^2 u}{\partial y^2}+\frac{\partial^2 u}{\partial z^2}\right] \tag{6-3}$$

$$\rho_L\left(\frac{\partial v}{\partial t}+u\frac{\partial v}{\partial x}+v\frac{\partial v}{\partial y}+w\frac{\partial v}{\partial z}\right)=\rho_L g_y-\frac{\partial p}{\partial y}+\mu_L\left[\frac{\partial^2 v}{\partial x^2}+\frac{\partial^2 v}{\partial y^2}+\frac{\partial^2 v}{\partial z^2}\right] \tag{6-4}$$

$$\rho_L\left(\frac{\partial w}{\partial t}+u\frac{\partial w}{\partial x}+v\frac{\partial w}{\partial y}+w\frac{\partial w}{\partial z}\right)=\rho_L g_z-\frac{\partial p}{\partial z}+\mu_L\left[\frac{\partial^2 w}{\partial x^2}+\frac{\partial^2 w}{\partial y^2}+\frac{\partial^2 w}{\partial z^2}\right] \tag{6-5}$$

And the continuity equation is:

$$\frac{\partial u}{\partial x}+\frac{\partial v}{\partial y}+\frac{\partial w}{\partial z}=0 \tag{6-6}$$

Introducing the following dimensionless variables:

$$\begin{gathered}\hat{u}=\frac{u}{v_s},\hat{v}=\frac{v}{v_s},\hat{w}=\frac{w}{v_s},\hat{p}=\frac{p}{\rho_L {v_s}^2},x^*=\frac{x}{(D/2)},y^*=\frac{y}{(D/2)},z^*=\frac{z}{L_{TB}},\\ \hat{t}=t\left(\frac{v_s}{L_{TB}}\right),{g_x}^*=\frac{g_x}{g},{g_y}^*=\frac{g_y}{g},{g_z}^*=\frac{g_z}{g},{\sigma_x}^*=\frac{\sigma_x}{\sigma},\sigma_y^*=\frac{\sigma_y}{\sigma},\sigma_z^*=\frac{\sigma_z}{\sigma},\\ K^*=\frac{K}{(1/D^2)}\ with\ v_s=\frac{\mu_L}{L_{TB}\rho_L}\end{gathered} \tag{6-7}$$

Substituting the dimensionless variables given in (6-7) into the momentum equation given in (6-3) would lead to:

$$\begin{aligned}&\rho_L\frac{{v_L}^2}{{L_{TB}}^3}\left[\frac{\partial\hat{u}}{\partial\hat{t}}+\left(\frac{2L_{TB}}{D}\right)\hat{u}\frac{\partial\hat{u}}{\partial x^*}+\left(\frac{2L_{TB}}{D}\right)\hat{v}\frac{\partial\hat{u}}{\partial y^*}+\hat{w}\frac{\partial\hat{u}}{\partial z^*}\right]\\ &\quad=\rho_L g{g_x}^*-\rho_L\frac{{v_L}^2}{{L_{TB}}^3}\left(\frac{2L_{TB}}{D}\right)\frac{\partial\hat{p}}{\partial x^*}+\left(\frac{\mu_L{v_L}^2}{{L_{TB}}^3}\right)\left(\frac{2L_{TB}}{D}\right)^2\left[\frac{\partial^2\hat{u}}{\partial x^{*2}}+\frac{\partial^2\hat{u}}{\partial y^{*2}}+\left(\frac{D}{L_{TB}}\right)^2\frac{\partial^2\hat{u}}{\partial z^{*2}}\right]\end{aligned} \tag{6-8}$$

Dividing equation (6-8) by $\left(\frac{\rho_L {v_L}^2}{{L_{TB}}^3}\right)$ and $\left(\frac{2L_{TB}}{D}\right)^2$ and rearranging the terms would give the following:

$$\left(\frac{D}{2L_{TB}}\right)^2 \frac{\partial \hat{u}}{\partial \hat{t}} + \left(\frac{D}{2L_{TB}}\right) \hat{u} \frac{\partial \hat{u}}{\partial x^*} + \left(\frac{D}{2L_{TB}}\right) \hat{v} \frac{\partial \hat{u}}{\partial y^*} + \left(\frac{D}{2L_{TB}}\right)^2 \widehat{w} \frac{\partial \hat{u}}{\partial z^*}$$
$$= \left[\left(\frac{g{L_{TB}}^3}{{\nu_L}^2}\right)\left(\frac{D}{2L_{TB}}\right)^2\right] {g_x}^* - \left(\frac{D}{2L_{TB}}\right)\frac{\partial \hat{p}}{\partial x^*} + \left[\frac{\partial^2 \hat{u}}{\partial x^{*2}} + \frac{\partial^2 \hat{u}}{\partial y^{*2}} + \left(\frac{D}{L_{TB}}\right)^2 \frac{\partial^2 \hat{u}}{\partial z^{*2}}\right] \tag{6-9}$$

Performing the same steps to equations (6-4) to (6-6), the dimensionless form of continuity and Navier Stokes equations could be summarised as follow:

$$\frac{\partial \hat{u}}{\partial x^*} + \frac{\partial \hat{v}}{\partial y^*} + \left(\frac{D}{2L_{TB}}\right)\frac{\partial \widehat{w}}{\partial z^*} = 0 \tag{6-10}$$

$$\left(\frac{D}{2L_{TB}}\right)^2 \frac{\partial \hat{u}}{\partial \hat{t}} + \left(\frac{D}{2L_{TB}}\right) \hat{u} \frac{\partial \hat{u}}{\partial x^*} + \left(\frac{D}{2L_{TB}}\right) \hat{v} \frac{\partial \hat{u}}{\partial y^*} + \left(\frac{D}{2L_{TB}}\right)^2 \widehat{w} \frac{\partial \hat{u}}{\partial z^*}$$
$$= \left[\left(\frac{g{L_{TB}}^3}{{\nu_L}^2}\right)\left(\frac{D}{2L_{TB}}\right)^2\right] {g_x}^* - \left(\frac{D}{2L_{TB}}\right)\frac{\partial \hat{p}}{\partial x^*} + \left[\frac{\partial^2 \hat{u}}{\partial x^{*2}} + \frac{\partial^2 \hat{u}}{\partial y^{*2}} + \left(\frac{D}{L_{TB}}\right)^2 \frac{\partial^2 \hat{u}}{\partial z^{*2}}\right] \tag{6-11}$$

$$\left(\frac{D}{2L_{TB}}\right)^2 \frac{\partial \hat{v}}{\partial \hat{t}} + \left(\frac{D}{2L_{TB}}\right) \hat{u} \frac{\partial \hat{v}}{\partial x^*} + \left(\frac{D}{2L_{TB}}\right) \hat{v} \frac{\partial \hat{v}}{\partial y^*} + \left(\frac{D}{2L_{TB}}\right)^2 \widehat{w} \frac{\partial \hat{v}}{\partial z^*}$$
$$= \left[\left(\frac{g{L_{TB}}^3}{{\nu_L}^2}\right)\left(\frac{D}{2L_{TB}}\right)^2\right] {g_y}^* - \left(\frac{D}{2L_{TB}}\right)\frac{\partial \hat{p}}{\partial y^*} + \left[\frac{\partial^2 \hat{v}}{\partial x^{*2}} + \frac{\partial^2 \hat{v}}{\partial y^{*2}} + \left(\frac{D}{L_{TB}}\right)^2 \frac{\partial^2 \hat{v}}{\partial z^{*2}}\right] \tag{6-12}$$

$$\left(\frac{D}{2L_{TB}}\right)^2 \frac{\partial \widehat{w}}{\partial \hat{t}} + \left(\frac{D}{2L_{TB}}\right) \hat{u} \frac{\partial \widehat{w}}{\partial x^*} + \left(\frac{D}{2L_{TB}}\right) \hat{v} \frac{\partial \widehat{w}}{\partial y^*} + \left(\frac{D}{2L_{TB}}\right)^2 \widehat{w} \frac{\partial \widehat{w}}{\partial z^*}$$
$$= \left[\left(\frac{g{L_{TB}}^3}{{\nu_L}^2}\right)\left(\frac{D}{2L_{TB}}\right)^2\right] {g_z}^* - \left(\frac{D}{2L_{TB}}\right)\frac{\partial \hat{p}}{\partial z^*} + \left[\frac{\partial^2 \widehat{w}}{\partial x^{*2}} + \frac{\partial^2 \widehat{w}}{\partial y^{*2}} + \left(\frac{D}{L_{TB}}\right)^2 \frac{\partial^2 \widehat{w}}{\partial z^{*2}}\right] \tag{6-13}$$

It can be inferred that the influential parameters are the so-called reduced Galilei number $Ga_R = f\left[\left(\frac{g{L_{TB}}^3}{{\nu_\mathrm{L}}^2}\right), \left(\frac{D}{2L_{TB}}\right)^2\right]$ and the pipe diameter to bubble length ratio.

Based on the fact that the gravity and viscous effects predominate the inertia effects, the following orders can be introduced:

$$x^* = o(1), y^* = o(1), z^* = o(1), \widehat{w} = o(1), \hat{t} = o(1), {g_x}^* = o\left(\frac{D}{L_{TB}}\right)$$
$${g_y}^* = o(1),\ {g_z}^* = o\left(\frac{D}{L_{TB}}\right),\ K^* = o(1),\ \sigma_x^* = o(1),\ \sigma_y^* = o(1),\ \sigma_z^* = o(1) \tag{6-14}$$

Introducing the orders given in (6-14) to the dimensionless form of continuity equation (6-10) would give the following:

$$\frac{\overbrace{\partial \hat{u}}^{o\left(\frac{D}{L_{TB}}\right)}}{\underbrace{\partial x^*}_{o(1)}} + \frac{\overbrace{\partial \hat{v}}^{o\left(\frac{D}{L_{TB}}\right)}}{\underbrace{\partial y^*}_{o(1)}} + \left(\frac{D}{2L_{TB}}\right)\frac{\overbrace{\partial \hat{w}}^{o(1)}}{\underbrace{\partial z^*}_{o(1)}} = 0 \qquad (6\text{-}15)$$

Thus, to keep the continuity equation intact, $\hat{u}$ and $\hat{v}$ should be of the order $o\left(\frac{D}{L_{TB}}\right)$.

Similarly, introducing the same orders to the dimensionless form of momentum equations in the x-direction (equation (6-11)) would give the following:

$$\left(\frac{D}{2L_{TB}}\right)^2 \frac{\overbrace{\partial \hat{u}}^{o\left(\frac{D}{L_{TB}}\right)}}{\underbrace{\partial \hat{t}}_{o(1)}} + \left(\frac{D}{2L_{TB}}\right) \overbrace{\hat{u}}^{o\left(\frac{D}{L_{TB}}\right)} \frac{\overbrace{\partial \hat{u}}^{o\left(\frac{D}{L_{TB}}\right)}}{\underbrace{\partial x^*}_{o(1)}} + \left(\frac{D}{2L_{TB}}\right) \overbrace{\hat{v}}^{o\left(\frac{D}{L_{TB}}\right)} \frac{\overbrace{\partial \hat{u}}^{o\left(\frac{D}{L_{TB}}\right)}}{\underbrace{\partial x^*}_{o(1)}} + \left(\frac{D}{2L_{TB}}\right)^2 \overbrace{\hat{w}}^{o(1)} \frac{\overbrace{\partial \hat{u}}^{o\left(\frac{D}{L_{TB}}\right)}}{\underbrace{\partial z^*}_{o(1)}}$$

$$= \underbrace{Ga_R}_{o\left(\frac{D}{L_{TB}}\right)} \underbrace{g_x{}^*}_{o\left(\frac{D}{L_{TB}}\right)} - \left(\frac{D}{2L_{TB}}\right)\frac{\overbrace{\partial \hat{p}}^{o(1)}}{\underbrace{\partial x^*}_{o(1)}} + \left[\frac{\overbrace{\partial^2 \hat{u}}^{o\left(\frac{D}{L_{TB}}\right)}}{\underbrace{\partial x^{*2}}_{o(1)}} + \frac{\overbrace{\partial^2 \hat{u}}^{o\left(\frac{D}{L_{TB}}\right)}}{\underbrace{\partial y^{*2}}_{o(1)}} + \left(\frac{D}{L_{TB}}\right)^2 \frac{\overbrace{\partial^2 \hat{u}}^{o\left(\frac{D}{L_{TB}}\right)}}{\underbrace{\partial z^{*2}}_{o(1)}}\right] \qquad (6\text{-}16)$$

Similarly, the momentum equations in y-direction results into the following orders:

$$\left(\frac{D}{2L_{TB}}\right)^2 \frac{\overbrace{\partial \hat{v}}^{o\left(\frac{D}{L_{TB}}\right)}}{\underbrace{\partial \hat{t}}_{o(1)}} + \left(\frac{D}{2L_{TB}}\right) \overbrace{\hat{u}}^{o\left(\frac{D}{L_{TB}}\right)} \frac{\overbrace{\partial \hat{v}}^{o\left(\frac{D}{L_{TB}}\right)}}{\underbrace{\partial x^*}_{o(1)}} + \left(\frac{D}{2L_{TB}}\right) \overbrace{\hat{v}}^{o\left(\frac{D}{L_{TB}}\right)} \frac{\overbrace{\partial \hat{v}}^{o\left(\frac{D}{L_{TB}}\right)}}{\underbrace{\partial y^*}_{o(1)}}$$

$$+ \left(\frac{D}{2L_{TB}}\right)^2 \overbrace{\hat{w}}^{o(1)} \frac{\overbrace{\partial \hat{v}}^{o\left(\frac{D}{L_{TB}}\right)}}{\underbrace{\partial z^*}_{o(1)}} = \underbrace{Ga_R}_{o\left(\frac{D}{L_{TB}}\right)} \underbrace{g_y{}^*}_{o(1)} - \left(\frac{D}{2L_{TB}}\right)\frac{\partial \hat{p}}{\partial y^*} + \left[\frac{\overbrace{\partial^2 \hat{v}}^{o\left(\frac{D}{L_{TB}}\right)}}{\underbrace{\partial x^{*2}}_{o(1)}} + \frac{\overbrace{\partial^2 \hat{v}}^{o\left(\frac{D}{L_{TB}}\right)}}{\underbrace{\partial y^{*2}}_{o(1)}} + \left(\frac{D}{L_{TB}}\right)^2 \frac{\overbrace{\partial^2 \hat{v}}^{o\left(\frac{D}{L_{TB}}\right)}}{\underbrace{\partial z^{*2}}_{o(1)}}\right] \qquad (6\text{-}17)$$

Additionally, the momentum equations in z-direction results into the following orders:

$$\left(\frac{D}{2L_{TB}}\right)^2 \frac{\overbrace{\partial\hat{w}}^{o(1)}}{\underbrace{\partial\hat{t}}_{o(1)}} + \left(\frac{D}{2L_{TB}}\right) \overbrace{\hat{u}}^{o\left(\frac{D}{L_{TB}}\right)} \frac{\overbrace{\partial\hat{w}}^{o(1)}}{\underbrace{\partial x^*}_{o(1)}} + \left(\frac{D}{2L_{TB}}\right) \overbrace{\hat{v}}^{o\left(\frac{D}{L_{TB}}\right)} \frac{\overbrace{\partial\hat{w}}^{o(1)}}{\underbrace{\partial y^*}_{o(1)}} + \left(\frac{D}{2L_{TB}}\right)^2 \overbrace{\hat{w}}^{o(1)} \frac{\overbrace{\partial\hat{w}}^{o(1)}}{\underbrace{\partial z^*}_{o(1)}}$$

$$= \left[\underbrace{Ga_R}_{o\left(\frac{D}{L_{TB}}\right)} \quad \underbrace{g_z{}^*}_{o\left(\frac{D}{L_{TB}}\right)}\right]_{very\ small\ order} - \left(\frac{D}{2L_{TB}}\right)\frac{\partial\hat{p}}{\partial z^*} + \left[\frac{\overbrace{\partial^2\hat{w}}^{o(1)}}{\underbrace{\partial x^{*2}}_{o(1)}} + \frac{\overbrace{\partial^2\hat{w}}^{o(1)}}{\underbrace{\partial y^{*2}}_{o(1)}} + \left(\frac{D}{L_{TB}}\right)^2 \frac{\overbrace{\partial^2\hat{w}}^{o(1)}}{\underbrace{\partial z^{*2}}_{o(1)}}\right] \tag{6-18}$$

It can be concluded from equations (6-16) to (6-18) that the inertia terms are of the order $o\left(\frac{D}{L_{TB}}\right)^2$, while, the viscous terms are of the order $o\left(\frac{D}{L_{TB}}\right)$ in equations (6-16) and (6-17) and of the order $o(1)$ in equation (6-18). Accordingly, the momentum equations in all directions can be expressed in the following form:

$$\left(\frac{D}{2L_{TB}}\right)^2 \frac{\partial\hat{u}}{\partial\hat{t}} = -\left(\frac{D}{2L_{TB}}\right)\frac{\partial\hat{p}}{\partial x^*} + \left[\frac{\partial^2\hat{u}}{\partial x^{*2}} + \frac{\partial^2\hat{u}}{\partial y^{*2}}\right] \tag{6-19}$$

$$\left(\frac{D}{2L_{TB}}\right)^2 \frac{\partial\hat{v}}{\partial\hat{t}} = Ga_R g_y{}^* - \left(\frac{D}{2L_{TB}}\right)\frac{\partial\hat{p}}{\partial y^*} + \left[\frac{\partial^2\hat{v}}{\partial x^{*2}} + \frac{\partial^2\hat{v}}{\partial y^{*2}}\right] \tag{6-20}$$

$$\left(\frac{D}{2L_{TB}}\right)^2 \frac{\partial\hat{w}}{\partial\hat{t}} = -\left(\frac{D}{2L_{TB}}\right)\frac{\partial\hat{p}}{\partial z^*} + \left[\frac{\partial^2\hat{w}}{\partial x^{*2}} + \frac{\partial^2\hat{w}}{\partial y^{*2}}\right] \tag{6-21}$$

Although, the local inertia terms have a small order of magnitude o $\left(\frac{D}{2L_{TB}}\right)^2$, they are kept only to account for the time-dependent nature of the equations (unsteadiness).

Hence, it can be concluded that the flow is governed solely by the reduced Galilei number (Ga_R) with the order of magnitude $o\left(\frac{D}{L_{TB}}\right)$.

On the gas-liquid interface, the following conditions are applied:

$$0 = Ga_R g_x{}^* - \left[\left(\frac{D}{2L_{TB}}\right)\frac{\partial\hat{p}}{\partial x^*}\right]_S + \left[\frac{\partial^2\hat{u}}{\partial x^{*2}} + \frac{\partial^2\hat{u}}{\partial y^{*2}}\right]_S + \left[\frac{Ga_R}{Eo}\sigma_x{}^* K^*\right]_S \tag{6-22}$$

$$0 = Ga_R g_y{}^* - \left[\left(\frac{D}{2L_{TB}}\right)\frac{\partial\hat{p}}{\partial y^*}\right]_S + \left[\frac{\partial^2\hat{v}}{\partial x^{*2}} + \frac{\partial^2\hat{v}}{\partial y^{*2}}\right]_S + \left[\frac{Ga_R}{Eo}\sigma_y{}^* K^*\right]_S \tag{6-23}$$

$$\left(\frac{D}{2L_{TB}}\right)^2 \frac{\partial \widehat{w}}{\partial \hat{t}} + \left(\frac{D}{2L_{TB}}\right)^2 \widehat{w} \frac{\partial \widehat{w}}{\partial z^*} = Ga_R \left[g_z{}^* + \frac{1}{Eo}\sigma_z{}^* K^*\right]_S - \left[\left(\frac{D}{2L_{TB}}\right)\frac{\partial \hat{p}}{\partial z^*}\right]_S + \left[\frac{\partial^2 \widehat{w}}{\partial x^{*2}} + \frac{\partial^2 \widehat{w}}{\partial y^{*2}}\right]_S \tag{6-24}$$

Applying the same analysis to the boundaries (equations (6-22) to (6-24)) would give the following:

$$0 = \underbrace{Ga_R}_{o\left(\frac{D}{L_{TB}}\right)} \underbrace{g_x{}^*}_{o\left(\frac{D}{L_{TB}}\right)} - \left[\left(\frac{D}{2L_{TB}}\right)\frac{\partial \hat{p}}{\partial x^*}\right]_S + \left[\frac{\overbrace{\partial^2 \hat{u}}^{o\left(\frac{D}{L_{TB}}\right)}}{\underbrace{\partial x^{*2}}_{o(1)}} + \frac{\overbrace{\partial^2 \hat{u}}^{o\left(\frac{D}{L_{TB}}\right)}}{\underbrace{\partial y^{*2}}_{o(1)}}\right]_S + \left[\frac{\overbrace{Ga_R}^{o\left(\frac{D}{L_{TB}}\right)}}{\underbrace{Eo}_{o\left(\frac{L_{TB}}{D}\right)}} \underbrace{\sigma_x{}^*}_{o(1)} \underbrace{K^*}_{o(1)}\right]_{S_S} \tag{6-25}$$

$$0 = \underbrace{Ga_R}_{o\left(\frac{D}{L_{TB}}\right)} \underbrace{g_y{}^*}_{o(1)} - \left[\left(\frac{D}{2L_{TB}}\right)\frac{\partial \hat{p}}{\partial y^*}\right]_S + \left[\frac{\overbrace{\partial^2 \hat{v}}^{o\left(\frac{D}{L_{TB}}\right)}}{\underbrace{\partial x^{*2}}_{o(1)}} + \frac{\overbrace{\partial^2 \hat{v}}^{o\left(\frac{D}{L_{TB}}\right)}}{\underbrace{\partial y^{*2}}_{o(1)}}\right]_S + \left[\frac{\overbrace{Ga_R}^{o\left(\frac{D}{L_{TB}}\right)}}{\underbrace{Eo}_{o\left(\frac{L_{TB}}{D}\right)}} \underbrace{\sigma_y{}^*}_{o(1)} \underbrace{K^*}_{o(1)}\right]_S \tag{6-26}$$

$$\left(\frac{D}{2L_{TB}}\right)^2 \frac{\overbrace{\partial \widehat{w}}^{o(1)}}{\underbrace{\partial \hat{t}}_{o(1)}} + \left(\frac{D}{2L_{TB}}\right)^2 \overbrace{\widehat{w}}^{o(1)} \frac{\overbrace{\partial \widehat{w}}^{o(1)}}{\underbrace{\partial z^*}_{o(1)}} = \underbrace{Ga_R}_{o\left(\frac{D}{L_{TB}}\right)} \left[\underbrace{g_z{}^*}_{o\left(\frac{D}{L_{TB}}\right)} + \frac{1}{\underbrace{Eo}_{o\left(\frac{L_{TB}}{D}\right)}} \underbrace{\sigma_z{}^*}_{o(1)} \underbrace{K^*}_{o(1)}\right]_S - \left[\left(\frac{D}{2L_{TB}}\right)\frac{\partial \hat{p}}{\partial z^*}\right]_S + \left[\frac{\overbrace{\partial^2 \widehat{w}}^{o(1)}}{\underbrace{\partial x^{*2}}_{o(1)}} + \frac{\overbrace{\partial^2 \widehat{w}}^{o(1)}}{\underbrace{\partial y^{*2}}_{o(1)}}\right]_S \tag{6-27}$$

Hence, for the boundaries, if the surface tension is assumed to have the same order as the gravity term, this implies that Eötvös number (Eo) should be of order $o\left(\frac{L_{TB}}{D}\right)$.

To sum up, based on the dimensionless analysis of the equations of motions followed by order of magnitude analysis in all directions and on the boundaries the following conclusions are drawn for the near horizontal pipe case ($70° < \gamma \leq 90°$):

1. In order to keep the continuity equation intact, $\hat{u}$ and $\hat{v}$ should be of the order $o\left(\frac{D}{L_{TB}}\right)$;
2. The flow is governed solely by the reduced Galilei number (Ga_R) with the order of magnitude $o\left(\frac{D}{L_{TB}}\right)$;

3. If the surface tension applied to the boundaries, is assumed to have the same order as the gravity term, Eötvös number (Eo) should be of the order $o\left(\frac{L_{TB}}{D}\right)$.

When the pipe is approximately horizontal, that is for $\gamma \approx 90°$, with the conditions that the absence of the axial pressure gradient $\left(\frac{\partial \hat{p}}{\partial z^*}\right)$, and the bubble is approximately stagnant axially ($\hat{w} \approx 0$), the governing equations reduce to the following form:

$$\left(\frac{D}{2L_{TB}}\right)^2 \frac{\partial \hat{u}}{\partial \hat{t}} = -\left(\frac{D}{2L_{TB}}\right)\frac{\partial \hat{p}}{\partial x^*} + \left(\frac{\partial^2 \hat{u}}{\partial x^{*2}} + \frac{\partial^2 \hat{u}}{\partial y^{*2}}\right) \tag{6-28}$$

$$\left(\frac{D}{2L_{TB}}\right)^2 \frac{\partial \hat{v}}{\partial \hat{t}} = Ga_R {g_y}^* - \left(\frac{D}{2L_{TB}}\right)\frac{\partial \hat{p}}{\partial y^*} + \left(\frac{\partial^2 \hat{v}}{\partial x^{*2}} + \frac{\partial^2 \hat{v}}{\partial y^{*2}}\right) \tag{6-29}$$

$$\frac{\partial \hat{u}}{\partial x^*} + \frac{\partial \hat{v}}{\partial y^*} = 0 \tag{6-30}$$

The limiting case when the bubble is stagnant in an entirely horizontal pipe ($\gamma = 90°$) gives the following equations for the boundaries:

$$0 = \rho_L g_x - \frac{\partial p}{\partial x} + K\sigma_x \tag{6-31}$$

$$0 = \rho_L g_y - \frac{\partial p}{\partial y} + K\sigma_y \tag{6-32}$$

The following dimensionless variables can be used to perform dimensionless analysis for the governing equations in the horizontal pipe case:

$$x^* = \frac{x}{(D/2)}, y^* = \frac{y}{(D/2)}, \bar{p} = \frac{p}{\rho_L g \frac{D}{2}}, {g_x}^* = \frac{g_x}{g}, {g_y}^* = \frac{g_y}{g}, {\sigma_x}^* = \frac{\sigma_x}{\sigma},$$
$$\sigma_y^* = \frac{\sigma_y}{\sigma}, K^* = \frac{K}{(1/D^2)} \tag{6-33}$$

The final form of the dimensionless governing equations for the horizontal pipe case is given by:

$$0 = {g_x}^* - \frac{\partial \bar{p}}{\partial x^*} + \frac{K^* {\sigma_x}^*}{Eo} \tag{6-34}$$

$$0 = g_y{}^* - \frac{\partial \bar{p}}{\partial y^*} + \frac{K^* \sigma_y{}^*}{Eo} \tag{6-35}$$

To put it briefly, it is obvious that equations (6-34) and (6-35) govern the static pressure distribution around the stagnant deformed bubble. The primary governing parameter that regulates the pressure filed is Eötvös number, where Galilei number also ceases to be effective and Reynolds and Froude numbers are no longer influencing parameters. Additionally, for Taylor bubble to exist in a horizontal pipe, large values of Eötvös number are needed. Hence, for large Eötvös number values, equations (6-34) and (6-35) would lead to the following:

$$\begin{gathered} \frac{\partial \bar{p}}{\partial x^*} = 0 \; and \; \frac{\partial \bar{p}}{\partial y^*} = g_y{}^* \\ Therefore \; \frac{dp}{dy} = g_y{}^* = g \end{gathered} \tag{6-36}$$

$$Therefore \; p = gy + c \tag{6-37}$$

It can be concluded from (6-37) that linear pressure distribution is responsible for developing the stagnant deformed bubble in a horizontal pipe with large Eötvös number.

In summary, the dimensionless analysis based on both methods discussed, Buckingham-Pi theorem and the dimensionless analysis of governing equations, show the following:

- For the near horizontal cases $(70° < \gamma < 90°)$, where the drift velocity is vanishingly small, the main physical parameters influencing the flow are the so-called reduced Galilei number (Ga_R) and Eötvös number, with the following magnitudes that Ga_R should be of order $o\left(\frac{D}{L_{TB}}\right)$ and Eo should be of the order $\left(\frac{L_{TB}}{D}\right)$, noticing that the Reynolds and Froude numbers are vanishingly small and are no more considered as influencing parameters.
- For the horizontal pipe case, that is for $\gamma = 90°$, the sole governing parameter that governs the pressure field distribution around the stagnant deformed bubble is Eötvös number (Eo). On the other hand, the reduced Galilei number (Ga_R) is no longer considered as an effective governing parameter, whereas Reynolds and Froude numbers are no longer considered as influencing parameters.

Regarding the independence of the cylindrical bubbles' velocity of the Taylor bubble length provided that the bubble is long enough (more than $1.5D_{pipe}$), the effect of the ratio of bubble size to the pipe diameter $(L_{TB}/D)_i$ is considerably negligible throughout this study. Accordingly, to support the developed logical approach to the problem, the main dynamic features of an individual Taylor bubble drifting through stagnant Newtonian liquids in an inclined pipe $(70° < \gamma \leq 90°)$ are investigated by applying computational fluid dynamics (CFD) simulation.

6.3 CFD Model Development

The 3D model, given in chapter 5, is used to simulate the drift of an individual Taylor bubble in a near horizontal pipe $(70° < \gamma < 90°)$ with stagnant liquid. However, there are some modifications done to the model to be applicable to predict the bubble dynamics in these inclination angles. This section discusses these modifications adapted to the 3D inclined model given in chapter 5. Additionally, in the horizontal pipe case, the developed bubble eventually has an infinite length. The problem can be simplified using a 2D-steady solution, where the only governing parameter is Eo, which governs the static pressure distribution around the stagnant deformed bubble. This simplified 2D model is used as well to predict the bubble dynamics in a near horizontal pipe (up to 5° with respect to the horizontal position). Hence, this section gives also details about the simplified 2D model.

6.3.1 The 3D Inclined Model -Modifications

In a near horizontal pipe, the developed bubble length increases significantly until it reaches an eventually infinite length in a horizontal pipe. Hence, to ensure the solution is not affected by either the boundaries of the pipe (pipe top and bottom) nor by the length of the developed Taylor bubble, a larger domain is used in these inclination ranges. Different lengths of the computational domain are tested, and it is concluded that a length of $14D_{pipe}$ is appropriate to simulate most of the cases investigated. The second modification is done to the distance from the pipe bottom, given by h_B, as shown in Figure 6-1. In chapter 5, it is fixed to $1.5D_{pipe}$ in all simulations. However, for the near horizontal pipe simulation cases, it is sometimes modified to 3D$_{pipe}$ for inclination angles ($\gamma = 87°$) with respect to the vertical position. However, for larger inclination angles ($89° \leq \gamma \leq 90$), the initial bubble is placed at the centre of the pipe.

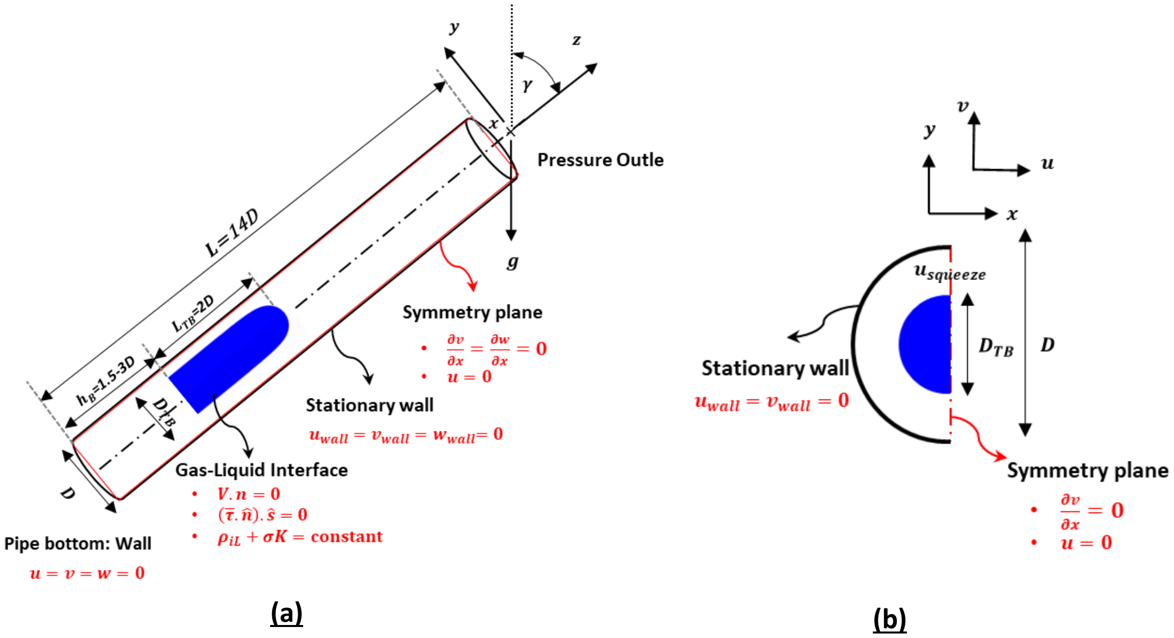

Figure 6-1. Schematic representation of the computational domain with the initial and boundary conditions for (a) 3D inclined model and (b) simplified 2D model.

6.3.2 Simplified 2D Model

Based on the discussion given in section 6.2.2, it can be seen that for the near horizontal pipe, the governing equations are 2D. Subsequently, a simplified 2D model is suggested to predict the developed Taylor bubble shape in these inclination ranges (up to 5° with respect to the horizontal position).

Figure 6-1 shows a schematic representation of the computational domain with the initial and boundary conditions for the 3D inclined model, with the modifications discussed above and the simplified 2D model. Details about the computational domain for the inclined pipe configuration and the initial bubble shape are discussed in chapter 3.

The 2D model is considered as xy section in the 3D model. Hence, the 2D solution domain is a circle with a diameter (D) and initial Taylor bubble with a diameter (D_{TB}). The effect of inclination is given by setting the angle between the pipe's axis and the gravity vector. Subsequently, it can be given through the gravitational vector components.

The initial and boundary conditions for the 3D inclined model are discussed in detail in chapter 3 and chapter 5. Referring to Figure 6-1, the boundary conditions are; at the wall no-slip condition is applied with $u_{wall} = v_{wall} = w_{wall} = 0$, and zero normal velocity and zero normal gradients for all variables at the symmetry plane. Additionally, all the velocity components are set at zero. Moreover, it is worth to mention that different Taylor bubble shapes, sizes and locations are tested, and they almost give the same solution for the 2D model. The only difference is in the convergence process. However, the selected Taylor bubble initial shape and location shows a well-converged solution.

Lastly, the initial 2D shape is simulated while tracking the developed Taylor bubble shape and the maximum squeeze liquid velocity in the liquid film until a steady terminal developed bubble shape is reached and a squeeze liquid velocity $u_{squeeze}$ reaches a value of 0.01m/s.

6.4 Results and Discussions

In this section, the main findings of this chapter are discussed. The results are divided into two main sections; section 6.4.1 covers the near horizontal section for the pipe inclination range of $70° < \gamma < 90°$, with the reduced Galilei number and Eötvös number acting as the main influencing parameters and section 6.4.2 examines the horizontal pipe section for $\gamma = 90°$ with Eötvös number being the only influencing parameter. In each section, the dynamics of the Taylor bubbles include the final shape of the developed Taylor bubble, the flow field around it (streamlines) and the Taylor bubble terminal drift velocity.

6.4.1 Near Horizontal Pipe ($70° < \gamma < 90°$)

As explained earlier, the dynamics of the Taylor bubble in this inclination range is governed mainly by the reduced Galilei number (Ga_R) and Eötvös number (Eo). To support the results of this dimensionless analysis, selected cases with inclination angles of 75° and 85°, Eötvös number values of 66 and 100, and Galilei number of 15, 50, and 200 are simulated. Table 6-1 shows the simulation cases with their corresponding results. These cases are based on the cases given in chapter 4. The average predicted ratio of the bubble size to the pipe diameter is given by $(L_{TB}/D)_{Pr}$. It should be pointed out that significant elongation in Taylor bubble length has been noticed for this inclination range with an infinite Taylor bubble length established in a horizontal pipe. Thus, a longer domain is essential for these cases with pipe length fixed to 14D$_{pipe}$.

Table 6-1. Simulation cases used to explore the effect of both reduced Galilei number (Ga_R) and Eötvös number (Eo) on the dynamics of the Taylor bubble for the inclination angle range of $70° < \gamma < 90°$*, with their corresponding results.*

Input Parameters				Predicted Values						
						Bubble Front region		Bubble body region		Bubble Tail region
Case No.	γ	Eo	Ga_R	Fr_{v_d}	$\left(\frac{L_{TB}}{D}\right)_{P}$	$\left(\frac{Z'_I}{D}\right)$	$\left(\frac{y_{tip}}{D}\right)$	$\left(\frac{\delta_{LF_I}}{D}\right)$	$\left(\frac{\tau_W}{\rho_L g D}\right)_{ma}$	$\left(\frac{L_{min_I}}{D}\right)$
Reduced Galilei number (Ga_R)										
1	75	66	15	0.0491	3.876	0.7449	0.2924	0.5007	0.4276	0.4331
	85			0.0262	5.033	0.7194	0.3367	0.5978	0.4405	0.5027
2	75	66	50	0.0875	3.830	0.7545	0.2937	0.4838	0.4235	0.4364
	85			0.0470	5.008	0.7202	0.3382	0.5985	0.4380	0.5051
3	75	66	200	0.1602	3.658	0.7613	0.2953	0.4818	0.4151	0.4560
	85			0.0916	4.972	0.7243	0.3390	0.5910	0.4273	0.5122
Effect of Eötvös number (Eo)										
4	75	66	200	0.1602	3.658	0.7613	0.2953	0.4818	0.4151	0.4560
	85			0.0916	4.972	0.7243	0.3390	0.5910	0.4273	0.5122
5	75	100	200	0.1696	3.878	0.7626	0.2920	0.4950	0.4138	0.3364
	85			0.1041	5.506	0.7194	0.3345	0.5964	0.4265	0.4009

6.4.1.1 Effect of Reduced Galileo Number

The Taylor bubble drift velocity significantly decreases for the pipe inclination range of $70° < \gamma < 90°$, until the bubble stops moving in the horizontal orientation. Based on that, the reduced Galilei number (Ga_R), which represents the ratio between the gravitational and the viscous forces based on characteristic velocity (v_s) that treats low Reynolds values, is suggested to govern the bubble dynamics. To explore the effect of Ga_R on the dynamics of Taylor bubbles, Table 6-1 shows the simulation cases with their corresponding results.

Figure 6-2 shows the terminal bubble shape and the streamlines in the yz plane for cases 1 and 3 in Table 6-1 for Ga_R values of 15 and 200. Long, streamlined bubbles are noticed to develop for this inclination range for all Ga_R values. The bubble occupies the upper part of the pipe with a thinly formed upper liquid film. With regards to cases 1 to 3 in Table 6-1, it can be noted that the increase in Ga_R values increases the bubble motion, but generally, all cases has low Fr_{v_d}values.

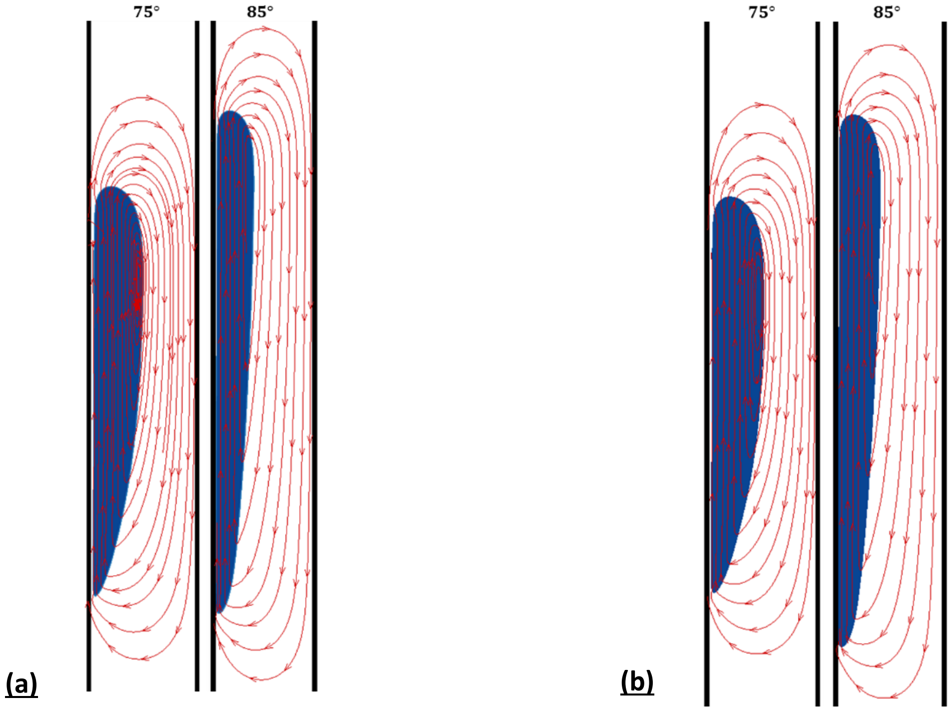

Figure 6-2. Streamlines in yz plane for the inclination angle range of $75° \leq \gamma < 90°$ *(a)* $Ga_R = 15$, *(b)* $Ga_R = 200,$ *with* $Eo = 66.$

The effect of Ga_R on the main hydrodynamic characteristics of Taylor bubbles in inclined pipes is similar to the role of Re_{v_d} in the inclined pipe cases, discussed in chapter 5. The increase in Ga_R reduces the length of developed Taylor bubble. The reduction in viscous forces enhances larger distances to balance the gravity force in both the bubble nose and tail region $\left(\frac{Z'_I}{D} \;\&\; \frac{L_{min_I}}{D}\right)$. Wider bubble are noticed with higher values of Ga_R, which is reflected in lower $\left(\frac{\delta_{LF_I}}{D}\right)$. The dimensionless wall shear stress decreases as Ga_R increases.

6.4.1.2 Effect of Eötvös number

The effect of Eötvös number on the dynamics of Taylor bubbles in near horizontal cases is investigated for cases 4 and 5 in Table 6-1, with a fixed Ga_R value of 200 and Eötvös number values of 66 and 100. Streamlined bubbles are also noticed to develop for all Eo values. Figure 6-3 shows the effect of Eo on the bubble shape profile for cases 4 and 5 in Table 6-1. It can be noticed that the increase in Eo values reduces the sizes of the developed bubble as well as enhances its elongation. This is reflected into higher values of $\left(\frac{\delta_{LF_I}}{D}\right)$ with the increase in

Eo values. Additionally, the increase in Eo reduces the interaction distances in both the bubble nose and tail region $\left(\frac{Z'_I}{D} \;\&\; \frac{L_{min_I}}{D}\right)$.

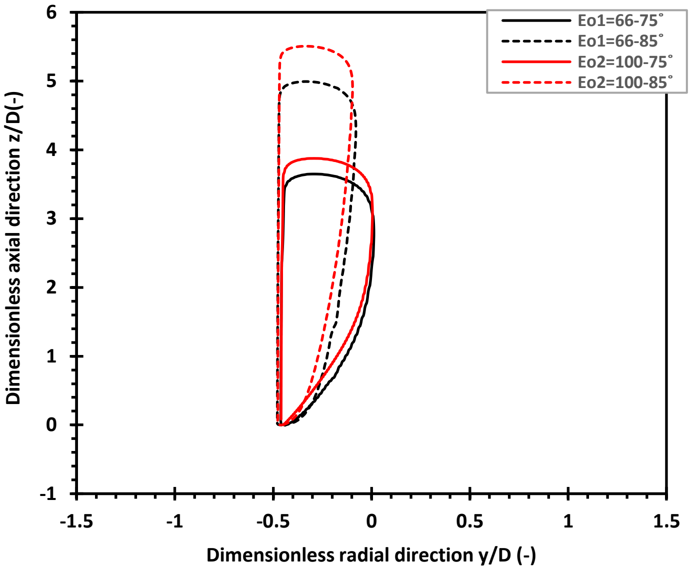

Figure 6-3. Bubble shape profile for inclination angle range $75° \le \gamma < 90°$ *(a)* $Eo = 66$, *(b)* $Eo = 100$, *with* $Ga_R = 200$.

It can be concluded that the bubble motion in this inclination range is considerably low in comparison to other inclination angles. The effect of the reduced Galilei number is mainly reflected in the bubble's motion, however, the bubble's length does not significantly change with Ga_R. Eo effect is still vital similar to the other inclination angles. The effect of Eo can be seen in the developed bubble length and size, bubble shape, as well as Fr_{v_d} values. Additionally, it is worth mentioning that according to the simulated cases, larger values of Eo ($Eo \ge 40$) are essential for the Taylor bubble to exist within this inclination range.

The governing equations, given in section 6.2.2, show that when the pipe inclination approaches the horizontal position ($\gamma \approx 90°$), the problem can be approximated using the 2D-transient analysis. To support this conclusion, for inclination angles of 85°, 87° and 89°, the 3D transient model is tested against the 2D-transient model, as indicated in Figure 6-4 to Figure 6-6. It is worth mentioning that Eo is of order $o\left(\frac{L_{TB}}{D}\right)$ for all these angles of inclination.

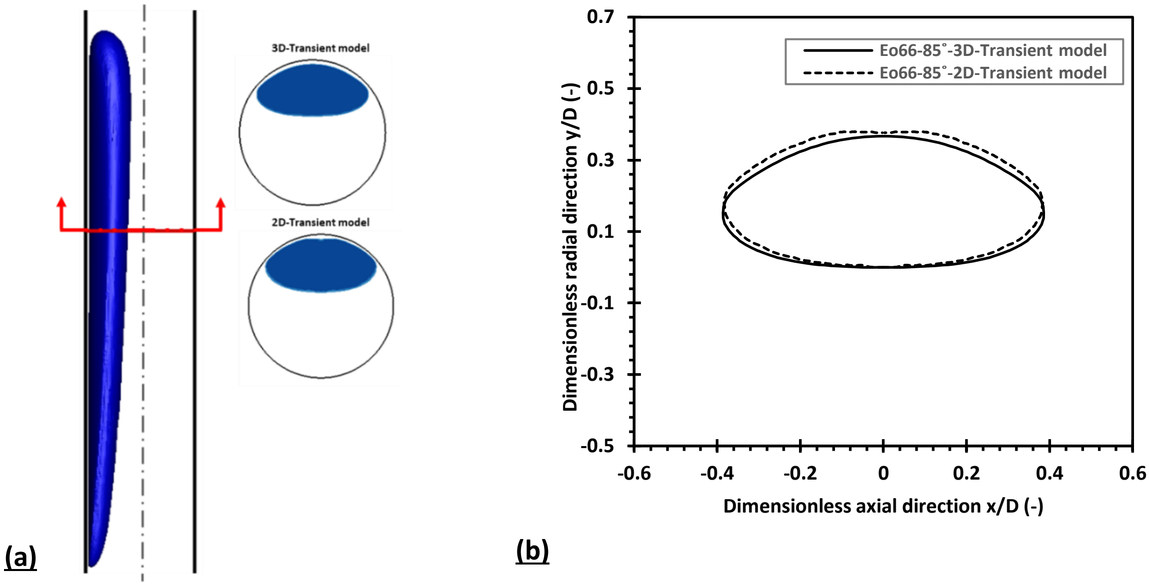

Figure 6-4. (a) Developed 3D Taylor bubble shape in the yz plane for inclination angle $85°$ *(*$Eo = 66$ *and* $Ga_R = 200$*) and (b) bubble shape profile using the 3D-Transient model and the 2D-Transient model.*

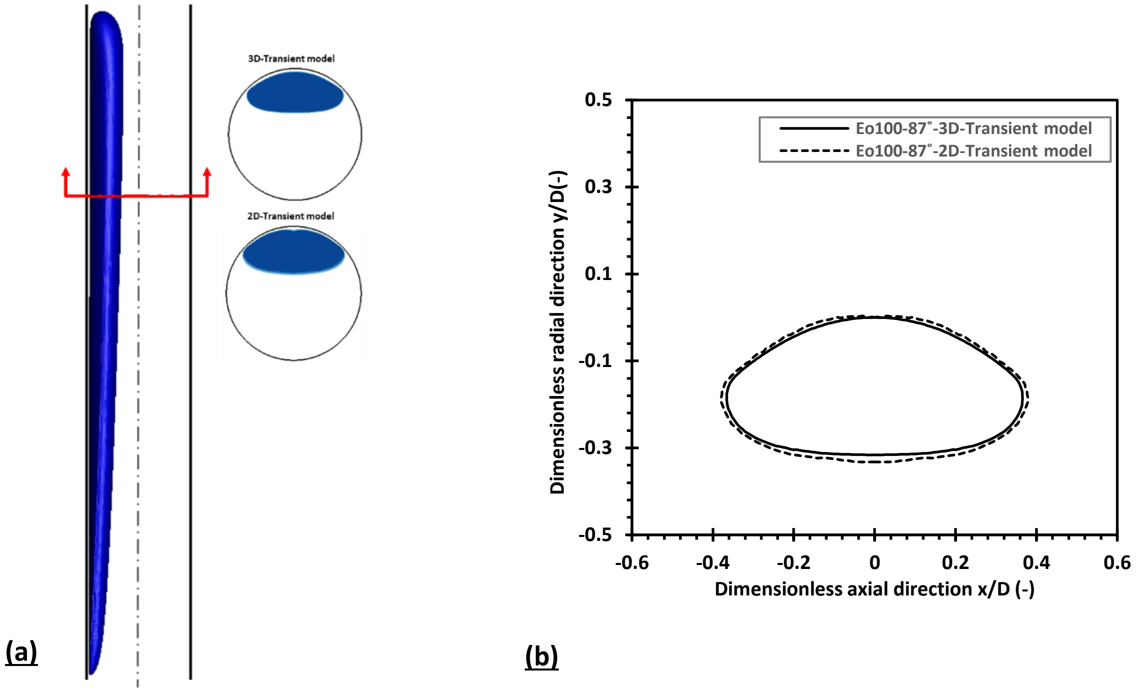

Figure 6-5. (a) Developed 3D Taylor bubble shape in the yz plane for inclination angle $87°$ *(*$Eo = 10$ *and* $Ga_R = 200$*) and (b) bubble shape profile using the 3D-Transient model and the 2D-Transient model.*

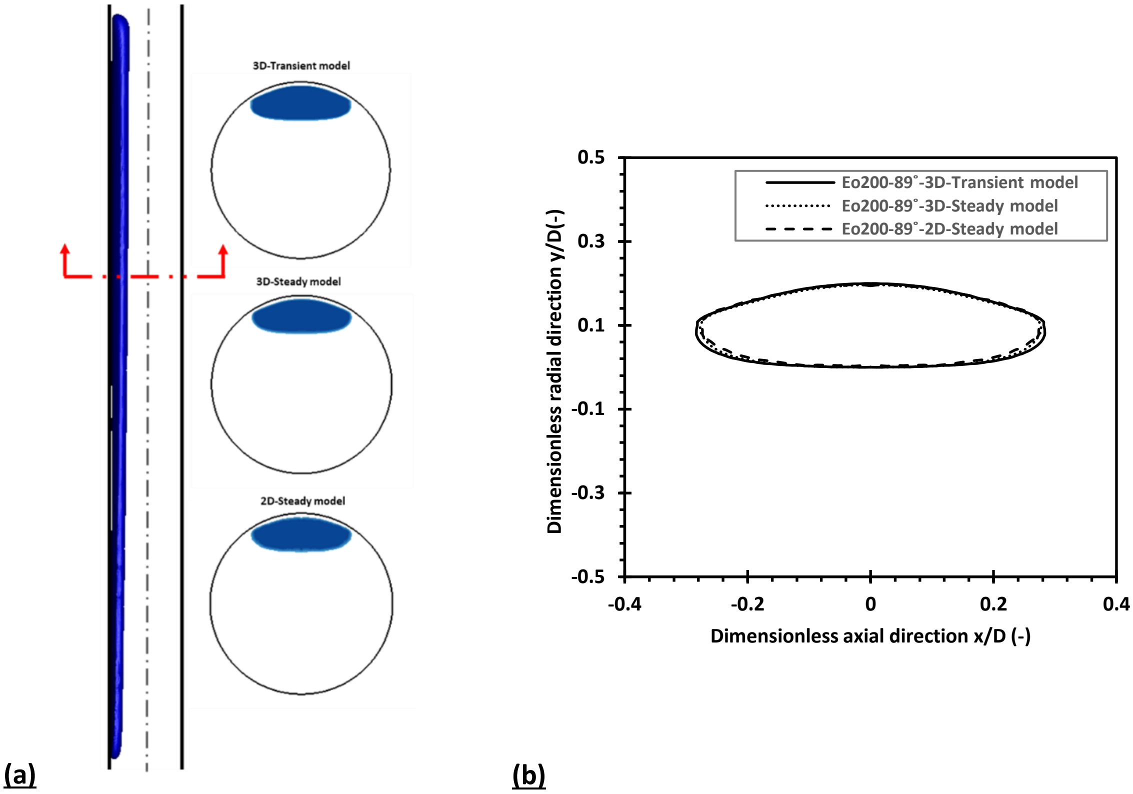

Figure 6-6. (a) Developed 3D Taylor bubble shape in the yz plane for inclination angle $89°$ *(*$Eo = 200$ *and* $Ga_R = 200$*) and (b) bubble shape profile using the 3D-Transient model, the 3D-steady model and the 2D-steady model.*

However, as the inclination angle moves towards the horizontal position, the developed bubble's length becomes significantly large. Hence, for instance, for an angle of 85° Eo should be ≥ 40 to ensure a stable formation of the Taylor bubble, while larger angles, such as 89°, Eo should be ≥ 100. It can be generally deduced that the 2D-transient model can offer an approximate solution for Taylor bubble shapes for angles of 85° to 87°. However, for larger angles ($\gamma = 89°$) the solution can be more simplified by using the 2D-steady model.

6.4.2 Horizontal Pipe ($\gamma = 90°$)

As the pipe inclination approaches the horizontal orientation, the bubble velocity diminishes until it becomes zero at the horizontal position. In literature, various discussions are describing the bubble behaviour in horizontal pipes. For instance, based on the fact that gravity does not act in a horizontal direction, Wallis (1969) and Dukler and Hubbard (1975) state that there is no bubble motion in a horizontal system. Whereas, others suggest that the bubble propagates in the horizontal pipe due to the pressure difference between the top and the bottom of the bubble nose(Weber, 1981; Bendiksen, 1984) which is not the case for the present zero pressure gradient analysis.

In the literature, most of the experimental work measures the bubble velocity at different inclinations including the horizontal position either by measuring the liquid drainage velocity or by creating an axial pressure gradient, by opening the pipe's top, that enhances the bubble motion (Spedding and Nguyen, 1978; Weber, 1981; Gokcal et al., 2010; Jeyachandra et al., 2012). However, the main argument is that the Froude number's estimation should not be based on either of these cases. Hence, the present work is based on the real case with zero axial pressure gradient analysis in a horizontal pipe.

In the horizontal pipe case, the developed bubble eventually has an infinite length. The problem can be simplified using a 2D-steady solution, where the only governing parameter is Eo, which governs the static pressure distribution around the stagnant deformed bubble. A selected case with a high Eo value of 300 is simulated using the 3D-transient model, 3D-steady model and the simplified 2D-steady model. As indicated in Figure 6-7, the 2D-steady model successfully predicts the developed Taylor bubble shape.

Additionally, the dimensionless analysis given in section 6.2 shows that pressure distribution around the developed stagnant liquid is linear. Hence, to support this conclusion, Figure 6-8 (a) shows the linear pressure distribution around the developed deformed stagnant Taylor bubble in a horizontal pipe using the 2D-steady model.

Additionally, Figure 6-8 (b) shows the squeeze velocity in the liquid film as vectors around the deformed bubble. It can be seen that the simulation is stopped when this velocity is almost approaching zero value.

Finally, using the 2D-steady model, the effect of Eo on the predicted Taylor bubble can be investigated using Eo values of 300, 500, 700 and 1000. It can be concluded from Figure 6-9, that Eo affects the size of the developed Taylor bubble, where the increase in Eo leads to a more flattened bubble.

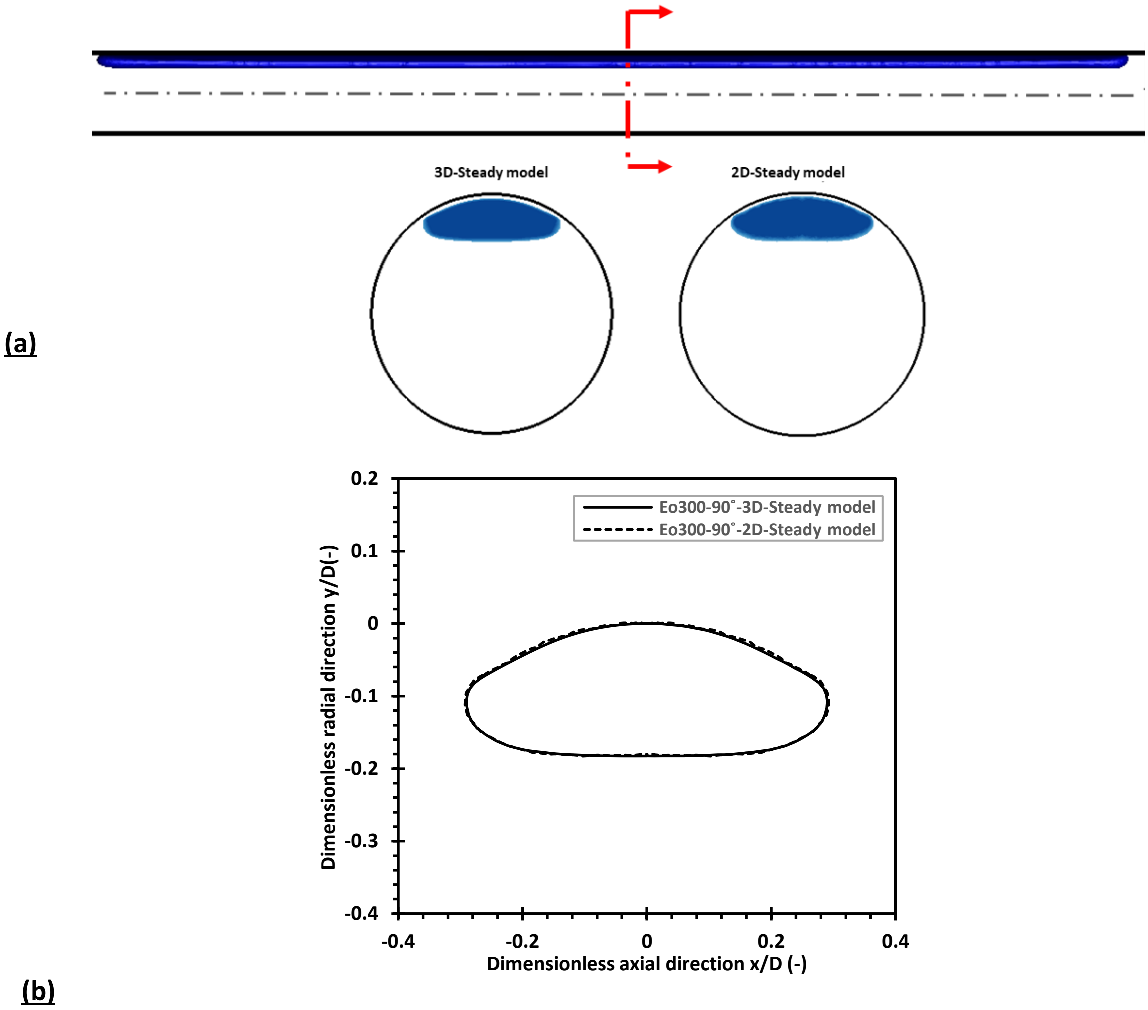

Figure 6-7. (a) Developed 3D Taylor bubble shape in the yz plane for horizontal pipe ($\gamma = 90°$) with $Eo = 300$ and (b) bubble shape profile using thr 3D-steady model and the 2D-steady model.

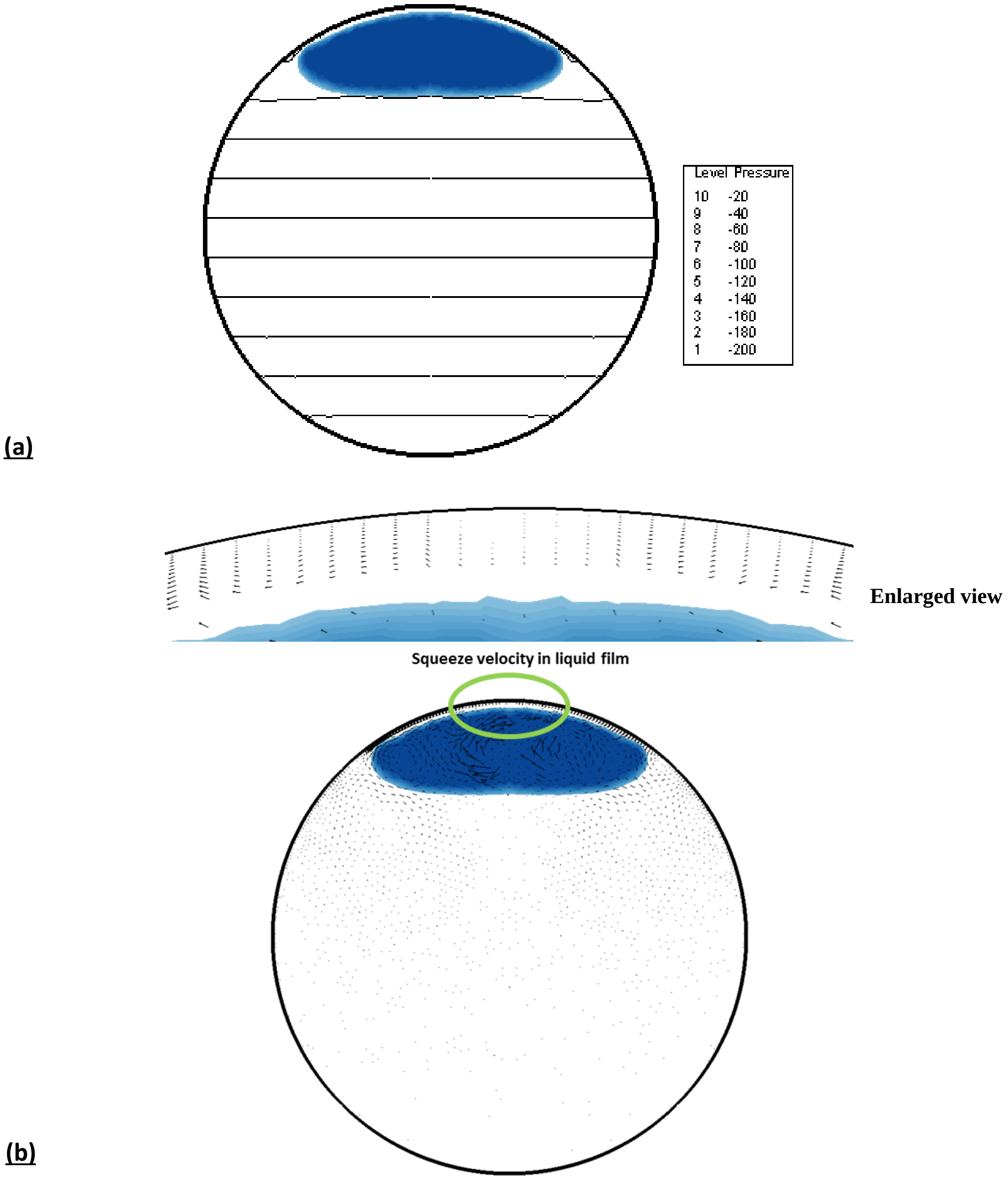

Figure 6-8. (a) The pressure distribution around the deformed stagnant Taylor bubble in a horizontal pipe horizontal pipe ($\gamma = 90°$) with $Eo = 300$ and (b) velocity vectors around the deformed Taylor bubble showing the squeeze velocity in the liquid film with an enlarged view.

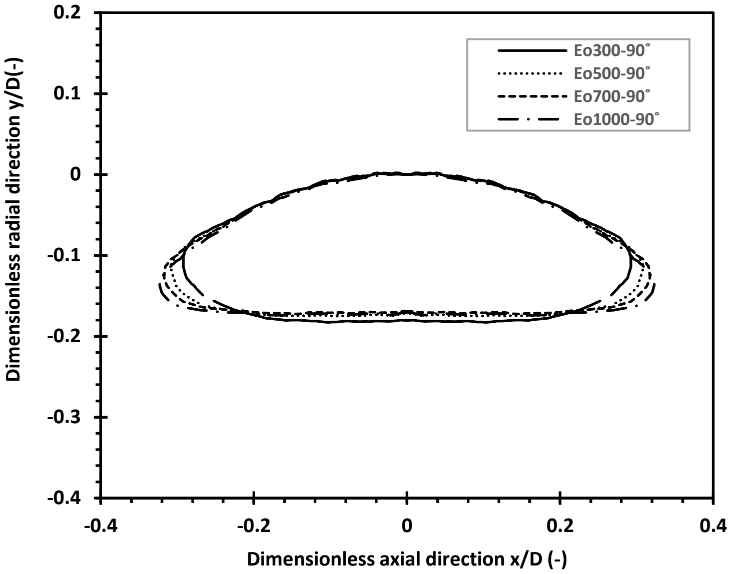

Figure 6-9. Effect of Eo *on the bubble shape profile for the horizontal pipe* ($\gamma = 90°$) *using the 2D-steady model for* $Eo = 300$, $Eo = 500$, $Eo = 70$ *and* $Eo = 1000$.

6.5 Concluding Remarks

The main purpose of this chapter is to perform a complete dimensionless analysis of single Taylor bubble drifting through a stagnant Newtonian liquid in a near horizontal and horizontal pipe, followed by order of magnitude analysis of the equations of motion. The main conclusion reached is that different governing parameters appear according to the range of pipe inclination angle. For the near horizontal cases ($70° < \gamma < 90°$) the main physical parameters influencing the flow are the so-called reduced Galilei number and Eötvös number, while taking into consideration that the Reynolds and Froude numbers are vanishingly small and are no longer acting as influencing parameters. As for the horizontal pipe case, the pressure field distribution around the stagnant deformed bubble is mainly governed by the Eötvös number, where the reduced Galilei number ceases to be effective similar to the Reynolds and Froude numbers. Using the guideline of the order of magnitude analysis and the dimensionless group analysis, a CFD study investigating the dynamics of single Taylor bubble drifting through a stagnant Newtonian liquid in an inclined pipe ($70° < \gamma \leq 90°$) is performed. Specifically, this chapter focuses on the main similarity parameters, that is Eötvös number (Eo) and the reduced Galilei number (Ga_R). The results focus on discussing the developed Taylor bubble shape, the flow field and the Taylor bubble drift velocity.

The main findings of this chapter can be summarised as follows:

- The bubble motion in near horizontal cases is considerably low with significant enhancement in the Taylor bubble length. Thus, a larger domain is essential for these angles. For the main aim of reducing the computational resources, a simplified 2D model, based on the dimensionless analysis developed in this chapter, is suggested to give an approximate solution to estimate the developed Taylor bubble shape.
- Additionally, for the horizontal pipe case, the simplified 2D-steady model effectively predicts the developed deformed stagnant Taylor shape and the linear pressure distributing around it.
- Finally, it can be deduced that the developed numerical results agree well with the order of magnitude analysis. For horizontal pipes, Eo shows different order of magnitude based on a large length of developed Taylor bubble, where larger Eo values are essential for a stable Taylor bubble to exist ($Eo \geq 200$). By using the simplified 2D model, Eo is the only governing parameter that significantly affects the developed Taylor bubble shape and size.

Chapter 7 Conclusions and Recommendations

This chapter summarises the conclusions drawn from this study together with proposed recommendations for future work. It also outlines the contributions and the new insights obtained from this study.

7.1 Discussion

The main aim of this thesis, as described in chapter 1, is performing a better understanding of slug flow in pipes. The slug flow is considered a complex, intermitted and challenging flow encountered in gas-liquid flow in pipes. The thesis focuses on studying the rise of an individual Taylor bubble through a stagnant liquid in pipes, which is considered an essential characteristic part of the slug flow regime in pipes. Understanding the governing parameters and the hydrodynamic characteristics of Taylor bubble flow are considered an essential characteristics part for the successful operation, simulation and optimisation of any system encountering slug flow.

The work given in chapter 2 presents a critical review on gas-liquid slug flow in pipes, specifically to the rise of Taylor bubbles in pipes with stagnant liquid. Based on this review, many studies investigate the problem of the rise of Taylor bubbles through a stagnant liquid in pipes by a number of dimensionless groups. These groups are Froude, Eötvös and Morton numbers. In some cases, other dimensionless groups are used as Archimedes number. It can be concluded that there is a lack of performing an accurate theoretical treatment to the problem. To the best of this author's knowledge, none of the studies investigates the problem using the order of magnitude analysis of equations of motions. This type of analysis is important for the visualisation of the real parameters or groups that influence the equations of motion. Besides, it is important for developing a phenomena-logical approach to the physical problem that can bring up useful relations between the system parameters. In addition, the order of magnitude analysis along with the dimensional analysis provides a way to show the relative merits of the different terms available in the governing equations, which makes the understanding of the problem more pronounced and any simplifications to the governing equations, if available, more reliable.

To achieve the main aim of the thesis a number of objectives are given in chapter 1. These objectives are achieved throughout the thesis and they are summarised in the following paragraphs.

Based on the literature review given in chapter 2, some studies conclude that the Taylor bubble flow starts to experience instabilities when the pipe's inclination reaches approximately 70°.

This is the reason for selecting a criterion for the pipe inclination ranges given in chapter 4, 5 and 6. The main objective, which is performing complete dimensionless analysis to the rise of Taylor bubble through a stagnant liquid in a vertical and inclined pipe, covering inclination range of $0 \leq \gamma \leq 90°$ with respect to the vertical position, is achieved at the beginning of chapters 4,5 and 6. Due to the nature of the problem, the N-S equations of motion has to be placed in different coordinate systems to suit the physical and geometrical nature of the problem under consideration and its boundary conditions. For this reason, three separate dimensionless analysis are given in chapters 4 to 6, covering the vertical and inclined pipe.

The second objective, which is using the guideline of the order of magnitude analysis and the dimensionless group analysis to perform CFD study investigating the dynamics of single Taylor bubble drifting through a stagnant liquid in pipe, is achieved in the second part of chapters 4 to 6. The results cover the three main regions of the flow field, including bubble nose, bubble body and bubble tail regions.

Chapter 3 covers the CFD model details, verification and validation. In chapter 3, two models are discussed in detail, covering the basic model for the vertical pipe case that assumes 2D axisymmetric flow, and the inclined model that is 3D with a symmetry plane model. It is known that two-phase CFD simulations require much longer run-times than single-phase flow. A discussion on the different reference frames, including the fixed and moving reference frames, and the compuattaional resources is given in chapter 3.

The CFD model is validated against published benchmark studies for some of the main hydrodynamic characteristics of the vertical and inclined pipe cases. For the vertical pipe case, the main limitation of the reliability of the experimental data is noticed in the wake measurements, where they use dye for wake measurements that is unable to consider the wake in the concave rear of the bubble. This was overcome by the simulations that accounted for the wake clearly in the whole concave bubble rear. On the other side, for the inclined pipe case, the main conclusion noticed is the differences in the experimental and theoretical prediction of Taylor bubble velocity, specifically in the near horizontal pipe cases. This is clealy discussed in chapter 6, where the last objective, which is understanding the flow of Taylor bubbles in the neighborhood of horizontal pipes, where the drift velocity becomes significantly slow and almost approaching zero at the horizontal pipe case, is achieved. Finally, based on the discussion given in chapter 3, the CFD model shows good correspondence when tested against other important experimental and theoretical data in the literature.

Based on the results developed in chapter 4, the third objective, which is suggesting correlations for Taylor bubble drift velocity and the wall shear stress to support other important theoretical and experimental work available in the literature, is achieved. An important issue is the reliability of the developed correlations that is tested by evaluating the goodness of the fit (checking the error using SSE, R-square and Root mean square) and checking the confidence and the prediction bonds.

An important issue is the implementation of the study performed in the thesis to the oil/gas/offshore industrial applications. It can be seen that the present study can be extended to real oil and gas production system as far as the moving fluid flow Reynolds number in these applications is practically small as is the case for dense liquids available in these systems. Accordingly, the stagnant liquid under investigation in the present work can to some extent predict the actual practical conditions. It is to be noted that Reynolds number can be calculated for dense liquids and their velocities available in the industry to show the low values of Reynolds number.

7.2 Conclusions

The main outcomes of this thesis are summarised as follows:

1. The rise of an individual Taylor bubble in a vertical pipe

- The dimensionless analysis showed that the main dimensionless parameters that govern the problem are $Re_{U_{TB}}$, $Fr_{U_{TB}}$ and Eo numbers and it is useless to use a dimensionless number like Morton number that does not seem to have a direct physical meaning.
- Based on this analysis, the main hydrodynamic features of rising of an individual Taylor bubble through stagnant vertical Newtonian liquid were investigated by applying computational fluid dynamics (CFD) simulation using the volume-of-fluid (VOF) methodology implemented in the commercial software ANSYS Fluent. The dynamics of

Taylor bubbles covered the Taylor bubble rise velocity, Taylor bubble shape, liquid film region and wake region.

- Eo showed a significant effect on all hydrodynamic features of Taylor bubbles. Mainly, the increase in surface tension increases the curvature of the bubble nose. Accordingly, the liquid film thickness increases, which in turns decreases the dimensionless velocity of fully developed falling liquid film. This would finally lead to increase in the wake intensity and size. Strong correspondence was noticed when comparing the numerical results for the flow in the liquid film with the theoretical predictions given by Brown (1965).
- $Re_{U_{TB}}$ showed a similar contribution to Eo number. The effect of $Re_{U_{TB}}$ is mainly noticed in the developed Taylor bubble shape where the shape alters from the long slender shape into shorter and flatter bubbles with the increase in $Re_{U_{TB}}$. Subsequently, this results in a reduction in the liquid film thickness.
- Additionally, the increase in $Re_{U_{TB}}$ consequences to a less viscous effect in the liquid surrounding the Taylor bubble that causes a decrement in wall shear stress. However, the wall shear stress increased with Eo. Though, it should be pointed out that lower values of Eo possessed different distribution for the wall shear stress with noticeable peak value right before the Taylor bubble rear due to the sharp flat and convex shape of the bubble attained at lower values of Eo. According to the developed numerical results, a proposed correlation to predict the maximum wall shear stress was developed and predicted results favourably matching with the theoretical predictions of Brown (1965).
- Furthermore, a phase diagram showing the presence and nature of wake and of the shape of the rear Taylor bubble was developed. For $Eo > 200$, unstable bubbles were developed which were characterized by the presence of small bubbles shedding off from main Taylor bubble into wake region.
- Finally, based on the numerical results and using guidelines from the order of magnitude analysis, a correlation to estimate Taylor bubble rise velocity (U_{TB}) as a function of only

Eo and $Re_{U_{TB}}$ was proposed and showed good prediction when compared with other well-known correlations in literature, especially with Viana et al. (2003)'s correlation.

2. The rise of an individual Taylor bubble in an inclined pipe

- The dimensionless analysis showed that different governing parameters appear according to the range of pipe inclination angle. For inclination range of $0 \leq \gamma \leq 70°$; the problem is mainly governed by Froude, Eötvös and Reynolds numbers. As for near horizontal cases $(70° < \gamma < 90°)$ the main physical parameters influencing the flow are the so-called reduced Galilei number and Eötvös number while taking into consideration that the Reynolds and Froude numbers are vanishingly small and are no longer acting as influencing parameters. Finally, for the horizontal pipe case, the pressure field distribution around the stagnant deformed bubble is mainly governed by the Eötvös number, where the reduced Galilei number ceases to be effectively similar to the Reynolds and Froude numbers.

- Using the guideline of the order of magnitude analysis and the dimensionless group analysis, a CFD study investigating the hydrodynamics of a single Taylor bubble drifting through a stagnant Newtonian liquid in an inclined pipe was performed. Particularly, the current study focused on the main similarity parameters, that is Froude number $\left(Fr_{v_d}\right)$, Reynolds number $\left(Re_{v_d}\right)$, Eötvös number (Eo) and the reduced Galilei number (Ga_R). The main hydrodynamic characteristics included the developed Taylor bubble shape, the flow field and the Taylor bubble drift velocity.

- The bubble motion followed the "peculiar trend" with the inclination angle, where the bubble velocity increases with inclination angle until it reaches a maximum value, then it starts to decrease once again. Bubble elongation was noticed with the increase in the inclination of the pipe.

- The effect of Eo was mainly reflected in both the bubble shape and velocity. The shape of the bubble tail was altered from a convex into a concave structure reflecting into wider wakes with the increase in Eo. The bubble drift velocity was increased due to the gravitational potential increment as a result of an increase in Eo values. Additionally, with larger Eo values, there was a tendency of change in maximum Froude number values with a larger inclination angle.

- Re_{v_d} showed a similar effect to Eo where the increase in Re_{v_d} altered the bubble shape from the long slender bubble into shorter and flatter ones. Blunter bubble nose was observed at low Re_{v_d}, which subsequently led to a reduction in the bubble motion.

- As for Ga_R, it mainly affected the bubble motion with a negligible effect on the bubble shape. The increase of gravitational forces due to the increase in Ga_R, increased the bubble motion, but generally, all cases had low Fr_{v_d}values.

- In a near horizontal pipe, the bubble motion was considerably low with significant enhancement in the Taylor bubble length. Thus, a larger domain was essential for this inclination range. Aiming to reduce the computational resources, a simplified 2D model, based on the dimensionless analysis, was suggested to give an approximate solution to estimate the developed Taylor bubble shape.

- Moreover, it can be realised that the developed numerical results agreed well with the order of magnitude analysis. For horizontal pipes, Eo showed different order of magnitude based on a large length of developed Taylor bubble, where larger Eo values were essential for a stable Taylor bubble to exist $(Eo \geq 200)$. By using the simplified 2D model, Eo was the only governing parameter that significantly affected the developed Taylor bubble shape and size.

- Furthermore, the simulation results showed a reasonable agreement when tested against the previous experimental data and the main correlations available in the literature. It can be noticed that further improvements are still necessary for predicting the Taylor bubble drift velocity.

Finally, the study reported here is an attempt to provide a theoretical treatment of Taylor bubble flow problem and to support this treatment by performing a CFD study to investigate the flow features and characteristics consequently to provide a deeper understanding of its relevant parameters.

7.3 Contributions of the Study

The novelty of this study is developing a better theoretical understanding of the problem of Taylor bubble flow in vertical and inclined pipes in terms of the governing forces and their orders of magnitudes. This is supported by a CFD study that investigates the effect of the main governing parameters on the dynamics of the Taylor bubbles. The theoretical and CFD treatments developed in this thesis are essential for the understanding of governing forces that affect the flow features of Taylor bubble flow in pipes, which is essential characteristics part for the successful operation, simulation and optimisation of any system encountering slug flow.

The contributions of the study at hand are outlined as follows:

1. For Taylor bubble flow in a vertical pipe, the dimensionless analysis followed by order of magnitude analysis of Navier-Stokes equations of motion shows that the main parameters affecting the dynamics of Taylor bubble are Froude number, Reynolds number and Eötvös number.
2. The flow field in Taylor bubble flow in a vertical pipe is numerically investigated within three flow regions in Taylor bubble nose, liquid film and wake region.
3. Correlations for the Taylor bubble rise velocity in a vertical pipe, and the wall shear stress distribution is proposed, which showed a deviation of ±10% from the well-known correlations in the literature.
4. For Taylor bubble flow in an inclined pipe, the dimensionless analysis of Navier-Stokes equations of motion shows that the main parameters affecting the dynamics of Taylor bubble are Froude, Eötvös and Reynolds numbers for the inclination angle range of $0 \leq \gamma \leq 70°$.
5. For the near horizontal cases $(70° < \gamma < 90°)$, where the drift velocity is vanishingly small, the main physical parameters influencing the flow are the reduced Galilei number and Eötvös number, while taking into consideration that the Reynolds and Froude numbers are vanishingly small and are no longer acting as influencing parameters.
6. For the horizontal pipe case, that is for $\gamma = 90°$, the sole governing parameter that governs the pressure field distribution around the stagnant deformed bubble is Eötvös

number. The reduced Galilei number ceases to be effective, whereas Reynolds and Froude numbers are no longer influencing parameters.

7. A simplified 2D model is suggested to solve the challenging problem of the three-dimensional Taylor bubble in the near horizontal and horizontal pipes to get quick solution.

7.4 Recommendations

This research is proposed to give a better understanding of the problem of Taylor bubble motion in pipes. Though due to the limited computational resource available, this research still has some shortcomings, and the numerical analysis for Taylor bubble flow was carried out under only a limited range of operating conditions.

The analysis created in this work is only a start; it is essential that further studies are conducted across more dimensionless physical parameters and different contexts to allow a more comprehensive understanding of the problem. Recommendations for further improvements to the CFD tool and the operating conditions are outlined below.

The adopted CFD method used in this study is computationally demanding, and hence, improvement in the computational efficiency and reduction in the execution time are essential to be further considered.

The thesis focused on treating the basic Taylor bubble flow problem, where the surrounding liquid is stagnant, to build a deeper physical understanding of the problem. Further recommendations include performing a similar analysis to more practical cases that include flowing liquid rather than a stagnant one. Hence, in such cases, turbulence needs to be considered. Detached eddy simulations (DES) and large eddy simulations (LES) would rather be considered than the unsteady RANS CFD simulations performed in this work.

One of the limitations of the current work under consideration is the absence of any roughness (debris) and/or waviness in the pipe wall for the sensitivity of the analysis to be examined against geometrical defects. In addition, the liquid phase in the present analysis is considered to be pure that is free from any fine solid particles.

Concerning the hydrodynamic features of Taylor bubbles, some important questions are still open. Firstly, the maximum Eötvös number at which Taylor bubble exists in the inclined pipe still needs to be further investigated. Based on the developed results, Eötvös number varies according to the pipe inclination range and significantly increases in near horizontal pipes. Secondly, the flow characteristics for consecutive Taylor bubbles should also be assessed in inclined pipes for which there is a considerable lack of available data. Thirdly, it is worth noting that placing the inverse viscosity number $\left(N_f\right)$ instead of $Re_{U_{TB}}$ to judge turbulence or the onset of hydrodynamic instability in vertical pipes is debatable. Fundamentally, N_f effectively is the ratio of the gravity force to the viscous force, which can hardly be indicative of the onset of turbulence. As discussed in chapter 4, it is also to be noted that large values of N_f cannot only be attributed to large values of $Re_{U_{TB}}$ but to small values of $Fr_{U_{TB}}$ too. The similarity requirements posed by Froude and Reynolds numbers can typically not be satisfied simultaneously.

This study suggests the following critical points for future investigation regarding slug flow in pipes:

1. The flow of Taylor bubbles in a bend connecting two vertical pipes,
2. The transport of solids in Taylor bubble wakes.
3. Although the research on the flow of Taylor bubbles through complex liquids in inclined pipes (Non-Newtonian fluids) has already started to take place in the literature, yet further analysis is still needed.

References

ABDUL-MAJEED, G. H. 2000. Liquid slug holdup in horizontal and slightly inclined two-phase slug flow. *Journal of Petroleum Science and Engineering,* 27**,** 27-32.

AIAA 1998. AIAA Guide for the Verification and Validation of Computational Fluid Dynamics Simulations (G-077-1998). AIAA.

AKAGAWA, K. & SAKAGUCHI, T. 1966. Fluctuation of Void Ratio in Two-Phase Flow: 2nd Report, Analysis of Flow Configuration Considering the Existence of Small Bubbles in Liquid Slugs. *Bulletin of JSME,* 9**,** 104-110.

ALVES, I. N., SHOHAM, O. & TAITEL, Y. 1993. Drift velocity of elongated bubbles in inclined pipes. *Chemical engineering science,* 48**,** 3063-3070.

AMANI, E., AHMADPOUR, A. & TOHIDI, M. 2019. A numerical study of the rise of a Taylor bubble through a sudden/gradual expansion in Newtonian and shear-thinning liquids. *International Journal of Mechanical Sciences,* 152**,** 236-246.

AMBROSE, S. 2015. *The rise of Taylor bubbles in vertical pipes.* PhD Thesis, University of Nottingham.

AMBROSE, S., LOWNDES, I. S., HARGREAVES, D. M. & AZZOPARDI, B. 2017. Numerical modelling of the rise of Taylor bubbles through a change in pipe diameter. *Computers & Fluids,* 148**,** 10-25.

ANSARI, M. & SHOKRI, V. 2011. Numerical modeling of slug flow initiation in a horizontal channels using a two-fluid model. *International Journal of Heat and Fluid Flow,* 32**,** 145-155.

ARAÚJO, J., MIRANDA, J. & CAMPOS, J. 2013a. Simulation of slug flow systems under laminar regime: Hydrodynamics with individual and a pair of consecutive Taylor bubbles. *Journal of Petroleum Science and Engineering,* 111**,** 1-14.

ARAÚJO, J., MIRANDA, J. & CAMPOS, J. 2013b. Flow of two consecutive Taylor bubbles through a vertical column of stagnant liquid—A CFD study about the influence of the leading bubble on the hydrodynamics of the trailing one. *Chemical Engineering Science,* 97**,** 16-33.

ARAÚJO, J., MIRANDA, J. & CAMPOS, J. 2017. Taylor bubbles rising through flowing non-Newtonian inelastic fluids. *Journal of Non-Newtonian Fluid Mechanics,* 245**,** 49-66.

ARAÚJO, J., MIRANDA, J., PINTO, A. & CAMPOS, J. 2012. Wide-ranging survey on the laminar flow of individual Taylor bubbles rising through stagnant Newtonian liquids. *International Journal of Multiphase Flow,* 43**,** 131-148.

BAKER, D. 1954. Simultaneous Flow of Oil and Gas. *Oil and Gas Journal,* 53**,** 183-195

BEHAFARID, F., JANSEN, K. & PODOWSKI, M. 2015. A study on large bubble motion and liquid film in vertical pipes and inclined narrow channels. *International Journal of Multiphase Flow,* 75**,** 288-299.

BENDIKSEN, K. H. 1984. An experimental investigation of the motion of long bubbles in inclined tubes. *International journal of multiphase flow,* 10**,** 467-483.

BENDIKSEN, K. H. 1985. On the motion of long bubbles in vertical tubes. *International journal of multiphase flow,* 11**,** 797-812.

BENDIKSEN, K. H., MAINES, D., MOE, R. & NULAND, S. 1991. The dynamic two-fluid model OLGA: Theory and application. *SPE production engineering,* 6**,** 171-180.

BENJAMIN, T. B. 1968. Gravity currents and related phenomena. *Journal of Fluid Mechanics,* 31**,** 209-248.

BHAGWAT, S. M. & GHAJAR, A. J. 2016. Experimental investigation of non-boiling gas-liquid two phase flow in upward inclined pipes. *Experimental Thermal and Fluid Science,* 79**,** 301-318.

BLACK, J. E., ISAACS, K. R., ANDERSON, B. J., ALCANTARA, A. A. & GREENOUGH, W. T. 1990. Learning causes synaptogenesis, whereas motor activity causes angiogenesis, in cerebellar cortex of adult rats. *Proceedings of the National Academy of Sciences,* 87**,** 5568-5572.

BONNECAZE, R., ERSKINE, W. & GRESKOVICH, E. 1971. Holdup and pressure drop for two-phase slug flow in inclined pipelines. *AIChE Journal,* 17**,** 1109-1113.

BRACKBILL, J., KOTHE, D. B. & ZEMACH, C. 1992. A continuum method for modeling surface tension. *Journal of computational physics,* 100**,** 335-354.

BRATLAND, O. 2010. Pipe Flow 2: Multi-phase Flow Assurance. *Ove Bratland Flow Assurance Consulting, Chonburi, Thailand.*

BRETHERTON, F. 1961. The motion of long bubbles in tubes. *Journal of Fluid Mechanics,* 10**,** 166-188.

BROWN, R. 1965. The mechanics of large gas bubbles in tubes: I. Bubble velocities in stagnant liquids. *The Canadian Journal of Chemical Engineering,* 43**,** 217-223.

BUGG, J., MACK, K. & REZKALLAH, K. 1998. A numerical model of Taylor bubbles rising through stagnant liquids in vertical tubes. *International Journal of Multiphase Flow,* 24**,** 271-281.

BUGG, J. & SAAD, G. 2002. The velocity field around a Taylor bubble rising in a stagnant viscous fluid: numerical and experimental results. *International Journal of Multiphase Flow,* 28**,** 791-803.

CAMPOS, J. & DE CARVALHO, J. G. 1988. An experimental study of the wake of gas slugs rising in liquids. *Journal of Fluid Mechanics,* 196**,** 27-37.

CLANET, C., HÉRAUD, P. & SEARBY, G. 2004. On the motion of bubbles in vertical tubes of arbitrary cross-sections: some complements to the Dumitrescu–Taylor problem. *Journal of Fluid Mechanics,* 519**,** 359-376.

CLARKE, A. & ISSA, R. 1997. A numerical model of slug flow in vertical tubes. *Computers & fluids,* 26**,** 395-415.

COUËT, B. & STRUMOLO, G. S. 1987. The effects of surface tension and tube inclination on a two-dimensional rising bubble. *Journal of Fluid Mechanics,* 184**,** 1-14.

DAVIES, R. & TAYLOR, G. The mechanics of large bubbles rising through extended liquids and through liquids in tubes. *Proceedings of the Royal Society of London A: Mathematical, Physical and Engineering Sciences*, 1950. The Royal Society, 375-390.

DE AZEVEDO, M. B., DOS SANTOS, D., FACCINI, J. L. & SU, J. 2017. Experimental study of the falling film of liquid around a Taylor bubble. *International Journal of Multiphase Flow,* 88**,** 133-141.

DEJESUS, J., AHMAD, W. & KAWAJI, M. 1995. Experimental study of flow structure in vertical slug flow. *Multiphase Flow 1995.* Elsevier.

DIREITO, F., MORGADO, A., ROCHA, L., MIRANDA, J. & CAMPOS, J. 2017. Experimental and numerical 3D study of a Taylor drop rising in a stagnant heavier liquid. *Physics of Fluids,* 29**,** 037109.

DUKLER, A. E. & HUBBARD, M. G. 1975. A model for gas-liquid slug flow in horizontal and near horizontal tubes. *Industrial & Engineering Chemistry Fundamentals,* 14**,** 337-347.

DUMITRESCU, D. T. 1943. Strömung an einer Luftblase im senkrechten Rohr. *ZAMM-Journal of Applied Mathematics and Mechanics/Zeitschrift für Angewandte Mathematik und Mechanik,* 23**,** 139-149.

FABRE, J. & LINÉ, A. 1992. Modeling of two-phase slug flow. *Annual review of fluid mechanics,* 24**,** 21-46.

FERNANDES, R., SEMIAT, R. & DUKLER, A. 1983. Hydrodynamic model for gas-liquid slug flow in vertical tubes. *AIChE Journal,* 29**,** 981-989.

FLUENT, A. 2015. Theory Guide and User's Guide. *Ansys Inc, USA.*

FRECHOU, D. 1986. *Étude de l'écoulement vertical ascendant à trois fluides en conduite verticale.* These Inst Natl Polythech, Toulouse, France.

FULFORD, G. D. 1964. The flow of liquids in thin films. *Advances in Chemical Engineering,* 5**,** 151-236.

GOKCAL, B., AL-SARKHI, A., SARICA, C. & AL-SAFRAN, E. M. 2010. Prediction of slug frequency for high-viscosity oils in horizontal pipes. *SPE Projects, Facilities & Construction,* 5**,** 136-144.

GOKCAL, B., AL-SARKHI, A. S. & SARICA, C. 2009. Effects of high oil viscosity on drift velocity for horizontal and upward inclined pipes. *SPE Projects, Facilities & Construction,* 4**,** 32-40.

GOLDSMITH, H. & MASON, S. 1962. The movement of single large bubbles in closed vertical tubes. *Journal of Fluid Mechanics,* 14**,** 42-58.

GUTIÉRREZ, E., BALCAZAR, N., BARTRONS, E. & RIGOLA, J. 2017. Numerical study of Taylor bubbles rising in a stagnant liquid using a level-set/moving-mesh method. *Chemical Engineering Science,* 164**,** 158-177.

HASAN, A. R. & KABIR, C. S. 1988. Predicting multiphase flow behavior in a deviated well. *SPE Production Engineering,* 3**,** 474-482.

HAYASHI, K., KURIMOTO, R. & TOMIYAMA, A. 2011. Terminal velocity of a Taylor drop in a vertical pipe. *International Journal of Multiphase Flow,* 37**,** 241-251.

HERNANDEZ-PEREZ, V., ABDULKADIR, M. & AZZOPARDI, B. 2010. Slugging frequency correlation for inclined gas–liquid flow. *World Acad Sci Eng Technol,* 37**,** 44-51.

HERNANDEZ-PEREZ, V., ABDULKADIR, M. & AZZOPARDI, B. 2011. Grid generation issues in the CFD modelling of two-phase flow in a pipe. *The Journal of Computational Multiphase Flows,* 3**,** 13-26.

HERNANDEZ PEREZ, V. 2008. *Gas-liquid two-phase flow in inclined pipes.* University of Nottingham.

HEWITT, G. F. & ROBERTS, D. 1969. Studies of two-phase flow patterns by simultaneous x-ray and flast photography. Atomic Energy Research Establishment, Harwell, England (United Kingdom).

HIRT, C. W. & NICHOLS, B. D. 1981. Volume of fluid (VOF) method for the dynamics of free boundaries. *Journal of computational physics,* 39**,** 201-225.

HUA, Z., SHUHUA, W. & JING, W. 2009. Experimental study of motion of nitrogen Taylor bubbles and liquid slugs in inclined tubes. *Chinese Journal of Aeronautics,* 22**,** 349-354.

ISHII, M. 1975. Thermo-fluid dynamic theory of two-phase flow. *NASA STI/Recon Technical Report A,* 75**,** 29657.

ISSA, R. & UBBINK, O. Numerical prediction of Taylor bubble dynamics using a new interface capturing technique. *In Proceedings of the 3rd ASME/JSME, San Francisco, California, USA. Joint Fluids Engineering Conference*, 1999.

ISSA, R. I. 1986. Solution of the implicitly discretised fluid flow equations by operator-splitting. *Journal of computational physics,* 62**,** 40-65.

JEYACHANDRA, B., GOKCAL, B., AL-SARKHI, A., SARICA, C. & SHARMA, A. 2012. Drift-velocity closure relationships for slug two-phase high-viscosity oil flow in pipes. *SPE Journal,* 17**,** 593-601.

JOSEPH, D. D. 2003. Rise velocity of a spherical cap bubble. *Journal of Fluid Mechanics,* 488**,** 213-223.

KANG, C.-W., QUAN, S. & LOU, J. 2010. Numerical study of a Taylor bubble rising in stagnant liquids. *Physical Review E,* 81**,** 066308.

KAWAJI, M., DEJESUS, J. & TUDOSE, G. 1997. Investigation of flow structures in vertical slug flow. *Nuclear Engineering and Design,* 175**,** 37-48.

KURIMOTO, R., HAYASHI, K. & TOMIYAMA, A. 2013. Terminal velocities of clean and fully-contaminated drops in vertical pipes. *International Journal of Multiphase Flow,* 49**,** 8-23.

KUZMIN, A., JANUSZEWSKI, M., ESKIN, D., MOSTOWFI, F. & DERKSEN, J. 2013. Lattice Boltzmann study of mass transfer for two-dimensional Bretherton/Taylor bubble train flow. *Chemical engineering journal,* 225**,** 580-596.

LAIRD, A. & CHISHOLM, D. 1956. Pressure and forces along cylindrical bubbles in a vertical tube. *Industrial & Engineering Chemistry,* 48**,** 1361-1364.

LEONARD, B. & MOKHTARI, S. 1990. ULTRA-SHARP nonoscillatory convection schemes for high-speed steady multidimensional flow.

LIBERZON, D., SHEMER, L. & BARNEA, D. 2006. Upward-propagating capillary waves on the surface of short Taylor bubbles. *Physics of fluids,* 18**,** 048103.

LIZARRAGA-GARCÍA, E. 2016. *A study of Taylor bubbles in vertical and inclined slug flow using multiphase CFD with level set.* Doctoral dissertation, Massachusetts Institute of Technology.

LIZARRAGA-GARCIA, E., BUONGIORNO, J. & BUCCI, M. 2016. An analytical film drainage model and breakup criterion for Taylor bubbles in slug flow in inclined round pipes. *International Journal of Multiphase Flow,* 84**,** 46-53.

LOSI, G. & POESIO, P. 2016. An experimental investigation on the effect of viscosity on bubbles moving in horizontal and slightly inclined pipes. *Experimental Thermal and Fluid Science,* 75**,** 77-88.

LU, X. & PROSPERETTI, A. 2008. A numerical study of Taylor bubbles. *Industrial & Engineering Chemistry Research,* 48**,** 242-252.

MANDAL, T. K., DAS, G. & DAS, P. K. 2010. An appraisal of liquid–liquid slug flow in different pipe orientations. *International Journal of Multiphase Flow,* 36**,** 661-671.

MANDHANE, J., GREGORY, G. & AZIZ, K. 1974. A flow pattern map for gas—liquid flow in horizontal pipes. *International Journal of Multiphase Flow,* 1**,** 537-553.

MANERI, C. & ZUBER, N. 1974. An experimental study of plane bubbles rising at inclination. *International Journal of Multiphase Flow,* 1**,** 623-645.

MAO, Z.-S. & DUKLER, A. 1990. The motion of Taylor bubbles in vertical tubes. I. A numerical simulation for the shape and rise velocity of Taylor bubbles in stagnant and flowing liquid. *Journal of computational physics,* 91**,** 132-160.

MATLAB@ 2015a. *version 8.5.0197613 (R2015a).* The Math Works Inc., Natick, Massachusetts.

MAYOR, T., FERREIRA, V., PINTO, A. & CAMPOS, J. 2008a. Hydrodynamics of gas–liquid slug flow along vertical pipes in turbulent regime–An experimental study. *International Journal of Heat and Fluid Flow,* 29**,** 1039-1053.

MAYOR, T., PINTO, A. & CAMPOS, J. 2007a. Hydrodynamics of Gas− Liquid Slug Flow along Vertical Pipes in the Laminar Regime Experimental and Simulation Study. *Industrial & engineering chemistry research,* 46**,** 3794-3809.

MAYOR, T., PINTO, A. & CAMPOS, J. 2008b. On the gas expansion and gas hold-up in vertical slugging columns—A simulation study. *Chemical Engineering and Processing: Process Intensification,* 47**,** 799-815.

MAYOR, T., PINTO, A. & CAMPOS, J. 2008c. Vertical slug flow in laminar regime in the liquid and turbulent regime in the bubble wake—comparison with fully turbulent and fully laminar regimes. *Chemical Engineering Science,* 63**,** 3614-3631.

MAYOR, T. S., PINTO, A. & CAMPOS, J. 2007b. Hydrodynamics of gas–liquid slug flow along vertical pipes in turbulent regime: A simulation study. *Chemical Engineering Research and Design,* 85**,** 1497-1513.

MAZZA, R., ROSA, E. & YOSHIZAWA, C. 2010. Analyses of liquid film models applied to horizontal and near horizontal gas–liquid slug flows. *Chemical Engineering Science,* 65**,** 3876-3892.

MEDINA, C. D. P., BASSANI, C. L., COZIN, C., BARBUTO, F. A. D. A., JUNQUEIRA, S. L. & MORALES, R. E. 2015. Numerical simulation of the heat transfer in fully developed horizontal two-phase slug flows using a slug tracking method. *International Journal of Thermal Sciences,* 88**,** 258-266.

MOREIRAS, J., PEREYRA, E., SARICA, C. & TORRES, C. F. 2014. Unified drift velocity closure relationship for large bubbles rising in stagnant viscous fluids in pipes. *Journal of Petroleum Science and Engineering,* 124**,** 359-366.

MORGADO, A., MIRANDA, J., ARAUJO, J. & CAMPOS, J. 2016. Review on vertical gas–liquid slug flow. *International Journal of Multiphase Flow,* 85**,** 348-368.

NDINISA, N., WILEY, D. & FLETCHER, D. 2005. Computational fluid dynamics simulations of Taylor bubbles in tubular membranes: model validation and application to laminar flow systems. *Chemical Engineering Research and Design,* 83**,** 40-49.

NEMOTO, R. H. & BALIÑO, J. L. 2012. Modeling and simulation of severe slugging with mass transfer effects. *International Journal of Multiphase Flow,* 40**,** 144-157.

NICKLIN, D., WILKES, J. & DAVIDSON, J. 1962. Two-phase flow in vertical tubes. *Trans. Inst. Chem. Eng,* 40**,** 61-68.

NOGUEIRA, S., RIETHMULER, M., CAMPOS, J. & PINTO, A. 2006a. Flow in the nose region and annular film around a Taylor bubble rising through vertical columns of stagnant and flowing Newtonian liquids. *Chemical Engineering Science,* 61**,** 845-857.

NOGUEIRA, S., RIETHMULLER, M., CAMPOS, J. & PINTO, A. 2006b. Flow patterns in the wake of a Taylor bubble rising through vertical columns of stagnant and flowing Newtonian liquids: An experimental study. *Chemical engineering science,* 61**,** 7199-7212.

NOGUEIRA, S., SOUSA, R., PINTO, A., RIETHMULLER, M. & CAMPOS, J. 2003. Simultaneous PIV and pulsed shadow technique in slug flow: a solution for optical problems. *Experiments in Fluids,* 35**,** 598-609.

PETALAS, N. & AZIZ, K. 2000. A mechanistic model lbr multiphase flow in pipes. *Journal of Canadian Petroleum Techno-logy,* 39.

POKUSAEV, B., NEKRASOV, D. & KHRAMTSOV, D. 2016. Modeling slug flow and mass transfer in inclined pipes. *Theoretical Foundations of Chemical Engineering,* 50**,** 237-241.

POLONSKY, S., SHEMER, L. & BARNEA, D. 1999. The relation between the Taylor bubble motion and the velocity field ahead of it. *International Journal of Multiphase Flow,* 25**,** 957-975.

ROITBERG, E., BARNEA, D. & SHEMER, L. 2016. Elongated bubble shape in inclined air-water slug flow. *International Journal of Multiphase Flow,* 85**,** 76-85.

ROITBERG, E., SHEMER, L. & BARNEA, D. 2008. Hydrodynamic characteristics of gas–liquid slug flow in a downward inclined pipe. *Chemical Engineering Science,* 63**,** 3605-3613.

SHEMER, L. 2003. Hydrodynamic and statistical parameters of slug flow. *International journal of heat and fluid flow,* 24**,** 334-344.

SHEMER, L., GULITSKI, A. & BARNEA, D. 2007. On the turbulent structure in the wake of Taylor bubbles rising in vertical pipes. *Physics of Fluids,* 19**,** 035108.

SHOSHO, C. E. & RYAN, M. E. 2001. An experimental study of the motion of long bubbles in inclined tubes. *Chemical engineering science,* 56**,** 2191-2204.

SHUHUA, W., ZHANG, H. & JING, W. 2009. Cryogenic liquid slug and Taylor bubble length distributions in an inclined tube. *Chinese Journal of Chemical Engineering,* 17**,** 20-26.

SOUSA, R., RIETHMULLER, M., PINTO, A. & CAMPOS, J. 2006. Flow around individual Taylor bubbles rising in stagnant polyacrylamide (PAA) solutions. *Journal of non-newtonian fluid mechanics,* 135**,** 16-31.

SPEDDING, P. & NGUYEN, V. T. 1978. Bubble rise and liquid content in horizontal and inclined tubes. *Chemical Engineering Science,* 33**,** 987-994.

TAHA, T. & CUI, Z. 2006. CFD modelling of slug flow in vertical tubes. *Chemical Engineering Science,* 61**,** 676-687.

TAITEL, Y. & BARNEA, D. 1990. A consistent approach for calculating pressure drop in inclined slug flow. *Chemical engineering science,* 45**,** 1199-1206.

TAITEL, Y. & DUKLER, A. 1976. A model for predicting flow regime transitions in horizontal and near horizontal gas-liquid flow. *AIChE Journal,* 22**,** 47-55.

TAITEL, Y., SARICA, C. & BRILL, J. 2000. Slug flow modeling for downward inclined pipe flow: theoretical considerations. *International journal of multiphase flow,* 26**,** 833-844.

TOMIYAMA, A., SOU, A. & SAKAGUCHI, T. 1996. Numerical simulation of a Taylor bubble in a stagnant liquid inside a vertical pipe. *JSME International Journal Series B Fluids and Thermal Engineering,* 39**,** 517-524.

TUNG, K. W. & PARLANGE, J.-Y. 1976. Note on the motion of long bubbles in closed tubes-influence of surface tension. *Acta Mechanica,* 24**,** 313-317.

VAN HOUT, R., GULITSKI, A., BARNEA, D. & SHEMER, L. 2002. Experimental investigation of the velocity field induced by a Taylor bubble rising in stagnant water. *International Journal of Multiphase Flow,* 28**,** 579-596.

VERMEULEN, L. & RYAN, J. 1971. Two-phase slug flow in horizontal and inclined tubes. *The Canadian Journal of chemical engineering,* 49**,** 195-201.

VERSTEEG, H. K. & MALALASEKERA, W. 2007. An introduction to computational fluid dynamics: the finite volume method, Pearson Education.

VIANA, F., PARDO, R., YANEZ, R., TRALLERO, J. L. & JOSEPH, D. D. 2003. Universal correlation for the rise velocity of long gas bubbles in round pipes. *Journal of Fluid Mechanics,* 494**,** 379-398.

WALLIS, G. B. 1969. One-dimensional two-phase flow, McGraw Hill, New York.

WEBER, M., ALARIE, A. & RYAN, M. 1986. Velocities of extended bubbles in inclined tubes. *Chemical engineering science,* 41**,** 2235-2240.

WEBER, M. E. 1981. Drift in intermittent two-phase flow in horizontal pipes. *The Canadian Journal of Chemical Engineering,* 59**,** 398-399.

WEISMAN, J. 1983. Two-phase flow patterns. *In:* CHEREMISINOFF, N. P. & GUPTA, A. R. (eds.) *Handbook of Fluids in Motion.* Ann Arbor Science.

WHITE, E. & BEARDMORE, R. 1962. The velocity of rise of single cylindrical air bubbles through liquids contained in vertical tubes. *Chemical Engineering Science,* 17**,** 351-361.

XING, L., YEUNG, H., GENG, Y., CAO, Y. & SHEN, J. 2014. Study on hydrodynamic slug flow mitigation with wavy pipe using a 3D–1D coupling approach. *Computers & Fluids,* 99**,** 104-115.

YAN, K. & CHE, D. 2011. Hydrodynamic and mass transfer characteristics of slug flow in a vertical pipe with and without dispersed small bubbles. *International journal of multiphase flow,* 37**,** 299-325.

YOUNGS, D. L. 1982. Time-dependent multi-material flow with large fluid distortion. *Numerical methods for fluid dynamics, K. W. Morton M. J. Baines, Academic Press, New York,* 273.

ZHANG, H., WANG, S. & WANG, J. 2009. Experimental study on boiling flow of liquid nitrogen in inclined tubes—Velocities and length distributions of Taylor bubbles. *Journal of the Taiwan Institute of Chemical Engineers,* 40**,** 431-438.

ZHENG, D. & CHE, D. 2006. Experimental study on hydrodynamic characteristics of upward gas–liquid slug flow. *International journal of multiphase flow,* 32**,** 1191-1218.

ZHENG, D. & CHE, D. 2007b. An investigation on near wall transport characteristics in an adiabatic upward gas–liquid two-phase slug flow. *Heat and mass transfer,* 43**,** 1019-1036.

ZHENG, D., HE, X. & CHE, D. 2007a. CFD simulations of hydrodynamic characteristics in a gas–liquid vertical upward slug flow. *International journal of heat and mass transfer,* 50**,** 4151-4165.

ZUKOSKI, E. 1966. Influence of viscosity, surface tension, and inclination angle on motion of long bubbles in closed tubes. *Journal of Fluid Mechanics,* 25**,** 821-837.

Appendices

Appendix A Buckingham-Pi Theorem-Vertical Pipe Case

The hydrodynamic characteristics of gas-liquid slug flow are governed by viscous, inertial, gravitational and interfacial forces. Using the Buckingham-Pi theorem, the Taylor bubble rise velocity can be expressed as follows:

$$U_{TB} = f\ [\rho_L, \rho_G, \mu_L, \mu_G, g,\ L_{TB}, D, \sigma] \qquad A\text{–}1$$

According to relation A–1, the number of relevant variables (n) is 9, the number of repeating variables (k) (scaling independent dimensions) is $3\ (M, L \text{ and } T)$ and the number of dimensionless groups $(\Pi s), n - k = 6$. This result in the following set of dimensionless groups:

$$\Pi_1 = L_{TB}\ D\ \mu_L\ \rho_L \qquad A\text{–}2$$
$$\Pi_2 = \sigma\ D\ \mu_L\ \rho_L \qquad A\text{–}3$$
$$\Pi_3 = g\ D\ \mu_L\ \rho_L \qquad A\text{–}4$$
$$\Pi_4 = U_{TB}\ D\ \mu_L\ \rho_L \qquad A\text{–}5$$
$$\Pi_5 = \rho_G\ D\ \mu_L\ \rho_L \qquad A\text{–}6$$
$$\Pi_6 = \mu_G\ D\ \mu_L\ \rho_L \qquad A\text{–}7$$

where M is the mass, L is the length and T is the time. The three repeating variables (k), are given by a, b and c. According to the MLT system, these parameters are chosen to make each of the above relations in a dimensionless form, and given by D, μ_L and ρ_L. The dimensions are defined as follows:

$$\rho = ML^{-3}$$
$$\mu = ML^{-1}T^{-1} \qquad A\text{–}8$$

$g = LT^{-2}$

$L_{TB} = L$

$D = L$

$\sigma = MT^{-2}$

$U_{TB} = LT^{-1}$

Accordingly, the relations A–2 to A–7 are resolved as follows:

$$\Pi_6 = M^0L^0T^0 = (ML^{-1}T^{-1})(L)^{a_6}(ML^{-1}T^{-1})^{b_6}(ML^{-3})^{c_6}$$
$$M^0L^0T^0 = L^{-1+a_6-b_6-3c_6}M^{1+b_6+c_6}T^{-1-b_6}$$
$$b_6 = -1, c_6 = 0 \; and \; a_6 = 0 \qquad A\text{–}9$$
$$\Pi_6 = \mu_G\mu_L{}^{-1} = \frac{\mu_G}{\mu_L}$$

According to relation A–6:

$$\Pi_5 = M^0L^0T^0 = (ML^{-3})(L)^{a_5}(ML^{-1}T^{-1})^{b_5}(ML^{-3})^{c_5}$$
$$M^0L^0T^0 = L^{-3+a_5-b_5-3c_5}\, M^{1+b_5+c_5}\, T^{-b_5}$$
$$b_5 = 0, c_5 = -1 \; and \; a_5 = 0 \qquad A\text{–}10$$
$$Therefore \;\; \Pi_5 = \rho_G\rho_L{}^{-1} = \frac{\rho_G}{\rho_L}$$

According to relation A–5:

$$\Pi_4 = M^0L^0T^0 = (LT^{-1})(L)^{a_4}(ML^{-1}T^{-1})^{b_4}(ML^{-3})^{c_4}$$
$$M^0L^0T^0 = L^{1+a_4-b_4-3c_4}\, M^{b_4+c_4}T^{-1-b_4}$$
$$b_4 = -1, c_4 = 1 \; and \; a_4 = 1 \qquad A\text{–}11$$
$$Therefore \;\; \Pi_4 = \frac{\rho_L U_{TB} D}{\mu_L}$$

According to relation A–4:

$$\Pi_3 = M^0L^0T^0 = (LT^{-2})(L)^{a_3}(ML^{-1}T^{-1})^{b_3}(ML^{-3})^{c_3}$$
$$M^0L^0T^0 = L^{1+a_3-b_3-3c_3}\, M^{b_3+c_3}T^{-2-b_3}$$
$$b_3 = -2, c_3 = 2 \; and \; a_3 = 3 \qquad A\text{–}12$$
$$Therefore \; \Pi_3 = g\mu_L{}^{-2}\rho_L{}^2D^3 = \frac{g\rho_L{}^2D^3}{\mu_L{}^2}$$

According to relation A–3:

$$\Pi_2 = M^0L^0T^0 = (MT^{-2})(L)^{a_2}(ML^{-1}T^{-1})^{b_2}(ML^{-3})^{c_2}$$
$$M^0L^0T^0 = L^{a_2-b_2-3c_2}\ M^{1+b_2+c_2}T^{-2-b_2}$$
$$b_2 = -2, c_2 = 1\ and\, a_2 = 1 \qquad A\text{–}13$$
$$Therefore\ \Pi_2 = \sigma D {\mu_L}^{-2}\rho_L = \frac{\sigma D\rho_L}{{\mu_L}^2}$$

And finally, according to relation A–2:

$$\Pi_1 = M^0L^0T^0 = (L)(L)^{a_1}(ML^{-1}T^{-1})^{b_1}(ML^{-3})^{c_1}$$
$$M^0L^0T^0 = L^{1+a_1-b_1-3c_1}\ M^{b_1+c_1}T^{-b_1}$$
$$b_1 = 0, c_1 = 0\ and\ a_1 = -1 \qquad A\text{–}14$$
$$Therefore\ \Pi_1 = \frac{L_{TB}}{D}$$

The final step is setting out the dimensionless relationship and rearranging the terms, which is done through the following steps:

$$\frac{\Pi_3}{\Pi_2} = \left(\frac{g{\rho_L}^2D^3}{{\mu_L}^2}\right)\left(\frac{{\mu_L}^2}{\sigma D\rho_L}\right) = \frac{g\rho_L D^2}{\sigma} = Eo \qquad A\text{–}15$$

$$\frac{\Pi_3}{{\Pi_2}^3} = \left(\frac{g{\rho_L}^2D^3}{{\mu_L}^2}\right)\left(\frac{{\mu_L}^2}{\sigma D\rho_L}\right)^3 = \frac{g{\mu_L}^4}{\sigma^3\rho_L} = M \qquad A\text{–}16$$

$$\frac{{\Pi_4}^2}{\Pi_3} = \left(\frac{\rho_L U_{TB} D}{\mu_L}\right)^2\left(\frac{{\mu_L}^2}{g{\rho_L}^2D^3}\right) = \frac{{U_{TB}}^2}{gD} = \sqrt{Fr_{U_{TB}}} = Fr_{U_{TB}} \qquad A\text{–}17$$

And since

$$\Pi_4 = Re_{U_{TB}} = \frac{\rho_L U_{TB} D}{\mu_L}, {Fr_{U_{TB}}}^4 = \frac{{Re_{U_{TB}}}^4{\mu_L}^4}{{\rho_L}^4D^4g^2D^2},\ g^2 = \frac{{Re_{U_{TB}}}^4{\mu_L}^4}{{\rho_L}^4D^6{Fr_{U_{TB}}}^4}$$

$$Therefore\ From\ A\text{–}15\ \ Eo^3 = \frac{g^3{\rho_L}^3D^6}{\sigma^3} = \left(\frac{g^2{\rho_L}^4D^6}{{\mu_L}^4}\right)\left(\frac{g{\mu_L}^4}{\rho_L\sigma^3}\right) = \left(\frac{g^2{\rho_L}^4D^6}{{\mu_L}^4}\right)M$$

$$Eo^3 = \left(\frac{{\rho_L}^4D^6}{{\mu_L}^4}\right)\left(\frac{{Re_{U_{TB}}}^4{\mu_L}^4}{{\rho_L}^4D^6{Fr_{U_{TB}}}^4}\right)M = \left(\frac{Re_{U_{TB}}}{Fr_{U_{TB}}}\right)^4 M \qquad A\text{–}18$$

$$Therefore\ \frac{Re_{U_{TB}}}{Fr_{U_{TB}}} = \left(\frac{Eo^3}{M}\right)^{1/4}$$

However,

$$\frac{Re_{U_{TB}}}{Fr_{U_{TB}}} = \frac{\rho_L U_{TB} D}{\mu_L} \times \frac{g^{1/2} D^{1/2}}{U_{TB}} = \frac{\rho_L g^{1/2} D^{3/2}}{\mu_L} = \left(\frac{\rho_L{}^2 g D^3}{\mu_L{}^2}\right)^{1/2} = \frac{\sqrt{gD^3}}{\nu_L} = N_f$$
$$Therefore\ N_f = \frac{Re_{U_{TB}}}{Fr_{U_{TB}}} = \left(\frac{Inertia\ force}{Viscous\ force}\right)\left(\frac{Garvity\ force}{Inertia\ force}\right) = \frac{Garvity\ force}{Viscous\ force} \qquad A\text{–}19$$

Therefore,

$$\frac{\Pi_4{}^2}{\Pi_3} = f\left[\frac{\Pi_3}{\Pi_2}, \frac{\Pi_3}{\Pi_2{}^3}, \frac{1}{\Pi_5}, \frac{1}{\Pi_6}, \Pi_1\right]$$
$$Therefore\ \frac{U_{TB}{}^2}{gD} = f\left[Eo\ = \frac{g\rho_L D^2}{\sigma}, M = \frac{g\mu_L{}^4}{\sigma^3 \rho_L}, \Gamma_\rho = \frac{\rho_L}{\rho_G}, \Gamma_\mu = \frac{\mu_L}{\mu_G}, \frac{L_{TB}}{D}\right] \qquad A\text{–}20$$

From equation A–20, it is correspondent to say that the Froude number can be given by:

$$Fr_{U_{TB}} = \frac{U_{TB}}{\sqrt{gD}} = f_1\left[Eo\ = \frac{g\rho_L D^2}{\sigma}, M = \frac{g\mu_L{}^4}{\sigma^3 \rho_L}, \Gamma_\rho = \frac{\rho_L}{\rho_G}, \Gamma_\mu = \frac{\mu_L}{\mu_G}, \frac{L_{TB}}{D}\right] \qquad A\text{–}21$$

Using equation A–18, it can be shown in this respect that Morton number (M) does not represent any particular physical quantity as it can be written as:

$$M = \left(\frac{Fr_{U_{TB}}}{Re_{U_{TB}}}\right)^4 Eo^3 = \frac{Eo^3}{Nf^4} \qquad A\text{–}22$$

Where the inverse viscosity number (N_f) is defined as:

$$N_f = \frac{Re_{U_{TB}}}{Fr_{U_{TB}}} = \frac{\rho_L (gD^3)^{0.5}}{\mu_L} \qquad A\text{–}23$$

Thus, equation A–20 can be represented as:

$$Fr_{U_{TB}} = \frac{U_{TB}}{\sqrt{gD}} = f\left[Eo, \left(\frac{Fr_{U_{TB}}}{Re_{U_{TB}}}\right)^4 Eo^3, \frac{\rho_L}{\rho_G}, \frac{\mu_L}{\mu_G}, \frac{L_{TB}}{D}\right]$$
$$Therefore\ Fr_{U_{TB}} = \frac{U_{TB}}{\sqrt{gD}} = f_2\left[Eo, N_f, \frac{\rho_L}{\rho_G}, \frac{\mu_L}{\mu_G}, \frac{L_{TB}}{D}\right] \qquad A\text{–}24$$

It can be easily shown here that using the Buckingham-Pi theorem can lead to the same form of the dimensionless groups with Morton number replaced by Reynolds number that is given by:

$$Fr_{U_{TB}} = \frac{U_{TB}}{\sqrt{gD}} = f_3\left[Eo = \frac{g\rho_L D^2}{\sigma}\ , Re_{U_{TB}} = \frac{\rho_L U_{TB} D}{\mu_L}\ , \Gamma_\rho = \frac{\rho_L}{\rho_G}, \Gamma_\mu = \frac{\mu_L}{\mu_G}, \frac{L_{TB}}{D}\ \right] \qquad A\text{–}25$$

Appendix B Buckingham-Pi Theorem-Inclined Pipe Case

Using the Buckingham-Pi theorem, the Taylor bubble drift velocity (v_d) can be expressed as follows:

$$v_d = f\ [\rho_L, \mu_L, g, \sigma,\ L_{TB}, D] \qquad B\text{–}1$$

The effect of inclination is introduced in the gravitational acceleration (g), that can have three components g_x, g_y and g_z. According to relation B–1, the number of relevant variables (n) is 7, the number of repeating variables (k) (scaling independent dimensions) is $3(M, L$ and $T)$ and the number of dimensionless groups (Πs), $n - k = 4$. This result in the following set of dimensionless groups:

$$\Pi_1 = g\ {\rho_L}^{a1}\ {\mu_L}^{b1} D^{c1} \qquad B\text{–}2$$
$$\Pi_2 = v_d\ {\rho_L}^{a2}\ {\mu_L}^{b2} D^{c2} \qquad B\text{–}3$$
$$\Pi_3 = \sigma\ {\rho_L}^{a3}\ {\mu_L}^{b3} D^{c3} \qquad B\text{–}4$$
$$\Pi_4 = L_{TB}\ {\rho_L}^{a4}\ {\mu_L}^{b4} D^{c4} \qquad B\text{–}5$$

where M is the mass, L is the length and T is the time. The three repeating variables (k), are given by a, b and c. According to the MLT system, these parameters are chosen to make each of the above relations in a dimensionless form and given by ρ_L, μ_L and D. The dimensions are defined as follows:

$$\begin{aligned} \rho &= ML^{-3} \\ \mu &= ML^{-1}T^{-1} \\ g &= LT^{-2} \\ L_{TB} &= L \qquad B\text{–}6 \\ D &= L \\ \sigma &= MT^{-2} \\ v_d &= LT^{-1} \end{aligned}$$

Accordingly, the relations B–2 to B–5 are resolved as follows:

$$\Pi_1 = M^0L^0T^0 = (LT^{-2})(ML^{-3})^{a_1}(ML^{-1}T^{-1})^{b_1}(L)^{c_1}$$
$$M^0L^0T^0 = L^{1-3a_1-b_1+c_1}\ M^{a_1+b_1}\ T^{-2-b_1}$$
$$b_1 = -2,\ a_1 = 2\ and\ c_1 = 3 \qquad B\text{–}7$$
$$Therefore\ \Pi_1 = g\ {\rho_L}^2\ {\mu_L}^{-2}D^3 = \frac{g\ {\rho_L}^2D^3}{{\mu_L}^2}$$

According to relation B–3:

$$\Pi_2 = M^0L^0T^0 = (LT^{-1})(ML^{-3})^{a_2}(ML^{-1}T^{-1})^{b_2}(L)^{c_2}$$
$$M^0L^0T^0 = L^{1-3a_2-b_2+c_2}\ M^{a_2+b_2}\ T^{-1-b_2}$$
$$b_2 = -1,\ a_2 = 1\ and\ c_2 = 1 \qquad B\text{–}8$$
$$Therefore\ \Pi_2 = v_d\ {\rho_L}^1\ {\mu_L}^{-1}D^1 = \frac{\rho_L v_d D}{\mu_L} = Re_{v_d}$$

From relations B–7 and B–8, it can be shown that

$$\frac{\Pi_2}{{\Pi_1}^{1/2}} = \frac{\rho_L v_d D}{\mu_L} \times \frac{\mu_L}{\rho_L(g\ D^3)^{1/2}} = \frac{v_d}{(gD)^{1/2}} = Fr_{v_d} \qquad B\text{–}9$$

According to relation B–4:

$$\Pi_3 = M^0L^0T^0 = (MT^{-2})(ML^{-3})^{a_3}(ML^{-1}T^{-1})^{b_3}(L)^{c_3}$$
$$M^0L^0T^0 = L^{-3a_3-b_3+c_3}\ M^{1+a_3+b_3}\ T^{-2-b_3}$$
$$b_3 = -2,\ a_3 = 1\ and\ c_3 = 1 \qquad B\text{–}10$$
$$Therefore\ \Pi_3 = \sigma\ {\rho_L}^1\ {\mu_L}^{-2}D^1 = \frac{\sigma\ \rho_L D}{{\mu_L}^2}$$

From relations B–7 and B–10, it can be shown that:

$$\frac{\Pi_1}{\Pi_3} = \left(\frac{g\ {\rho_L}^2D^3}{{\mu_L}^2}\right)\left(\frac{{\mu_L}^2}{\sigma\ \rho_L D}\right) = \frac{g\ \rho_L D^2}{\sigma} = Eo \qquad B\text{–}11$$

Lastly, according to relation B–5:

$$\Pi_4 = M^0L^0T^0 = (L)(ML^{-3})^{a_4}(ML^{-1}T^{-1})^{b_4}(L)^{c_4}$$
$$M^0L^0T^0 = L^{1-3a_4-b_4+c_4}\ M^{a_4+b_4}\ T^{-b_4} \qquad B\text{–}12$$
$$b_4 = 0,\ a_4 = 0\ and\ c_4 = -1$$

$$Therefore\ \Pi_4 = L_{TB}\ \rho_L{}^0\ \mu_L{}^0 D^{-1} = \frac{L_{TB}}{D}$$

The final step is setting out the dimensionless relationship and rearranging the terms, which is done through the following steps:

$$\frac{\Pi_2}{\Pi_1{}^{1/2}} = f\left[\frac{\Pi_1}{\Pi_3}\ ,\ \Pi_2, \Pi_4\right] \tag{B–13}$$

Hence, $Fr_{v_d} = \frac{{v_d}^2}{gD} = f\left[Eo\ = \frac{g\rho_L D^2}{\sigma}, Re_{v_d} = \frac{\rho_L v_d D}{\mu_L}\ , \frac{L_{TB}}{D}\ \right]$

Appendix C Buckingham-Pi Theorem – Near horizontal and horizontal Pipe Case

Using the Buckingham-Pi theorem, the problem of drifting of Taylor bubbles through a stagnant liquid in a ***near horizontal pipe*** with surface tension (σ) can be expressed as follows:

$$\sigma = f\ [\rho_L, \mu_L, g, L_{TB}, D] \qquad C\text{–}1$$

The effect of inclination is introduced in the gravitational acceleration (g), that can have three components g_x, g_y and g_z. According to relation C–1, the number of relevant variables (n) is 6, the number of repeating variables (k) (scaling independent dimensions) is 3 (M, L and T) and the number of dimensionless groups (Πs), $n - k = 3$. This result in the following set of dimensionless groups:

$$\Pi_1 = g\ \rho_L{}^{a1}\ \mu_L{}^{b1} D^{c1} \qquad C\text{–}2$$
$$\Pi_2 = \sigma\ \rho_L{}^{a2}\ \mu_L{}^{b2} D^{c2} \qquad C\text{–}3$$
$$\Pi_3 = L_{TB}\ \rho_L{}^{a3}\ \mu_L{}^{b3} D^{c3} \qquad C\text{–}4$$

where M is the mass, L is the length and T is the time. The three repeating variables (k), are given by a, b and c. According to the MLT system, these parameters are chosen to make each of the above relations in a dimensionless form and given by ρ_L, μ_L and D. The dimensions are defined as follows:

$$\left.\begin{aligned} \rho &= ML^{-3} \\ \mu &= ML^{-1}T^{-1} \\ g &= LT^{-2} \\ L_{TB} &= L \\ D &= L \\ \sigma &= MT^{-2} \end{aligned}\right. \qquad C\text{–}5$$

Accordingly, the relations C–2 to C–4 are resolved as follows:

$$\Pi_1 = M^0L^0T^0 = (LT^{-2})(ML^{-3})^{a_1}(ML^{-1}T^{-1})^{b_1}(L)^{c_1} \qquad C\text{–}6$$

$$M^0L^0T^0 = L^{1-3a_1-b_1+c_1}\ M^{a_1+b_1}\ T^{-2-b_1}$$

$$b_1 = -2,\ a_1 = 2\ and\ c_1 = 3$$

$$Therefore\ \Pi_1 = g\ {\rho_L}^2\ {\mu_L}^{-2}D^3 = \frac{g\ {\rho_L}^2D^3}{{\mu_L}^2} = \left(\frac{g\ {L_{TB}}^3}{{\nu_L}^2}\right)\left(\frac{D}{L_{TB}}\right)^3$$

According to relation C–3:

$$\Pi_2 = M^0L^0T^0 = (LT^{-1})(ML^{-3})^{a_2}(ML^{-1}T^{-1})^{b_2}(L)^{c_2}$$

$$M^0L^0T^0 = L^{-3a_2-b_2+c_2}\ M^{1+a_2+b_2}\ T^{-2-b_2}$$

$$b_2 = -2,\ a_2 = 1\ and\ c_2 = 1 \qquad C\text{–}7$$

$$Therefore\ \Pi_2 = \sigma\ {\rho_L}^1\ {\mu_L}^{-2}D^1 = \frac{\rho_L\sigma D}{{\mu_L}^2}$$

From relations C–6 and C–7, it can be shown that:

$$\frac{\Pi_1}{\Pi_2} = \left(\frac{g\ {\rho_L}^2D^3}{{\mu_L}^2}\right)\left(\frac{{\mu_L}^2}{\rho_L\sigma D}\right) = \frac{g\rho_L D^2}{\sigma} = Eo \qquad C\text{–}8$$

According to relation C–4:

$$\Pi_3 = M^0L^0T^0 = L(ML^{-3})^{a_3}(ML^{-1}T^{-1})^{b_3}(L)^{c_3}$$

$$M^0L^0T^0 = L^{1-3a_3-b_3+c_3}\ M^{a_3+b_3}\ T^{-b_3}$$

$$b_3 = 0,\ a_3 = 0\ and\ c_3 = -1 \qquad C\text{–}9$$

$$Therefore\ \Pi_3 = L_{TB}D^{-1} = \frac{L_{TB}}{D}$$

From relations C–6 and C–9, it can be shown that:

$$\Pi_1\Pi_3 = \left(\frac{g\ {L_{TB}}^3}{{\nu_L}^2}\right)\left(\frac{D}{L_{TB}}\right)^3\left(\frac{L_{TB}}{D}\right) = \left(\frac{g\ {L_{TB}}^3}{{\nu_L}^2}\right)\left(\frac{D}{L_{TB}}\right)^2 = Ga_R \qquad C\text{–}10$$

That is $Ga_R = f\left[Eo, \frac{L_{TB}}{D}\right]$

It can be concluded that the sole governing parameters for the near horizontal case are the reduced Galilei number (Ga_R), Eötvös number (Eo) and $\frac{L_{TB}}{D}$.

However, for the case when the pipe is horizontal, that is $\gamma = 90°$, the problem can be expressed as follows:

$$\sigma = f\;[\rho_L, g, L_{TB}, D] \qquad C\text{–}11$$

According to relation C–11, the number of relevant variables (n) is 5, the number of repeating variables(k) is 3 $(M, L$ and $T)$ and the number of dimensionless groups (Πs), $n - k = 2$. This results in the following set of dimensionless groups:

$$\Pi_1 = \sigma\,{\rho_L}^{a1} g^{b1} D^{c1} \qquad C\text{–}12$$

$$\Pi_2 = L_{TB}\,{\rho_L}^{a2} g^{b2} D^{c2} \qquad C\text{–}13$$

Using the dimensions defined in C–5, the relations C–12 and C–13 are resolved as follows:

$$\begin{aligned}
&\Pi_1 = M^0L^0T^0 = (MT^{-2})(ML^{-3})^{a_1}(LT^{-2})^{b_1}(L)^{c_1}\\
&M^0L^0T^0 = L^{b_1+c_1-3a_1}\,M^{1+a_1}\,T^{-2-2b_1}\\
&b_1 = -1,\ a_1 = -1\ and\ c_1 = -2 \qquad C\text{–}14\\
&Therefore\ \ \Pi_1 = \sigma{\rho_L}^{-1}g^{-1}\,D^{-2} = \frac{\sigma}{\rho_L g\,D^2} = \frac{1}{Eo}
\end{aligned}$$

According to relation C–13:

$$\begin{aligned}
&\Pi_2 = M^0L^0T^0 = (L)(ML^{-3})^{a_2}(LT^{-2})^{b_2}(L)^{c_2}\\
&M^0L^0T^0 = L^{1+c_2+b_2}\,M^{a_2}\,T^{-2b_2}\\
&b_2 = 0,\ a_2 = 0\ and\ c_2 = -1 \qquad C\text{–}15\\
&Therefore\ \ \Pi_2 = L_{TB}D^{-1} = \frac{L_{TB}}{D}
\end{aligned}$$

That is $Eo = f\left[\frac{L_{TB}}{D}\right]$

To sum up, referring to equations C–14 and C–14, it can be concluded that the sole governing parameters that governs the pressure field distribution around the stagnant deformed bubble are Eötvös number (Eo) and $\frac{L_{TB}}{D}$.

List of Publications

- Massoud, E.Z., Xiao, Q., Teamah, M.A. and Saqr, K.M., 2016. Numerical study of hydrodynamic characteristics of gas liquid slug flow in vertical pipes. *Journal of Applied Mechanical Engineering*, *5*(6) – *Global Summit and Expo on Fluid Dynamics & Aerodynamics Conference, London, UK*
- Massoud, E.Z., Xiao, Q., El-Gamal, H.A. and Teamah, M.A., 2018. Numerical study of an individual Taylor bubble rising through stagnant liquids under laminar flow regime. *Ocean Engineering*, *162*, pp.117-137.
- Massoud, E.Z., Xiao, Q. and El-Gamal, H.A., 2019. Numerical Study of an Individual Taylor Bubble Drifting through Stagnant Liquid in an Inclined Pipe *(under review in Ocean Engineering).*